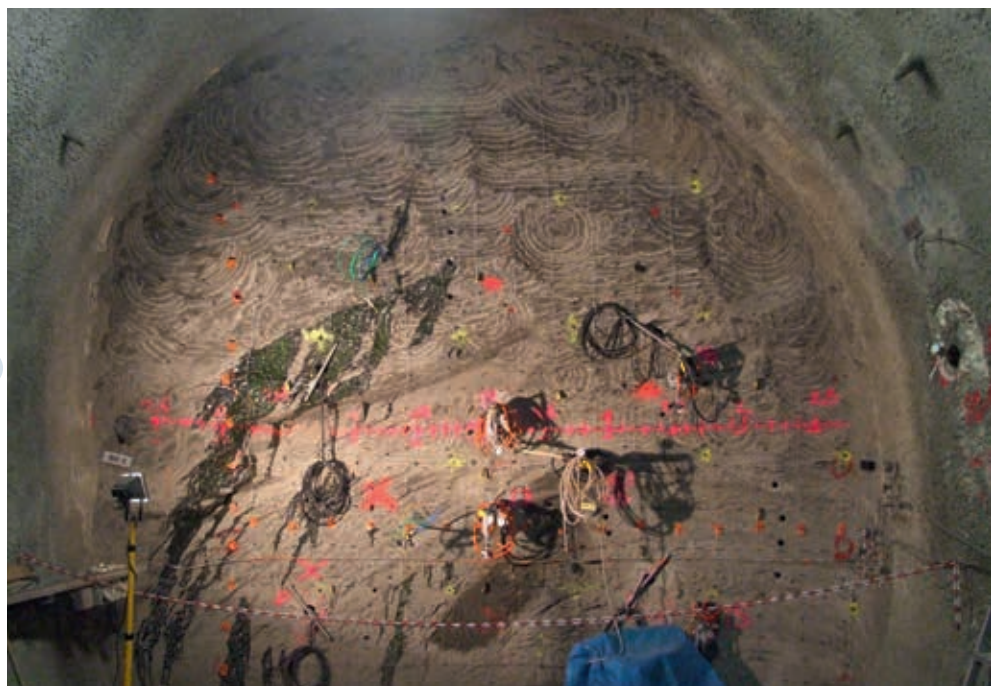


Mont Terri Rock Laboratory

Geophysical investigation of the Excavation Damaged Zone
during a mine-by experiment



Berichte der Landesgeologie
Rapports du Service géologique national
Rapporti del Servizio geologico nazionale
Reports of the Swiss Geological Survey

Christophe Nussbaum and Paul Bossart
Editors



Schweizerische Eidgenossenschaft
Confédération suisse
Confederazione Svizzera
Confederaziun svizra

Federal Department of Defence,
Civil Protection and Sport DDPS
armasuisse
Federal Office of Topography swisstopo
www.swisstopo.ch

Mont Terri Rock Laboratory

Geophysical investigation of the Excavation Damaged Zone
during a mine-by experiment

Reports of the Swiss Geological Survey
Berichte der Landesgeologie
Rapports du Service géologique national
Rapporti del Servizio geologico nazionale

Christophe Nussbaum and Paul Bossart
Editors



Schweizerische Eidgenossenschaft
Confédération suisse
Confederazione Svizzera
Confederaziun svizra

Federal Department of Defence,
Civil Protection and Sport DDPS
armasuisse

Federal Office of Topography swisstopo
www.swisstopo.ch

Editor

Swiss Geological Survey (SGS)

Recommended quotation

NUSSBAUM, C. & BOSSART, P. (2014): Mont Terri Rock Laboratory – Geophysical investigation of the Excavation Damaged Zone during a mine-by experiment. – Ber. Landesgeol. 5.

Cover photo

View of the GA04 face (GM80) before excavation. Mont Terri Rock Laboratory. © swisstopo

Impression

1500 copies

Order

swisstopo, CH-3084 Wabern, or e-mail to mapsales@swisstopo.ch

Copyright

© swisstopo, CH-Wabern, 2014

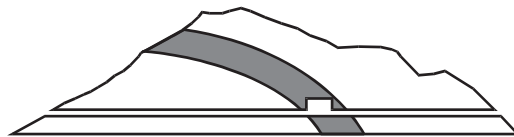
ISSN 1661-9285

ISBN 978-3-302-40090-7



Schweizerische Eidgenossenschaft
Confédération suisse
Confederazione Svizzera
Confederaziun svizra

Federal Department of Defence,
Civil Protection and Sport DDPS
armasuisse
Federal Office of Topography swisstopo
www.swisstopo.ch



Mont Terri Project



Supported by:
Federal Ministry
of Education
and Research
on the basis of a decision
by the german Bundestag

Funded by ANDRA and CNRS through FORPRO II



Organisations involved

Project Partners

ANDRA	Agence nationale pour la gestion des déchets radioactifs, France
BGR	Bundesanstalt für Geowissenschaften und Rohstoffe, Germany
CHEVRON	Chevron Energy Technology ETC, US
CRIEPI	Central Research Institute of Electric Power Industry, Japan
DOE	U.S. Department of Energy, Office of Nuclear Energy, US
ENRESA	Empresa Nacional de Residuos Radiactivos, S.A., Spain
ENSI	Swiss Federal Nuclear Safety Inspectorate, Switzerland
GRS	Gesellschaft für Anlagen- und Reaktorsicherheit mbH, Germany
IRSN	Institut de radioprotection et de sûreté nucléaire, France
JAEA	Japanese Atomic Energy Agency, Japan
NAGRA	National Cooperative for the Disposal of Radioactive Waste, Switzerland
NWMO	Nuclear Waste Management Organisation, Canada
OBAYASHI	Obayashi Corporation, Japan
SCK•CEN	Studiecentrum voor Kernenergie, Centre d'étude de l'énergie nucléaire, Belgium
swisstopo	Federal Office of Topography, Switzerland

Direction of the Project and Project Management

swisstopo	Federal Office of Topography
-----------	------------------------------

Responsible for the Mont Terri motorway tunnel system

FEDRO	Federal Roads Office, Switzerland
-------	-----------------------------------

Authorisations

RCJU	République et Canton du Jura, Département de l'Environnement et de l'Équipement
------	---

Authors and Chapters

Extended Summary

C. Nussbaum, D. Gibert, Y. Guéguen, Y. Le Gonidec, F. Nicollin, A. Maineult, B. Thomas, P.M. Adler

1 Description of the mine-by experiment

D. Gibert, C. Nussbaum, Y. Guéguen, P. Pinettes, Y. Le Gonidec, F. Nicollin, A. Maineult, B. Thomas

2 Excavation history of the EZ-G08 segment

P. Bossart, F. Burrus, C. Nussbaum

3 Geological characterisation of the investigated rock mass

C. Nussbaum, C. Girardin, N. Badertscher

4 Statistical analysis of the fracture network

J.-F. Thovert, V.V. Mourzenko, P.M. Adler, C. Nussbaum

5 Acoustic experiments: seismic survey and micro-seismicity

Y. Le Gonidec, J. Sarout, J. Wassermann, A. Schubne, D. Gibert, C. Nussbaum, B. Kergosien, A. Maineult, Y. Guéguen

6 Geo-electrical experiments

F. Nicollin, D. Gibert, C. Nussbaum, N. Lesparre

7 A noble gas study in the Excavation Damaged Zone (EDZ)

B. Thomas, B. Lavielle, A. Maineult, C. Nussbaum, E. Gilabert

8 Self-potential monitoring in BEZ-G5 borehole

A. Maineult, C. Nussbaum, K. Wieczorek, D. Gibert, B. Kergosien, F. Nicollin, K. Mahiouz, N. Lesparre

9 Recommendations for further works and perspectives

J. Wassermann, Y. Le Gonidec, D. Gibert, F. Nicollin, A. Maineult, B. Thomas

List of Authors

C. Nussbaum, P. Bossart	swisstopo, St-Ursanne, Switzerland	 Schweizerische Eidgenossenschaft Confédération suisse Confederazione Svizzera Confederaziun svizra
D. Gibert, A. Mainault, N. Lesparre, K. Mahiouz	Institut de Physique du Globe, UMR 7174, Paris, France	
Y. Le Gonidec, F. Nicollin, B. Kergosien	Géosciences Rennes, Université de Rennes 1, UMR 6118 CNRS, Rennes, France	
A. Schubnel, Y. Guéguen	ENS: Laboratoire de Geologie, Ecole Normale Supérieure de Paris, CNRS/INSU UMR 8538 Paris, France	
J. Wassermann	Géosciences et Environnement Cergy, Université de Cergy-Pontoise, France	
P.M. Adler	Université Pierre et Marie Curie, Metis, Paris, France	
J.-F. Thovert, V.V. Mourzenko	CNRS, Institut PPRIME, SP2MI, Futuroscope, France	
B. Thomas, B. Lavielle, E. Gilabert	CNAB: Centre d'Etudes Nucléaires de Bordeaux, Université Bordeaux 1, UMR 5797 CNRS, Gradignan, France	
J. Sarout	CSIRO, Earth Science and Resource Engineering, Perth, Australia	
K. Wiczorek	GRS, Gesellschaft für Anlagen- und Reaktorsicherheit (GRS) mbH, Braunschweig, Germany	 Supported by Federal Ministry of Education and Research on the basis of a decision by the German Bundestag
F. Burrus	Groupe Grands Travaux, Delémont, Switzerland	
C. Girardin, N. Badertscher	Institut Géotechnique SA, Bassecourt, Switzerland	
P. Pinettes	CEREGE/G.IS., Université de Nîmes, France, GeophyConsult, Montpellier, France	

swisstopo is pleased to present this report on the geophysical investigation of the Excavation Damaged Zone during a mine-by experiment in the international Mont Terri rock laboratory.

The Mont Terri rock laboratory started operation in January 1996 as part of the international Mont Terri project. Research is carried out in the underground facility, which is located sideways of the Mont Terri motorway tunnel (Canton Jura, Switzerland). The aim of the project is the geological, hydrogeological, geochemical and geotechnical characterisation of clay formations, specifically the Opalinus Clay. Fifteen partners from European countries, Canada, the United States and Japan now participate in the project: ANDRA, BGR, CHEVRON, CRIEPI, DOE, ENRESA, ENSI, GRS, IRSN, JAEA, NAGRA, NWMO, OBAYASHI, SCK•CEN and swisstopo.

swisstopo has acted as the operator of the rock laboratory since 2006 and is responsible for the implementation of the research programmes decided on by the partners.

This work was financially supported by CNRS and ANDRA through the GNR FORPRO II (actions 2007.1 and 2008.6). Up to 10 research organisations, mainly French universities, were involved in this mine-by experiment.

A large number of scientists, engineers and technicians have contributed significantly to the success of the research and the present report. The editors would especially like to thank Prof. J. Lancelot from FORPRO, the initiator of the EZ-G mine-by test, and his colleagues Prof. M. Cathelineau, A. Le Bauzec, P. Pinettes, and P. Verdoux. Thanked is also ANDRA, especially J. Delay and P. Lebon for their scientific and financial support. Site support provided by T. Theurillat, N. Badertscher, C. Girardin, C. Veuve, V. Risse and G. Joliat is acknowledged.

swisstopo
Director Mont Terri Project
Dr. Paul Bossart

swisstopo freut sich, Ihnen hier den Bericht über geophysikalische Untersuchungen in der Auflockerungszone präsentieren zu dürfen. Es handelt sich um ein Mine-by-Experiment aus dem internationalen Mont-Terri-Felslabor.

Das Felslabor Mont Terri besteht seit Januar 1996. Im Rahmen des internationalen Mont-Terri-Projektes wird seitlich des Mont-Terri-Autobahntunnels (Kanton Jura, Schweiz) geforscht. Das Hauptziel dieses Projektes ist die geologische, hydrogeologische, geochemische und geotechnische Charakterisierung von Tongesteinen, im speziellen des Opalinus-Tons. Heute sind 15 Partner aus Europa, Kanada, den USA und Japan am Projekt beteiligt. Es sind dies ANDRA, BGR, CHEVRON, CRIEPI, DOE, ENRESA, ENSI, GRS, IRSN, JAEA, NAGRA, NWMO, OBAYASHI, SCK•CEN und swisstopo.

swisstopo ist seit 2006 der Betreiber des Felslabors Mont Terri und ist verantwortlich für die Umsetzung der von den Partnern beschlossenen Forschungsprogramme.

Diese Arbeit wurde durch die CNRS und die ANDRA via die GNR FORPRO II finanziert (actions 2007.1 und 2008.6). Bis zu 10 Forschungsorganisationen, vor allem aus französischen Universitäten, beteiligten sich an diesem Mine-by-Experiment

Eine grosse Anzahl von Wissenschaftlern, Ingenieuren und Technikern haben wesentlich zum Forschungserfolg und zum vorliegenden Bericht beigetragen. Der Herausgeber dankt speziell Prof. J. Lancelot, FORPRO, dem Initiator des EZ-G Mine-by-Experimentes, und seinen Kollegen, Prof. M. Cathelineau, A. Le Bauzec, P. Pinettes und P. Verdoux. Der Dank geht auch an ANDRA, speziell erwähnt sind hier J. Delay und P. Lebon für ihre wissenschaftliche und finanzielle Unterstützung. Die technische Unterstützung vor Ort durch T. Theurillat, N. Badertscher, C. Girardin, C. Veuve, V. Risse und G. Joliat sei hier erwähnt und verdankt.

swisstopo
Direktor Mont-Terri-Projekt
Dr. Paul Bossart

swisstopo a l'honneur de vous présenter à travers le présent volume une synthèse des résultats d'une expérience de mine-by réalisée dans le laboratoire international du Mont Terri. Cette expérience avait pour objectif l'investigation de la zone endommagée par le creusement d'une galerie par différentes méthodes géophysiques.

Le projet international du Mont Terri a débuté en janvier 1996 dans le laboratoire souterrain du Mont Terri, excavé en annexe de la galerie de sécurité du tunnel du même nom proche de St-Ursanne (Canton du Jura, Suisse). La caractérisation géologique, hydrogéologique, géochimique et géotechnique d'une formation argileuse, en particulier de l'Argile à Opalinus, est l'objectif principal de ce projet. Quinze partenaires provenant d'Europe, de l'Amérique du nord et du Japon se sont réunis autour de ce projet. Il s'agit de l'ANDRA, BGR, CHEVRON, CRIEPI, DOE, ENRESA, GRS, IFSN, IRSN, JAEA, NAGRA, NWMO, OBAYASHI, SCK•CEN et swisstopo.

Depuis 2006, swisstopo est responsable de l'exploitation du laboratoire souterrain ainsi que de la gestion du Projet Mont Terri, et en particulier de la mise en œuvre du programme de recherche établi par les partenaires.

Cette étude a reçu le financement du CNRS et de l'ANDRA à travers du groupement national de recherche français GNR FORPRO II (actions 2007.1 et 2008.6). Pas moins de 10 organisations de recherche, principalement françaises, ont œuvré à la réalisation et au succès de cette expérience de mine-by.

L'élaboration de ce rapport est le fruit de la contribution d'un nombre important de scientifiques, d'ingénieurs et de techniciens qui ont œuvré au succès de l'expérience mine-by présentée dans ce volume. De nombreuses réunions de travail fructueuses ont eu lieu au laboratoire souterrain ou ailleurs, sans oublier les semaines et mois d'installation et de mesures effectuées par les techniciens et ingénieurs. Les éditeurs adressent leurs remerciements aux Prof. J. Lancelot et Prof. M. Cathelineau, directeurs respectifs de FORPRO I et II. Leurs collègues, A. Le Bauzec, P. Pinettes, P. Verdoux et C. Léonard sont également remerciés. J. Delay et P. Lebon sont également chaleureusement remerciés pour leur soutien scientifique et financier à travers l'ANDRA. Le soutien technique et logistique sur site offert par T. Theurillat et J. Joliat ainsi que la documentation géologique réalisée par N. Badertscher, C. Girardin, C. Veuve et V. Risse sont également à relever et à remercier.

swisstopo
Directeur du Projet Mont Terri
Dr. Paul Bossart

swisstopo ha l'onore di presentavi, attraverso il presente volume, una sintesi dei risultati di un esperimento di mine-by realizzata nel laboratorio internazionale di Mont Terri. Questo esperimento aveva come obiettivo, attraverso differenti metodi geofisici, l'investigazione della zona danneggiata dallo scavo di una galleria.

Il progetto internazionale di Mont Terri è iniziato nel gennaio 1996 nel laboratorio sotterraneo di Mont Terri, scavato adiacente la galleria di sicurezza del tunnel omonimo vicino a St-Ursanne (Canton Giura, Svizzera). La caratterizzazione geologica, idrogeologica, geochemica e geotecnica di una formazione argillosa, in particolare dell'Argilla a Opalinus, è l'oggetto principale di questo progetto. Quindici partner provenienti dall'Europa, dell'America del nord e dal Giappone si sono riuniti attorno a questo progetto. Si tratta di ANDRA, BGR, CHEVRON, CRIEPI, DOE, ENRESA, GRS, IFSN, IRSN, JAEA, NAGRA, NWMO, OBAYASHI, SCK•CEN e swisstopo.

Dal 2006 swisstopo è il gestore del laboratorio sotterraneo e il responsabile del Progetto Mont Terri e in particolare, dell'attuazione del programma di ricerca stabilito dai partner.

Questo studio ha ricevuto il finanziamento del CNRS e dell'ANDRA attraverso il raggruppamento nazionale di ricerca francese GNR FORPRO II (azioni 2007.1 e 2008.6). Non meno di 10 organizzazioni di ricerca, principalmente francesi, hanno lavorato alla realizzazione e al successo di questa esperienza mine-by.

L'elaborazione di questo rapporto è il frutto della contribuzione di un importante numero di scienziati, d'ingegneri e di tecnici che hanno contribuito al successo dell'esperienza mine-by presentata in questo volume. Numerose e fruttuose riunioni di lavoro hanno avuto luogo nel laboratorio sotterraneo e altrove, senza dimenticare le settimane e mesi d'installazione e di misurazioni effettuate dai tecnici e dagli ingegneri. I redattori indirizzano i loro ringraziamenti ai Prof. J. Lancelot e Prof. M. Cathelineau, direttori rispettivi di FORPRO I e II. I loro colleghi, A. Le Bauzec, P. Pinettes, P. Verdoux et C. Léonard sono ugualmente ringraziati. J. Delay et P. Lebon sono altrettanto calorosamente ringraziati per il loro sostegno scientifico e finanziario attraverso l'ANDRA. Il sostegno tecnico e logistico sul posto offerto da T. Theurillat et J. Joliat, come la documentazione geologica realizzata da N. Badertscher, C. Girardin, C. Veuve et V. Risse, sono ugualmente da citare e ringraziare.

swisstopo
Direttore del Progetto Mont Terri
Dr. Paul Bossart

Glossary

CLVD	Compensated Linear Vector Dipole seismic source
DC	Double-Couple seismic source
EDZ	Excavation Damaged Zone
EdZ	Excavation Disturbed Zone
ERT	Electrical Resistivity Tomography
EZ-G08 segment	abbreviation given to the investigated rock mass in this study
ISO	Isovolumetric seismic source
Ga04	End-face of Gallery 04 at gallery metre GM 167 (or GM 80 according to the Gallery 04 nomenclature)
Ga08	Front of Gallery 08 at gallery metre GM 159
MSE	Micro-Seismic Event
SP	Spontaneous Potential

Extended Summary

C. NUSSBAUM, D. GIBERT, Y. GUÉGUEN, Y. LE GONIDEC, F. NICOLLIN, A. MAINEULT, B. THOMAS & P.M. ADLER

The Opalinus Clay has been selected to be the host for the deep geological disposal of nuclear waste in Switzerland. Construction of an underground opening perturbs the surrounding rock mass and leads to the creation of an Excavation Damaged/Disturbed Zone (EDZ/EdZ). Degradation of the rock mass may or may not lead to significant changes in flow and transport properties; the former in case of EDZ and the latter in case of EdZ. In the context of deep geological disposal, it is of prime importance to understand the processes through which excavation-induced perturbations are created both in terms of time and space, as well as their impact on the properties of the host rock.

In 2008, the excavation of Gallery 08 provided the opportunity to study the junction between two galleries: an existing one represented by the end-face of Gallery 04 (Ga04) and the gallery under construction called “Gallery 08”. The rock mass segment in between, called “EZG-08 segment”, had a length of 8 metres and was located between Gallery location GM 159 (GM = Gallery metre) and GM 167 (cutting through). This rock mass was excavated in July and August 2008. Before its excavation, this rock mass had been extensively instrumented with a number of geophysical methods to monitor evolution of the Excavation Damaged Zone (EDZ in both time and space during and after the excavation process). This configuration allowed us to study two EDZ with different ages: the existing Ga04 face, which was 4 years old, as the new Gallery 08 (Ga08) was still under excavation. In total, 37 boreholes were drilled in the course of this mine-by experiment. They were drilled into the Ga04 face (28 boreholes) and the Ga08 face (9 boreholes). The excavation process stopped on July 11, 2008 when the front reached GM 159. After a two-week break between July 28 and August 5, 2008, which was necessary to instrument the Ga08 front, the upper part of the first section (from GM 159.1 to GM 163.0) was excavated. The lower part of the profile was then excavated until August 13, 2008. From August 18 to August 22, 2008, the main tunnel was excavated up to GM 166.0. The breakthrough finally took place on August 25 at 10:00 hours.

Statistical analysis of the fracture network

We describe the analysis and characterisation of the fracture network which was mapped in Gallery 08 and its modelling in order to use it later for a realistic reconstruction of numerical fracture networks and the determination of flow properties.

A previous work dealt with the reconstruction of a fracture network observed in Gallery 04. The trace maps of the Gallery 04 and of the EZ-G08 segment were first digitized and then used in various ways to characterize the data. The traces were divided into two groups, i.e., the pre-existing

faults in the gallery and the fractures of the excavated damaged zone (EDZ) in the niche. Each group was analysed individually. The number of data for the faults turned out to be statistically significant, though it was very limited for the EDZ fractures. The major statistical characteristics of the traces were extracted in both cases, and a reconstruction procedure developed and tested. A full example was worked out; a gallery immersed in a reconstructed fractured porous medium was meshed, and the electrical field created by a dipole at the wall calculated by solving the three dimensional Laplace equations in the fractures and the porous medium.

The present work addresses the fracture network in Gallery 08 in the same site. We drew exhaustive trace maps for the invert, ceiling, and side walls, and for the excavation front at successive positions, recording the pre-existing faults, the excavation-induced fractures and the stratigraphic bedding. Orientations were also recorded for a subset of the traces. However, although several niches were dug from the gallery, no information regarding the extension of the EDZ fractures within the embedding rock could be obtained. We focus on the quantification of the observations of various kinds of objects on the gallery walls in terms of density, orientation distribution, and spatial arrangement. Since the gallery consists of a curved and a straight section, it was possible to examine the correlation between the EDZ fracture orientation and the faulting, bedding and digging directions. Finally, we propose methods for three-dimensional modelling of the fracture network and for determining EDZ transport properties.

Seismic survey and micro-seismicity

Among the geophysical methods applied during these experiments, we developed and carried out acoustic experiments aiming at detecting any space-time changes of the EZ-G08 segment induced by the excavation procedure. The purpose of the present contribution is to better understand the EDZ initiation processes and short-term evolution during the excavation of an underground gallery in an argillaceous formation. The experiments consisted of two complementary measurements. The first was an active seismic method involving a controlled acoustic source. In the following we refer to this as seismic survey measurements. We used this method to characterize the elastic properties of the rock mass, in particular in terms of P-wave velocity. The second dealt with a passive seismic method based on the detection of acoustic emissions, i.e. micro-seismic events (MSEs).

We acquired a very large set of acoustic data, including both active and passive measurements. The active measurements indicated a strong elastic anisotropy of the P-wave velocity wavefield: a low velocity of 2750 m/s in the direction of

wave propagation perpendicular to the bedding structure, and a high velocity of 3300 m/s along the bedding. This velocity model was used to locate the active acoustic surveys, evidencing the efficiency of the location algorithm. After completing pre-processing steps to organize and control the passive acoustic measurements, i.e. the acoustic emission detected during the experiment, we could identify only a few hundreds of events as micro-seismic events.

A burst of micro-seismic events was highlighted in the shaly facies sidewall of the gallery, but unfortunately, we could not determine the associated source mechanisms due to the low signal-to-noise ratio of the recorded waveforms. A second cluster of 61 micro-seismic events occurred on July 12 and 13, i.e., in the course of the first two days after the excavation had stopped. Both their spatial and temporal locations and their damage mechanisms are consistent and allow us to interpret the damages induced in the rock mass surrounded by the excavation operation. In the vicinity of the excavation front, we highlight a dominant DC component due to the shear movement along pre-existing features, such as bedding-parallel faults and bedding planes oriented sub-parallel to the major axis of the ambient stress field. In the middle part of the shaly facies sidewall of the front-face, the dominant CLVD component suggests an axial splitting, and indicates a possible zone of spalling damage initiation.

In conclusion, the EDZ initiation during a mine-by of the Opalinus Clay developed in a particularly complex tectonic zone, in relation with the lithology (MSEs detected in the shaly facies, none in the sandy facies. Both facies are anisotropic, with contrasting mechanical properties) and a complex perturbation of the stress field (increase, decrease and rotation of the stress around the opening. These *in situ* results are consistent with previously published observations in crystalline rocks and clearly contribute to filling our knowledge gap for clayey formations.

Geo-electrical experiment

We performed electrical conductivity measurements in the EZ-G08 segment from December 2007 to August 2008 to study the evolution of the EDZ at time scales ranging from hours to months. These measurements were carried out from the end of the Gallery 04, using arrays of electrodes installed on the face and in boreholes perpendicular to the face. In December 2007, we performed a resistivity survey of the EDZ at the back of the Gallery 04 using Wenner measurements along profiles from the gallery face. In April and May 2008, we measured the anisotropy of the electrical resistivity using combinations of square arrays both on the Ga04 face and in eight small boreholes perpendicular to the face. In May 2008, we equipped four long boreholes perpendicular to the face and in July 2008 we repeated daily resistivity measurements in the EZ-G08 segment. During this period, the excavation of the Gallery 08 was in progress: in May 2008, the front was a few tens of m from the EZ-G08 segment; on July 1, 2008, the front was 22 m from the Ga04 face, and the mean excavation rate was then about 1.3 m per day; the north-west edge of the EZ-G08 segment, 8 m away from the Ga04 face (GM 159), was reached on July 11, and the excavation stopped until July 28. Between July 29 and August 5, an additional 4 metres were excavated, and the last 4 me-

tres were excavated during the second half of August 2008.

By inverting the anisotropy data, we could recover the resistivity tensor characteristic of the electrical properties associated with about 1 m depth in 18 areas of the Ga04 face. The data analysis of the monitoring performed in July 2008 showed spatial and temporal variations of the electrical properties in the EZ-G08 segment when it was reached by the Ga08 excavation front.

The geo-electrical experiments performed in the EZ-G08 segment show that resistivity is a useful parameter to characterize and monitor the EDZ. The inversion of data devoted to the study of anisotropy yielded a resistivity tensor whose geometry in Opalinus Clay appears controlled by both the stratigraphy and the presence of an EDZ at the rear of a gallery. All the data acquired from boreholes for monitoring the EZ-G08 segment during the last steps of the Ga08 excavation are very consistent and reflect: i) a transition of the shaly facies to sandy facies a few m at the rear to the Ga04 face, ii) an old Ga04 EDZ, iii) a new EDZ caused by the Ga08 excavation, with changes observed even after cessation of excavation up to several m behind the Ga08 front, iv) displacements of pore water by suction effects due to decompression.

Noble gas study

Noble gases are particularly suitable for studying gas transport processes in rocks and the existence of connected fracture networks since they do not react with constituents of the host media. In claystones, radiogenic ^4He atoms are produced by alpha decay of thorium and uranium. They are released from the host mineral by recoil during the production and then diffuse through damages created in the minerals by energetic alpha particles. They accumulate in pore water as a function of the transfer rate between rock and water and of the diffusive process occurring since the formation time of the rock. Depletion in He can be observed in the EDZ. Other noble gases (Neon, Argon, Krypton and Xenon) trapped in the claystones have essentially an atmospheric origin, with the exception of ^{40}Ar , which is produced *in situ* by decay of radioactive potassium ^{40}K . Their content can consequently increase as desaturation processes occur.

We carried out the measurements reported here to characterize the evolution of profiles of noble gas concentrations in the EDZ and interpret them in terms of gaseous exchanges between the rock-mass and the atmosphere of the gallery. In other words, we would like to determine how the *in situ* gases diffuse to the gallery. And, reciprocally, how deep can the air of the gallery invade the rock mass? To access to the long-term dynamics of the noble gas evolution, we studied the core of the 12 m long borehole BEZ-G5. This borehole was drilled in the end-face of Gallery 04 on September 12, 2007, 4 years after the tunnelling. For short-term dynamics, we considered the cores of the 3-m long boreholes BEZ-G36, BEZ-G39 and BEZ-G44 drilled close to each other in the front of Ga08 on July 14, 21 and 28, 2008, respectively, i.e., during the pause in the excavation of Gallery 08 from July 11, 2008.

Noble gas concentrations in the core of borehole BEZ-G5 evidenced that the first two metres of rock mass behind the end-face of Gallery 04 exhibit behaviour different from

the deeper ones. The noble gas content attests the development of an EDZ after the excavation of Gallery 04, yielding desaturation and exchange processes by reactivating pre-existing tectonic fractures that accommodated the stress change in the near field, rather than the development of new fractures induced by tunnelling. Noble gas concentrations in BEZ-G36, G39 and G44 show that the loss in He is very rapid (on the order of days), at least in the first 50 cm, meaning that dynamic gas transfer occurred in fractures created or reactivated by the excavation process, here again attesting to the formation of an EDZ.

Self-potential monitoring

A few weeks after drilling borehole BEZ-G5 in September 2007, inflows of water occurred that continued until the junction of galleries Ga08 and Ga04 in August 2008. The water produced by the borehole muddied the surface of end-face Ga04.

Even though the hydraulic conductivity of Opalinus Clay is extremely low, in the range 10^{-14} to 10^{-12} m s⁻¹, volumes of water amounting to a few litres were commonly released in other boreholes and are called “wet-spots”. Analysis of water routinely sampled from this area yielded a chemical fingerprint of ancient seawater trapped during the deposition of the sediments 175 Ma ago. The Opalinus Clay Formation acting as an aquiclude. Indeed, in the fine pores of Opalinus Clay about 150 litres of water is trapped in each cubic metre of rock mass. A small proportion of this water can be squeezed out of the rock when a pressure change is applied, for instance, as a result of stress modifications induced by tunnel construction.

To obtain information about the water flow-paths and their dynamics, we monitored natural electrical potentials, or self-potentials (SP), on the end-face of Gallery 04 and in borehole BEZ-G5, from February 21 to April 25, 2008. SP signals result from movement of fluids and/or diffusion of ionic concentration or temperature fronts. Interestingly, they are sensitive to any change occurring in these fluid movements. The so-called electrokinetic potential difference between two given points, denoted ΔV , which originates through movement of a circulating electrolyte through a porous medium. This potential is directly proportional to the hydraulic pressure difference, denoted ΔP , applied between these two points, provided that the mineral surface is electrically charged and that fluid can circulate. The electrokinetic coupling coefficient C , equal to the ratio $\Delta V/\Delta P$, depends on the surface properties of the rock and on the chemical properties of the fluid, such as its salinity, pH, or temperature. Due to the small size of pores and to the high electrically charged surface of minerals, the behaviour of C can be rather complex in clayey materials. Water saturation also has a major influence. In the context of the underground rock laboratory, we argue that the only possible

source for SP signals is the electrokinetic phenomenon, since pore water does not present significant variations in salinity or temperature. Since the existence of a hydraulic pressure difference results in a hydraulic flow, provided that the medium is adequately permeable, any local variation of the potential could be reasonably associated with a flow-path. Moreover, any change in ΔP which could be related to a modification of the local permeability or of the hydraulic pressure field linked to damage or stress field, will result in a proportional change in ΔV .

The SP monitoring could therefore provide clues on the temporal dynamics of water flow. To date, only few studies report on the use of the SP method to characterize the fluid circulation in fractured media. We note that in all these works, fluid movement was artificially forced by pumping, contrary to the case reported here, in which the fluid movement, i.e. the natural inflow of pore water into the borehole, occurred naturally.

The SP anomalies evidenced that the first two metres of the rock mass behind the end-face of Gallery 04 exhibit behaviour different from the deeper ones. This is consistent with the conclusions drawn from the geoelectrical measurements and from the noble gas concentrations.

We relate the dynamic SP anomalies occurring after the drilling of boreholes BEZ-G12 to G19 in the end-face of Gallery 04 to modifications in the near stress field, which lead to free water being released from the claystone. This subsequently resulted in a variation of pore pressure and thus to fluid circulation. The comparison of the location of the SP anomalies with the position of fractures mapped after the excavation of segment Ga08 suggest that the drilling operations (primarily the earlier excavation of Gallery 04) have reactivated pre-existing, sealed, macroscale faults, which then acted as flow-paths. We also observed some anomalies located in sandy lenses, which could result from fluid circulation in microscale fractures. Inflow of water in boreholes (observed from the tunnel construction in 1998, or in BEZ-G12 to 15 in July 2008 at the end of the tunnelling of Gallery 08) probably resulted from similar processes induced by excavation operations.

A tentative explanation for the origin and amount of inflowing fluids may be the existence of suitable petrophysical and mechanical properties of Opalinus Clay. Mechanical strain (“squeezing”) of grain skeleton and pore space due to stress redistribution can be considered to cause release of free pore water, even if modifications in pore pressure triggered by drilling and excavation are very small. Water is also unlikely to be released from sandy lenses, since they are less porous and permeable, as well as being highly cemented.

Even though the mechanism of water production is not understood, we argue that self-potential measurements could be used as a passive tool for the monitoring of “wet spots” in argillaceous formations.

Table of Contents

Organisations involved	4	5. Acoustic experiments: seismic survey and micro-seismicity	58
Authors and Chapters	5	5.1 Introduction	58
List of Authors	6	5.2 Description of the experimental setups	58
Preface of the Editors	7	5.2.1 Borehole utilities	58
Vorwort des Herausgebers	7	5.2.2 Acoustic source in BEZ-G5 for seismic survey measurements	58
Preface de l'éditeur	8	5.2.3 Array of acoustic receivers in BEZ-12-15 boreholes	60
Prefazione dell'editore	8	5.2.4 Array of acoustic receivers in BEZ-G16-19 boreholes	60
Glossary	9	5.3 Seismic surveys experiments	61
Extended Summary	10	5.3.1 Description of the experiments	61
List of Figures	15	5.3.2 Temporal changes of the EZ-G08 segment	62
List of Tables	19	5.3.3 P-wave velocity model of the EZ-G08 segment	63
1. Description of the mine-by experiment	21	5.3.4 Location method performed on the seismic surveys	65
1.1 Objectives and strategy	21	5.4 Micro-seismic events: space-time identification and location	66
1.2 Experimental layout	21	5.4.1 Description of the experiments	66
1.3 Experimental layout	25	5.4.2 Identification of micro-seismic events in the raw data set	68
References	26	5.4.3 Spatial location of the micro-seismic events	69
2. Excavation history of the EZ-G08 segment	27	5.4.4 Analysis of damage initiation and propagation in the Opalinus Clay formation	69
References	29	5.5 Conclusion	71
3. Geological characterisation of the investigated rock mass	30	References	75
3.1 Geological setting	30	6. Geo-electrical experiments	76
3.1.1 Facies description	30	6.1 Introduction	76
3.1.2 Fault systems identified in the rock laboratory	30	6.2 Experimental setup	76
3.1.3 Excavation Damaged Zone	33	6.2.1 Layout of electrode arrays	76
3.1.4 Geological and structural mapping of the EZ-G08 segment	34	6.2.2 Measurement principle	76
3.1.5 Geological mapping of drillcores	39	6.3 Field experiment	77
3.2 Visualisation of the fracture network by resin impregnation	39	6.3.1 Electrical resistivity at rear to the Ga04 face	77
3.2.1 Methodology	39	6.3.2 Electrical anisotropy at rear to the Ga04 face	78
3.2.2 Field work	41	6.3.3 Geo-electrical monitoring in the EZ-G08 segment	80
3.2.3 Macroscopic observation of the connectivity of the fracture network	42	6.4 Inversion of the anisotropy data	82
3.2.4 Structural analysis of resin-impregnated drillcores	42	6.4.1 The forward problem	83
3.2.5 Microscopic investigations on thin sections	42	6.4.2 The inverse problem	83
3.3 <i>In-situ</i> stress state	43	6.4.3 Results	83
3.4 Discussion and conclusion	44	6.4.4 Discussion	85
References	44	6.5 Monitoring in the EZ-G08 segment	85
4. Statistical analysis of the fracture network	45	6.5.1 Orientation of the boreholes	85
4.1 Introduction	45	6.5.2 Wenner profiles	85
4.2 Data collection	46	6.5.3 Cross-hole measurements	87
4.3 Spatial distribution in the linear part (40–127 m)	46	6.5.4 Spatial variations	88
4.4 Orientation distributions	48	6.5.5 Temporal variations	88
4.4.1 Fault orientations	48	6.6 Conclusion	91
4.4.2 Orientations of the bedding traces	49	References	91
4.4.3 Orientations of the EDZ fractures	49	7. A noble gas study in the Excavation Damaged Zone	92
4.5 Relative spatial organisation of the faults and of EDZ fractures	50	7.1 Introduction	92
4.6 Trace length distribution	54	7.2 Method	92
4.7 Connectivity and percolation of the EDZ fracture network	54	7.3 Results	92
4.8 Conclusion	57	7.3.1 BEZ-G5 borehole	92
References	57		

7.3.2	BEZ-G36, BEZ-G39 and BEZ-G44 boreholes . . .	97
7.4	Discussion	98
7.5	Conclusion	98
	References	98
8.	Self-potential monitoring in BEZ-G5 borehole	100
8.1	Introduction	100
8.2	Instrumentation	100
8.3	Raw self-potentials	101
8.4	Self-potential anomalies	106
8.4.1	Static anomaly	106
8.4.2	Dynamic anomaly	108
8.5	Interpretation	108
8.6	Conclusion	111
	References	111
9.	Recommendations for further works and perspectives	112
9.1	Recommendation 1: experiment scaling, geometry and orientation	112
9.2	Recommendation 2: instrument characteristics and their emplacement in the monitored rock mass	112
9.3	Perspectives	113
	References	114

List of Figures

Fig. 1-1: View of the Mont Terri rock laboratory and the tunnel system with the position of the 8m-long EZG-08 segment. The investigated rock mass was located at the junction between the existing Gallery 04 (in yellow) and the Gallery 08 (in red) under excavation before and during the mine-by experiment.	22	Fig. 3-7: Vertical profile A-A' along the EZ-G08 segment. The resin injected into BEZ-G20 and BEZ-G21 flowed out from the interconnected tectonic fracture network created by the combination of SE- and SW-dipping faults.	38
Fig. 1-2: A) View of the Ga04 face (GM 80) with position of all boreholes. B) View of the GA08 front (GM 159) with position of all boreholes including those which cut the rock segment through from the opposite face (Ga04).	23	Fig. 3-8: Vertical profile B-B' along the EZ-G08 segment. This profile shows one of the injection boreholes in the Ga08 face at GM 159. The position of the BEZ-G5 borehole is indicated as well, as this borehole intersects the entire EZ-G08 segment and was used in numerous geophysical surveys.	38
Fig. 1-3: Positions of the instrumented boreholes: side-view (a) along the axis of Ga04 near its end-face, indicated by the dashed line in the top-view (b) . The crosses correspond to positions acquired with a laser-theodolite. Positions of electrodes placed on the end-face of Ga04 for geo-electrical measurements are indicated by coloured dots (see NICOLLIN et al. 2010), which provide a good idea of the shape of the end-face.	24	Fig. 3-9: The drillcore of BEZ-G5 is characterised by the occurrence of numerous white sandy layers, especially from a depth of 9.30m onwards. The transition between shaly and sandy facies is located between 1.5 and 2 m from the Ga04 face at GM 80, though characterised by discrete and scarce sandy layers.	39
Fig. 2-1: Situation map before the excavation of the EZG-08 segment. The excavation face was at GM 159.	27	Fig. 3-10: Positions of resin injection boreholes and surrounding sampling boreholes on the Ga04 face and Ga08 front. Two resin injections were carried out on each face. Since the Ga04 face is divided by a major fault (in blue) delimiting two distinct compartments, a resin injection was carried out above (BEZ-G20) and below the fault (BEZ-G21). In absence of a characteristic structure on the Ga08 front, both injections (BEZ-G37 and BEZ-G38) were performed at the same height to investigate a common volume.	40
Fig. 2-2: A special type of excavation machine, i.e. a road header (hydraulic drum cutter Erkat ER 600) mounted on an excavator machine was used for the excavation.	28	Fig. 3-11: View of the Ga04 face after resin injection. a) Resin outflow occurred along low angle SW-dipping faults (upper part) and SE-dipping faults, subparallel to bedding planes (lower part). The reader can compare this with Fig. 3-12; b) Detail of resin outflow along a SE-dipping fault and the position of injection borehole BEZ-G21. The mesh size is 50 cm.	41
Fig. 2-3: End of excavation of the EZ-G08 segment which also coincides with the breakthrough of Gallery 08 on 25 August 2008.	28	Fig. 3-12: View of an impregnated drillcore (BEZ-G30) under UV light (upper part). Corresponding structural mapping of the resin-impregnated BEZ-G30 drillcore (lower part). The impregnated fracture network consists of a combination of tectonic faults and EDZ fractures.	42
Fig. 2-4: Specific profile of EZ-G08 segment.	29	Fig. 3-13: Thin section from BEZ-G30 sample (depth: 17 cm from tunnel wall) under UV light (upper) and corresponding structural sketch (lower). This sample shows that the impregnated fracture network is composed of unloading joints (EDZ) partly connected by shear fractures. Intersection lines between both fracture sets seem to build some channels filled by resin.	43
Fig. 3-1: Geological map of the Mont Terri rock laboratory with the position of the EZ-G08 segment (rectangle) at the transition between the shaly and sandy facies.	31	Fig. 3-14: Thin section from the BEZ-G30 sample (depth: 17 cm from tunnel wall) under UV light. The impregnated fracture corresponds to a connection between an apparent horizontal SW dipping fault and to bedding traces dipping with 45° to the SE.	43
Fig. 3-2: Section of the basal strata of the Opalinus Clay at the "Galerie de Reconnaissance" of the Mont Terri Rock Laboratory (in REISDORF et al. 2014, modified after BLÄSI et al. 1996). Colour coding of the facies types is the same as in Fig. 3-1.	32	Fig. 4-1: Example of traces in the Gallery 08 (40 < x < 70 m). The digitized traces are shown in the central part (gallery ground). Colours are for: pre-existing faults (magenta), lithological (blue) and EDZ (black).	45
Fig. 3-3: Structural mapping of the Ga04 face (Gallery 04, GM 80) before excavation of the EZ-G08. The face is characterised by a major fault dipping to SW at low angle (in blue) that divides the face into two compartments.	35	Fig. 4-2: Overall map of the invert fracture network observed in Gallery 08.	46
Fig. 3-4: Extract of the geological map of the Gallery 04. This map shows the decametric scale (greater than 40 m) of the low angle SW-dipping fault that intersects the Ga04 face at GM 80 and the tunnel wall of Gallery 04. Note that the other fault systems were projected into this figure to show the SW-dipping fault.	36		
Fig. 3-5: Structural mapping of the Ga08 front (Gallery 08, GM 159) before excavation of the EZ-G08 segment.	37		
Fig. 3-6: Structural mapping of the invert, location of faces Ga04 and Ga08 and of both vertical profiles A-A' and B-B'. Note the occurrence of two SW-dipping faults (in blue) between GM 161 and GM 165. They are interrupted by the significant SE-dipping fault shown in Figs. 3-7 and 3.8.	37		

Fig. 4-3: Fracture analysis by scan lines.	47	Fig. 4-15: Example of two rectangular EDZ fractures which intersect at the point I below the exposed rock surface. View from the top (a). The thick lines are the traces on the ground surface. Vertical cross section (b) at the position indicated by the dash-dotted arrow in (a).	57
Fig. 4-4: Density profiles C [m/m ²] as functions of x . Data are for faults (red) and EDZ (black).	47	Fig. 5-1: (a) Schematic illustration of the principles of the experiments. (b) Instrumented Ga04 face with the location of the boreholes: an acoustic source introduced in BEZ-G5 (black dot) and two arrays of acoustic receivers introduced in BEZ-G12-15 (blue dots) and BEZ-G16-19 (red dots).	59
Fig. 4-5: Density maps C [m/m ²] on the ground of the linear portion ($40 < x < 127$ m) of the Gallery 08.	48	Fig. 5-2: Network of the boreholes for the seismic experiments and position of acoustic sensors: (a) as seen from the Ga04 face and (b) as seen from the top of the gallery.	60
Fig. 4-6: Normed semivariograms $\gamma(n)/\sigma_s^2$ for the fault ground traces (red) and EDZ (black) in the linear portion of the Gallery 08 ($40 < x < 127$ m).	48	Fig. 5-3: (a) Acoustic source composed by a piezoelectric element and an inflatable membrane. (b) Schematic of the acoustic source introduced in the borehole with a long metal rod (c).	61
Fig. 4-7: Distribution of normals to faults in the curved portion $0 \leq x \leq 40$ m (upper line) and in the linear portion $40 \leq x \leq 127$ m (lower line) in the Gallery 08, on the excavation front (left), on the ground (middle) and on the walls (right). The axis of the gallery is parallel to the red arrows; it is constant in the lower line and variable in the upper one, namely from W for $x=0$ to SSE for $x=40$ m.	50	Fig. 5-4: (a) One of the four acoustic arrays of 16 receivers each introduced in boreholes BEZ-G12:15 (array A1). (b) Schematic of the internal structure of an array, where the blue balloon (c) ensures the mechanical coupling with the wall of the borehole.	62
Fig. 4-8: The normals to the lithological faults (●), pole of the Fisher distribution (◐) and circles containing 68% and 95% of the data.	51	Fig. 5-5: Acoustic poles of 4 receivers each, introduced into each borehole BEZ-G16 to BEZ-G19 comprising the acoustic array A2.	63
Fig. 4-9: Distribution of the normals to the EDZ fractures in the curved $0 \leq x \leq 40$ m (upper line) and linear $40 \leq x \leq 127$ m (lower line) portions of the Gallery 08, on the front, on the ground, on the left and right walls (from left to right). View from the top in a fixed reference frame. The red arrows correspond to the direction of the gallery axis, fixed (below) or variable (above) from W for $x=0$ to SSE for $x=40$ m. The blue, red and magenta curves correspond to the most probable families for the traces on the front and on the ground.	51	Fig. 5-6: Principles of the acquisition system of the acoustic array A2 introduced in boreholes BEZ-G16 to BEZ-G19.	64
Fig. 4-10: Distribution of the normals to the EDZ fractures in the curved $0 \leq x \leq 40$ m (upper line) and linear $40 \leq x \leq 127$ m (lower line) portions of the Gallery 08, on the front, on the ground, on the left and right walls (from left to right). View from the top in a reference frame linked to the gallery axis. The blue, red and magenta curves correspond to the most probable families for the traces on the front, on the ground and on the left wall.	52	Fig. 5-7: Distances between the acoustic source and 64 receivers of the A1 acoustic array.	64
Fig. 4-11: Distribution of the normals to the EDZ fractures in the curved $0 \leq x \leq 40$ m (upper line) and linear $40 \leq x \leq 127$ m (lower line) portions of the Gallery 08, on the front, on the ground, on the left and right walls (from left to right). View from the gallery axis (G). The blue, red and magenta curves correspond to the most probable families for the traces on the front, on the ground and on the left wall.	52	Fig. 5-8: Proxy of the acoustic energy measured at one receiver of (a) the borehole BEZ-G12 and (b) BEZ-G13, as a function of the date.	65
Fig. 4-12: Poles of the various Fisher distributions and gallery axis (upper); directions of the faults, lithology and EDZ fractures in a vertical cross section containing the gallery axis (lower).	53	Fig. 5-9: Ratio of the temporal energy variations (from LE GONIDEC et al., 2012). The black arrow indicates when the excavation front reached BEZ-G5.	66
Fig. 4-13: Locations of the recorded fault and EDZ fracture orientations on the front (upper line) and on the ground (lower line) in the linear portion of the gallery. Data are for: FF1 (red), FF2 (magenta), FF3 (blue). Segments have an arbitrary length, but their inclinations correspond with the measured orientation in the vertical plane that contains the gallery axis. The black segments correspond to the recorded faults. The sketches on the right illustrate the general organisation of FF1, FF2 and of the faults. At the front, FF1 (resp. FF2) is located in the upper part (resp. lower) of the front, according to the geologists who recorded the data.	55	Fig. 5-10: Illustration of the waveforms recorded during a seismic survey with an acoustic source located at 4.8 m deep inside BEZ-G5. The red curve is the source wavelet signal.	67
Fig. 4-14: Normalized histogram of the EDZ trace lengths on the invert of the straight gallery section $40 \text{ m} \leq x \leq 127 \text{ m}$ (symbols). The solid line is the model distribution (8).	56	Fig. 5-11: Acoustic waveforms recorded at one receiver as a function of the date.	67
		Fig. 5-12: Compilation of the P-wave velocities determined from the seismic surveys along different ray paths relative to the bedding plane.	68
		Fig. 5-13: Spatial location of the active acoustic sources introduced at different positions inside the borehole BEZ-G5 (red). The blue lines and crosses indicate the positions of the acoustic receivers inside the four boreholes (modified from LE GONIDEC et al. 2014).	69
		Fig. 5-14: Acoustic events identified with the 16 receivers introduced in BEZ-G12: (a) acoustic event associated to rock-breaking (sledgehammer) equipment and (b) acoustic event associated to a micro-seismic event.	70
		Fig. 5-15: Identification of the P- and S-waves and their velocities (red lines) from a recorded event induced at the Ga08 front during the excavation procedure (modified from LE GONIDEC et al. 2012).	71
		Fig. 5-16: Spatial location of manually selected acoustic events. The 16 acoustic receivers located in the four boreholes of the A2 acoustic network are indicated by the black symbols.	71

Fig. 5-17: Time history of the events detected (a) during the excavation and (b) after the excavation stopped (modified from LE GONIDEK et al.2014).	72	green dots represent negative values of apparent resistivity.	80
Fig. 5-18: Spatial location of the events identified as micro-seismic events (MSEs), detected on July 11 (blue), 12 (green) and 13 (red). The four dark blue lines represent the boreholes with the 16 acoustic receivers (blue stars). The red line is the BEZ-G5 borehole. The yellow surface indicates the face of Ga04 Gallery (modified from LE GONIDEK et al.2014).	73	Fig. 6-6: Geometrical setup of electrodes used for cross-hole measurements: 8 pairs of electrodes <i>M</i> and <i>N</i> are used to measure the electrical potential when the current is injected by 2 electrodes <i>A</i> and <i>B</i> , as shown in two examples marked in black and in grey.	80
Fig. 5-19: (a) Hudson T-k plot showing the damage mechanisms of microseismic events recorded on July 12 and 13 after the excavation stopped (from LE GONIDEK et al.2014). (b) Illustrations of the DC, ISO and CLVD mechanisms.	73	Fig. 6-7: Pseudosections of apparent resistivity measured on Wenner profiles in May 2008, in the near part of the boreholes (left) and in the distant part of the boreholes (right).	81
Fig. 5-20: Spatial location of the MSEs, where the colour scale indicates the failure mechanism (dominant CLVD, DC and ISO in blue, green and red, respectively). The red and blue lines represent the BEZ-G5 borehole and the four boreholes with the 16 acoustic receivers (blue stars). The black polygon and dots stand for the Ga08 front and Ga04 faces, respectively (modified from LE GONIDEK et al.2014).	74	Fig. 6-8: Variations between May and July of the apparent resistivity measured on Wenner profiles in the near part of the G14 borehole (top) and in the distant part (bottom). Red colour denotes an increase in resistivity, blue colour denotes a decrease in resistivity.	82
Fig. 5-21: Conceptual representation of the stress pattern around the excavated Gallery 08 (modified from LE GONIDEK et al.2014): (a) View from Ga08 in the direction of the excavation front and (b) Side view from shaly facies sidewall (modified from NUSSBAUM et al.2011).	74	Fig. 6-9: Apparent resistivity obtained from cross-hole measurements in the distant part of the G12 and G14 boreholes between July 3 and 24, 2008.	83
Fig. 6-1: View of the electrical monitoring system installed on the Ga04 face. A tectonic fracture (SW dipping fault N120–20°) is clearly visible on the face and marked by a black dashed line. The white mesh represents the horizontal and vertical lines of the electrode array on the gallery face, the green and yellow dots mark the long and short boreholes respectively. Two long boreholes were equipped with lines of electrodes coupled to the wall with blue inflated balloons.	77	Fig. 6-10: Maximum value of the resistivity tensor found by inversion in the 18 areas of the Ga04 face.	84
Fig. 6-2: Electrical tomography of the Ga04 face with Wenner profiles performed using the electrode array of the face: pseudosections of apparent resistivity ρ_a measured along the horizontal lines (left) and along the vertical lines (right).	78	Fig. 6-11: Wulff stereographic projection (lower hemisphere) showing the results of the inversion of the 18 data sets of the Ga04 face. The maximum value of resistivity is plotted with a filled circle, the minimum value of resistivity is plotted with an empty circle, and the intermediate value of resistivity is plotted as a star. The plane N51–57°SE, normal to the direction of the mean value of maximum resistivity, is represented as a dashed line. The bedding plane (N60–48°SE) is represented as a black line and its normal with a black cross.	86
Fig. 6-3: Location of the electrical anisotropy measurements: 18 areas of 32 electrodes on the Ga04 face and two series of four boreholes equipped with lines of 16 electrodes. Five areas of the face and one group of boreholes were located in the domain above the fracture, while the other 13 areas and the other group of boreholes were located in the lower domain.	79	Fig. 6-12: Wulff stereographic projection (lower hemisphere) showing the spatial organisation of the borehole measurements. The direction N138–0° of the four boreholes is represented with a black empty circle; the cross-hole planes are represented with coloured lines each containing the current injection direction represented with a filled circle; the bedding plane is represented with a grey line; the mean direction of maximum resistivity is represented with a grey cross and its normal plane is represented with a grey dashed line.	86
Fig. 6-4: Square array for (a) a set of 32 electrodes on the face (59 squares of various orientations and sizes shown in (b)) and (c) 64 electrodes in the four boreholes of the lower domain (56 squares of various orientations and sizes shown in (d)). The depth of investigation is of the order of size of the side of the square, and the measurement orientation is given by the angle between one side of the square and the horizontal axis.	79	Fig. 6-13: Variations of apparent resistivity between consecutive days during the first period, measured on a Wenner profile in the distant part of the G12 borehole. Red color denotes an increase in resistivity, blue color denotes a decrease in resistivity.	86
Fig. 6-5: Polar diagrams showing the apparent resistivity measured using the square array configuration, in the 18 areas of the face (diagrams with black border) and in the two areas of four boreholes (diagrams with grey border). The diagram radius represents the resistivity between 0 and 316 Ω .m using a logarithmic scale. The angle from the horizontal axis of the diagram corresponds to the dip of the AB segment in the local plane. Black dots represent positive values of apparent resistivity,		Fig. 6-14: Variations of apparent resistivity between consecutive days during the second period, measured on a Wenner profile in the near part of the G12 borehole. Red color denotes an increase in resistivity, blue color denotes a decrease in resistivity.	87
		Fig. 6-15: Mean apparent resistivity measured on Wenner profiles, in the distant part of the boreholes (5–8 m from the Ga04 face) during the first period (top), and in the near part of the boreholes (1–3 m from the Ga04 face) during the second period (bottom).	87
		Fig. 6-16: Cross-hole measurements made with three spacings between the current and potential electrodes: the apparent resistivity is averaged over the length of the lines placed in the distant part (5–8 m from the Ga04 face) of the G12 and G14 boreholes.	88
		Fig. 6-17: Mean apparent resistivity averaged over the two periods of cross-hole measurement for the six pairs of boreholes: between July 3 and 24 in the distant part (bottom) and between July 24 and August 7 in the near part (top).	89

Fig. 6-18: Mean apparent resistivity averaged over 1 m in three zones of cross-hole measurement for the six pairs of boreholes: between 7 and 8 m from the Ga04 face during the period July 3 to 24 (top), between 5 and 6 m from the Ga04 face during the period July 3 to 24 (middle) and between 2 and 3 m from the Ga04 face during the period July 24 to August 7 (bottom).	89	Fig. 8-7: a) example of raw self-potential signals recorded in borehole BEZ-G5 at 6.35 m (CH22, red) and 6.65 m (CH20, blue). b) close-up of the period during which drilling operations were carried out in end-face Ga04. c) and d) perturbations resulting from ERT acquisitions carried out on the end-face and also from the resaturation of the reference electrode (around day 40.5).	105
Fig. 6-19: Views of the Ga08 front at GM 159: the end of BEZ-G13 was opened July 11 when the upper part of the gallery was excavated (left photo, 11/07/2008 evening), the end of BEZ-G12 was opened July 12 when the lower part of the gallery was excavated (right photo, 14/07/2008 evening).	90	Fig. 8-8: Raw self-potential differences between the electrodes placed on end-face Ga04 and reference electrode BIG5.	106
Fig. 7-1: Vacuum-tight cells for the samples.	93	Fig. 8-9: Initial (static) self-potential anomaly in borehole BEZ-G5 after the stabilisation of the reference electrode and before the drilling operations. A change in the baseline can be observed between 1.5 and 2 m. An anomaly also seems to appear around 6 m.	107
Fig. 7-2: Extraction equipment for gas analysis.	93	Fig. 8-10: Evolution of the self-potential variations with respect to the initial, static anomaly in borehole BEZ-G5, in wiggle view (a) and time shots (b) . In a) , the grey zone denotes the period of drilling operations. In b) , Greek letters stand for the noticeable anomalies of the self-potential variation.	107
Fig. 7-3: Water content, concentration of noble gases, and geological facies in the core of borehole BEZ-G5.	95	Fig. 8-11: a) evolution of the self-potential variations with respect to the initial anomaly at 6.35 m (CH22, red) and 6.65 m (CH20, blue) in BEZ-G5. b) and c) absolute and relative evolution of the pore pressure measured in packed-off boreholes BEZ-G6, BEZ-G7 and BEZ-G8.	109
Fig. 7-4: Water content and concentration in noble gases of the cores of boreholes BEZ-G36, BEZ-G39 and BEZ-G44.	96	Fig. 8-12: Comparison between the self-potential anomalies in borehole BEZ-G5 and the geology, i.e. the interpreted core of borehole BEZ-G5 (initial state) and the last 13 metres of the structural cartography of the wall of segment Ga08 drawn after its excavation (final state). Fractures labelled F_1 to F_8 were observed in the core, whereas fractures labelled f_1 to f_8 were not, since they were sealed with calcite and clay minerals. Fractures f_1 to f_8 are unlikely to result from drilling operations and/or excavation of Gallery 08, but could have been reactivated by them. Greek letters denote the noticeable self-potential anomalies (blue: linked to macroscale faults; yellow: possibly linked to microscale fractures).	110
Fig. 7-5: Helium content in boreholes BEZ-G36, G39 and G44, and in borehole WS-A5 (RÜBEL et al., 1997).	97		
Fig. 8-1: Close-up view of the end-face of borehole Ga04, showing traces of water that outflowed from borehole BEZ-G5 during the acoustic measurements carried out in July 2008 (see Chapter 5 and LE GONIDEC et al. 2012).	101		
Fig. 8-2: a) PVC-pipes before assembly. b) close-up view of the PVC annuli for the electrodes. c) fixing the IDE wire inside the assembled “caterpillar”. d) welding lead strips inserted in each annulus to the internal IDE wire. e) IDE wires at the tail of the caterpillar. f) saturating the sponges placed over one of two lead strips. g) top-view of the head of the caterpillar. The coloured sponges correspond to the unpolarisable electrodes and the grey (exposed) lead strips to the normal ones.	102		
Fig. 8-3: Tail of the caterpillar after insertion into the borehole, before (a) and after (b) inflating the internal pipe.	102		
Fig. 8-4: a) unpolarisable electrodes for end-face Ga04. b) inserting an electrode into a cm hole drilled in the end-face.	103		
Fig. 8-5: Network of unpolarisable electrodes on end-face Ga04 (February 21, 2008). Note that electrode B2G3 corresponds to electrode CH64 of the caterpillar. Electrode BIG5 served as reference electrode for all the measured potential differences.	103		
Fig. 8-6: Raw self-potential differences between the electrodes in borehole BEZ-G5 and reference BIG5. Drilling operations in BEZ-G12 to G19 took place between March 10 and March 14, 2008. The recorder went out of order between March 21 and March 28. Finally, electrical resistivity tomography measurements were carried out on end-face Ga04 between March 31 and April 3.	104		

List of Tables

Tab.1-1: Characteristics of the boreholes. Bracketed values are estimations not based on systematic laser-positioning. Dip angles are positive upwards.	25
Tab.2-1: Effective time schedule and main tasks of the excavation of the EZ-G08 segment.	29
Tab.4-1: Trace densities in the whole area of the linear gallery portion ($40 < x < 127$ m) and in four zones of width 1 m.	46
Tab.4-2: Number of orientation observations for each trace family and each section.	49
Tab.4-3: Parameters of the Fisher distributions fitting the fault observations in various parts of the Gallery 08.	50
Tab.4-4: Parameters of the Fisher distributions corresponding to the mapped EDZ fractures in Gallery 08. In the linear portion, azimuths are measured either in a fixed reference frame or in a variable one, depending on the gallery axis, in the direction of increasing values of x (denoted by “G”). In the curved part, only the second analysis reveals distinct families.	54
Tab.4-5: Spatial correlation coefficients between the fracture degree for FF1, FF2, and the faults, evaluated on the ground (a) and the front (b)	55
Tab.6-1: Results of inversion of the 18 data sets measured on the Ga04 face, divided into three subsets: subset A above the tectonic fracture (five data sets), subset B in the SW half below the tectonic fracture (six data sets), subset B in the NE half below the tectonic fracture (seven data sets). A direction indicated with a negative dip at a given azimuth is equivalent to the direction of opposite dip at the azimuth $\pm 180^\circ$	84
Tab.7-1: Content in water (in weight-%) and concentrations in noble gases (in 10^{-7} cc STP g^{-1}) with analytical errors (twice the standard deviation) of the core of borehole BEZ-G5.	94
Tab.7-2: Content in water (in weight-%) and concentrations in noble gases (in 10^{-7} cc STP g^{-1}) with analytical errors (twice the standard deviation) of the core of boreholes BEZ-G36, G39 and G44.	94

1. Description of the mine-by experiment

D. GIBERT, C. NUSSBAUM, Y. GUÉGUEN, P. PINETTES, Y. LE GONIDEC, F. NICOLLIN, A. MAINEULT & B. THOMAS

1.1 Objectives and strategy

Damage induced by the excavation of galleries – located in a zone around the created openings, known as the Excavation Damaged Zone (or EDZ) – strongly affects physical, mechanical and hydraulic properties of the rock (MARTINO & CHANDLER 2004, BLÜMLING et al. 2007). For nuclear waste geological repository, the EDZ can constitute a pathway for radionuclides to escape from cavity to the hydrosphere and/or atmosphere. The extent of EDZ, its mechanical and transport properties, and their respective evolution in time are thus of crucial importance.

Geophysical methods are now widely used to investigate the EDZ characteristics in sedimentary or crystalline rock mass. These methods, based mostly on seismic velocity measurements (e.g., ALHEID et al. 1996, SATO et al. 2000, WRIGHT et al. 2000, MALMGREN et al. 2007, YOUNG & COLLINS 2001), allow a non-invasive investigation of a large volume of rock mass surrounding an excavation. Likewise, acoustic emission monitoring is used to quantify and localize rock mass damage (FALLS & YOUNG 1998, CAI et al. 2001) as well as to monitor the EDZ evolution during the excavation process. Geoelectric methods and radar reflection surveys in crystalline rock mass (KWON et al. 2009) are also employed. Hydraulic and pneumatic methods, including hydraulic conductivity measurements, gas injection, or extraction tests in boreholes, form a localized invasive implementation of delineating EDZ and to estimate its transport properties (JAKUBICK & FRANZ 1993, SOULEY et al. 2001; BOSSART et al. 2002, MATRAY et al. 2007, SHAO et al. 2008). Geophysical methods such as these that yield quantitative results are often used in combination with each other (FALLS & YOUNG 1998, CABRERA et al. 1999). Others techniques such as visual inspection (MARTINI et al. 1997), core drilling analysis (BOSSART et al. 2002), and convergence measurements (SHENG et al. 2002), provide additional qualitative and quantitative but localized information about EDZ characteristics.

The excavation of Gallery 08 (Ga08) joining the existing Gallery 04 (Ga04) offered the opportunity to study short-term evolution of damage of argillaceous rock mass in the vicinity of a 4 year-old EDZ (from the Ga04 excavated face) during the excavation of a new gallery (Ga08). EZ-G08 experiments proposed to characterise and monitor the effects of the excavation on i) electrical properties of the Opalinus Clay Formation, ii) its changes due to fluid circulation (through self-potential measurements), iii) its acoustical properties, and iv) its fracture properties (with structural geology observations and noble gas sampling). To the best knowledge of the authors – in comparison with previous mine-by experiments – the particularity of the EZ-G08

mine-by test consists in its multiple and multidisciplinary approaches or methods (geophysical, geochemical and geo-technical) acting together and being coordinated to the excavation process. We conducted a large series of experiments before and during the excavation of the junction between Gallery 08 and the Ga04 face. These investigations consisted of:

- Geological and structural surveys combined with resin impregnation techniques to characterize the EDZ fracture network
- Electric tomography
- Acoustic velocity survey
- Micro-seismic (acoustic emission) monitoring
- Self-potential monitoring
- Analysis of noble gas concentrations in borehole cores
- Pore pressure measurements
- Geodetic survey

Different research teams, named in the next section, coordinated together in conducting these field investigations. This enabled them to be flexible in adapting the experiments to observations over time.

1.2 Experimental layout

We conducted the experiments in the 8-m-long EZ-G08 segment between GM 159 and GM 167 joining the Gallery 08 under construction and the existing Gallery 04 (Fig. 1-1). This rock mass segment is delimited by two faces in the course of the experiment: the 4-year-old Ga04 face and the newly excavated Ga08 face at GM 159. The Ga04 face corresponds to the cutting through face between Gallery 04 and Gallery 08. Therefore, it can be identified by two different positions in the gallery: gallery-metre (GM) 80 in relation with Gallery 04 and GM 167 with Gallery 08. The excavation of Gallery 08 provided the opportunity to study two EDZ with different ages: the Ga04 face was 4 years old and Ga08 was still under excavation during the experiment.

In total, 37 boreholes were drilled in the course of this mine-by experiment. They were drilled from the Ga04 face (28 boreholes) and the Ga08 front (9 boreholes). Figure 1-2 provides an overview of the Ga04 face with the positions of boreholes and the main structural faults, as well as for the opposite Ga08 front.

We drilled the 28 following boreholes from the Ga04 end face:

- BEZ-G5 – This borehole (116 mm in diameter and 12 m in length) was air-drilled in September 2007 to provide

Rock Laboratory Mont Terri

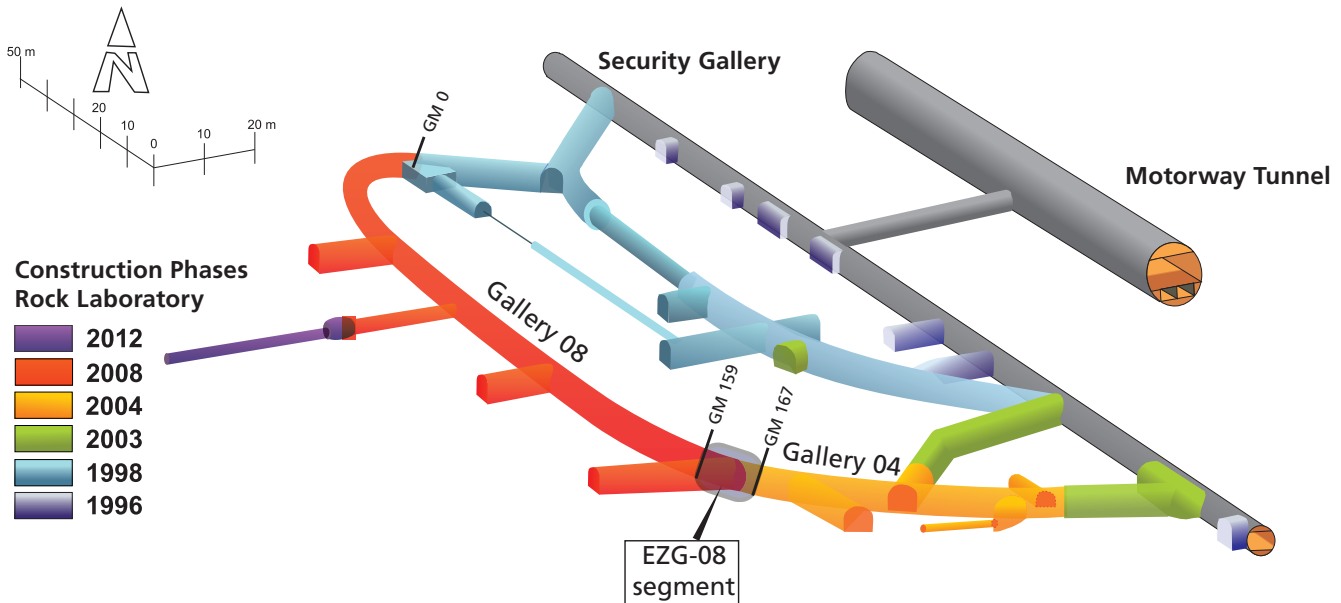


Fig. 1-1: View of the Mont Terri rock laboratory and the tunnel system with the position of the 8m-long EZG-08 segment. The investigated rock mass was located at the junction between the existing Gallery 04 (in yellow) and the Gallery 08 (in red) under excavation before and during the mine-by experiment.

core samples for noble gas analysis. It was later used for spontaneous potential monitoring, electrical tomography, and to host the acoustic source used for active acoustical tomography.

- BEZ-G6 to BEZ-G8: These 3 boreholes (BEZ-G8 is not visible on Fig. 1-2 since it was drilled on the sidewall of Gallery 04) contained the mini-piezometers installed by GRS for pore pressure measurements.
- BEZ-G12 to BEZ-G15: These 4 boreholes contained the lines of electrodes and of acoustical receivers.
- BEZ-G16 to BEZ-G19: These 4 boreholes were equipped with the array of accelerometers for acoustical emission monitoring.
- BEZ-G20 to BEZ-G21: These 2 boreholes were used to inject resin into the rock mass to impregnate the EDZ fracture network.
- BEZ-G22 to BEZ-G29: These 8 short boreholes were equipped with electrodes for measurements to study anisotropy of electrical conductivity on the Ga04 face.
- BEZ-G30 to BEZ-G35: These 6 boreholes allowed us to recover core samples after resin injections to image the EDZ fracture network of a 4-years old tunnel face.

All boreholes that were used for seismic (both active and passive monitoring), geoelectrical measurements and noble gas analysis are shown in Figure 1-3. The corresponding borehole data are reported in Table 1-1. For clarity, the boreholes used for the structural characterization of the EDZ fracture network and the 8 short boreholes drilled on the Ga04 face are not indicated on Figure 1-3.

We drilled nine boreholes into the Ga08 front:

- BEZ-G36, BEZ-G39 and BEZ-G44: These 3 boreholes were drilled to provide core samples of a newly excavated front for noble gas analysis.
- BEZ-G37, BEZ-G38: These 2 boreholes were used to inject resin into the rock mass to impregnate the EDZ fracture network.
- BEZ-G40 to BEZ-G43: These 4 boreholes permitted us to recover core samples after resin injections to image the EDZ fracture network of a newly excavated gallery.

The following research teams were involved in the field investigations during the *in-situ* experiment:

- Géosciences Rennes for the geoelectrical survey of the excavation-induced process, for electric tomography of the Ga04 face, and for near field acoustic passive or active monitoring.
- IPGP, for self-potential monitoring.
- CNAB, for the study of noble gas concentrations.
- ENS Paris, for the far field acoustical survey.
- The geological and structural surveys, including the *in-situ* resin impregnation, were carried out by the Geotechnical Institute Ltd.
- GRS for pore pressure monitoring.

For full names of these research teams, the reader is referred to the list of authors.

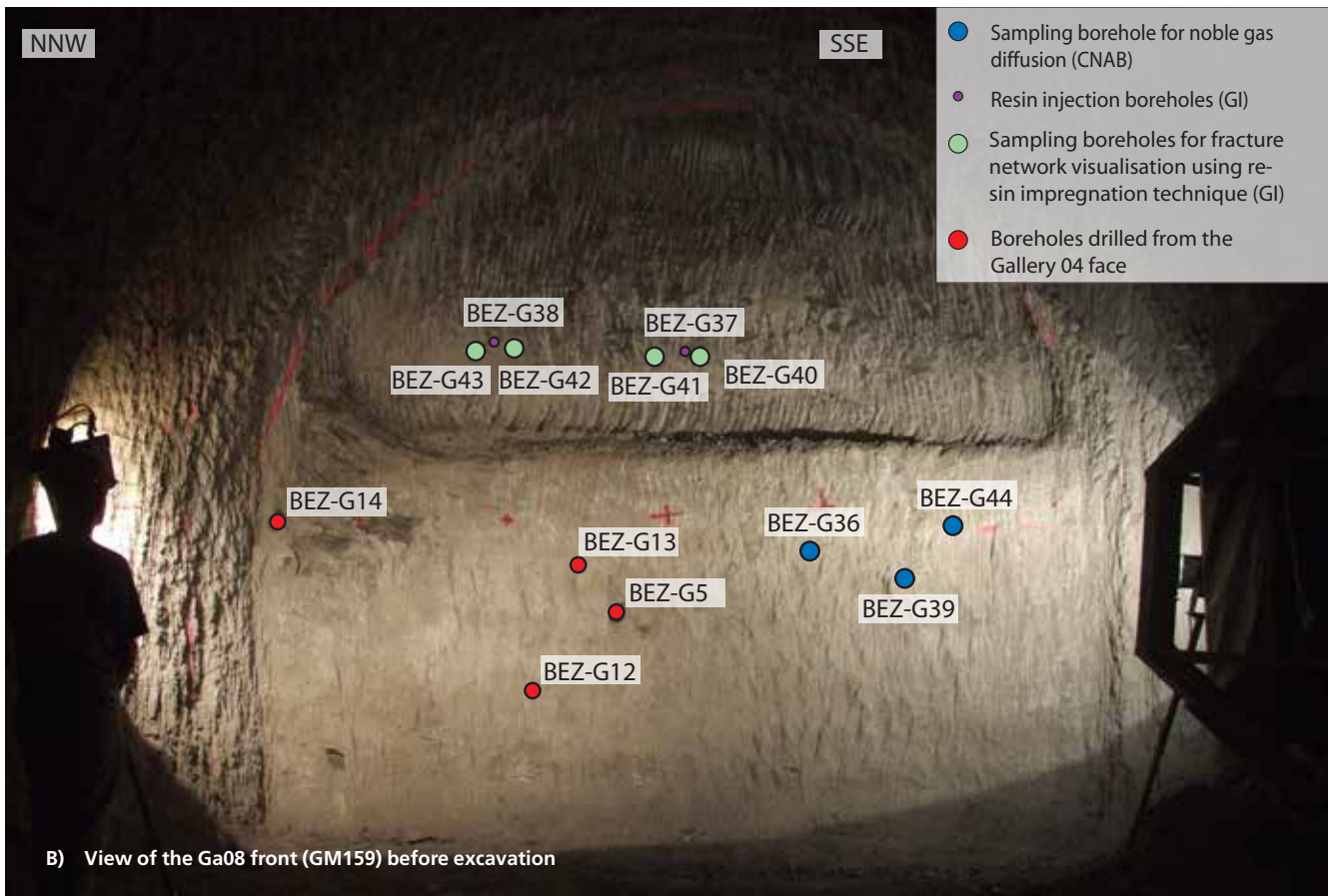
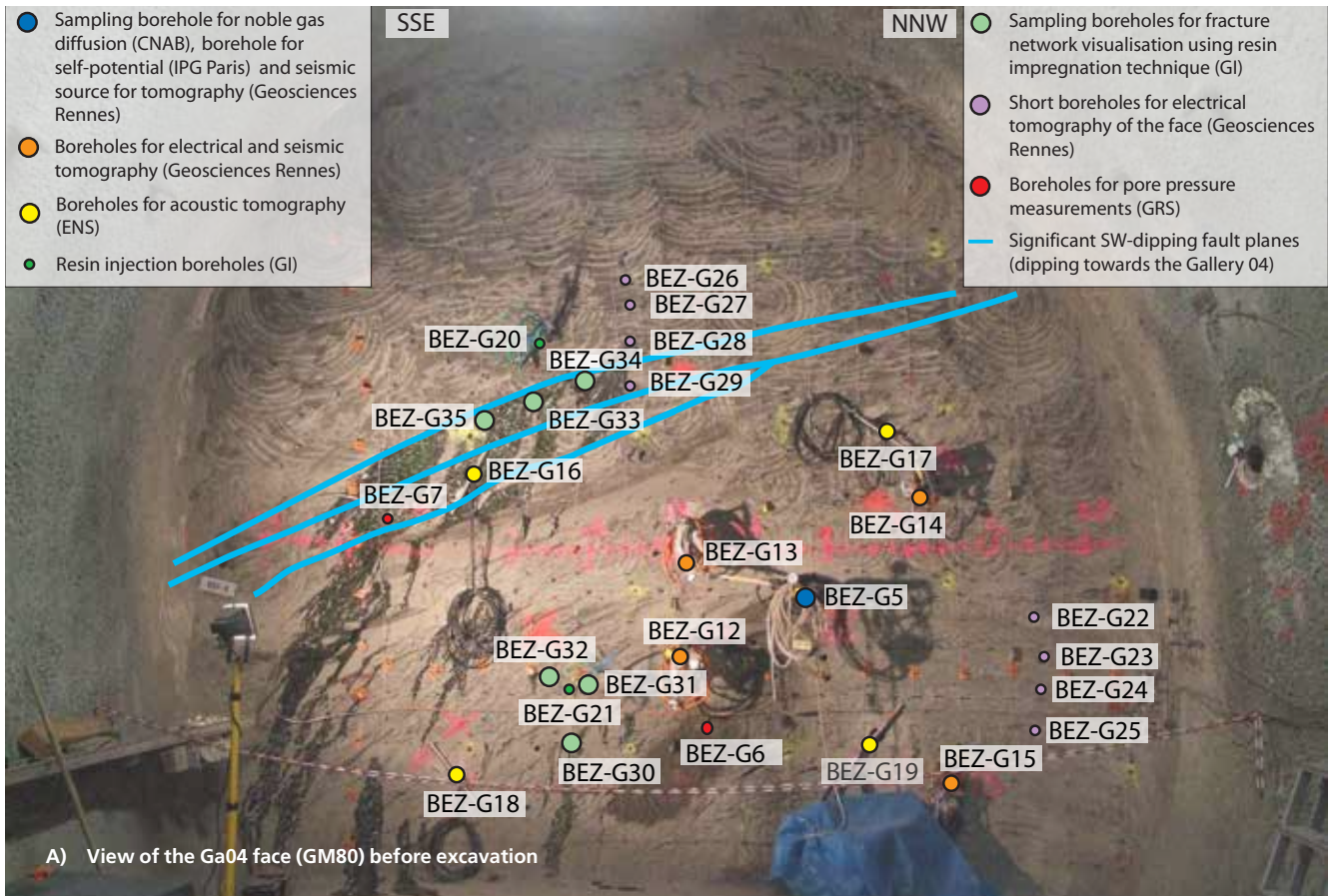


Fig. 1-2: **A)** View of the Ga04 face (GM80) with position of all boreholes. **B)** View of the GA08 front (GM159) with position of all boreholes including those which cut the rock segment through from the opposite face (Ga04).

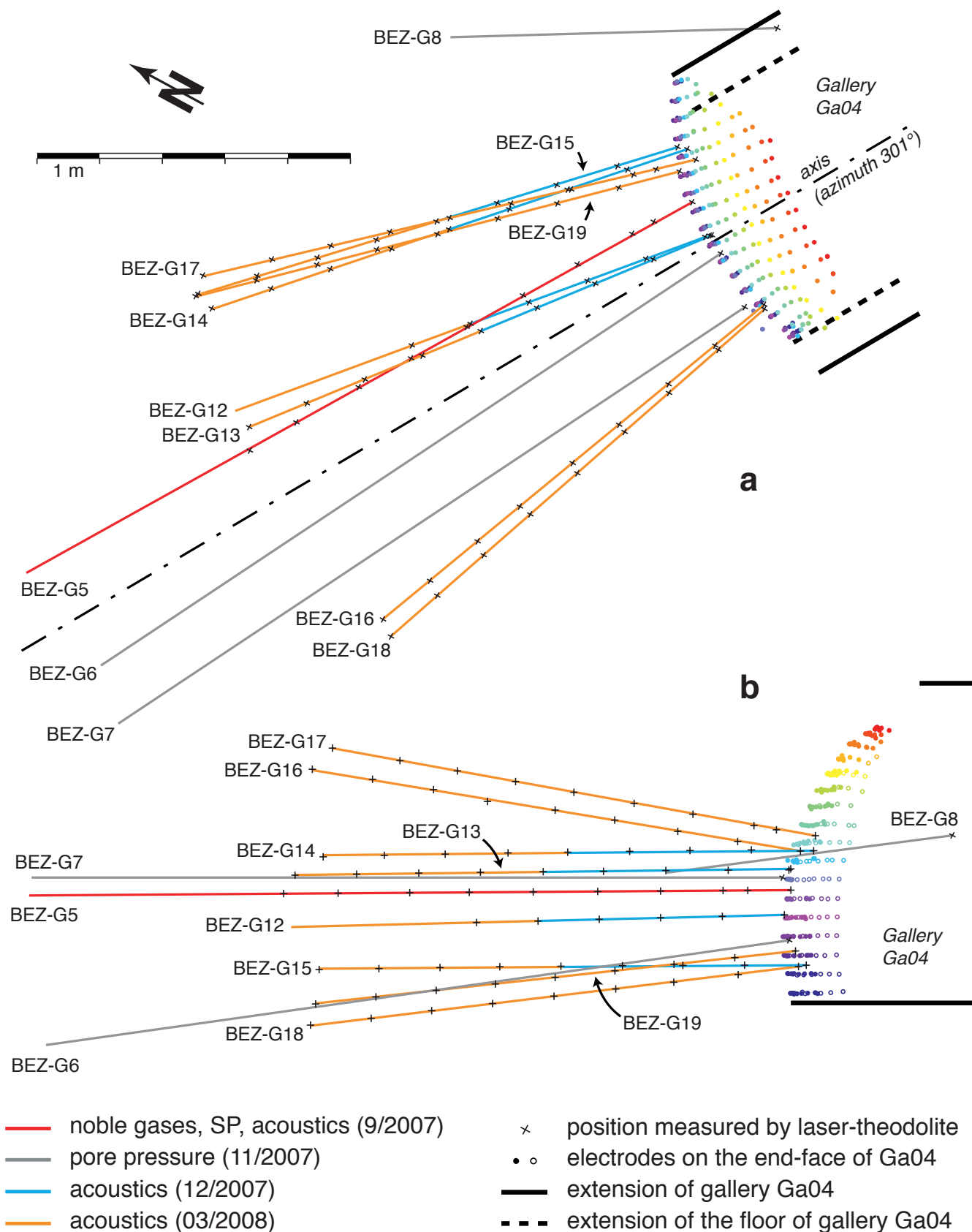


Fig. 1-3: Positions of the instrumented boreholes: side-view (a) along the axis of Ga04 near its end-face, indicated by the dashed line in the top-view (b). The crosses correspond to positions acquired with a laser-theodolite. Positions of electrodes placed on the end-face of Ga04 for geoelectrical measurements are indicated by coloured dots (see NICOLLIN et al. 2010), which provide a good idea of the shape of the end-face.

1.3 Experimental layout

This report is written in a paper format so that each chapter stands alone. As a result, the literature is disseminated and may be repeated throughout the report. The literature review was expanded in the chapter in which it was most relevant.

Chapter 2 briefly summarises the excavation history of the EZ-G08 segment, the applied excavation technique, and the profile type and lining.

Chapter 3 gives a summary about the geological setting of the Mont Terri rock laboratory, including both tectonic faults and EDZ fracture network, and a structural characterisation of the EZ-G08 segment. The connectivity of the fracture network is assessed by the use of the resin impregnation technique which allows imaging of the fractures.

Chapter 4 provides a statistical analysis of the fracture network along the Gallery 08 based on tunnel wall mapping. These findings serve the characterisation of the fracture network (tectonic vs. EDZ).

Chapter 5 explores acoustic velocity surveys and micro-seismic (acoustic emission) monitoring. The experiments consisted of two complementary measurements. The first experiment used an active seismic method involving a controlled acoustic source. This method was used to character-

ize the elastic properties of the rock mass, in particular in terms of P-wave velocity. The second experiment dealt with a passive seismic method based on the detection of acoustic emissions, i.e. micro-seismic events (MSEs).

Chapter 6 investigates the electrical resistivity measurements performed in order to study the evolution of the excavation damaged zone for time periods ranging from hours to weeks. These data show spatial and temporal variations of the electrical properties in the EZG-08 segment during its excavation.

Chapter 7 examines noble gases in order to study gas transport processes in rock and the existence of connected fracture networks, as they do not react with the constituents of the host media. The measurements reported in this chapter aimed at characterizing the evolution of the profiles of noble gas concentrations in the EDZ, and to interpret them in terms of gaseous exchanges between the rock-mass and the atmosphere of the gallery. In other words, how the *in-situ* gases diffuse to the gallery.

Chapter 8 provides information about the water flow-paths and their dynamics. The natural electrical potentials, or self-potentials (SP), were monitored on the end-face of Gallery 04 and in borehole BEZ-G5.

Chapter 9 provides an assessment of the field methods along with recommendations for future work.

Tab. 1-1: Characteristics of the boreholes. Bracketed values are estimations not based on systematic laser-positioning. Dip angles are positive upwards.

Name	Type of measurements	Drilling date	Diameter [mm]	Length [m]	Azimuth [°]	Dip angle [°]
BEZ-G5	Noble gases/SP/acoustics/ERT	12/09/2007	116	(12.16)	302.5	-0.4
BEZ-G6	Pore pressure	15/11/2007	46	(12)	(298)	(-8)
BEZ-G7	Pore pressure	12/11/2007	20	(12)	(298)	(0)
BEZ-G8	Pore pressure	13/11/2007	20	(5.25)	(330)	(-6.5)
BEZ-G12	Acoustics/ERT	5-7/12/2007 12/03/2008	56	(4) (8)	311.3	-1.4
BEZ-G13	Acoustics/ERT	12/12/2007 10-12/03/2008	56	(4) 7.99	309.1	-0.7
BEZ-G14	Acoustics/ERT	12/12/2007 12/03/2008	56	(4) 8.01	313.0	-0.5
BEZ-G15	Acoustics/ERT	13/12/2007 10-12/03/2008	56	(4) 8.00	314.5	-0.4
BEZ-G16	Acoustics	14/03/2008	92	7.99	292.1	9.3
BEZ-G17	Acoustics	12-14/03/2008	92	8.20	318.3	9.8
BEZ-G18	Acoustics	12-14/03/2008	92	7.98	290.4	-6.8
BEZ-G19	Acoustics	12-14/03/2008	92	8.02	317.1	-6.0

References

- ALHEID, H.J., KNECHT, M. & LUDELING, R. (1998): Investigation of the long-term development of damaged zones around underground openings in rock salt. – *Int. J. Rock Mech. Min. Sci.* 35/4, 589–590.
- BLÜMLING, P., BERNIER, F., LEBON, P. & MARTIN, C.D. (2007): The excavation damaged zone in clay formations: time-dependent behaviour and influence on performance assessment. – *Phys. Chem. Earth* 32, 588–599.
- BOSSART, P., MEIER, P.M., MOERI, A., TRICK, T. & MAYOR, J.C. (2002). Geological and hydraulic characterisation of the excavation disturbed zone in the Opalinus Clay of the Mont Terri Rock Laboratory. – *Eng. Geol.* 66/1, 19–38.
- CABRERA, J., VOLANT, P., BAKER, C., PETTITT, W. & YOUNG, R.P. (1999): Structural and geophysical investigations of the EDZ (Excavation Disturbed Zone) in indurated argillaceous media: the tunnel and the galleries of the IPSN Tournemire site (France). – *Vail Rocks* 99.
- CAI, M., KAISER, P.K. & MARTIN, C.D. (2001): Quantification of rock mass damage in underground excavations from microseismic event monitoring. – *Int. J. Rock Mech. Min. Sci.* 38/8, 1135–1145.
- FALLS, S.D. & YOUNG, R.P. (1998): Acoustic emission and ultrasonic-velocity methods used to characterise the excavation disturbance associated with deep tunnels in hard rock. – *Tectonophysics* 289/1, 1–15.
- JAKUBICK, A.T. & FRANZ, T. (1993): Vacuum testing of the permeability of the excavation damaged zone. – *Rock Mech. Rock Eng.* 26/2, 165–182.
- KWON, S., LEE, C.S., CHO, S.J., JEON, S.W. & CHO, W.J. (2009): An investigation of the excavation damaged zone at the KAERI underground research tunnel. – *Tunnelling and Underground Space Technol.* 24/1, 1–13.
- MALMGREN, L., SAIANG, D., TÖYRÄ, J. & BODARE, A. (2007): The excavation disturbed zone (EDZ) at Kiirunavaara mine, Sweden – by seismic measurements. – *J. appl. Geophys.* 61/1, 1–15.
- MARTINI, C.D., READ, R.S. & MARTINO, J.B. (1997): Observations of brittle failure around a circular test tunnel. – *Int. J. Rock Mech. Min. Sci.* 34/7, 1065–1073.
- MARTINO, J.B. & CHANDLER, N.A. (2004): Excavation-induced damage studies at the underground research laboratory. – *Int. J. Rock Mech. Min. Sci.* 41/8, 1413–1426.
- MATRAY, J.M., SAVOYE, S. & CABRERA, J. (2007): Desaturation and structure relationships around drifts excavated in the well-compacted Tournemire's argillite (Aveyron, France). – *Eng. Geol.* 90/1, 1–16.
- NICOLLIN, F., GIBERT, D., LESPARRE, N. & NUSSBAUM, C. (2010): Anisotropy of electrical conductivity of the excavation damaged zone in the Mont Terri Underground Rock Laboratory. – *Geophys. J. int.* 181, 303–320.
- SATO, T., KIKUCHI, T. & SUGIHARA, K. (2000): In-situ experiments on an excavation disturbed zone induced by mechanical excavation in Neogene sedimentary rock at Tono mine, central Japan. – *Dev. geotech. Eng.* 84, 105–116.
- SHAO, H., SCHUSTER, K., SÖNNKE, J. & BRÄUER, V. (2008): EDZ development in indurated clay formations – In situ borehole measurements and coupled HM modelling. – *Phys. Chem. Earth A/B/C*, 33, 388–395.
- SHENG, Q., YUE, Z.Q., LEE, C.F., THAM, L.G., & ZHOU, H. (2002): Estimating the excavation disturbed zone in the permanent shiplock slopes of the Three Gorges Project, China. – *Int. J. Rock Mech. Min. Sci.* 39/2, 165–184.
- SOULEY, M., HOMAND, F., PEPA, S. & HOXHA, D. (2001): Damage-induced permeability changes in granite: a case example at the URL in Canada. – *Int. J. Rock Mech. Min. Sci.* 38/2, 297–310.
- WRIGHT, C., WALLS, E.J. & DE J. CARNEIRO, D. (2000): The seismic velocity distribution in the vicinity of a mine tunnel at Thabazimbi, South Africa. – *J. appl. Geophys.* 44/4, 369–382.
- YOUNG, R.P. & COLLINS, D.S. (2001): Seismic studies of rock fracture at the Underground Research Laboratory, Canada. – *Int. J. Rock Mech. Min. Sci.* 38/6, 787–799.

2. Excavation history of the EZ-G08 segment

P. BOSSART, F. BURRUS & C. NUSSBAUM

Gallery 08 was excavated from the northern part towards the southern part of the rock laboratory, joining the DI niche at the rear end of Gallery 04 in the south (Fig. 2-1). Some experiments have been linked to the realisation of Gallery 08. These are the MB (mine-by test) experiment, the RC (rock mass characterisation) experiment, the SR (low-pH shotcrete for rock support) experiment and the EZ-G (geophysical characterisation of EDZ) experiment. The present report compiles the experimental setup and key results of the EZ-G experiment. The so called “EZ-G08 segment” is located between GM 159 and GM 167, which corresponds to the rear end of the Gallery 04 at GM 80 before cutting through. In total, we mapped 11 front walls for this study, including both boundary faces Ga04 (at GM 80 or GM 167) and Ga08 (at GM 159). The documentation of the excavation technique and history of Gallery 08 is reported in BURRUS et al. (2010). The complete geological documentation is documented by NUSSBAUM et al. (2010).

Due to the limited availability of space, the consortium mandated for the excavation, ATNB-mtp, selected a particular excavation machine, i.e. a road header (hydraulic drum cutter Erkat ER 600) mounted on an excavator machine

(Fig. 2-2.). For the EZ-G08 segment – from GM 159.1 to GM 167.2 – the gallery had to be excavated in total profile and the advancing excavation length per day was not limited. We divided the excavation of this last section of the main gallery into several individual steps. A section of 4m had to be maintained for the EZ-G experiment and to ensure the stability of the last section of rock mass still not excavated. Thus, we did not excavate the EZG-08 segment in full section as had generally been the case for Gallery 08. The upper part of the first section (from GM 159.1 to GM 163.0) was excavated by August 5, 2008. The lower part of the profile was then excavated by August 13, 2008. From August 18 to 22, the main tunnel was excavated up to GM 166.0. Finally, breakthrough took place on August 25, 2008 at 10:00 AM. (Fig. 2-3). This step coincided with the end of *in-situ* investigations of the EZ-G experiment.

In regards to the lining of the EZ-G08 segment, the project required that no metal materials be introduced due to the use of geoelectrical methods. At the first construction meeting, this requirement was abandoned and metal fibres and rock bolts replaced the synthetic materials.

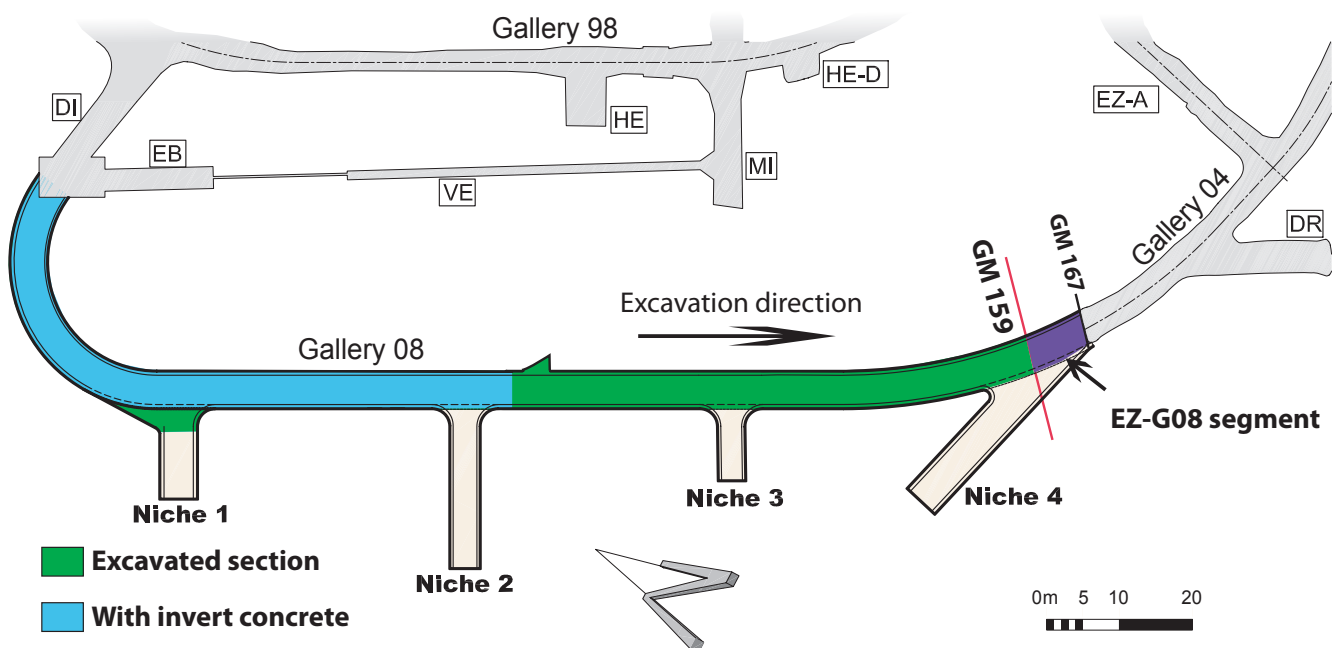


Fig. 2-1: Situation map before the excavation of the EZG-08 segment. The excavation face was at GM 159.



Fig. 2-2: A special type of excavation machine, i.e. a road header (hydraulic drum cutter Erkat ER 600) mounted on an excavator machine was used for the excavation.



Fig. 2-3: End of excavation of the EZ-G08 segment which also coincides with the breakthrough of Gallery 08 on 25 August 2008.

Specific profile of EZ-G08 segment 1:100

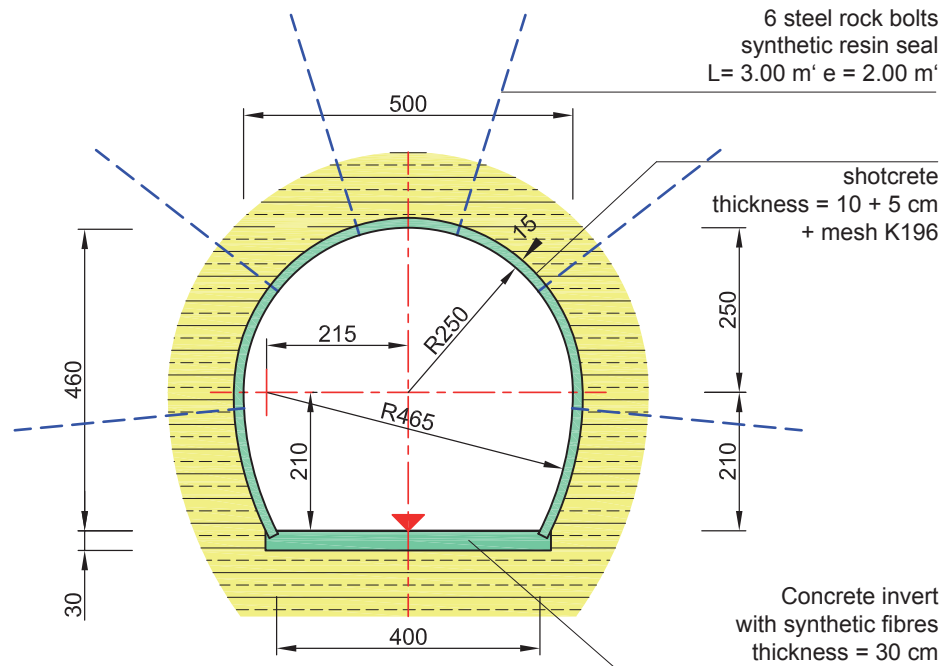


Fig. 2-4: Specific profile of EZ-G08 segment.

Tab. 2-1: *Effective time schedule and main tasks of the excavation of the EZ-G08 segment.*

Excavation period	Gallery metre
from 20/06/2008 to 11/07/2008	Excavation and lining of the upper part of the profile
from 11/07/2008 to 12/07/2008	Excavation and lining of the lower part of the profile from GM 136.5
from 14/07/2008 to 28/07/2008	Break EZ-G and concreting of the invert from GM 88.0 to GM 130.0
from 28/07/2008 to 22/08/2008	Excavation and lining of section EZ-G, alternating between the upper and lower part of the profile, from GM 159.1 to GM 166.0
25/08/2008	Excavation from GM 166.0 to GM 167.2 and breakthrough of Gallery 08 at GM 167.2 at 10.00 a.m.
from 25/08/2008 to 26/08/2008	End of the excavation and lining at GM 167.2

The effective time schedule for the EZ-G08 segment is summarized in Table 2-1. The excavation part before reaching GM 159 is indicated as well. Due to the hardness of the rock encountered in the region of the Main Fault, we decided that excavation should continue with a reduced profile (17 m² instead of 23 m²) from GM 137.5. We decided on this measure to avoid compromising the start date of the EZ-G break, set for July 11, 2008. The lower part of the profile would be excavated later. This time schedule also required a modification of the lining, because it could only be completed partially (3 rock bolts and wire mesh on the roof). The rest of the lining would be completed once the lower part of the profile had been excavated.

From July 1 to 11, 2008, a third team was engaged for night-time excavation. As such, there were activities by night during 10 days before the EZ-G break.

References

- BURRUS, F., BOSSART, P. & NUSSBAUM, C. (2010): Gallery 08: Documentation of the excavation and the convergence measurements. – Mont Terri tech. Note TN 2008-10.
- NUSSBAUM, C., GIRARDIN, G., BADERTSCHER, N., RISSE, V., VEUVE, C., MAYORAZ, J. & BOSSART, P. (2010): Extension of the rock laboratory: Geological documentation of the Gallery 08 and adjacent niches (DR-A, MB, niche 3 and TT). – Mont Terri tech. Note TN 2008-12.

3. Geological characterisation of the investigated rock mass

C. NUSSBAUM, C. GIRARDIN & N. BADERTSCHER

3.1 Geological setting

In this chapter we present the geological and particularly the structural setting of the investigated area, the EZ-G08 segment. The structural characterisation consists of a description of the geometry of pre-existing faults (i.e. fractures of tectonic origin) and those of the EDZ fracture network. The collected structural data serves as an input for understanding and interpretation different geophysical measurements carried out in the course of this mine-by experiment. In order to obtain a representative view of the structural pattern, we used different methods: classical tunnel wall mapping of the EZ-G08 segment, drillcore documentation and resin impregnation techniques for the characterisation of the EDZ network on a microscale. The EZ-G08 segment is located at the transition between the sandy and shaly facies. The exact location is shown on the geological map of the Mont Terri rock laboratory in Figure 3-1.

3.1.1 Facies description

The Opalinus Clay of the Mont Terri region – differing from observations of more eastern regions of Switzerland – consists of three main facies types: an argillaceous facies, rich in clay minerals of illite, mixed-layered illite-smectites, chlorite and kaolinite (BOSSART et al. 2008), which represents about 65% of the strata between the bordering Passwang Formation on top, and the Staffelegg Formation at the base (Fig. 3-1); about 30% is represented by sandy facies, with quartz contents up to 30% and more; and 5% is represented by an exotic carbonate-rich facies, consisting of bioclastic layers of crinoids and debris of bivalves, occurring in elongated lenses of cm- to dm-thickness. The section of basal strata of the Opalinus Clay is shown in Fig. 3-2).

WETZEL & ALLIA (2003) provided a depositional model for the Opalinus Clay of northern Switzerland: the formation was accumulated under completely marine conditions in a shallow basin, which was affected by differential syndimentary subsidence. The depositional water depth was 20–50 m, and thus within range of, and slightly below, the storm-wave base. This hypothesis is supported by an abundance of sedimentary structures and storm-induced accumulations of well-sorted beds of crinoids and bivalves in the Mont Terri area (MÜLLER & JAEGGI 2012). Furthermore, at Mont Terri, all deposits are bioturbated to a certain degree; however, in many stratigraphic levels the original lamination is preserved, which points to high sedimentation rates rather than an anoxic environment. This also coincides with the depositional model of WETZEL & ALLIA (2003).

3.1.2 Fault systems identified in the rock laboratory

An exhaustive review of the geological and structural setting of the Mont Terri rock laboratory is found in NUSSBAUM et al. (2011). The authors try to correlate fault systems identified in the rock laboratory with the complex regional setting. The Mont Terri region is located at the junction between the intracontinental Rhine–Bresse transfer zone and the external front of the Jura fold-and thrust belt, i.e. the most external front of the deformed Alpine foreland.

Systematic small-scale mapping of the tunnel walls, floor and adjacent niches provides basic information about the geometry and kinematics of geological fractures intersected in the underground rock laboratory. In summary, the observed tectonic faults in the rock laboratory can be grouped into three different fault systems (NUSSBAUM et al. 2005, 2011): (1) moderately SE-dipping reverse faults, (2) low-angle, SW-dipping fault planes and flat-lying (subhorizontal) faults, and (3) moderately to steeply inclined N to NNE-striking sinistral strike-slip faults. The first two fault systems are related to the folding of the Mont Terri anticline during the formation of the Jura thrust-and fault belt. N to NNE-striking faults were inherited from the Eo-Oligocene intracontinental Rhine–Bresse transfer zone. These were initially activated as normal faults and later reactivated during the Jura folding phase as sinistral strike slip faults.

The SE-dipping fault system is mainly composed of fault planes that are sub-parallel to bedding planes. In the rock laboratory, bedding plane dips range from 30° in the northern part to 50° in the southern part, but the change in dip is not gradual. It occurs abruptly across the SE-dipping thrust zone called the Main Fault. Slickenside analysis of SE-dipping faults indicates that the slip direction trends down-dip with a top-to-NNW shear sense. This suggests that slip occurred between the bedding planes during the anticline folding by flexural slip. Most of these fault planes are traceable over entire tunnel faces and sidewalls, suggesting they are of metric scale. Fracture surfaces are either polished (dark) or striated. Shear sense was mainly deduced from striated surfaces formed by preferentially re-oriented clay particles or recrystallized clay and calcite fibres. Polished fractures, which developed as a result of scratching and gouging along the surface, do not provide well-constrained shear senses. Nevertheless, it is very likely that slip occurred along these planes. According to small striation lengths observed on striated surfaces, it can be assumed that displacement along these planes was typically limited to the cm-scale. Faults with larger displacements appear on average every 10 m along the tunnel. We also observed that fault planes are not necessarily parallel to bedding; some are more inclined

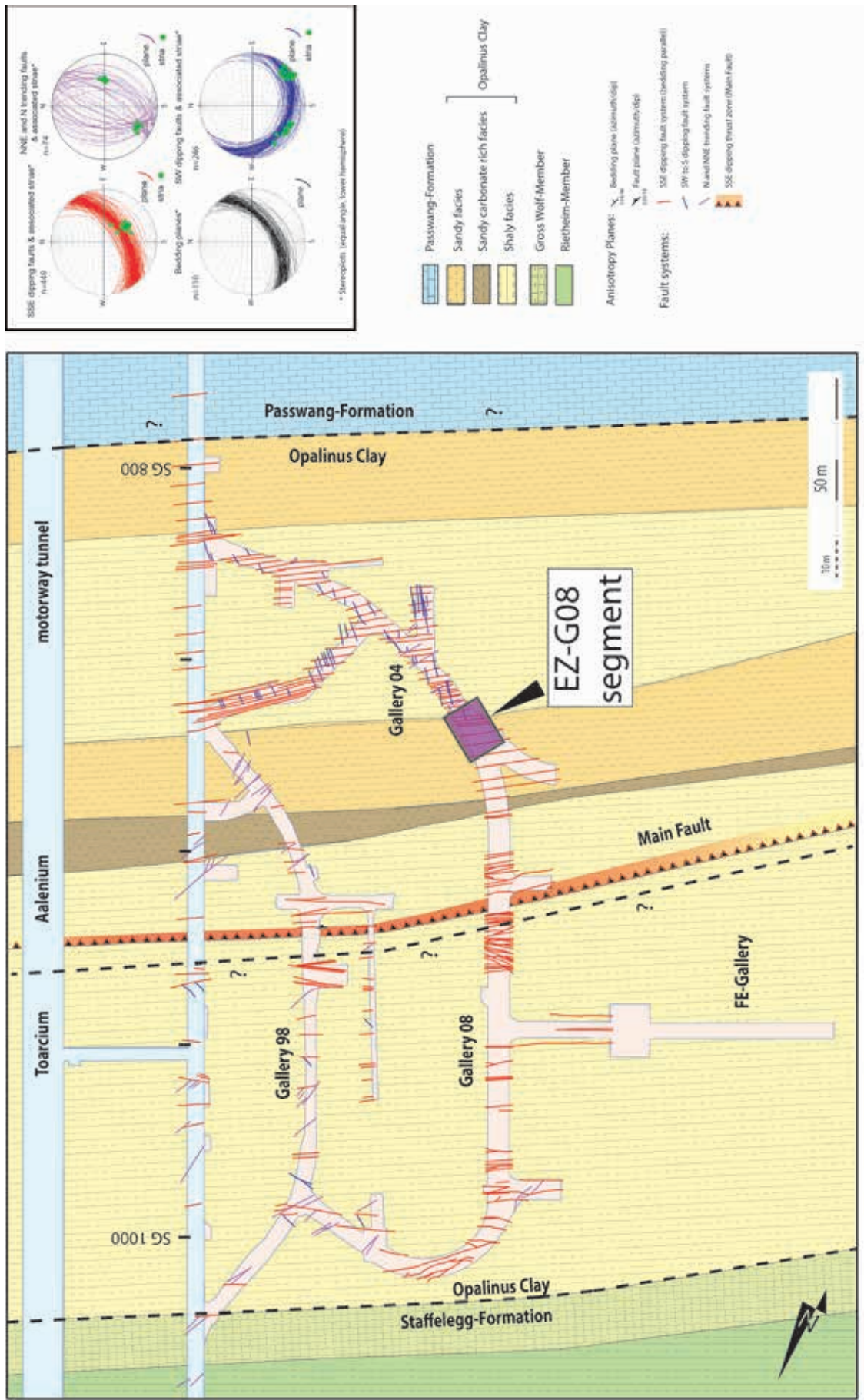


Fig.3-1: Geological map of the Mont Terri rock laboratory with the position of the EZ-G08 segment (rectangle) at the transition between the shaly and sandy facies.

section Mont Terri Rock Laboratory ("Galerie de Reconnaissance")
 coord. 2579.345/1247.740 – 2579.455/1247.500

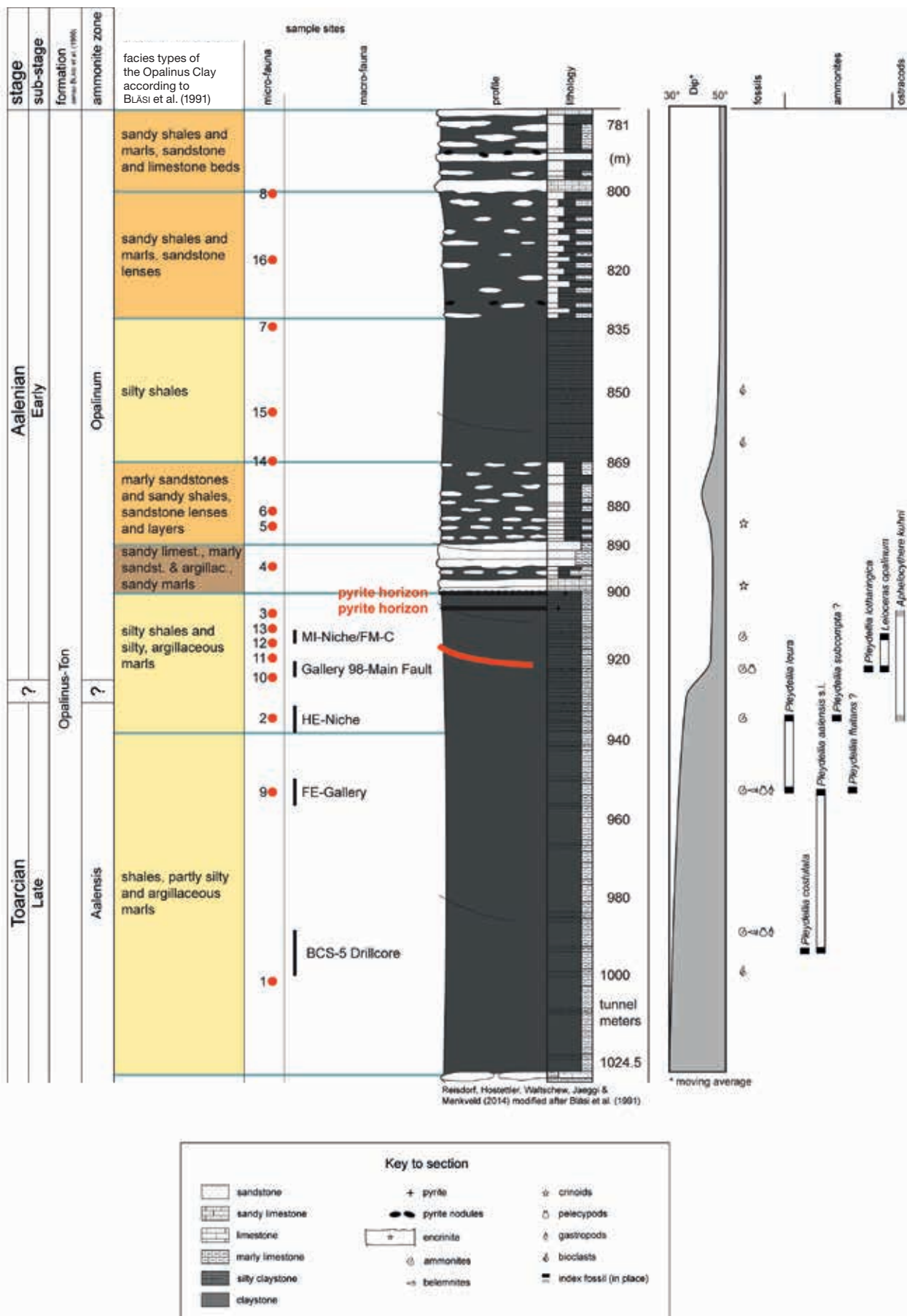


Fig. 3-2: Section of the basal strata of the Opalinus Clay at the “Galerie de Reconnaissance” of the Mont Terri Rock Laboratory (in REISDORF et al. 2014, modified after BLÄSI et al. 1996). Colour coding of the facies types is the same as in Fig. 3-1.

(with dips up to 70°) and form small ramps through the beds. Geometric evidence indicates that displacements along these ramps were limited to cm-scale. The faults are very heterogeneously distributed along the galleries. Considering all the galleries of the rock laboratory, the frequency ranges from 1 fault per 5 m to 20 faults per m.

The low angle SW-dipping faults extend in scale from m to several dm. Fracture planes are mainly striated with slickenfibres and sometimes stepped. Occasionally, two distinct striations were measured on SW-dipping fault planes: (1) down-dip to the SW and (2) sub-horizontal NW-trending. Shear sense indicates normal faulting for the SW-dipping striation and thrusting movement directed NNW for the second striation set. Crosscutting criteria indicate that the SW-trending lineation is overprinted by the NNW-directed striation. This latter striation consists of groove marks and fibrous steps that overgrow the SW-dipping striation. However, sometimes only one striation was observed on SW-dipping fractures. In such cases, the shear sense is systematically towards the NNW. Lithological markers in the clay matrix, such as sandy layers and/or oxidised layers bearing siderite, show offset due to these thrust faults in the range of 2–5 cm. These fault planes are very often associated with a 1–4 cm thick, white, coarse mineralization acting as a crack seal. The crack-seal accretion structures consist of idiomorphic celestite and calcite. These crack-seal accretion structures were observed to be locally folded or cut by the SSE-dipping fault planes. Folded veins are sheared off and exhibit *en échelon* geometry, indicating a thrusting displacement towards the NNW.

N- to NNE-striking fault planes were identified at various locations in the rock laboratory. N-S-striking fault planes dip moderately with angles varying between 20° and 60° (on average 45°) mainly to the east, while NNE-striking faults are steeply inclined and dip generally towards the WNW. For NNE-striking faults, slickenside analysis suggests an oblique slip direction composed of sinistral shear movements, possibly related to a transpressive regime. Bedding planes are drag-folded in the vicinity of NNE-striking faults. N-S-striking faults bear down-dip slickensides, indicating normal faulting. The extent of this fault system is of metric to decametric scale. These faults are arranged in two north-trending alignments on the scale of the rock laboratory. The first fault zone is located in the northern part and dips to the east, while the second dips to the west. The Main Fault is located between the two. Apart from the three fault systems described in the previous sections, we identified two significant E-W-striking reverse faults dipping towards the south at a high angle (70°) in Gallery 08. These fault planes are characterised by down-dip striation produced by scratching and gouging, and show a top-to-N sense of shear.

3.1.3 Excavation Damaged Zone

When a volume of rock is perturbed, damage processes depend on the location of critical geological structures and the ensuing stress redistribution. Rock mass perturbations can range in scale from microscopic (e.g. grain-scale microfracturing) to macroscopic (e.g. extensile around tunnels). If disturbed stresses are high enough, rock mass strength may

be exceeded, which leads to macrofracturing. However, if disturbed stresses are not high enough to reach the strength envelope, micro-damage can nonetheless be sustained. The *in-situ* stress state measured in the Mont Terri rock laboratory is described in Chapter 3.3.

According to BOSSART et al. (2002, 2004), the fracture network related to tunnel excavation in the Mont Terri rock laboratory can be subdivided into an inner and outer shell. The inner shell, with an average extent of 1 m from the tunnel circumference, is typically characterised by extensional fractures sub-parallel to the tunnel wall and smaller-scale shear fractures. These fractures developed mainly in the tunnel walls (sidewall, ceiling, floor) and tunnel faces. Extensional fractures are often linked by smaller-scale shear fractures, resulting in an interconnected fracture network. The presence of gypsum spots on fracture planes in the inner shell is probably due to pyrite oxidation (BOSSART et al. 2002) as a result of air circulation coming from the tunnel. Therefore, the fracture network is most likely related to the tunnel. The outer shell, located between 1 to 2 m from the tunnel circumference, is composed of individual extensional fractures that are not, or only partially, interconnected. Detailed mapping of the tunnel floor revealed metric-scale, sub-horizontal extensional fractures. These fracture surfaces are characterised by a plumose structure with ripple structures and well-developed fringe zones (e.g. *en-échelon* or *hackle* structures; BAHAT 1986) indicating the fracture nucleation point and the propagation direction. No evidence of slip can be observed along these rough fracture surfaces that develop exclusively in tensile mode, most likely as a consequence of unloading of the tunnel floor (BOSSART et al. 2002). It should be noted that similar plumose structures were often also found on vertical extensional fracture planes developed parallel to the sidewall and tunnel face.

It was also observed that extensional EDZ fractures seldom propagate through pre-existing natural discontinuities such as well-developed inclined bedding planes and/or fault planes (THOENY 2014, YONG 2008). The systematic mapping of the galleries showed that the spatial distribution of EDZ fractures is, to a certain extent, controlled by pre-existing faults. Numerous related observations were made, such as the set of extensional EDZ fractures which formed below tectonic faults. Whatever their orientation, pre-existing faults spatially limited the propagation of EDZ fractures into the adjacent rock mass. In tunnel sections in which only a few pre-existing faults were identified, the majority of EDZ fractures was Mode I (extensional) and the EDZ fracture network was better developed. Slip along pre-existing small-scale fault planes and bedding planes was also found in the EDZ fracture network. As a consequence of the above-mentioned rock mass heterogeneities (e.g. frequency of pre-existing fractures and fault zones) and their influence on stress redistribution, the EDZ is heterogeneous in both its mode and, possibly, depth of fracturing. In conclusion, the EDZ fracture network is composed of: (1) extensional fractures (Mode I) often associated with plumose structures. These fractures are sub-parallel to the gallery sidewalls or front walls, (2) excavation-induced shear fractures (Mode II) with the same strike as the bedding planes but dipping at a higher angle and (3) reactivated bedding and fault planes.

3.1.4 Geological and structural mapping of the EZ-G08 segment

The EZ-G08 segment lies at the transition between the shaly facies and the sandy facies. The shaly facies predominantly consists of a monotonous succession of dark grey silty clays with few sand lenses and dispersed biotrititic material. The sandy facies locally exhibits quartz contents of over 50% (PETERS et al. 2011) and lenticular accumulations of coarse-grained biotrititus, forming elongated carbonate lenses. Within the sandy facies, sedimentary structures are more easily recognizable due to the alternation of laminated clay and silt/sand.

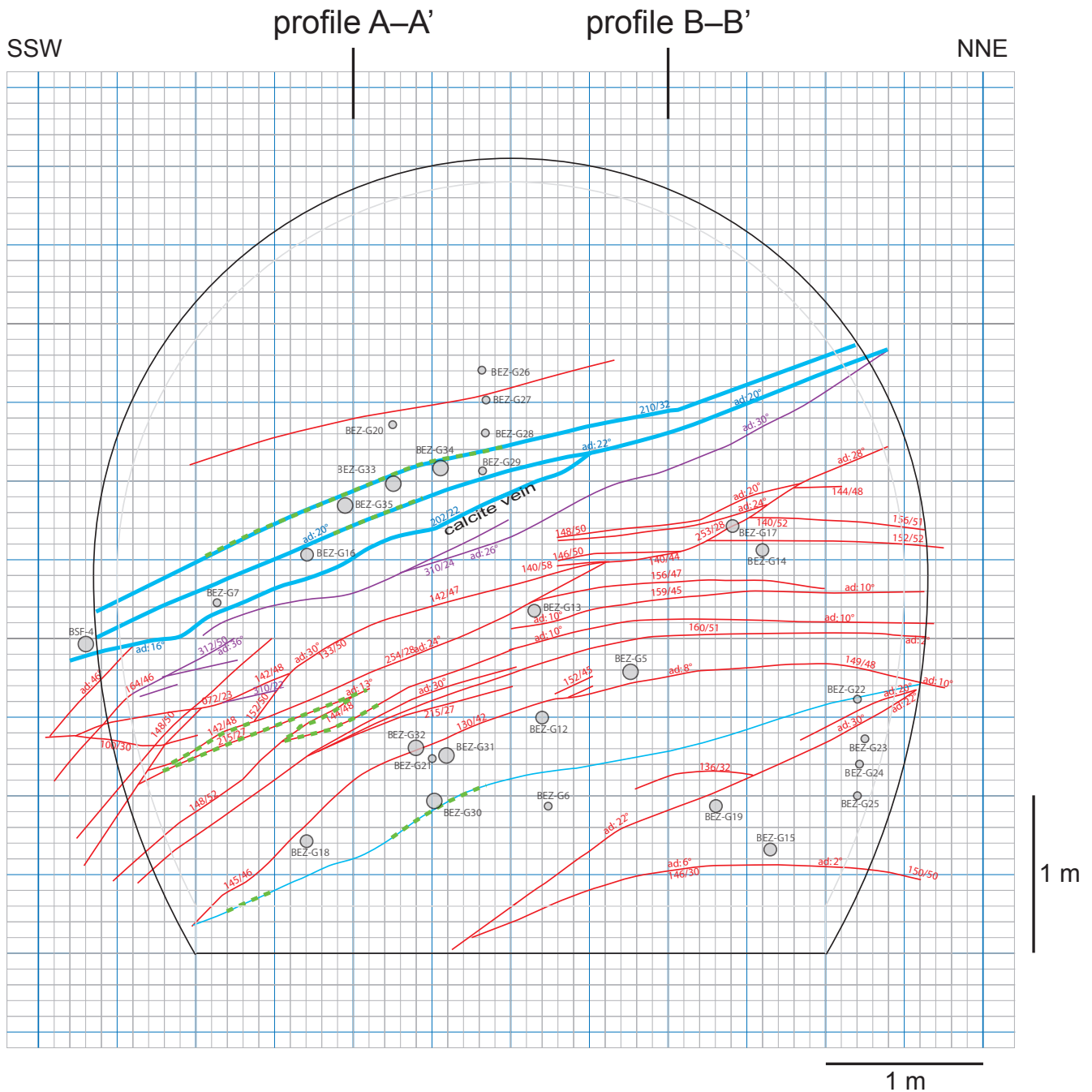
The Ga04 face is located in the shaly facies; its detailed structural mapping is indicated in Figure 3-3. The face is characterised by a major low angle SW-dipping fault (drawn in blue on Fig. 3.3). This fault is composed of three branches and divides the face into two compartments with different geophysical properties (NICOLLIN et al. 2010). According to the mapping of the adjacent front walls and side walls, it appears that this fault is interrupted by a significant SSE-dipping fault sub-parallel to the bedding. In turn, when looking towards SE into the Gallery 04, this fault exhibited a large extension since its initial identification and has been mapped in the side walls and ceiling between GM 40 and GM 80 (Fig. 3-4). At GM 40, this fault vanishes into the ceiling going out of the tunnel section. It is probable that it extends further. At the scale of the rock laboratory, this decametric fault may play a significant role. The structure of the Ga04 face is made more complex by the occurrence of NNE-trending fault, located below the major SW-dipping fault. This observation is in full accord with the mapping of the Gallery 04. Between GM 60 and GM 80, the Gallery 04 is intersected by a series of NNE-trending faults dipping to the WNW with different angles (from vertical to 20°). The lower half of the Ga04 face is mainly cut by a complex system made of numerous SE-dipping faults that are sub-parallel to the bedding planes. In the lower part of the face, the mouth of the BEZ-G30 borehole is intersected by a SW-dipping fault.

In contrast, the Ga08 front at GM 159 is located in the sandy facies and its face is intersected by only 4 single SE-dipping faults (Fig. 3-5). Neither SW-dipping nor NNE trending faults have been identified.

Structural mapping of the invert is compiled in Figure 3-6. The EZG-08 segment is mainly affected by SE-dipping faults with rare SW-dipping faults. These were later cut by SE-dipping faults. Two cross sections parallel to the gallery axis are shown in Figures 3-7 and 3-8. According to the orientation of the gallery in the EZ-G08 segment, the SE-dipping faults are more or less normal to the profiles, which means that apparent dips are very close to true dips (in the order of 40–45°). In turn, the SW-dipping faults have sub-horizontal apparent dips along these profiles. NNE trending faults plunge towards WNW with true dips. Both profiles reveal the same structures since they are only two m apart from each other. The EZ-G08 segment is characterised by two significant SE-dipping faults that end SW-dipping faults and, most notably, the major one intersecting Gallery 04 for 40 m. The NNE striking fault dipping to WNE is interrupted by the same SE-dipping fault that cuts the major SW-dipping

fault. One of the two SW-dipping faults identified in the invert between GM 161 and GM 165 (Fig. 3-6) are interrupted by the significant SE-dipping fault identified at about 5 m in the BEZ-G5 borehole. The EZ-G08 segment is characterised by a less deformed zone in the centre between GM 161 and GM 165, where only very few faults could be identified. Both cross sections show the facies boundary between the shaly and sandy facies. This transition is located very close to the Ga04 face since it intersects the invert between GM 166 and GM 167. In conclusion, the three fault systems known at Mont Terri were identified in the EZ-G08 segment and in particular on the Ga04 face.

On the scale of the tunnel, no distinct EDZ could be evidenced within the EZ-G08 segment. The EDZ fracture network resulted in the reactivation of pre-existing structures like fault planes or bedding planes. In turn, an EDZ fracture system to micro-scale was observed due to the resin impregnation technique (see Chap. 3.2).



Legend:

- | | | | |
|---|---|--|---------------|
| Tectonic Structures (pre-existing) | | Boreholes | |
| — | SE-dipping fault plane | ● | Boreholes |
| — | SW-dipping fault plane (~210/20) | - - - | Resin outflow |
| — | Rhenish NNE trending fault plane (~310/25) | | |
| 145/53 | Orientation measurement of plane (dip-direction/ dip) | | |
| ad: 23° | Angle of apparent dip of fault plane [°] | | |

Fig.3-3: Structural mapping of the Ga04 face (Gallery 04, GM 80) before excavation of the EZ-G08. The face is characterised by a major fault dipping to SW at low angle (in blue) that divides the face into two compartments.

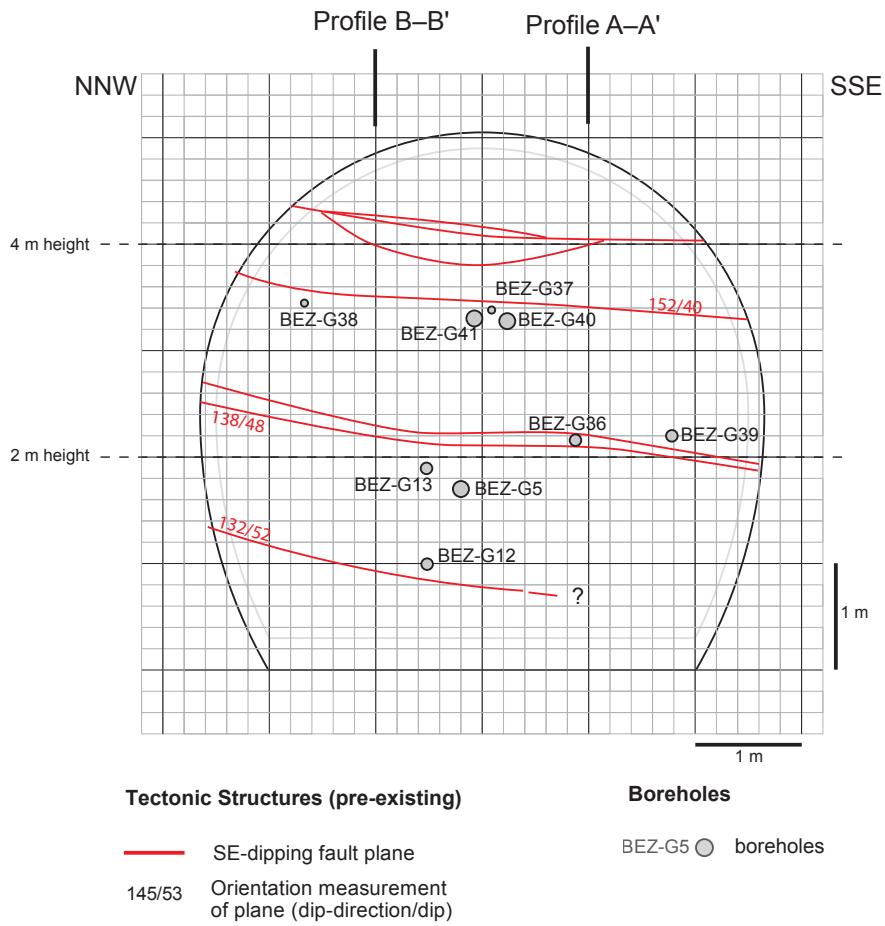


Fig. 3-5: Structural mapping of the Ga08 front (Gallery 08, GM 159) before excavation of the EZ-G08 segment.

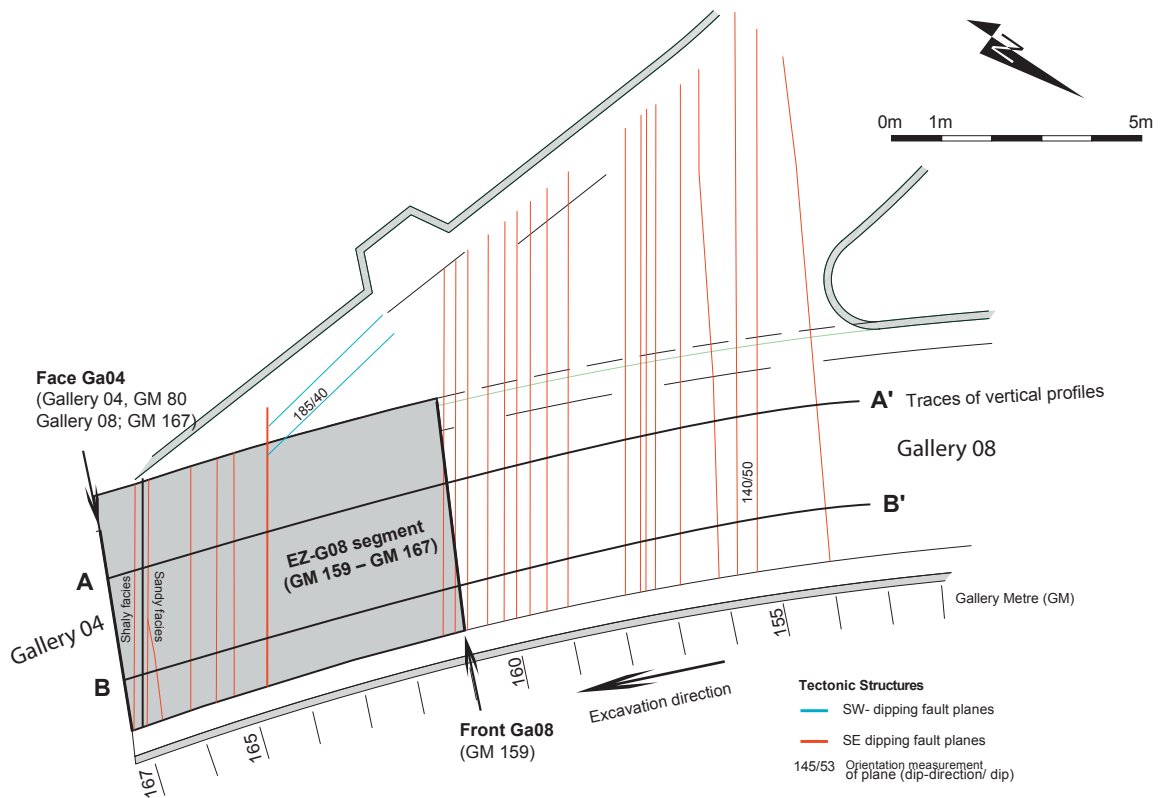


Fig. 3-6: Structural mapping of the invert, location of faces Ga04 and Ga08 and of both vertical profiles A-A' and B-B'. Note the occurrence of two SW-dipping faults (in blue) between GM 161 and GM 165. They are interrupted by the significant SE-dipping fault shown in Figs. 3-7 and 3.8.

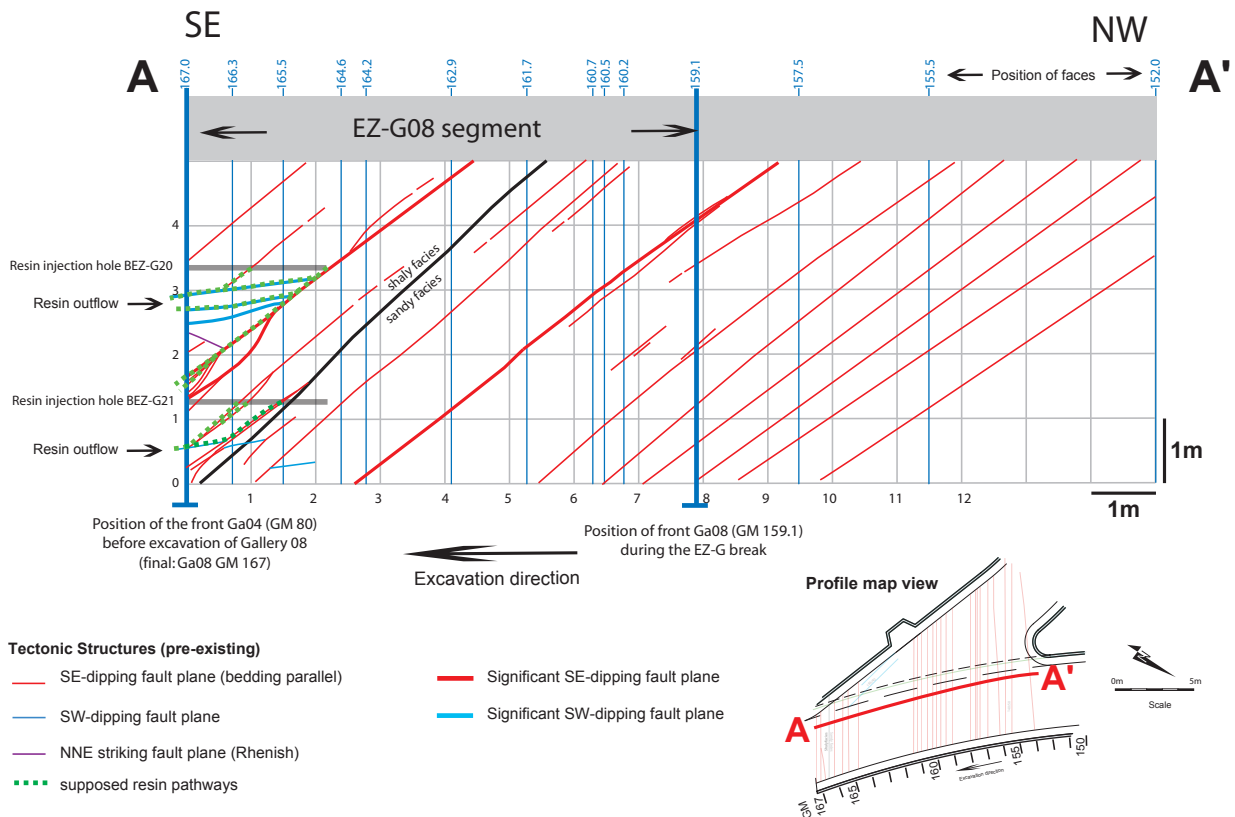


Fig. 3-7: Vertical profile A-A' along the EZ-G08 segment. The resin injected into BEZ-G20 and BEZ-G21 flowed out from the interconnected tectonic fracture network created by the combination of SE- and SW-dipping faults.

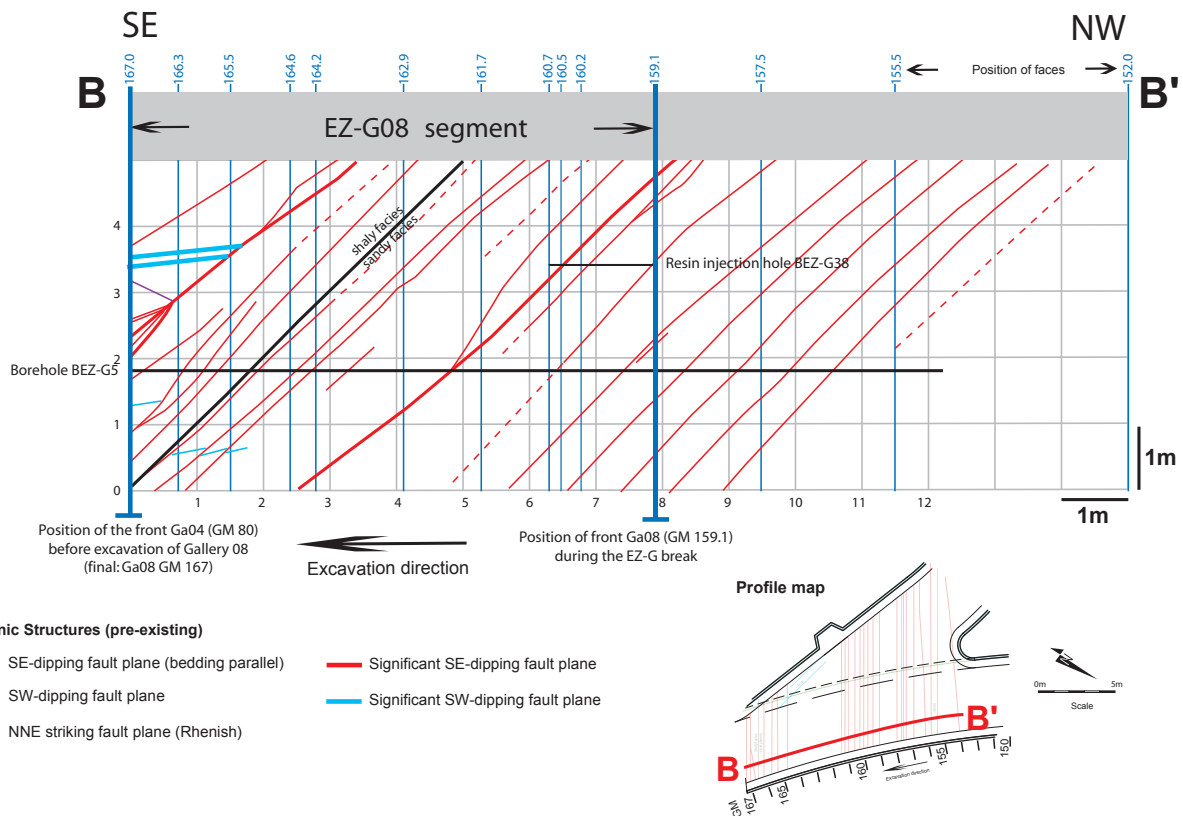


Fig. 3-8: Vertical profile B-B' along the EZ-G08 segment. This profile shows one of the injection boreholes in the Ga08 face at GM 159. The position of the BEZ-G5 borehole is indicated as well, as this borehole intersects the entire EZ-G08 segment and was used in numerous geophysical surveys.

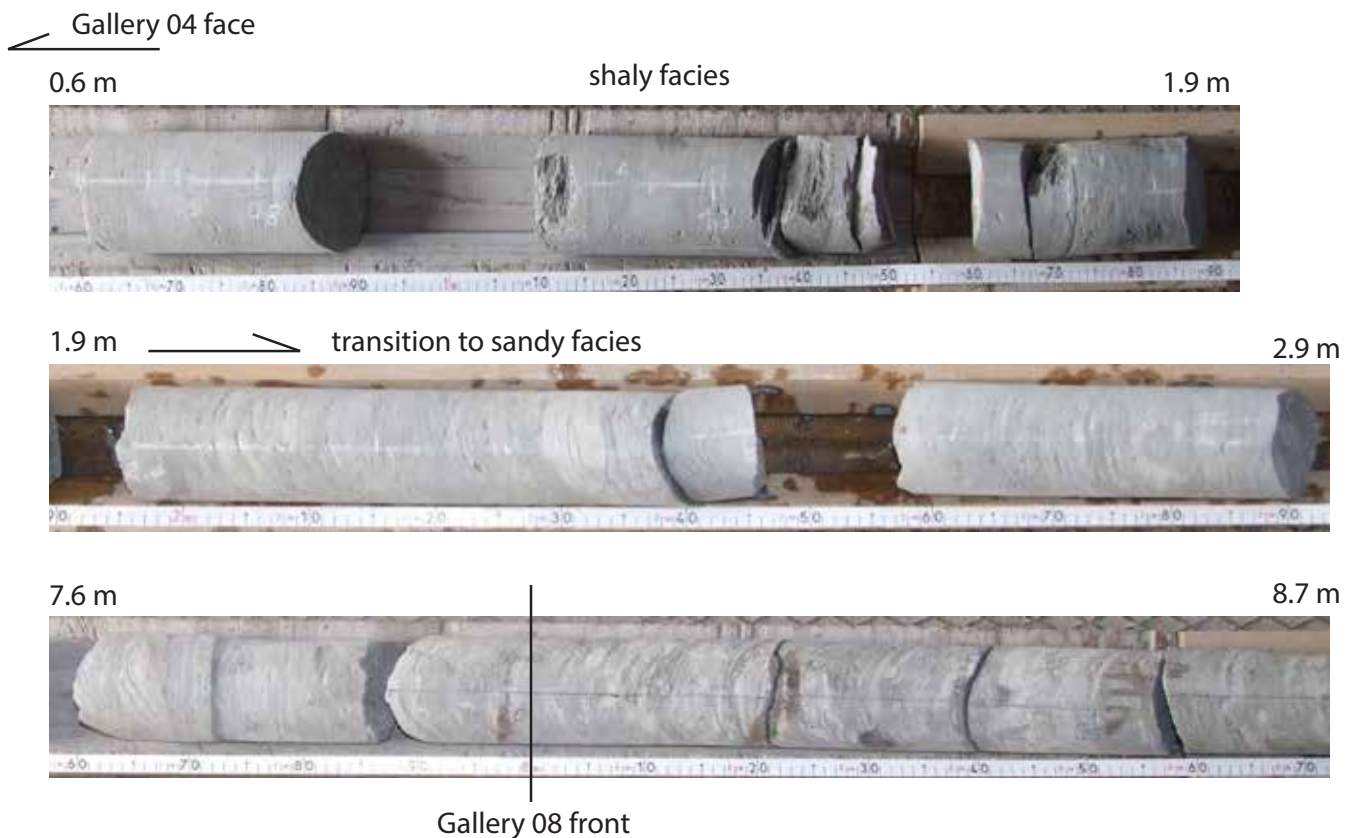


Fig. 3-9: The drillcore of BEZ-G5 is characterised by the occurrence of numerous white sandy layers, especially from a depth of 9.30 m onwards. The transition between shaly and sandy facies is located between 1.5 and 2 m from the Ga04 face at GM 80, though characterised by discrete and scarce sandy layers.

3.1.5 Geological mapping of drillcores

In total, we drilled 37 boreholes in the course of this experiment. They were drilled from the Ga04 face (28 boreholes) and Ga08 front (9 boreholes), and some of them cut through the entire EZ-G08 segment, such as the BEZ-G5 borehole, which is partly documented in Figure 3-9. By virtue of this borehole, the facies boundary between the shaly and sandy facies could be observed and mapped. The facies transition is located 2 m behind the Ga04 face. This lithological boundary is characterised by the transition between shaly facies composed of monotonous clays and sandy facies composed of marly siltstones and silty clays, silty and bioclastic lenses. The entire drillcore documentation of all boreholes has been reported in the Mont Terri Technical Note TN 2008-05 (GIRARDIN et al. 2005).

3.2 Visualisation of the fracture network by resin impregnation

The structural data collected by classical geological mapping were enhanced with new information provided by the visualisation of the fracture network using the *in-situ* resin impregnation technique developed by MÖRI & BOSSART (2000). This technique was applied behind both excavation faces (Ga04 and Ga08). The experimental concept consists of drilling small diameter pilot boreholes, which were used

for the injection of a specially designed fluorescein-doped epoxy resin. For resin injection, the pilot borehole is packed off with a mechanical single packer. The resin is then injected at pressures below the formation pressure in order to avoid artificial cracking of the rock. The injected resin fills the fractures and thus conserves the *in-situ* structures of the fracture network developed behind the tunnel wall. After auto-polymerisation of the two-component resin, subsequent overcoring of the pilot boreholes enables retrieval of large-diameter cores for structural analyses. Owing to the fluorescein in the resin, the impregnated fractures can be investigated under UV light at macro- and micro-scale.

3.2.1 Methodology

Resin injection was performed by means of an injection vessel connected with an injection tube to the injection interval. The injection interval was packed off by a mechanical packer installed at the borehole mouth so that it was completely emplaced in Opalinus Clay. A second line passing through the mechanical packer was used as an overflow line. This line reached the end of the injection interval at maximum borehole depth. The function of this second line is twofold: firstly, it allows the air in the injection interval to escape during the filling of the injection interval with resin and, secondly, it indicates the complete filling of the interval when the resin flows out of the borehole mouth. The resin needs to have a low viscosity to allow the impregnation of

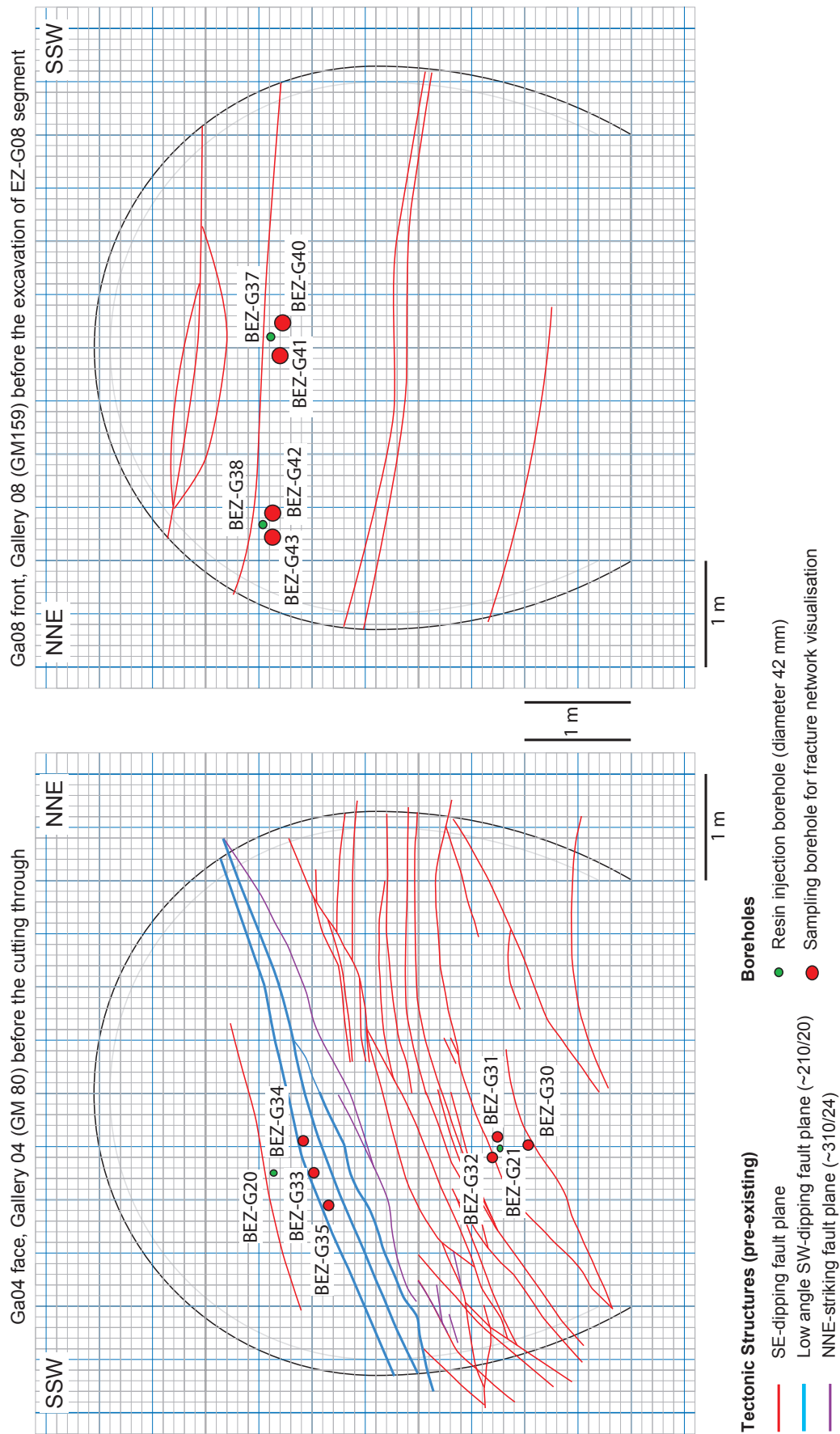


Fig. 3-10: Positions of resin injection boreholes and surrounding sampling boreholes on the Ga04 face and Ga08 front. Two resin injections were carried out on each face. Since the Ga04 face is divided by a major fault (in blue) delimiting two distinct compartments, a resin injection was carried out above (BEZ-G20) and below the fault (BEZ-G21). In absence of a characteristic structure on the Ga08 front, both injections (BEZ-G37 and BEZ-G38) were performed at the same height to investigate a common volume.

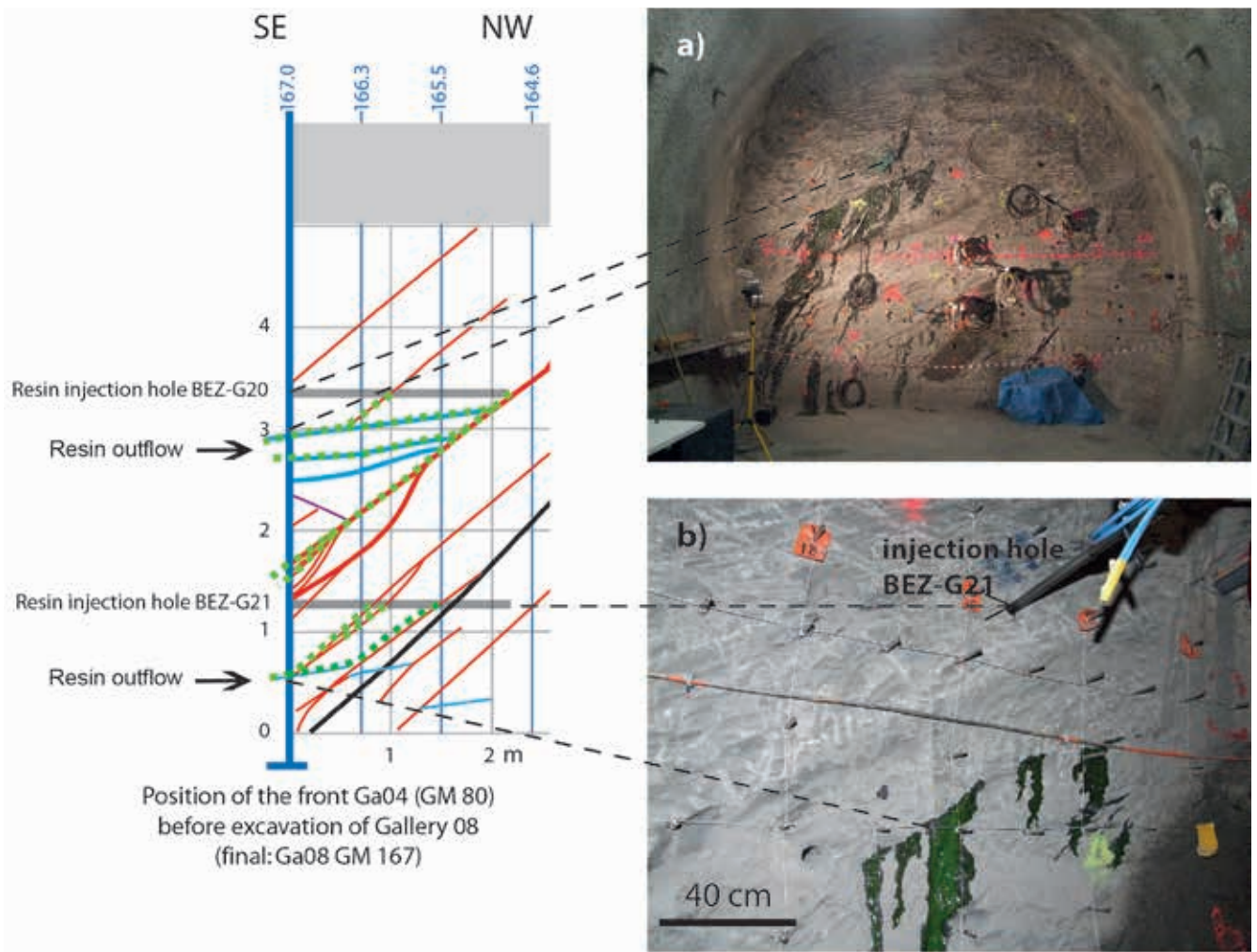


Fig. 3-11: View of the Ga04 face after resin injection. **a)** Resin outflow occurred along low angle SW-dipping faults (upper part) and SE-dipping faults, subparallel to bedding planes (lower part). The reader can compare this with Fig. 3-12; **b)** Detail of resin outflow along a SE-dipping fault and the position of injection borehole BEZ-G21. The mesh size is 50 cm.

small cracks and an isovolumetric polymerisation process to avoid the generation of new fractures. The injection vessel was placed on a balance connected to the data acquisition system to monitor the injection mass and rate. The injection pressure was applied with pressurised nitrogen and the pressure of the constant head injection was monitored as well. A maximum pressure of 4.4 bars was applied. The balance was set to zero at the beginning of the injection procedure. The injection valve was still held closed and nitrogen pressure was applied on the system. The valve of the overflow line was held open. Resin injection started with the opening of the injection valve. The in-flowing resin replaced the air in the interval. The air flowed out at the outflow line. As soon as the resin poured out of the overflow line at the borehole mouth, the valve of the overflow line was closed and resin injection into the rock mass began. Injection time and the mass of resin filling the injection interval were recorded. This record served to detect eventual injection problems and to determine the end of the resin injection. The resin injection was continued until the total mass of resin put into the pressure vessel was injected or until the injection rates were too small to be recorded.

3.2.2 Field work

We performed two field operations during the course of this experiment. The first action concerned the investigation of the Ga04 face. Two injection boreholes were drilled on June 2 and 3, 2008 by the local drilling team. The first one, called BEZ-G20, was located above the major SW-dipping fault plane that intersects the Ga04 face. The second one, called BEZ-G21, was drilled below the fault. Borehole positions are shown in Figure 3-10. On July 7, 8, and 9, 2008, two series of three sampling boreholes (BEZ-G30 to BEZ-G35) were drilled around both injection boreholes. The second operation took place on the Ga08 face with the drilling of two injection boreholes by July 14, 2008 (BEZ-37 and BEZ-G38). Since no significant structures or faults were recognised on the face, both injection boreholes were drilled at the same height to investigate the same volume with both injections. Two series of two sampling boreholes (BEZ-G40 to BEZ-G43) were drilled on July 21 and 28, 2008. Injection boreholes (diameter: 42 mm) were drilled with lengths ranging from 2.15 m to 2.60 m in order to ensure a representative impregnation of the fracture system. Lengths of sampling

boreholes (diameter: 116 mm) range from 2.5 to 3.5 m. The Geotechnical Institute Ltd performed the resin injection on June 3 and July 14, 2008 on the Ga04 and Ga08 faces, respectively. The injection pressure and the mass of injected resin were recorded for the four injection boreholes.

3.2.3 Macroscopic observation of the connectivity of the fracture network

A couple of minutes after the completion of resin injection through the Ga04 face, resin flowed out from the main tectonic structures, especially from the major SW-dipping fault as well as from SE-dipping faults (Fig. 3-11). The long injection time (81 minutes) that was required to completely fill up the 2 m long BEZ-G20 borehole with resin was an indication of resin leakage through some fractures. According to the profile shown in Figure 3-12, SE-dipping and SW-dipping faults together serve as flowpaths for the resin outflow. There, an interconnected fracture network was formed close to the gallery face. Around the BEZ-G21 injection borehole, located below the major SW-dipping fault, some resin outflows were observed as well. Again, interconnections between SE- and SW-dipping faults served as preferential flowpaths. After close inspection, it appeared that no EDZ fractures were impregnated by either of the injection boreholes on the Ga04 face.

In turn, the short injection time monitored for both boreholes BEZ-G37 and BEZ-G38 on the Ga08 face (31 and 19 minutes, respectively) indicated that the mass rock was less fractured and the fractures not, or only poorly, interconnected.

3.2.4 Structural analysis of resin-impregnated drillcores

In total, six sampling boreholes were drilled through the Ga04 face (BEZ-G30 to BEZ-G35) and four sampling boreholes from the Ga08 front (BEZ-G40 to BEZ-G43). Figure 3-10 illustrates all positions of sampling boreholes drilled for fracture visualisation and their respective locations in relation to the resin injection holes. BEZ-G30, BEZ-G31 and BEZ-G43 drillcores provided the best information on the resin-impregnated fracture network. BEZ-G30 and BEZ-31 were drilled from the Ga04 face, since BEZ-G43 from the Ga08 face.

A view of the first 27 cm of the BEZ-G30 core from Ga04 face is illustrated in Figure 3-12. The picture under UV light shows the impregnation of a large fracture, which corresponds to a SW-dipping fault (compare with the structural mapping in the lower part). This fault dips at an angle of 20° relative to the bedding planes and separates different fractures supposedly of EDZ origin. These fractures are either steeply inclined, being sub-parallel to the face, or parallel to bedding planes. They form an interconnected fracture system which may connect different tectonic faults together. The steeply inclined fractures were initiated in extension mode and correspond to unloading joints parallel to the excavation face, and the fractures parallel to bedding planes are probably associated with a shear component.

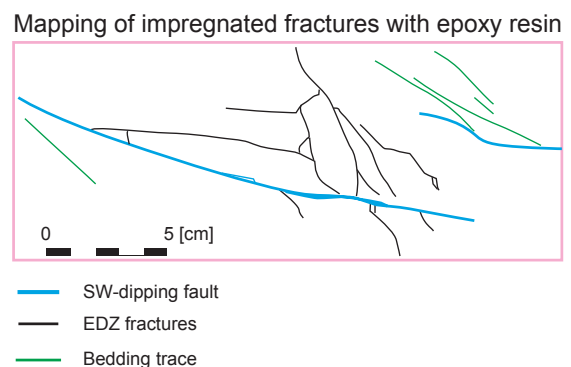


Fig. 3-12: View of an impregnated drillcore (BEZ-G30) under UV light (upper part). Corresponding structural mapping of the resin-impregnated BEZ-G30 drillcore (lower part). The impregnated fracture network consists of a combination of tectonic faults and EDZ fractures.

We note that only one sampling borehole from the Ga08 face provided traces of impregnated fractures: the BEZ-G43 core. The other drillcores did not exhibit any traces of resin or of fractures, which is consistent with the short injection time required to fill the injection boreholes. This observation can be tentatively explained by two factors: 1) The Ga08 face was excavated within the sandy facies containing numerous sandy lenses having a higher strength. The geological mapping of all sections through the sandy facies showed no traces of EDZ fractures. 2) The Ga08 face is significantly less affected by tectonic faults in comparison to the Ga04 face. Only four tectonic SE-dipping faults were identified on the entire face. The face was and remained quite stable even after some days.

3.2.5 Microscopic investigations on thin sections

According to the systematic observation of the resin-impregnated drillcores under UV light, we selected six interesting areas for thin sections taken from BEZ-G30, BEZ-31 and BEZ-G43. Two detailed photos from BEZ-G30 and one from BEZ-G31, accompanied by a structural mapping, are shown in Figs 3-13 and 3-14 respectively.

Figure 3-14 illustrates an impregnated EDZ fracture network without any interference with pre-existing faults. This

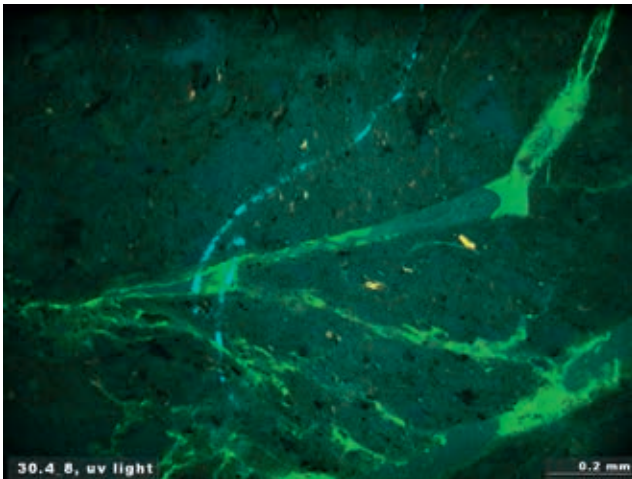


Fig.3-13: Thin section from BEZ-G30 sample (depth: 17 cm from tunnel wall) under UV light (upper) and corresponding structural sketch (lower). This sample shows that the impregnated fracture network is composed of unloading joints (EDZ) partly connected by shear fractures. Intersection lines between both fracture sets seem to build some channels filled by resin.

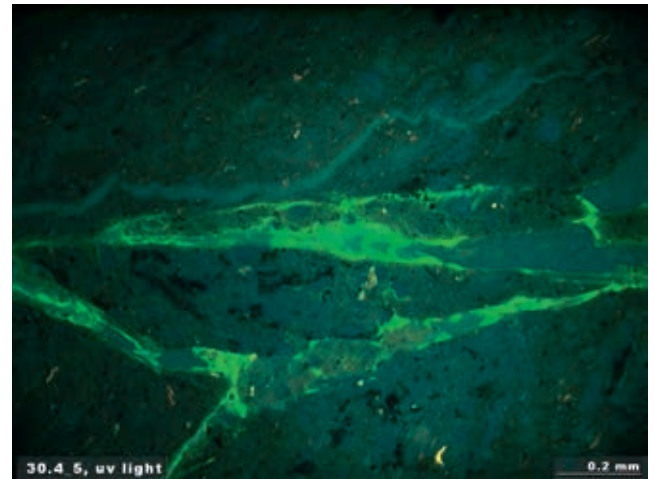


Fig.3-14: Thin section from the BEZ-G30 sample (depth: 17 cm from tunnel wall) under UV light. The impregnated fracture corresponds to a connection between an apparent horizontal SW dipping fault and to bedding traces dipping with 45° to the SE.

thin section was sampled from between two faults and enables us to visualise the internal structure of the rock not affected by pre-existing faults. Note that the depth is 17 cm, which is very close to the excavation face. The structure is composed of fractures lying parallel to bedding planes and sub-vertical fractures (unloading joints) sub-parallel to the face. The intersection lines where both fracture sets join seemed to create some channels filled by resin.

In Figure 3-15, the horizontal impregnated fracture corresponds to a SW dipping tectonic fault that was affected by the seasonal variations of tunnel ambient air humidity over a period of 4 years. This fault served as a resin pathway, as attested by the resin outflow observed a couple of minutes after the resin injection into the BEZ-G21 hole. Injected resin flowed along SE-dipping faults before reaching this SW-fault and outflowing from the Ga04 face (Fig. 4-14).

3.3 *In-situ* stress state

MARTIN & LANYON (2003) showed that *in-situ* stress measurements in the Opalinus Clay at the Mont Terri rock laboratory are challenging and their proposed stress tensor is uncertain. The *in-situ* stress state was estimated by the use of three-dimensional numerical modelling, stress-induced borehole breakouts, undercoring, overcoring, borehole slotter, and hydraulic fracturing tests. Due to the argillaceous nature of the material and the persistent and ubiquitous nature of the bedding planes, constraining the tensor was and remains a challenging task. Two different stress tensors were derived from the borehole slotter, and undercoring methods. The largest difference between these methods lies in the directions of the principal stresses. In the borehole slotter and overcoring methods, maximum (σ_1) and intermediate (σ_2) principal stress lies in the bedding planes while the mini-

mum principal stress (σ_3) is oriented normal to the bedding plane. In the undercoring method, σ_1 is sub-vertical while σ_2 and σ_3 are subhorizontal. MARTIN & LANYON (2003), through numerical modelling, found that the tensor derived from the undercoring method provided a better fit to the observations of borehole breakouts. In addition, the normal stress acting on the bedding determined from the undercoring method was also better suited with what was determined from hydraulic fracturing measurements. MARTIN & LANYON (2003) also reasoned that stress relief and erosion from valley formations to the southwest and northeast of the rock laboratory more adequately agreed with the orientation of σ_3 determined with the undercoring method. The elevation of the laboratory, above the valley bottoms, was also used to justify the abnormally low σ_3 magnitudes (i.e. 0.6 MPa) determined with both methods. Indeed, the magnitude of the minimum principle stress – which is less than the undisturbed pore pressure of about 2 MPa measured outside the excavation-disturbed zone (MARTIN & LANYON 2003) – is questionable. For this reason, BOSSART & WERMEILLE (2003) recommended an equivalent minimum value for σ_3 . CORKUM (2006) proposed a minimum principle stress magnitude of 2.2 MPa. Based on the results from hydraulic fracturing tests, EVANS et al. (1999) proposed a value of approximately 2.9 MPa for the minimum principle stress magnitude.

Finally, the best guess for the *in-situ* stress was indicated by MARTIN & LANYON (2003). They suggested a sub-vertical maximum principle stress orientation that is steeply (70°) inclined towards SSW with a magnitude of 6–7 MPa, a subhorizontal intermediate principle stress direction trending with 10° towards NW with a magnitude of 4–5 MPa, and a subhorizontal minimum principle stress direction trending towards NE with a corrected magnitude between 2–3 MPa as discussed previously. Note that the *in-situ* stress state in the surrounding competent formations is significantly different from that in the Opalinus Clay.

3.4 Discussion and conclusion

The tectonic structure of the EZ-G08 segment is quite complex and intersected by three fault systems identified in the Mont Terri rock laboratory: i) SE-dipping faults, ii) low angle SW-dipping faults and iii) NNE trending faults. Since these faults dip with different orientations, the resulting structural pattern is very heterogeneous in comparison to other locations in the rock laboratory, where the SE-dipping faults, subparallel to the bedding, largely predominate. The major SW-dipping fault that intersects the ceiling and side-walls of the Gallery 04 along more than 40 m cuts the Ga04 face of the investigated area. The signification and role of this decametric fault were confirmed by the electrical tomography carried out by NICOLLIN et al. (2010). According to these authors, the fault divides two compartments with different electrical resistivities.

Based on the inspection of drillcores and tunnel walls, we could not identify any EDZ fractures. The *in-situ* resin impregnation of the fracture network enabled us to reveal the presence of EDZ microfractures oriented parallel to the excavation face. These fractures were initiated in extension mode and correspond to unloading joints. The scarce occurrence of EDZ fractures may be explained by the omnipresence of tectonic faults inside the EZ-G08 segment rock mass. Previous studies demonstrated the role of pre-existing tectonic fractures as limiting structures for the coalescence of EDZ fracture (THÖNY 2014, YONG 2008, YONG et al. 2010). A well-developed tectonic fracture network significantly constrains the development of EDZ fractures.

The study of *in-situ* resin impregnation provided valuable information on the amount of connectivity of pre-existing tectonic faults. Resin outflows observed on the Ga04 face resulted from the interconnectivity and reactivation of SE- and SW-dipping faults during the excavation of Gallery 04. Since this face was exposed to tunnel ambient air for about four years and was not covered by any shotcrete layer significant desaturation occurred along these fractures.

There are significant natural heterogeneities of rock mass at the facies transition between the shaly and sandy facies, located about 2 metres behind the Ga04 face. This lithological boundary is characterised by the transition from argillaceous and marly shales to marly shales with layers of sandstones and lenses of grey, sandy limestones.

References

- BAHAT, D. (1986): Criteria for the differentiation of en échelon and hackles in fractured rocks. – *Tectonophysics* 17575, 197–206.
- BLÄSI, H.R., MÖRI, A. & BOSSART, P. (1996): Results of the Phase 1 Drilling Campaign. – Mont Terri tech. Rep. TR 1996-01.
- BOSSART, P., MEIER, P., MÖRI, A., TRICK, T. & MAYOR, J.C. (2002): Geological and hydraulic characterisation of the excavation disturbed zone in the Opalinus Clay of the Mont Terri Rock Laboratory. – *Eng. Geol.* 66, 19–38.
- BOSSART, P. & THURY, M. (2008): Mont Terri Rock Laboratory. Project, Programme 1996 to 2007 and Results. – Rep. Swiss geol. Survey 3.
- BOSSART, P., TRICK, T., MEIER, P.M. & MAYOR, J.C. (2004): Structural and hydrogeological characterisation of the excavation-disturbed zone in the Opalinus Clay (Mont Terri Project, Switzerland). – *Appl. Clay Sci.* 26, 429–448.
- BOSSART, P. & WERMELLE, S. (2003): The Stress Field in the Mont Terri Region – Data Compilation. – In: HEITZMANN, P. & TRIPET, J.-P. (Eds.): Mont Terri Project – Geology, paleohydrology and stress field of the Mont Terri Region. – Rep. fed. Office Water Geol. (FOWG) 4, 65–92.
- CORKUM, A.G. (2006): Non-linear behaviour of Opalinus Clay around underground excavations. – Ph.D. Thesis Univ. Alberta.
- EVANS, K., PIEDEVACHE, M. & PORTMANN, F. (1999): IS Experiment: Hydrofracture stress tests in boreholes BIS-C1 and BIS-C2. – Mont Terri tech. Note TN 1999-55.
- GIRARDIN, C., BADERTSCHER, N. & NUSSBAUM, C. (2008): Drilling campaign of Phase 13: Drilling data, photo documentation and drill-core documentation. – Mont Terri tech. Note TN 2008-05.
- MARTIN, C.D. & LANYON, G.W. (2003): Measurement of in-situ stress in weak rocks at Mont Terri Rock Laboratory, Switzerland. – *Int. J. Rock Mech. Min. Sci.* 40, 1077–1088.
- MÖRI, A. & BOSSART, P. (2000): FP (Fracture propagation) experiment: Method, results, interpretation. – Mont Terri tech. Note TN 99-72
- MÜLLER, P. & JAEGGI, D. (2012): Sedimentary structure in the sandy facies of the Opalinus Clay at Mont Terri rock laboratory. – Mont Terri tech. Note TN 2012-45
- NICOLLIN, F., GIBERT, D., LESPARRE, N., & NUSSBAUM, C. (2010): Anisotropy of electrical conductivity of the excavation damaged zone in the Mont Terri Underground Rock Laboratory. – *Geophys. J. int.* 181; 303–320. DOI 10.1111/j.1365-246X.2010.04517.x.
- NUSSBAUM, C., BOSSART, P., AMANN, F. & AUBOURG, C. (2011): Analysis of tectonic structures and excavation induced fractures in the Opalinus Clay, Mont Terri underground rock laboratory (Switzerland). – *Swiss J. Geosci.* 104/2; DOI 10.1007/s00015-011-0070.
- NUSSBAUM, C., BOSSART, P., BURRUS, F., BADERTSCHER, N., MEIER, O. & NOLD, A. (2005): A. Excavation of Gallery 04: General Documentation, Deformation Measurements and Geological Surveys (2005). – Mont Terri tech. Note TN 2005-05.
- NUSSBAUM, C., GIRARDIN, G., BADERTSCHER, N., RISSE, V., VEUVE, C., MAYORAZ, J. & BOSSART, P. (2010): Extension of the rock laboratory: Geological documentation of the Gallery 08 and adjacent niches (DR-A, MB, niche 3 and TT). – Mont Terri tech. Note TN 2008-12.
- PETERS, M., MAZUREK, M., JAEGGI, D. & MÜLLER, H.R. (2011): WS-H Experiment: Heterogeneities in the sandy facies of Opalinus Clay on a scale of millimeters to centimeters. – Mont Terri tech. Note TN 2010-76.
- REISDORF, A., HOSTETTLER, B., WALTSCHIEW, A., JAEGGI, D. & MENKVELD-GFELLER, U. (2014): SO (Sedimentology of Opalinus-Ton), biostratigraphy of the basal part of the Opalinus-Ton at the Mont Terri rock laboratory, Switzerland. – Mont Terri tech. Rep. TR 2014-07.
- THOENY, R. (2014): Geomechanical analysis of excavation-induced rock mass behavior of faulted Opalinus Clay at the Mont Terri Underground Rock Laboratory (Switzerland). – Ph.D. Thesis ETH Zürich.
- WETZEL, A. & ALLIA, V. (2003): Der Opalinuston in der Nordschweiz: Lithologie und Ablagerungsgeschichte. – *Eclogae geol. Helv.* 96, 451–469
- YONG, S. (2008): A three-dimensional analysis of excavation-induced perturbations in the Opalinus Clay at the Mont Terri Rock Laboratory. – Ph.D. Thesis ETH Zürich 17575.
- YONG, S., KAISER, P.K. & LOEW, S. (2010): Influence of tectonic shears on tunnel-induced fracturing. – *Int. J. Rock Mech. Min. Sci.* 47, 894–907.

4. Statistical analysis of the fracture network

J.-F. THOVERT, V.V. MOURZENKO, P.M. ADLER & C. NUSSBAUM

4.1 Introduction

This chapter provides a description of the analysis and characterisation of the fracture network which was mapped in Gallery 08 and its modelling in order to use it later for a realistic reconstruction of numerical fracture networks and the determination of flow properties.

A previous contribution dealt with the reconstruction of a fracture network observed in Gallery 04 (THOVERT et al., 2011). The trace maps of the Gallery 04 and of the EZ-G08 segment were first digitized and then used in various ways to characterize the data. The traces were divided into two groups, i.e., the pre-existing faults in the gallery and the fractures of the excavated damaged zone (EDZ) in the niche. Each group was analysed individually. The number of data for the faults turned out to be statistically significant, though it was very limited for the EDZ fractures. The major statistical characteristics of the traces were extracted in both cases, and a reconstruction procedure developed and tested. A full example was worked out; a gallery immersed in a reconstructed fractured porous medium was meshed, and the electrical field created by a dipole at the wall calculated by solving the three dimensional Laplace equations in the fractures and the porous medium.

The present work addresses the fracture network in Gallery 08 in the same site. We drew exhaustive trace maps for

the invert, ceiling, and side walls, and for the excavation front at successive positions, recording the pre-existing faults, the excavation-induced fractures and the stratigraphic bedding. Orientations were also recorded for a subset of the traces. However, although several niches were dug from the gallery, no information regarding the extension of the EDZ fractures within the embedding rock could be obtained. In the following, we will focus on the quantification of the observations of various kinds of objects on the gallery walls in terms of density, orientation distribution, and spatial arrangement. Since the gallery consists of a curved and a straight section, it was possible to examine the correlation between the EDZ fracture orientation and the faulting, bedding and digging directions. Finally, we propose methods for three-dimensional modelling of the fracture network and for determining EDZ transport properties.

This chapter is organized as follows. Chapter 4.2 presents a general view of the Gallery Ga08 and of the data which were measured in it. Chapter 4.3 analyses the data recorded in the linear portion of the gallery. Orientations of the various types of faults are described in Chapter 4.4. The relative spatial organization of the faults and of the EDZ fractures is discussed in Chapter 4.5. The trace length distribution of the EDZ fractures is examined in Chapter 4.6. A preliminary analysis of the connectivity and percolation of the EDZ fracture network is presented in Chapter 4.7. Finally, concluding remarks in Chapter 4.8 complete this chapter.

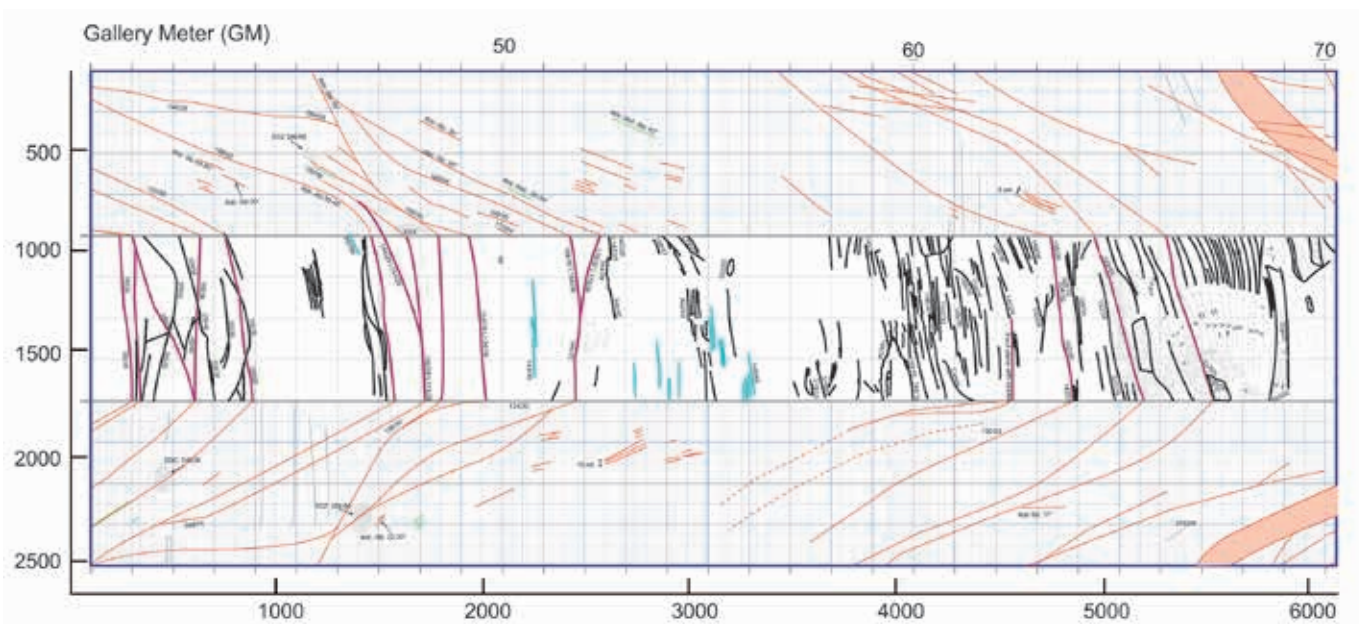


Fig. 4-1: Example of traces in the Gallery 08 ($40 < x < 70$ m). The digitized traces are shown in the central part (gallery ground). Colours are for: pre-existing faults (magenta), lithological (blue) and EDZ (black).

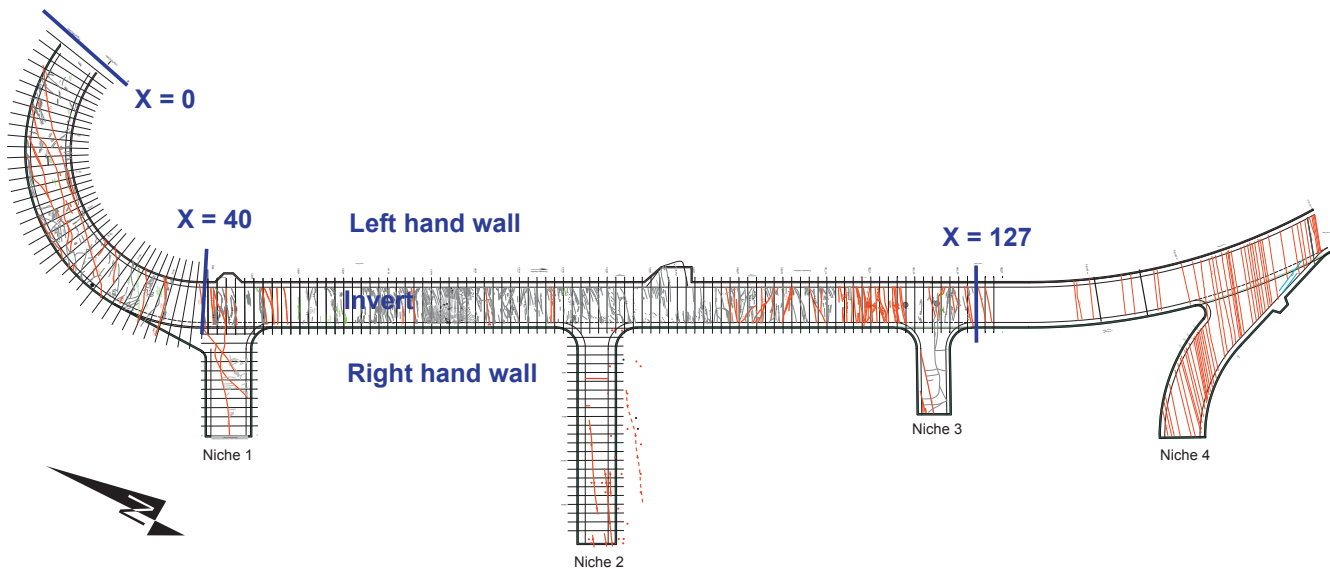


Fig. 4-2: Overall map of the invert fracture network observed in Gallery 08.

4.2 Data collection

The data essentially consist of a map of the observed traces on the ground and on the lateral walls of the Gallery 08 as well as at the excavation front in its successive stages during the digging. These stages are separated by approximately one m. An example is displayed in Figure 4-1. This map shows the bedding traces, the pre-existing faults and the EDZ fractures. In a first step, we manually digitized these traces with the aid of a computer.

These maps also provide the orientations (azimuth and dip) of an important subset of fractures which belong to these three categories. Moreover, orientations are provided in another file; the longitudinal position along the gallery of the corresponding traces was recorded, but there is no information on their length and lateral position.

The gallery consists of a curve followed by a straight line as shown in Figure 4-2. Let x be the abscissa with an origin located at the North end. The curve goes from $x=0$ to 40 m. The linear portion of the gallery goes from $x=40$ to 127 m. For $x > 127$ m, there is a facies transition from shaly to sandy, and, as a consequence, no trace was recorded. The names given to the walls, left (or NE) and right (or SW), correspond to a progression of increasing values of x . In addition, the y -axis is horizontal to its origin at the SW wall, and the z -axis is vertical with its origin located at the gallery ground.

First, we thoroughly analysed the ground traces in the linear portion. The curved portion was taken into account in a second step and only for orientation statistics.

4.3 Spatial distribution in the linear part (40–127 m)

Some elementary statistical characteristics should be provided first. Eighty-eight fault traces (with a total length of 242.2 m), 669 EDZ traces (with a total length of 583.2 m) and 27 lithological traces were recorded on the invert of this straight section.

A trace density C [m/m^2] can be determined by dividing the total length by the observation area. A slightly different measurement can be obtained from the frequency n_l [m^{-1}] of intersections between scan lines and traces. These scan lines are taken parallel to the gallery axis every 25 cm (Fig. 4-3). The densely faulted zone of about 5 m at $x \approx 115$ m was not taken into account. The traces are approximately perpendicular to the gallery axis. Therefore, the density n_l , which corresponds to the density of their projection on the y -axis, is slightly smaller than C . Results are given in Table 4-1.

The same measurements were also performed in four parallel zones with a width of 1 m in order to examine the density distribution as a function of the transversal location in relation to the gallery. As expected, the resulting distribution of fault traces is very homogeneous since they generally cross the whole section. However, the EDZ trace density is much larger in the vicinity of the NE wall than in the rest of the gallery ground.

Tab. 4-1: Trace densities in the whole area of the linear gallery portion ($40 < x < 127$ m) and in four zones of width 1 m.

Faults	C	n_l	EDZ	C	n_l
	[m/m^2]	[m^{-1}]		[m/m^2]	[m^{-1}]
Global	0.712	0.687	Global	1.777	1.680
NE walls	0.717	0.687	NE walls	2.283	2.129
	0.723	0.695		1.673	1.605
	0.719	0.697		1.536	1.454
SW walls	0.691	0.669	SW walls	1.615	1.531

Locally, trace density can be determined as a function of x per portions of 1 m along the gallery axis (i.e., on $1 \times 4 \text{ m}^2$ surfaces) or per portions of $1 \times 1 \text{ m}^2$. The density profiles corresponding to the first case are displayed in Figure 4-4; a large zone ($x=80 \sim 100$ m) does not contain any fault.

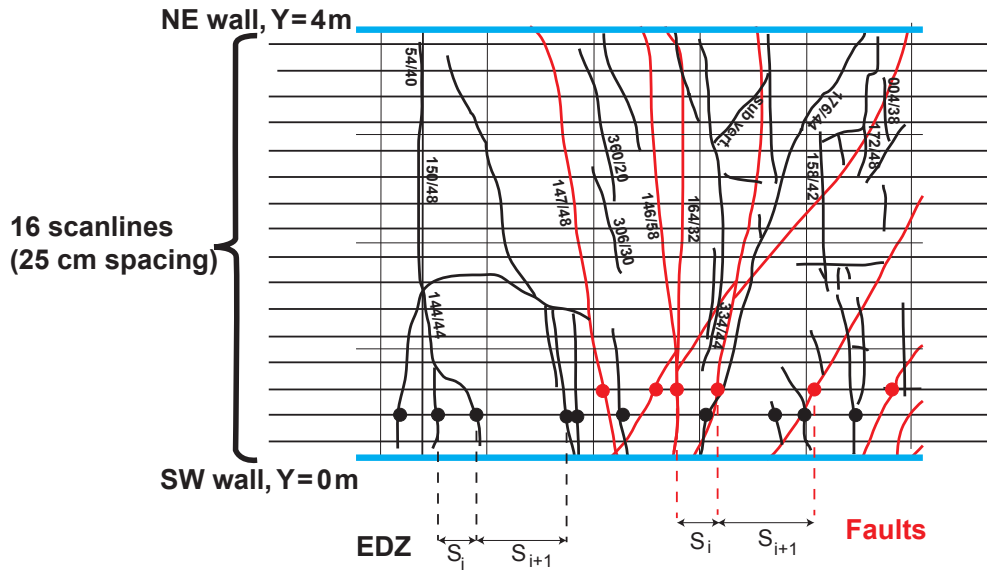


Fig. 4-3: Fracture analysis by scan lines.

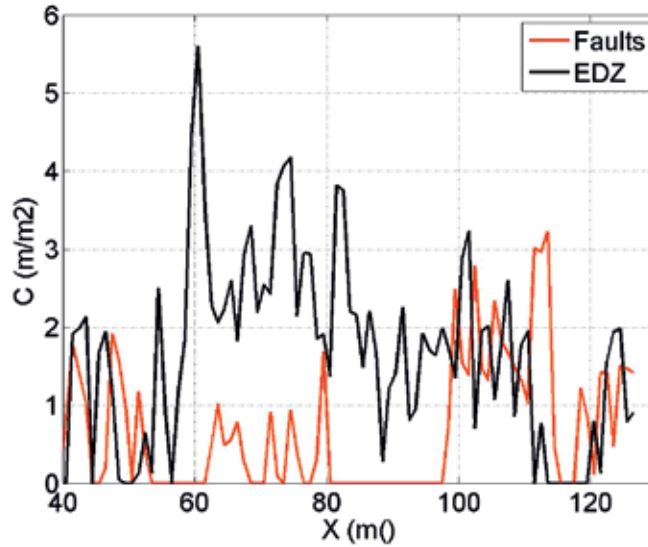


Fig. 4-4: Density profiles C [m/m²] as functions of x . Data are for faults (red) and EDZ (black).

The density profiles corresponding to the second case are displayed in Figure 5; the EDZ trace density is shown to be larger along the NE wall. The averages $\langle C \rangle$ and standard deviations σ_C of these local densities are

- (1a) Faults: $\langle C_F \rangle = 0.712 \text{ m}^{-1}$, $\sigma_{C,F} = 0.923 \text{ m}^{-1}$
 (1b) EDZ: $\langle C_{EDZ} \rangle = 1.777 \text{ m}^{-1}$, $\sigma_{C,EDZ} = 1.589 \text{ m}^{-1}$

The correlation coefficient is very small:

(2) $\text{covar}(C_F, C_{EDZ}) / \sigma_{C,F} \sigma_{C,EDZ} = -0.25$

Therefore, the occurrence of EDZ traces is not correlated with the local density of pre-existing faults.

The spatial organisation of the traces can be quantified by statistics on the spacings s_i of their intersections with scan lines (see Fig. 4-3). Their averages $\langle s \rangle$ and their standard deviations σ_s are equal to

- (3a) Faults: $\langle s \rangle = 1.496 \text{ m}$, $\sigma_s = 2.97 \text{ m}$
 (3b) EDZ: $\langle s \rangle = 0.608 \text{ m}$, $\sigma_s = 1.16 \text{ m}$

In both cases, σ_s is larger than $\langle s \rangle$. Therefore, the traces are clustered, since a Poissonian distribution of the traces without any spatial organisation would yield $\sigma_s = \langle s \rangle$, while a more regular distribution would yield $\sigma_s < \langle s \rangle$. This is confirmed by the semivariogram, i.e., the covariance between successive spacings

(4) $\gamma(n) = \frac{1}{2} \langle (s_i - s_{i+n})^2 \rangle$

This covariance between successive spacing is constant and equal to the variance when there is no spatial correlation. The measurements presented in Figure 6 do not show any short range correlation for the faults and for the EDZ ($\gamma(n)/\sigma_s^2 \approx 1$); however, the faults are organised on a larger

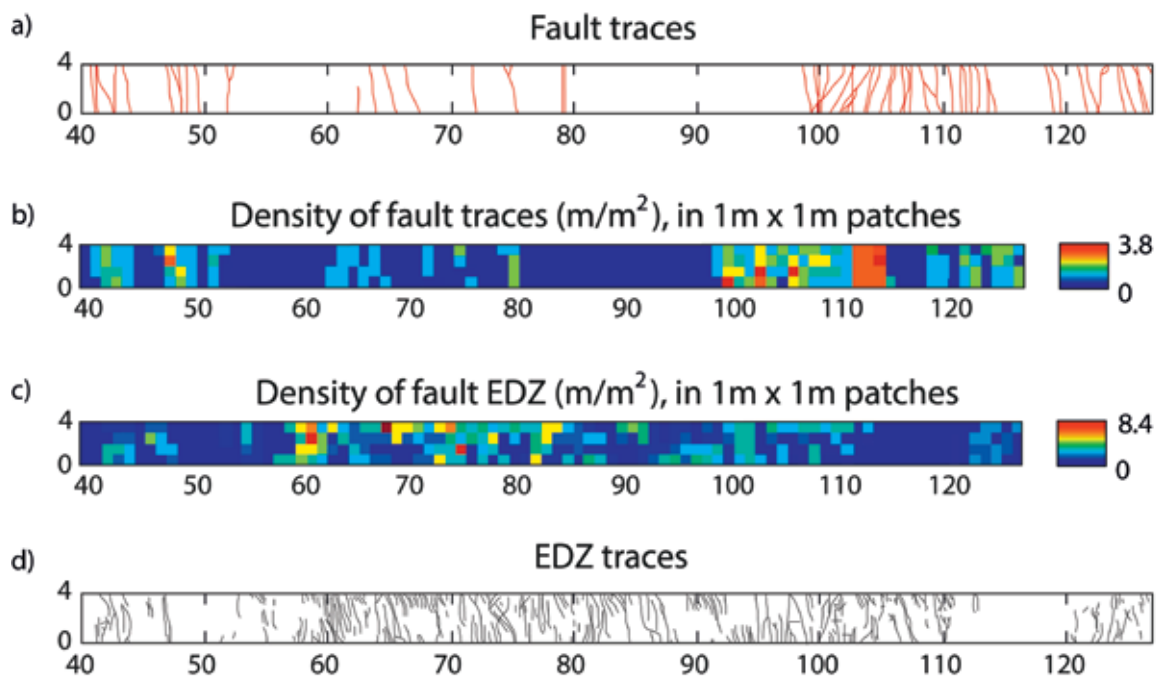


Fig. 4-5: Density maps C [m/m^2] on the ground of the linear portion ($40 < x < 127$ m) of the Gallery 08.

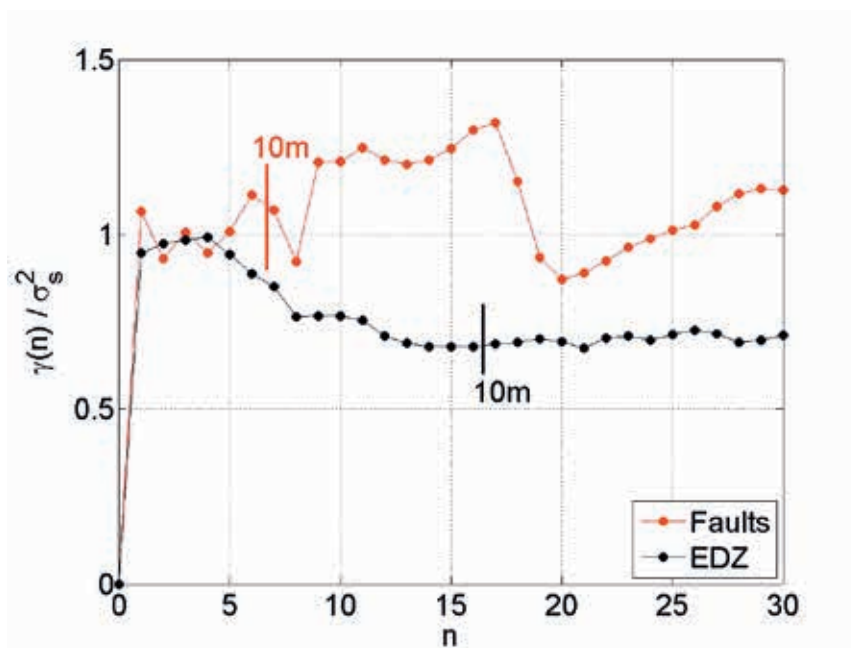


Fig. 4-6: Normed semivariograms $\gamma(n)/\sigma_s^2$ for the fault ground traces (red) and EDZ (black) in the linear portion of the Gallery 08 ($40 < x < 127$ m).

scale, as visible in Figure 4-3, where they appear in well-defined zones separated by large intervals without any fault.

4.4 Orientation distributions

The maps provide fracture orientations for some of the traces that are visible in the Gallery 08. In addition, a separate file contains a set of orientations. We used this latter file since it contains much more information than the maps in some zones of the gallery; however, it is not exhaustive. The longitudinal position is given, but the transversal one is not; therefore, observations in the upper and lower part of the ex-

cavation front cannot be distinguished. Moreover, as a result of the length of the corresponding traces not being given, only statistics in number – and not in length – can be given. The number of observations per trace family and per position is shown in Table 4-2.

4.4.1 Fault orientations

The normals to the faults are represented by hemispherical diagrams in Figure 4-7. Observations in the two portions of the gallery, on the ground, and on the two walls as well as on the excavation front in the curved portion are all very similar. This was to be expected, since the faults were pre-

Tab. 4-2: Number of orientation observations for each trace family and each section.

		Faults	Lithological faults	EDZ
Curved section (0–40 m)	Left wall	6	2	24
	Ground	31	6	53
	Right wall	30	2	28
	Front	75	8	10
Linear section (40–127 m)	Left wall	41	5	8
	Ground	43	5	98
	Right wall	30	2	6
	Front	173	16	76

sent before the gallery was dug. However, the typical dips are larger on the excavation front in the linear portion.

These data are well fit by a Fisher distribution, which is characterized by a pole \mathbf{p} and a parameter κ . The normals are parallel to \mathbf{p} when $\kappa \rightarrow \infty$ and they are isotropically distributed when $\kappa = 0$. The probability density of the angle between the normals and \mathbf{p} can be expressed as

$$(5) \quad f(\theta) = \frac{\kappa}{\sinh \kappa} \sin \theta \cosh(\kappa \cos \theta)$$

The average value of $\cos \theta$ is given by

$$(6) \quad \langle \cos \theta \rangle = \langle \mathbf{p} \cdot \mathbf{n} \rangle = 1 + \frac{1 - \cosh \kappa}{\kappa \sinh \kappa}$$

The pole direction is derived by maximizing the sum

$$(7) \quad \sum_i (\mathbf{p} \cdot \mathbf{n}_i)^2$$

The sum is done on all the measured normals \mathbf{n}_i . The value of κ is derived from (6).

The sampling is biased because of the relative orientations of the normals \mathbf{n}_i and of the observation plane, whose normal is \mathbf{v} . This bias is corrected by weighting each observation by $1/\sin \gamma_i$, where γ_i is the angle between \mathbf{n}_i and \mathbf{v} .

All the data for the faults are represented in Figure 4-7 in which the pole is indicated; the two circles contain 68% and 95% of the data (these values correspond to intervals of ± 1 or ± 2 standard deviations for a one-dimensional Gaussian distribution). The results of this analysis for each gallery portion are gathered in Table 4-3. Most of the pole inclinations make an angle of 30° with the vertical axis, with the exception of the excavation front in the linear portion. Note that this zone is the one which contains the most numerous data (namely 173 observations) and that it is considered as being very reliable by the geologists who recorded the data. The corresponding result will be conserved with a pole whose azimuth and dip are $N151^\circ$ and 47° and with a Fisher parameter equal to 16.4.

4.4.2 Orientations of the bedding traces

The 46 observations of the bedding traces can be considered in a very similar way as the faults, though they are less numerous. However, no difference was observed between

the two portions of the gallery on the various surfaces. The same processing was applied and the results are shown in Figure 4-8. The pole is oriented $N147^\circ$ with an angle of 35° to the vertical axis and $\kappa = 56$. This larger value of κ means that the orientations are less dispersed than those for the faults.

It should be noted that the poles of the distributions of the faults and of the lithological traces are approximately in the same vertical plane as the gallery axis in the linear portion ($N152^\circ$).

4.4.3 Orientations of the EDZ fractures

A priori, this analysis is more complex due to the EDZ fractures being generated by the excavation process. These fractures may have different statistical characteristics in the curved and linear portions of the gallery and in the various studied surfaces (front, ground, left and right walls). This is indeed the case in the instances shown in Figs. 4-9, 4-10 and 4-11, where the normals to the fractures are represented on the unit sphere viewed from above in a fixed reference frame (Fig. 4-9) or in a reference frame oriented with the gallery axis (Fig. 4-10), or viewed from the gallery axis (Fig. 4-11).

The front and ground traces in the linear portion clearly belong to three families indicated by the blue, red and magenta contours. Two of them correspond to numerous observations with a dip oriented towards SSE (FF1, red) or towards NNW (FF2, magenta). The third sub-horizontal family is less frequent (FF3, blue). Note that the dips of FF1 and FF2 are not the same on the front and on the ground.

The EDZ traces on the right and left walls of the linear portion correspond to fractures that are subvertical in most cases, with a large variety of azimuths. Their structure is not clear and their small number (see Table 4-2) makes any further statistical analysis difficult. In the curved portion of the gallery, Figure 4-9, which is in a fixed reference frame, does not reveal any structure. However, in a reference frame linked to the gallery axis (Figs. 4-10 and 4-11), the front and ground traces appear to be organized. Though less marked than in the linear portion, this organisation is similar; among other common characteristics, all poles are approximately located in the vertical plane that contains the gallery axis.

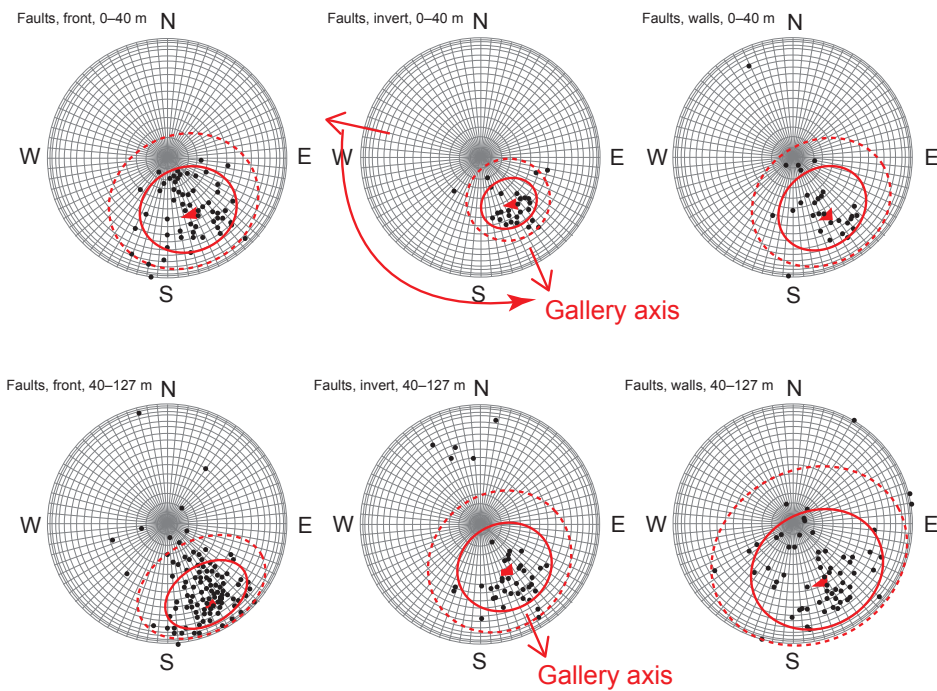


Fig. 4-7: Distribution of normals to faults in the curved portion $0 \leq x \leq 40$ m (upper line) and in the linear portion $40 \leq x \leq 127$ m (lower line) in the Gallery 08, on the excavation front (left), on the ground (middle) and on the walls (right). The axis of the gallery is parallel to the red arrows; it is constant in the lower line and variable in the upper one, namely from W for $x=0$ to SSE for $x=40$ m.

Tab. 4-3: Parameters of the Fisher distributions fitting the fault observations in various parts of the Gallery 08.

		Number of observations	Pole Azimuth	Pole Dip	κ
Curved portion ($0 \leq x \leq 40$ m)	Front	75	N157°	30°	13.2
	Ground	31	N147°	27°	42.4
	Walls	30	N150°	33°	15.1
Linear portion ($40 \leq x \leq 127$ m)	Front	173	N151°	47°	16.4
	Ground	43	N150°	26°	13.8
	Walls	71	N152°	31°	6.6

The left wall of the curved portion does not characteristics mentioned above. A set of traces can be partitioned into two groups of 16 and 6 fractures with very similar orientations. When observed in a short interval where the gallery axis does not strongly vary, they appear together in Figure 4-9 as well as in the variable reference frames of Figs. 4-10 and 4-11. However, these measurements are considered to be unreliable by the geologists who recorded them and they will not be considered further. The data observed on the right wall do not show any clear trend.

Therefore, the EDZ fracture on the front and on the ground is organized in relation to the digging direction. Analogous to the nomenclature in the linear portion, FF1 and FF2 denote the EDZ families plunging in the direction of the gallery axis with increasing, decreasing or constant values of x (FF1, FF2 or FF3, respectively). We applied the same data processing as for the faults and the lithological

traces to determine the parameters of the Fisher distribution corresponding to the various families of the EDZ. Results are given in Table 4-4.

Figure 4-12 illustrates the organisation of the various families on the front and on the ground for the linear portion in comparison to the fault and lithological directions. The families FF1 and FF2 might be conjugate with approximately symmetric dips.

4.5 Relative spatial organisation of the faults and of EDZ fractures

The relative distribution of the faults and of the EDZ fractures has already been briefly addressed in Section II, with the conclusion that no significant correlation could be found (see eq. 2).

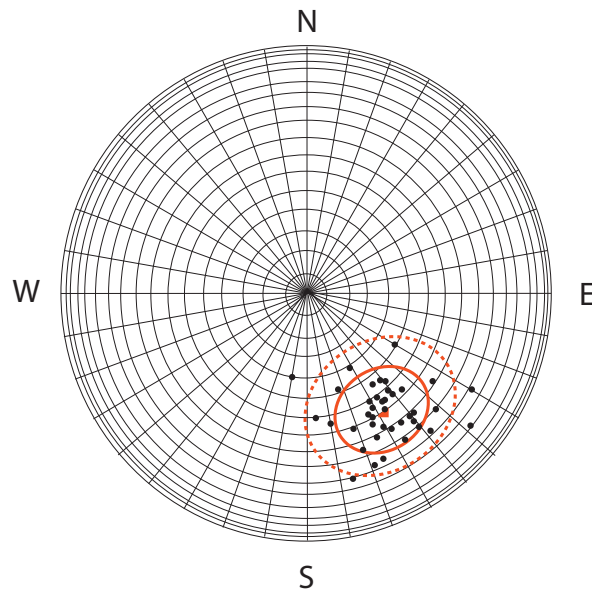


Fig. 4-8: The normals to the lithological faults (●), pole of the Fisher distribution (●) and circles containing 68% and 95% of the data.

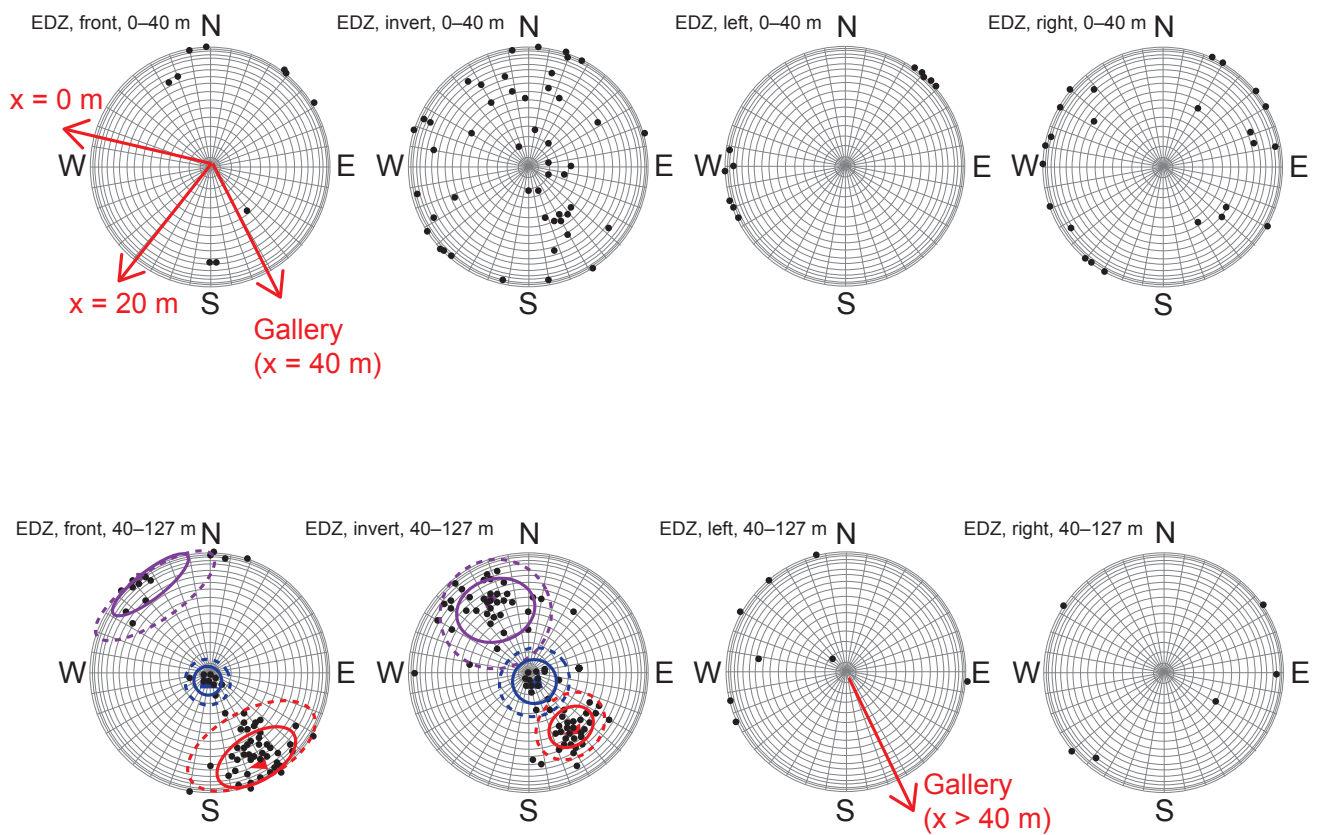


Fig. 4-9: Distribution of the normals to the EDZ fractures in the curved $0 \leq x \leq 40$ m (upper line) and linear $40 \leq x \leq 127$ m (lower line) portions of the Gallery 08, on the front, on the ground, on the left and right walls (from left to right). View from the top in a fixed reference frame. The red arrows correspond to the direction of the gallery axis, fixed (below) or variable (above) from W for $x=0$ to SSE for $x=40$ m. The blue, red and magenta curves correspond to the most probable families for the traces on the front and on the ground.

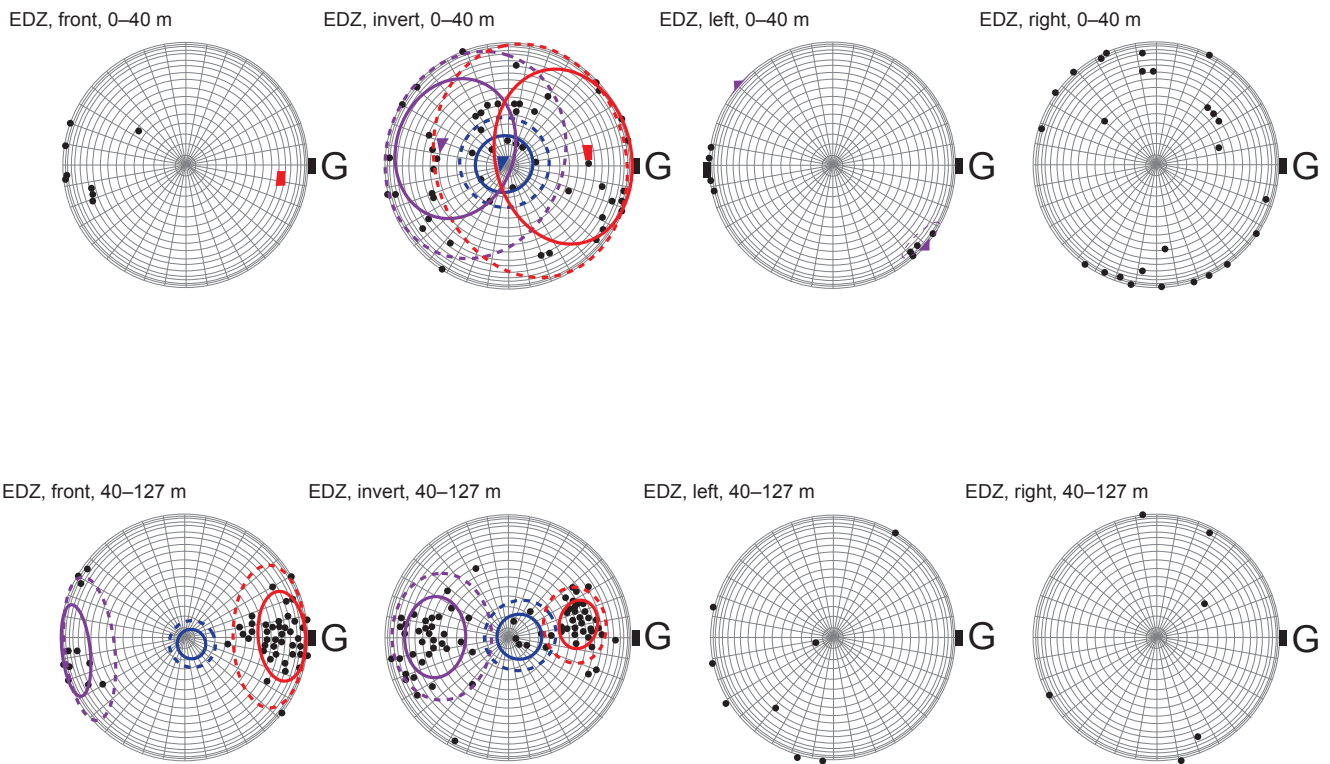


Fig. 4-10: Distribution of the normals to the EDZ fractures in the curved $0 \leq x \leq 40$ m (upper line) and linear $40 \leq x \leq 127$ m (lower line) portions of the Gallery 08, on the front, on the ground, on the left and right walls (from left to right). View from the top in a reference frame linked to the gallery axis. The blue, red and magenta curves correspond to the most probable families for the traces on the front, on the ground and on the left wall.

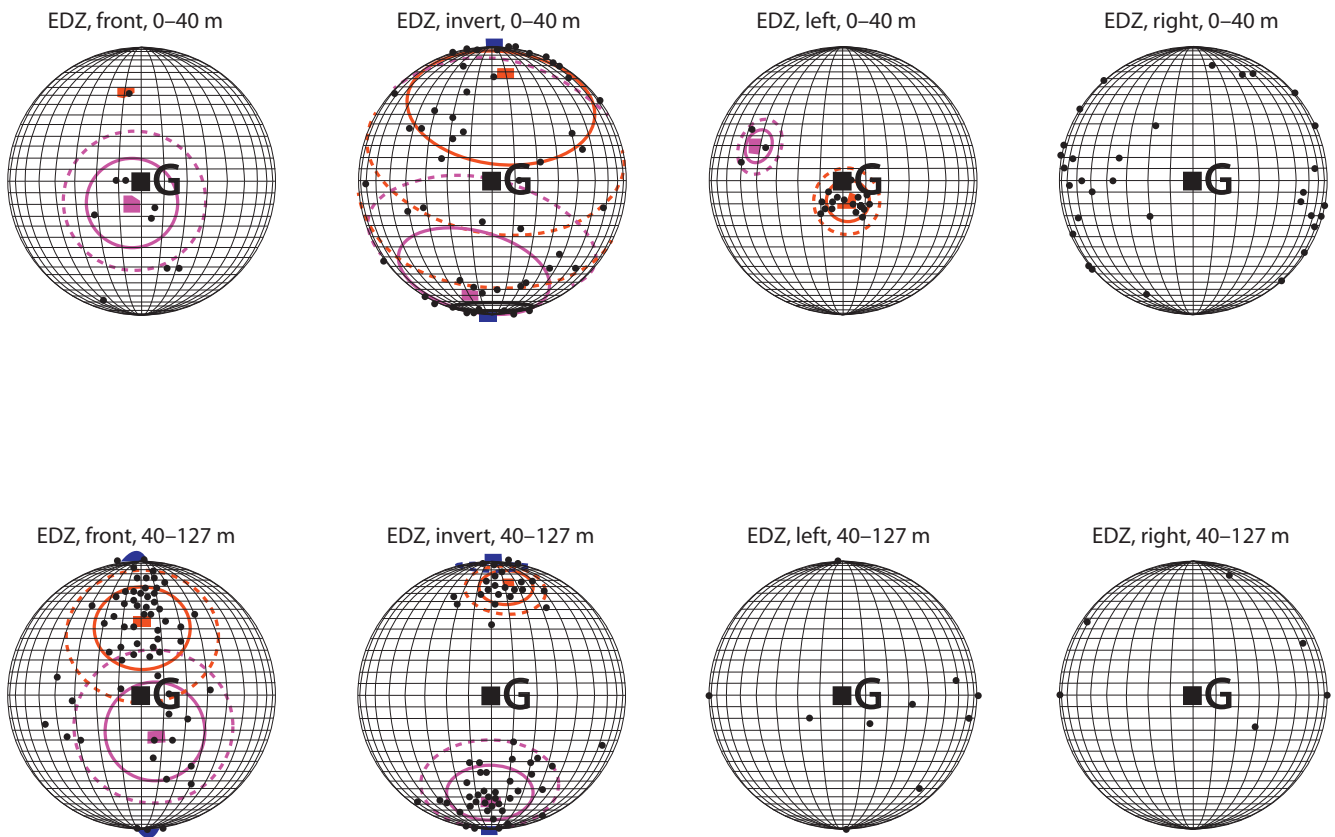


Fig. 4-11: Distribution of the normals to the EDZ fractures in the curved $0 \leq x \leq 40$ m (upper line) and linear $40 \leq x \leq 127$ m (lower line) portions of the Gallery 08, on the front, on the ground, on the left and right walls (from left to right). View from the gallery axis (G). The blue, red and magenta curves correspond to the most probable families for the traces on the front, on the ground and on the left wall.

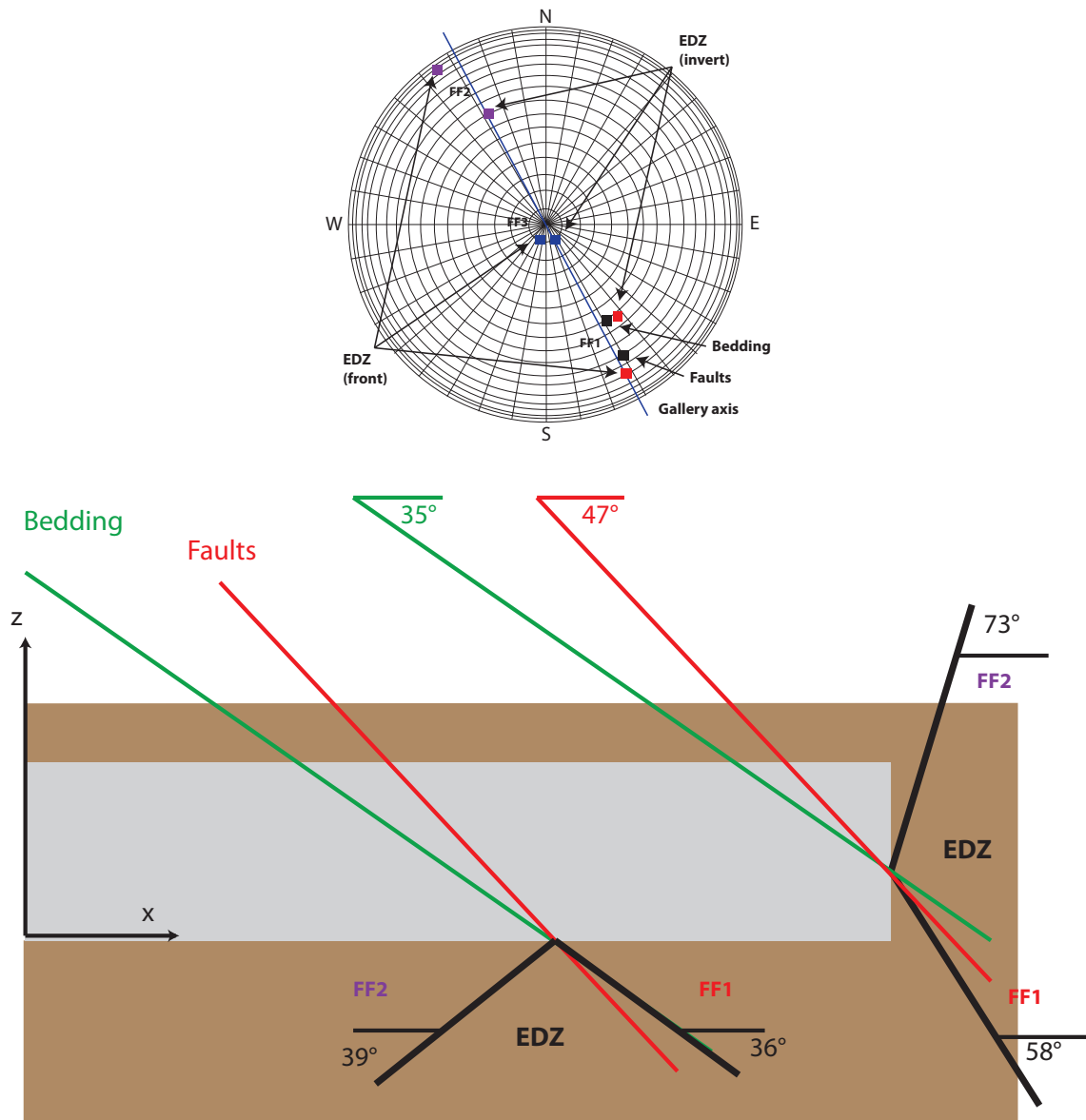


Fig. 4-12: Poles of the various Fisher distributions and gallery axis (upper); directions of the faults, lithology and EDZ fractures in a vertical cross section containing the gallery axis (lower).

This point should be analysed again while taking into account the existence of two sorts of EDZ fractures with dips towards SSE (FF1) and towards NNW (FF2). Consider the front and ground traces in the linear portion of the gallery, where these elements are better organized than in the curved portion. Note that the number of events is smaller than in Section II, since it is limited to traces for which no information is available on the orientations. Moreover, these orientation data are not associated to specific traces and averages can only be taken in numbers.

The locations of these traces are shown in Figure 4-13 in which the three EDZ families are distinguished. The locations of the recorded faults are indicated as well. The upper part of the figure corresponds to the front. FF1 (resp. FF2) is shown in the upper (resp. lower) part of the front in accordance with the comments of the geologists, but the exact location is not available. The lower part of the figure corresponds to the ground. A visual examination suggests three phenomena:

- The traces FF1 and FF2 seem to appear in distinct regions.
- The traces FF2 seem to be localised in zones where the fault density is high.
- The traces FF1 seem to be localised in zones where the fault density is low.

These effects can be quantified by measuring intercorrelation coefficients. First, local trace densities along the x-axis are measured over moving intervals with a length of 5 m. The intercorrelation coefficients are defined in a way similar to (2) and determined from the ground or front data; the results are given in Table 4-5. The only significant correlation (0.73) is relative to the simultaneous existence of faults and FF2 on the gallery ground. This is partially consistent (on the ground) with the visual impression (b). The two others (a, c) are not quantitatively confirmed. No other spatial correlation seems to exist between the fault and the EDZ densities. It should be added that there is no intercorrelation

Tab. 4-4: Parameters of the Fisher distributions corresponding to the mapped EDZ fractures in Gallery 08. In the linear portion, azimuths are measured either in a fixed reference frame or in a variable one, depending on the gallery axis, in the direction of increasing values of x (denoted by “G”). In the curved part, only the second analysis reveals distinct families.

		EDZ family	Data number	Pole Azimuth	Dip	κ
Linear portion ($40 \leq x \leq 127$ m)	Front	FF1	56	N151°	58°	17
		FF2	16	N325°	73°	16
		FF3	4	N195°	5°	165
	Ground	FF1	48	N141°	36°	62
		FF2	43	N332°	39°	21
		FF3	7	N145°	6°	71
Linear portion ($40 \leq x \leq 127$ m)	Front	FF1	56	G359°	58°	17
		FF2	16	G173°	73°	16
		FF3	4	G43°	5°	165
	Ground	FF1	48	G349°	36°	62
		FF2	43	G181°	39°	21
		FF3	7	G353°	6°	71
Curved portion ($0 \leq x \leq 40$ m)	Front	FF1	2	G8°	50°	2800
		FF2	8	G184°	80°	20
		FF3	—	—	—	—
	Ground	FF1	22	G350°	39°	3.9
		FF2	23	G197°	33°	6.3
		FF3	8	G209°	2°	44

between the EDZ fracture densities on the ground and on the front since the coefficients are equal to 0.23 and -0.28 for FF1 and FF2, respectively.

4.6 Trace length distribution

Only the trace lengths for the EDZ are analysed here, since pre-existing faults generally yield traces that fully cross the entire gallery. Furthermore, we only consider the EDZ traces on the invert of the straight section $40 \text{ m} < x < 127 \text{ m}$.

The lengths of 669 EDZ traces were measured on maps such as the one displayed in Figure 1 for the region $40 \text{ m} < x < 70 \text{ m}$. Note that the associated fracture orientations are generally not available. Aside from 8 small traces, the lengths are always equal to at least 10 cm. Since the EDZ traces are nearly orthogonal to the gallery axis, their lengths never significantly exceed the gallery width, i.e., 4 m.

The measured mean trace length is equal to $\langle c \rangle = 0.87 \text{ m}$. A histogram of the trace lengths is displayed in logarithmic scale in Figure 4-14. It can be tentatively fit by the probability distribution function

$$(8) \quad f_c(c) = \frac{\omega}{1 + (c/\lambda)^3} \quad c_m \leq c \leq c_M$$

with $c_m = 0.1 \text{ m}$, $c_M = 4 \text{ m}$, $\omega = 0.9275 \text{ m}^{-1}$ and $\lambda = 1 \text{ m}$.

The corresponding moments are

$$(9) \quad \langle c \rangle = 0.886 \text{ m}, \quad \langle c^2 \rangle = 1.209 \text{ m}^2, \quad \langle c^3 \rangle = 2.617 \text{ m}^3$$

4.7 Connectivity and percolation of the EDZ fracture network

The ability of the damaged zone to carry fluid over some distance along the walls of the gallery depends on the connectivity of the EDZ fractures and on the percolation status of the network that they constitute. Unfortunately, nothing is known about the shape and extension into the embedding rock of the fractures whose traces are observed on the gallery walls. Therefore, the following preliminary analysis relies on reasonable assumptions, which should be checked and possibly amended by complementary *in-situ* measurements. Furthermore, in view of the conjectural character of the geometrical model, the analysis is kept as simple as pos-

Tab. 4-5: Spatial correlation coefficients between the fracture degree for FF1, FF2, and the faults, evaluated on the ground (a) and the front (b).

At the ground	Faults	FF1	FF2	At the front	Faults	FF1	FF2
Faults		-0.03	0.73	Faults		0.16	-0.13
FF1	-0.03		0.03	FF1	0.16		0.06
FF2	0.73	0.03		FF2	0.13	0.06	

(a) (b)

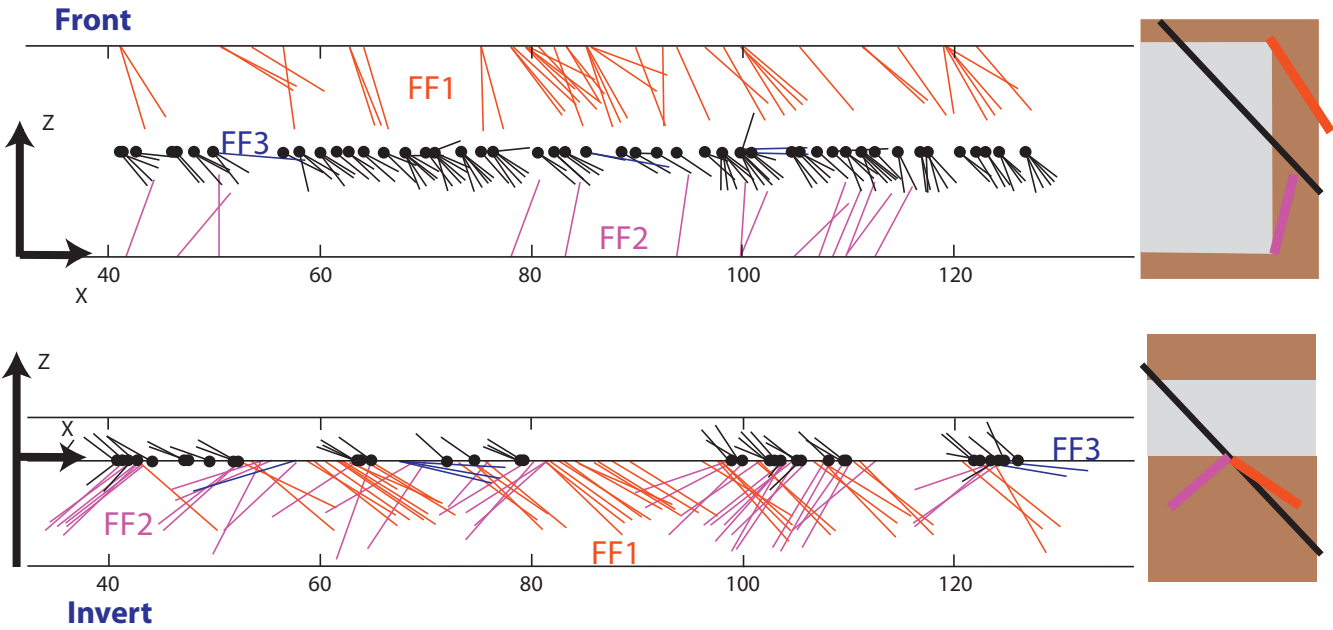


Fig. 4-13: Locations of the recorded fault and EDZ fracture orientations on the front (upper line) and on the ground (lower line) in the linear portion of the gallery. Data are for: FF1 (red), FF2 (magenta), FF3 (blue). Segments have an arbitrary length, but their inclinations correspond with the measured orientation in the vertical plane that contains the gallery axis. The black segments correspond to the recorded faults. The sketches on the right illustrate the general organisation of FF1, FF2 and of the faults. At the front, FF1 (resp. FF2) is located in the upper part (resp. lower) of the front, according to the geologists who recorded the data.

sible by use of various approximations. Their impact on the predictions is negligible compared to that of the geometrical uncertainty, and they could be easily avoided if the analysis were to be repeated with a deeper knowledge of the EDZ fractures characteristics. In the following, we consider only the invert of the straight section $40 \text{ m} \leq x \leq 127 \text{ m}$ of the gallery where the EDZ is best documented.

It is assumed that all EDZ fractures have a rectangular shape, $(c \times c/2)$, where c is the observed trace length and $c/2$ is the fracture extension in the embedding rock. An example with two such fractures is shown in Figure 4-15.

The distribution of EDZ fracture trace lengths has been quantified in Chapter 4.5 and can be described by the model (8). Since the data are missing to separately quantify the amount and size of distributions of the various families identified in Chapter 4.3, we here use the following simplified picture. We consider that the observed traces belong in equal amount and with the same size distribution (8) to the SSE-dipping family FF1 and to the NNW-dipping family FF2.

The sub-horizontal family FF3 is neglected. Furthermore, we simplify the orientational statistics by ignoring the angular dispersion and by approximating the poles in Table 4 by constant dip angles $\theta = \pm 37.5^\circ$ oriented along the gallery axis, i.e., with traces on the ground orthogonal to the gallery axis (see Fig. 4-15).

The densities, in length and in numbers, of the traces on the invert of the two families can be deduced from (1b) and (9):

$$(10a) \quad C = C_l = C = \langle C_{EDZ} \rangle / 2 = 0.889 \text{ m}^{-1}$$

$$(10b) \quad \Sigma_{ij} = \Sigma_{i2} = \Sigma_i = \langle C_{EDZ} \rangle / 2 \langle c \rangle = 1.003 \text{ m}^{-2}$$

The connectivity of the EDZ fracture network can be quantified by the mean number ρ' of intersections per fracture, which is estimated as described below. Note first that only fractures of different families can intersect. A fracture F_1 with size c_1 from FF1 is intersected by a fracture F_2 with size c_2 of FF2 if the trace of F_2 is centred in an interval of

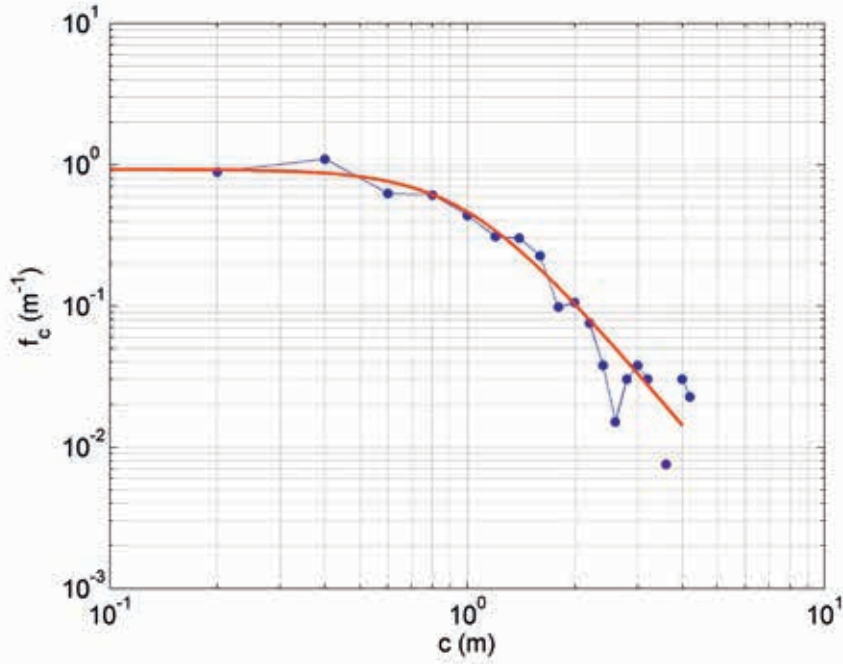


Fig. 4-14: Normalized histogram of the EDZ trace lengths on the invert of the straight gallery section $40 \text{ m} \leq x \leq 127 \text{ m}$ (symbols). The solid line is the model distribution (8).

width $c_1 + c_2$ in the y -direction, and if their traces are separated by less than $\min(c_1, c_2) \cos \theta$. The corresponding area on the invert is

$$(11) \quad A(c_1, c_2) = (c_1 + c_2) \min(c_1, c_2) \cos \theta$$

Therefore, disregarding any correlation between the EDZ fracture positions, the density Σ_I of fracture intersections per unit area of the invert is given by

$$(12) \quad \Sigma_I = \Sigma_{I1} \Sigma_{I2} \int_{c_m}^{c_M} \int_{c_m}^{c_M} dc_1 dc_2 f_c(c_1) f_c(c_2) (c_1 + c_2) \min(c_1, c_2) \cos \theta$$

The mean number of intersection per fracture is obtained by

$$(13) \quad \rho' = \Sigma_I / \Sigma_t = \Sigma_I \int_{c_m}^{c_M} \int_{c_m}^{c_M} dc_1 dc_2 f_c(c_1) f_c(c_2) (c_1 + c_2) \min(c_1, c_2) \cos \theta$$

Numerical integration with f_c given by (8) yields the mean number of intersections per fracture,

$$(14) \quad \rho' = 0.953$$

Finally, we note that percolation in fracture networks with size polydispersity is controlled by a modified version ρ_3' of this connectivity index, which accounts by a different evaluation for the fact that large fractures contribute more efficiently to transport over large distances and to percolation than small ones. It is obtained here as

$$(15) \quad \rho_3' = \frac{\langle c^3 \rangle}{\langle c \rangle \langle c^2 \rangle} \rho' = 2.29 \rho' \approx 2.2$$

It should be kept in mind in the following discussion that most of our knowledge about percolation and transport in fracture networks has been obtained from three-dimensional networks of randomly located fractures. The situation is different in our case, since all the EDZ fractures originate from the rock surface. Furthermore, the network and the potentially permeable zone are confined to a relatively thin lay-

er below the ground surface, with thickness in the order of the typical depth reached by the fracture $\sin \theta(c)/2 \approx 0.27 \text{ m}$. Hence, the general results are not expected to apply accurately. However, they can be used as guidelines to identify trends and to provide orders of magnitude.

The dimensionless density ρ' of three-dimensional fracture networks (or ρ_3' in polydisperse networks) was shown to control the network percolation, with a threshold value

$$(16) \quad \rho_c' \approx 2.3$$

that is nearly independent of the fracture shape, and weakly sensitive to anisotropy in the fracture orientation distribution and to spatial fluctuations of the density with moderate amplitude.

Hence, (15) suggests that the EDZ fracture network is in a near-critical state. The estimate (15) of ρ' can of course be inaccurate if the hypothesis of rectangular shape is not valid, and the percolation threshold in the present particular setting may also differ from the standard value (16). However, these possible artefacts are probably of negligible impact compared to that of the spatial fluctuations of the EDZ fracture density.

As shown by Figures 4.4 and 4.5, the local density C_{EDZ} of EDZ fracture traces on the invert ranges from zero to about three times the mean value $\langle C_{EDZ} \rangle$ in (1a). Hence ρ_3' , which is proportional to C_{EDZ} , significantly exceeds the percolation threshold (16) in some parts of the gallery. On the other hand, large regions without any EDZ fracture traces (see Fig. 1 and 5) prevent the percolation of the EDZ fracture network on the whole scale along the gallery direction. Nevertheless, relatively large connected clusters can exist, and these clusters can be connected to pre-existing faults. Therefore, a significant part of the area of the gallery invert can be connected to the faults via the EDZ fracture network.

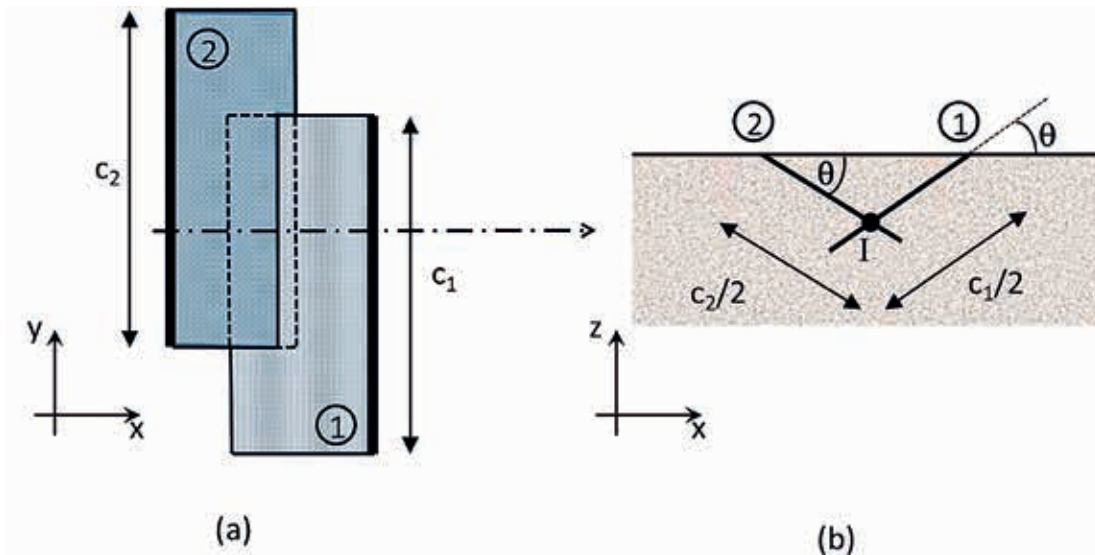


Fig. 4-15: Example of two rectangular EDZ fractures which intersect at the point I below the exposed rock surface. View from the top (a). The thick lines are the traces on the ground surface. Vertical cross section (b) at the position indicated by the dash-dotted arrow in (a).

This can be quantified by a direct reconstruction and connectivity test. Fracture networks representative of the EDZ can be stochastically generated based on the trace density map in Figure 4.5 by applying the aforementioned hypotheses regarding the shape and depth of the fractures. The influence of these hypotheses can also be tested by considering other variants. A direct reconstruction is also possible, starting from the explicit trace map (part of which is displayed in Fig. 4.1), by randomly assigning SSE or NNW dips to the associated fractures. In both stochastic and deterministic procedures, faults can be included according to the field observations and the EDZ fracture clusters connected to each of them can be determined.

4.8 Conclusion

Fracture densities of all kinds are well quantified, especially in the linear portion of the gallery. Faults appear to be generally independent and can be easily simulated. The only difficulty could lie in a large-scale structuration of the fault density. A decametric scale would be necessary and the length of the observation zone is too short to provide a precise statistical characterization. However, this difficulty could be avoided through the reconstruction of a numerical model by generating the EDZ stochastically with the real distribution of observed faults.

The orientation distributions relative to the traces that are visible on the invert and on the ground in the entire gallery are quantified and modelled in a reference frame aligned with the digging direction. Fisher distributions, which are easy to reproduce in a numerical model, can be used to rationalize the data from the linear portion of the gallery relative to the pre-existing faults, the lithological faults, and the three fracture families of the EDZ. No obvious spatial correlation exists between these populations, with the exception of one family of EDZ that appears to be

favoured by pre-existing faults. It should be noted that these observations are very different from those made in the Gallery 04, in which EDZ fractures are parallel to the wall (THOVERT et al. 2011).

The fault statistics are slightly different in the invert of the linear portion and in all the other zones of the gallery. The data in the invert are thought to be more reliable and they can be used for modelling. The statistics of the lithological faults are the same in the curved and linear portions of the gallery and all the observation surfaces (invert, ground and vertical walls). The orientation of EDZ traces on the vertical walls cannot be modelled due to the insufficient number of data.

Therefore, the surface observations provide good quality data for modelling. However, two crucial elements are missing for the prediction of hydromechanical properties:

- the depth reached by the EDZ fractures under the surface;
- the variations of the EDZ fracture density below the surface.

These two elements could be condensed into a single one if all the EDZ fractures are assumed to be visible on the observation surface. The data recorded on the walls of the niches dug from the Gallery 08 do not provide adequate elements. The records are scarce and the observed traces are probably related to the niche digging rather than to the gallery digging. Moreover, the ground data are more numerous than the data observed on the vertical walls.

References

- THOVERT, J.-F., MOURZENKO, V.V., ADLER, P.M., NUSSBAUM, C. & PINNETTES, P. (2011): Faults and fractures in Gallery 04 of the Mont Terri rock laboratory: characterization, simulation and application. - *Eng. Geol.* 117, 39-51.

5. Acoustic experiments: seismic survey and micro-seismicity

Y. LE GONIDEC, J. SAROUT, J. WASSERMANN, A. SCHUBNEL, D. GIBERT, C. NUSSBAUM, B. KERGOSIEN,
A. MAINEULT & Y. GUÉGUEN

5.1 Introduction

In August 2008, we excavated an 8 metre section between the end-face of the previous Gallery 04 and the front-face of the new Gallery (EZ-G08). Using many geophysical methods we then monitored this new section to study the evolution of the Excavation Damaged Zone (EDZ) in both time and space during and after the excavation process.

Among the geophysical methods applied for this purpose, we developed and carried out acoustic experiments aiming at detecting any space-time changes of the EZ-G08 segment induced by the excavation procedure. The purpose of the present contribution is to better understand the EDZ initiation processes and the short-term evolution during the excavation of an underground gallery in a shaly environment.

The experiments consisted in two complementary measurements. The first was an active seismic method involving a controlled acoustic source. In the following we refer to this as seismic survey measurements. We used this method to characterize the elastic properties of the rock mass, in particular, in terms of P-wave velocity. The second dealt with a passive seismic method based on the detection of acoustic emissions, i.e. micro-seismic events (MSEs).

In the first part (§5.2), we introduce the instrumented face of the Ga08 front where the experiments took place, i.e. the boreholes and the acoustic source and arrays of acoustic receivers. In a second part (§5.3), we present the seismic survey experiments, including the principle of the experiments, and the main results focusing on temporal changes and anisotropy of the EZ-G08 segment. These results have already been published in LE GONIDEC et al. (2012). In a third part (§5.4), we describe the experiments to detect and record micro-seismic events (MSEs). In particular, we present the raw data set of events recorded during the experiment and we identify and locate the events related to induced micro-seismicity. These results have been published in LE GONIDEC et al. (2014) where damage mechanisms associated to MSEs located around the excavation front have been studied. In the final chapter (§5.5), we compile and present all the major data from both of these papers and discuss them in terms of EDZ initiation.

5.2 Description of the experimental setups

The acoustic experiments consisted in three main experimental setups: (1) an acoustic source dedicated to the seismic survey experiments in order to probe the EZ-G08 seg-

ment by the use of a controlled acoustic signal, (2) a first array of acoustic receivers located close to the acoustic source and (3) a second array of acoustic receivers located further away. Each setup was introduced inside a borehole, drilled from the end-face of the previous Gallery 04 (Fig. 5-1).

5.2.1 Borehole utilities

The seismic monitoring of the EZ-G08 segment was performed when the rock mass segment was 8 m in length. Note that the elliptical cross-section of the gallery is around 4.5 m in diameter, i.e. roughly half the segment length. Before the excavation started, many boreholes had already been drilled from the Ga04 face and nine of them were used to install the acoustic setups described below:

- borehole BEZ-G5: length 13 m and diameter 116 mm (black in Fig. 5-1 and 5-2). Initially drilled to extract core samples, the borehole was used to introduce the acoustic source inside the EZ-G08 segment, down to 7.2 m from the Ga04 face. Note that until July 22, the source was positioned between 4.4 and 6.8 m deep at each 0.4 m step;
- boreholes BEZ-G12:15: length 8 m and diameter 56 mm (blue in Fig. 5-1 and 5-2). Inside each of these four boreholes, located close to the borehole BEZ-G5 (<1 m), we inserted an array of 16 acoustic sensors.
- boreholes BEZ-G16:19: length 8 m and diameter 76 mm (red in Fig. 5-1 and 5-2). Inside each of these four boreholes, located far from the borehole BEZ-G5 (>2.5 m), we inserted an array of 4 acoustic sensors.

5.2.2 Acoustic source in BEZ-G5 for seismic survey measurements

For the seismic survey measurements, an acoustic source was designed specially to be introduced into the horizontal borehole BEZ-G5. The source was a spherical piezoelectric transducer (Fig. 5-3a) fabricated of Channelite-5400 lead-zirconate-titanate ceramic (ITC-1032). The ITC acoustic source is omnidirectional and has a central frequency of 33 kHz for which the maximum transmitting voltage response is 149 dB/ μ Pa/V at 1 m and the maximum input power is 800 W. Note that because of the amplifier properties, the power was limited to 100 W during the experiments. The acoustic source signals used for the EZ-G08 experiments are Morlet wavelets, defined during preliminary experiments in a water tank and already used in previous experiments in the EZ-G04 zone (NICOLLIN et al. 2008). The central frequencies of the wavelets were set between 21 and 53 kHz and their amplitudes were controlled on the amplifier image around 12 V. The experimental setup was driven through a PXI system

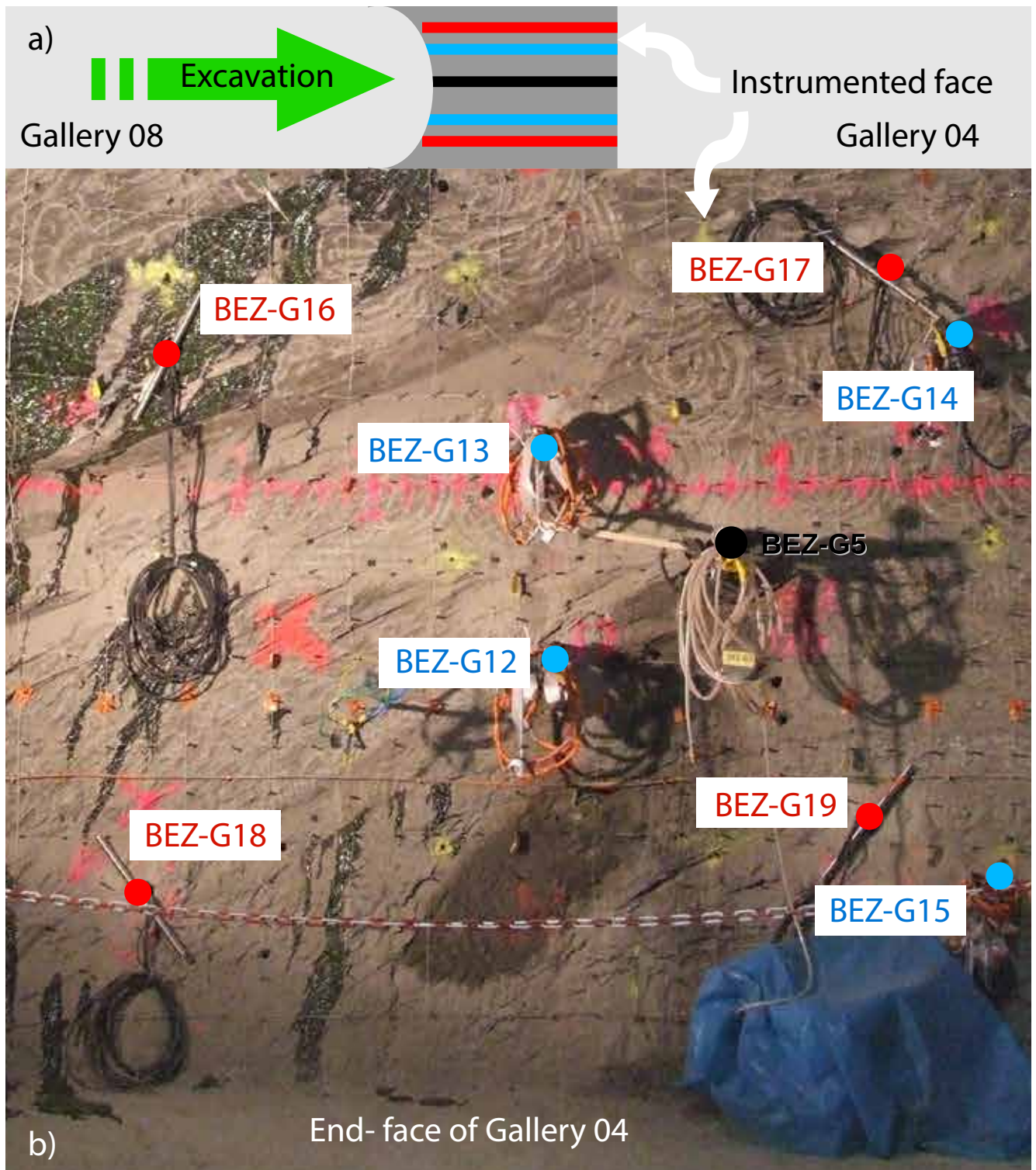


Fig. 5-1: (a) Schematic illustration of the principles of the experiments. (b) Instrumented Ga04 face with the location of the boreholes: an acoustic source introduced in BEZ-G5 (black dot) and two arrays of acoustic receivers introduced in BEZ-G12-15 (blue dots) and BEZ-G16-19 (red dots).

where the NI-5411 emission card was used to both control and emit the wavelet sources for the acoustic survey measurements.

In order to ensure good mechanical coupling between the ITC source inside BEZ-G5 and the wall of the borehole, we designed a specific setup for these experiments: the ITC source was inserted inside a watertight balloon which could be filled with oil up to 2 bars (Fig. 5-3b). The balloon did not

significantly attenuate the acoustic source signals and achieved an adequate coupling between the borehole wall and the source. The balloon was maintained in place with a long metal rod (Fig. 5-3c) and could be manually positioned inside the borehole. The rubber membrane of the balloon (Fig. 5-3a) was smooth enough to be easily inserted inside the borehole over large distances, up to 8 m inside BEZ-G5. When under pressure at 0.6 bar, the balloon provided a cor-

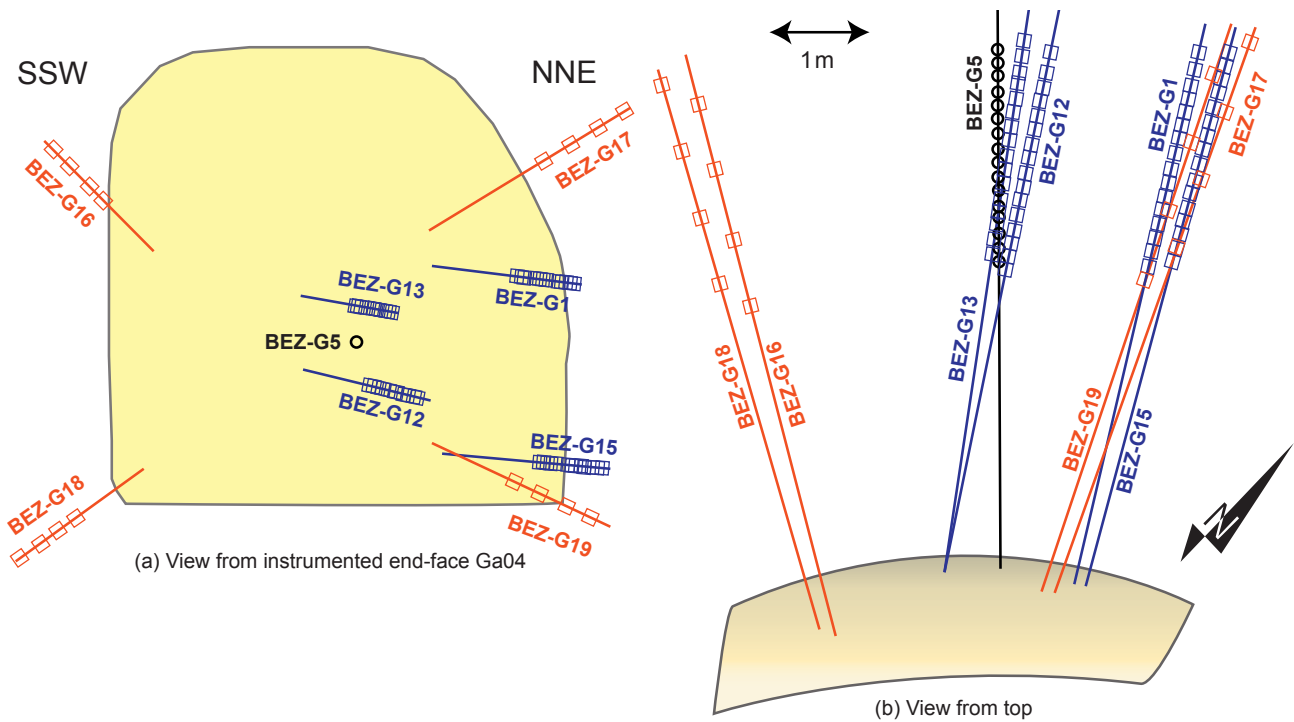


Fig. 5-2: Network of the boreholes for the seismic experiments and position of acoustic sensors: (a) as seen from the Ga04 face and (b) as seen from the top of the gallery.

rect mechanical coupling with the argillite. To change the position of the source, we dropped the pressure to 0.3 bar. With the metal rod, the source was manually introduced in BEZ-G5 between 4.4 and 7.2 m deep. As a consequence, source manipulation introduced two major uncertainties in the signal analysis: uncertainty of the position of the source inside the borehole (lower than 3 cm) affects the accuracy of the determination of the P-wave velocity field, and uncertainty in the amplitude of the signal, due to perturbations caused by the watertight balloon.

5.2.3 Array of acoustic receivers in BEZ-12-15 boreholes

Boreholes BEZ-G12 to BEZ-G15 are located close to the BEZ-G5 source borehole. In each borehole, we introduced an array of 16 acoustic receivers (Fig. 5-4a). The receivers were mounted onto a holding pole specifically designed at Géosciences Rennes to equip the small-diameter borehole with an array of electrodes, used for the electrical measurements (see Chap. 6). The acoustic and electrical arrays were mounted on two half cylinders separated by an inflatable membrane.

Filled with air, the membrane could be pressurized to 1.4 bar to ensure a good coupling of the acoustic receivers with the wall of the borehole. In view of the space available in the borehole, we had to minimize the cylinder diameter by using piezoelectric acoustic transducers. The properties of such transducer are such that they convert the mechanical vibrations transmitted by a source into an electrical signal sent to the acquisition system described below using 8 m-long reinforced cables. The disk-shaped piezoceramic-based

transducers (diameter 25 mm, thickness 4 mm) were inserted in a thin rigid foam sheath (Fig. 5-4b). The sheets of foam, manufactured at Géosciences Rennes by a high precision robot, are less than 1 cm thick and coated with a thin layer of epoxy resin enclosing the electronics and shaped to fit the borehole wall curvature (Fig. 5-4c). The 16 transducers were spaced 20 cm apart along the holding pole of 3.2 m in length. The pole was oriented towards the axis of the borehole BEZ-G5 and positioned close to the end of the borehole, i.e. the last four metres of the EZ-G08 segment were equipped with acoustic transducers. This acoustic receiver network of 64 transducers is referred to as A1 in the following.

We used two NI-5112 8-channel acquisition cards to simultaneously measure 16 signals. These cards were inserted into the PIX system that controlled the acoustic source to trigger reception with emission. The received signals were composed of 750 points sampled at 16 bit resolution with a sampling rate of 500 kHz, equivalent to a 1.5 ms time window. The data were recorded by in-house LabView software especially developed for these experiments. Finally, the global network of 64 acoustic transducers fixed on the four holding poles inside the rock mass were connected to a switch box designed for consecutive data recording from the four boreholes, 16 transducers at a time.

5.2.4 Array of acoustic receivers in BEZ-G16-19 boreholes

For this array we drilled subhorizontal boreholes BEZ-G16 to BEZ-G19 further away from the BEZ-G5 source borehole. Each borehole was equipped with an acoustic pole designed by ENS, including four broadband Physical Acous-

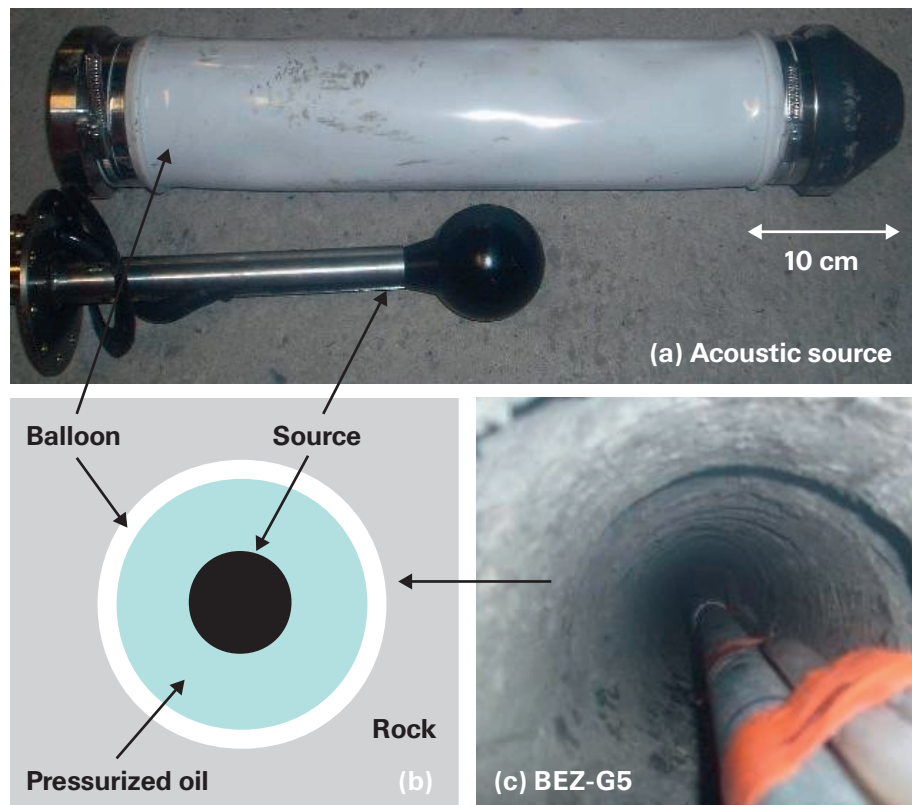


Fig. 5-3: (a) Acoustic source composed by a piezoelectric element and an inflatable membrane. (b) Schematic of the acoustic source introduced in the borehole with a long metal rod (c).

tics transducers (R0.45UC) located 1 m apart. On their surface, we glued an aluminium semi-spherical head to fit the curvature of the borehole wall ensuring a good mechanical coupling with the rock, a coupling allowed by mounting the transducer on a stiff spring (Fig. 5-5). This acoustic receiver network of 16 transducers is referred to as A2 in the following.

The frequency response of the transducers is quasi-flat between 2 Hz and 60 kHz. Note that this range is in accordance with the frequency range of the source wavelet signals used for the acoustic survey measurements. Because of the small diameter of the borehole, an ASC PAS (ASC Ltd.) amplifier was mounted outside the borehole to amplify the recorded signals at 60 dB. The amplifier was previously designed for other acoustic monitoring of the OMNIBUS project. The received signals are composed of 2048 points sampled at 12 bit resolution, with a sampling rate of 500 kHz, equivalent to a 4096 μ s time window. Acquisition, management, and processing of data were performed with Insite software (ASC Ltd.). The amplified signals were sent to a 16 channel trigger logic box (ASC Ltd.) (Fig. 5-6). In the active mode of the seismic surveys, the first channel was used to record the input source wavelet signal.

5.3 Seismic surveys experiments

5.3.1 Description of the experiments

We equipped boreholes BEZ-G12 to BEZ-G15 with the array A1 composed of 64 acoustic receivers on June 29. On July 10 boreholes BEZ-G16 to BEZ-G19 were equipped with the array A2 composed of 16 acoustic receivers. Both acoustic arrays were synchronized with the emission of the source signal emitted by the acoustic source, positioned at different depths inside the borehole BEZ-G5. The scheme of data acquisition for the acoustic survey was repeated with the same time basis for four successive wavelet frequencies (21, 25, 31, and 38 kHz). The signal-to-noise ratio of each measurement was improved by stacking 200 waveforms. Use of both the acoustic source and the receivers permitted us to assess the P-wave velocities of the EZ-G08 segment. This so-called velocity survey was performed at regular time intervals, nominally once a day, and ended on July 23.

Due to the source positions of the acoustic source relative to the acoustic receivers many different raypaths through the shale formation were sampled. The source was manually positioned every 0.4 cm at depths between 4.4 and 7.2 m from the Ga04 face. The distances between the acoustic source and the receivers of A1 are plotted for the range from 2.2 to 3.8 m in Figure 5-7.

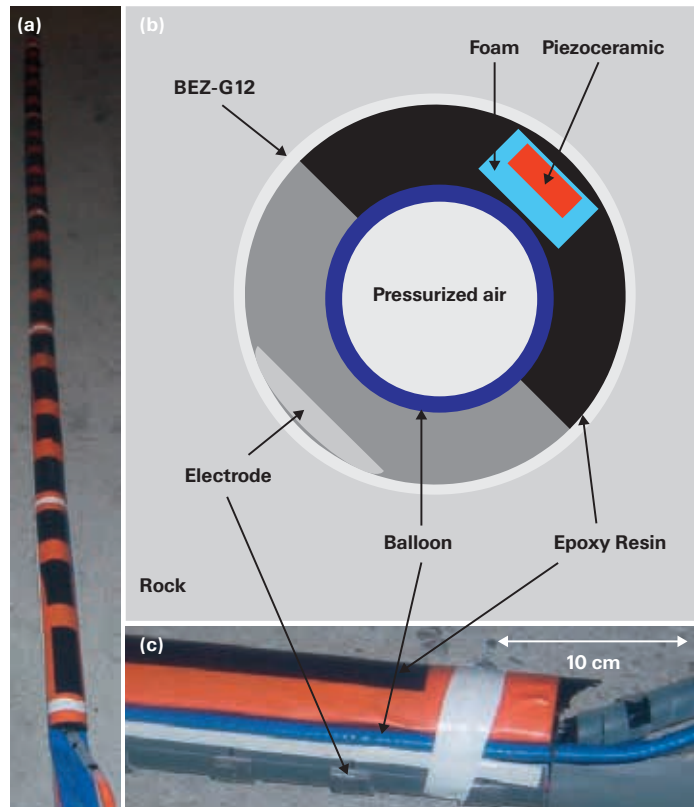


Fig. 5-4: (a) One of the four acoustic arrays of 16 receivers each introduced in boreholes BEZ-G12:15 (array A1). (b) Schematic of the internal structure of an array, where the blue balloon (c) ensures the mechanical coupling with the wall of the borehole.

5.3.2 Temporal changes of the EZ-G08 segment

Between two consecutive acoustic survey measurements, which involved a re-positioning of the acoustic source, we kept the source fixed and performed additional seismic surveys. These latter were repeated every two hours without changing the source position. We emphasize here that each acquired data set corresponded to sounding the shale formation at a given physical state, potentially influenced by the mechanical coupling of the source with the borehole wall. At the beginning of the experiments, the deepest achievable position was 7.2 m, reduced to 6.8 m until July 12, and then limited to 6.4 m until July 23. This observation suggested that the geometry of BEZ-G5 was progressively changing: the output diameter was getting smaller, suggesting borehole collapse effects (RAHMAN et al. 2000).

From July 1 to July 12, we acquired 13 such seismic survey data sets performed with the 64 sensors of the array A1, i.e. in the region around BEZ-G5. Between two consecutive data sets, the acoustic source was re-positioned and fixed at 6.8 m deep inside BEZ-G5. In order to identify the signature of the temporal changes of the borehole geometry with the acoustic measurements, we computed the energy content of the signals recorded at each acoustic sensor. The energy is defined using the integrated squared waveform only, because no absolute calibration was available for the acoustic sensors. As a consequence, we used this proxy for the energy and computed it as a function of time.

For each source-sensor position, the energy of the entire signal received was computed and normalized with the first

data. The energy fluctuations are relative to avoid both the source directivity pattern effects, which are unknown, and the acoustic responses of the sensors, which are all different. For the source-sensor position at 6.8 m, the 13 sets of energy fluctuations are illustrated in Figures 5-8a and 5-8b for one acoustic receiver in BEZ-G12 and one in BEZ-G13, respectively.

The data plotted correspond to the acquisition time of the trace. Each set corresponds to a fixed source-sensor configuration and is computed for the four source wavelet frequencies: 21, 25, 31 and 38 kHz. The measurements evidence clear variations of transmitted energy for a fixed experimental setup: each data set is characterized by many hours (roughly three hours) of strong increase, and then tends towards a constant value. The strong increase is similar for each set and can be attributed to a re-initialization of the mechanical coupling between the balloon of the acoustic source and the BEZ-G5 borehole wall.

If we assume that the coupling affects all the simultaneous measurements in a similar way, we can remove its effects by calculating the ratio of the energy measured at two different receivers. According to this approach, potential changes of the proxy should be attributed to changes of the rock mass only. We illustrate the result by estimating the ratio between the measurements performed at the two receivers in BEZ-G12 and BEZ-G13, respectively (Fig. 5-9).

The result evidences a particular long-term behaviour of the energy variations. During the first week of measurements, from July 1 to July 8, the energy ratio was nearly constant for all frequencies. This suggests that no changes oc-

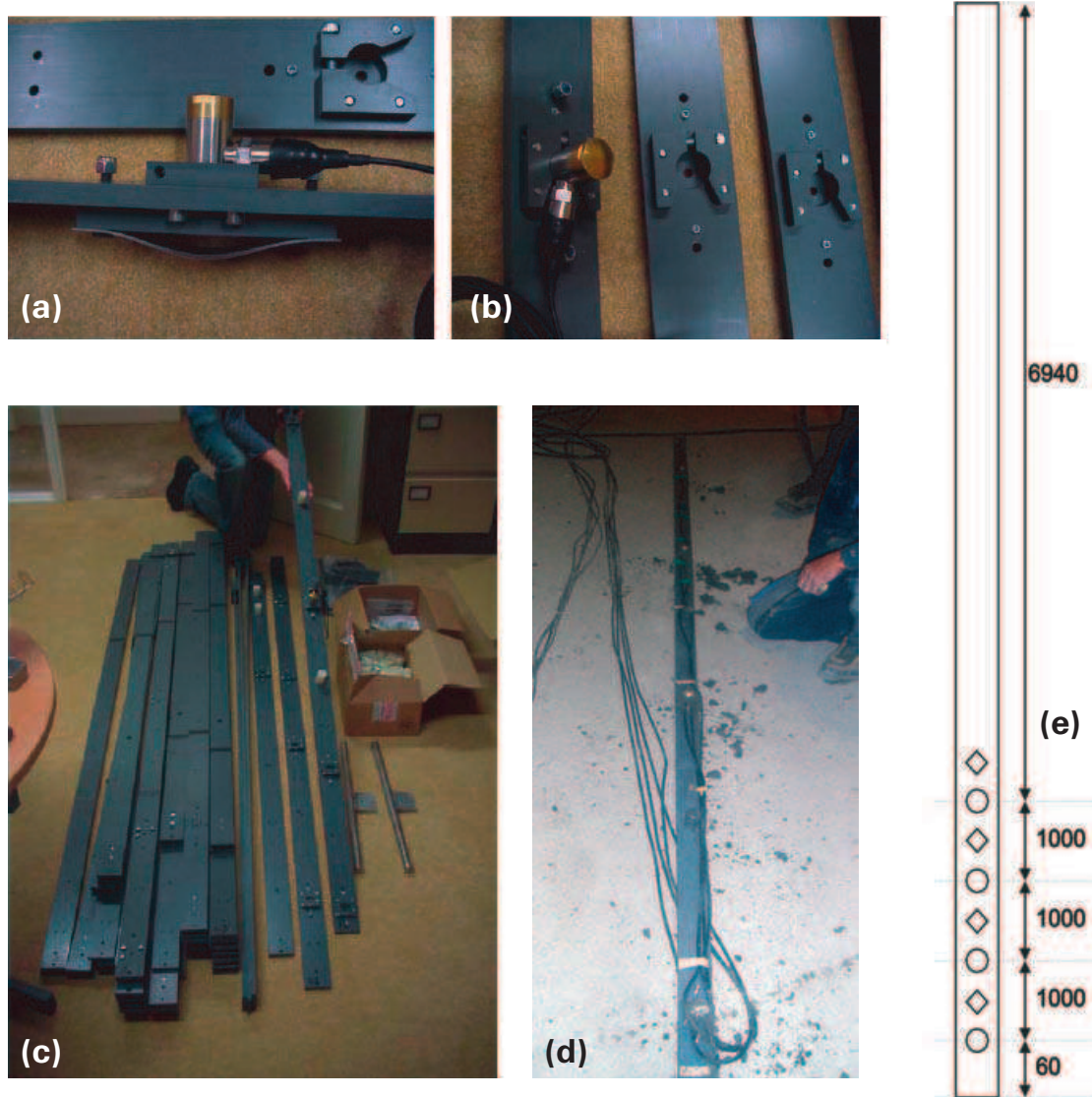


Fig. 5-5: Acoustic poles of 4 receivers each, introduced into each borehole BEZ-G16 to BEZ-G19 comprising the acoustic array A2.

curred in the rock mass, in particular in the surrounding of BEZ-G5. After this date, we observe an abrupt transition on July 8, when the Ga08 front reached a distance of 2.5 m from the end of BEZ-G5. Note that on July 9, the Ga08 front reached the borehole. Thus, the variations of the energy proxy can be linked to the variations of the borehole geometry, i.e. to collapsing effects.

5.3.3 P-wave velocity model of the EZ-G08 segment

The acquisition setup designed for acoustic surveys was synchronized daily with the source introduced in BEZ-G5 to measure the transmitted acoustic signals also at the 16 acoustic receivers of the network A2 located further away. The acoustic survey measurements were performed for different source positions, in steps of 0.4m between 4.4 and 6.8m deep within BEZ-G5. For each measurement, 200 stacks were performed to improve the signal to noise ratio. Typical recorded waveforms are represented in Figure 5-10 for a source frequency of 31 kHz and a source position at 4.8 m from the Ga04 face.

The waveform in red corresponds to the input source signal, i.e. only 15 waveforms are actually used for the study. Each acoustic array of four receivers can be identified in Figure 5-10, and the distance between the source and each receiver is noted on the right-hand side, ranging between 3.4 and 5.2 m.

Considering the different positions of the acoustic source and receivers, the ray path coverage (plunge and azimuth with respect to north) could partly be improved since most of the receivers “heard” the source in BEZ-G5, even for travel distances larger than 5 m. Along each ray path, the P-wave velocity is determined from the time of flight of the acoustic wavelet through the rock mass, i.e. the time of first arrival is picked for each recorded waveform. We observed no clear variation of this parameter with time. This was partly due to uncertainty in the source position inside BEZ-G5. To illustrate this we show in Figure 5-11 the successive 19 waveforms recorded at the acoustic receiver 13 between July 10 and July 22.

As a consequence, the whole set of first arrival times could be used to determine the average P-wave velocity as a

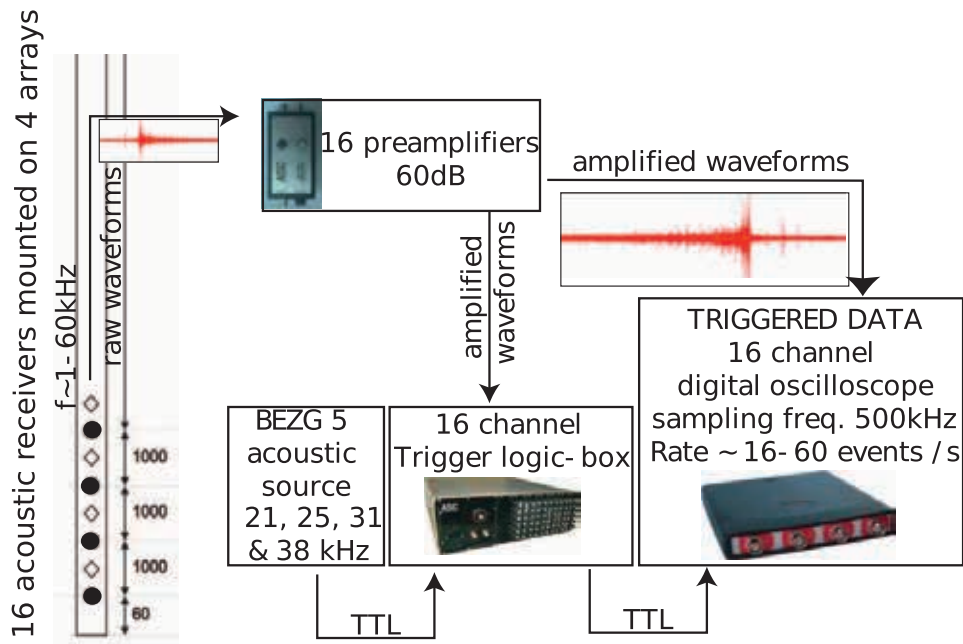


Fig5-6: Principles of the acquisition system of the acoustic array A2 introduced in boreholes BEZ-G16 to BEZ-G19.

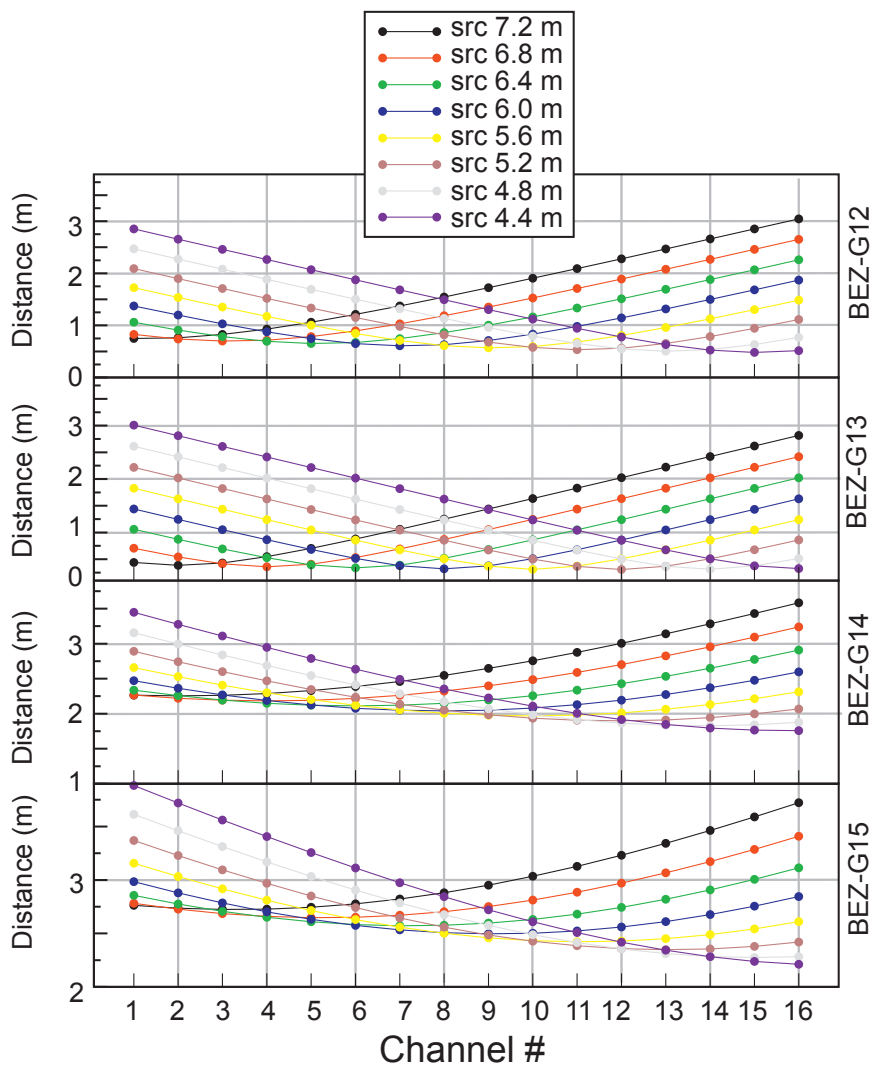


Fig.5-7: Distances between the acoustic source and 64 receivers of the A1 acoustic array.

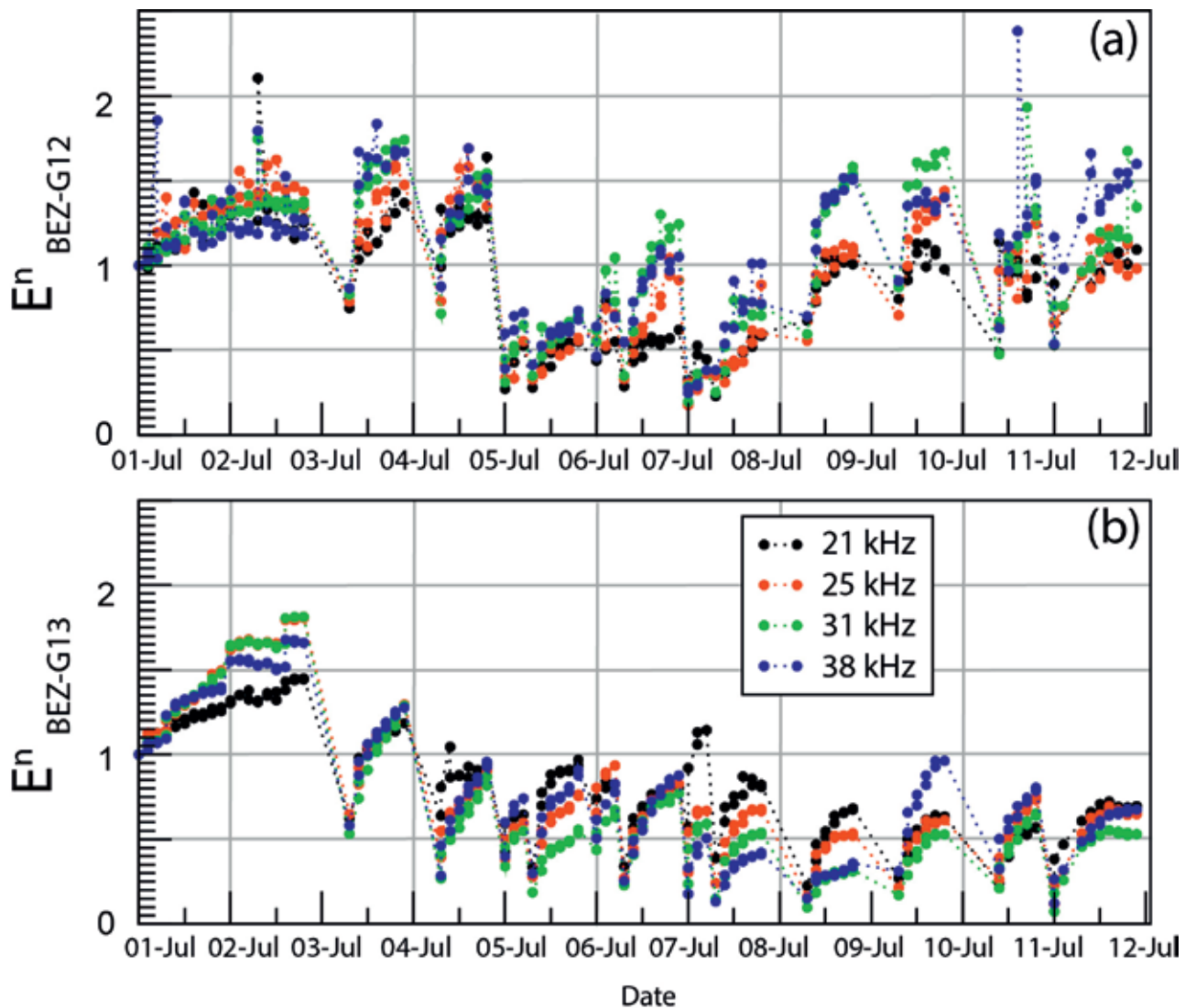


Fig. 5-8: Proxy of the acoustic energy measured at one receiver of (a) the borehole BEZ-G12 and (b) BEZ-G13, as a function of the date.

function of the apparent angle of the ray path relative to the bedding plane of the clay formation. The results, obtained by compiling all the existing data, are plotted in Figure 5-12 and evidence a decrease of velocity with increasing angle, from 3300 m/s at $\theta=0^\circ$ along the bedding plane to 2900 m/s at $\theta=70^\circ$.

Since the coverage was not complete, no data was available at greater angles. Using the Thomsen's Weak Transverse Isotropy model (THOMSEN 1986) to define the P-wave velocity field we calculated a velocity of about 2750 m/s perpendicular to the bedding plane.

5.3.4 Location method performed on the seismic surveys

As a first step, the seismic surveys measurements allowed us to determine the P-wave velocity structure of the EZ-G08 segment, as described above. A further step consisted in using these *in-situ* acoustic data to test and validate the parameterization of a location algorithm, performed to lo-

cate the different active source positions that are controlled during the seismic surveys.

The source location inversion minimizes the difference between two travel times: the one measured between the acoustic source and the receiver, and the one calculated with the P-wave velocity model determined from the Thomsen's parameters. The error is minimized with a Simplex iterative algorithm based on the Downhill Simplex Method (NELDER & MEAD 1965, PRESS et al. 1994). To ensure a confident location procedure, a minimum of six P-wave arrival times was required. We performed the approach for seven source positions in BEZ-G5 between 4.4 and 6.8 m from the Ga04 face using more than 450 data sets of 15 waveforms for the inversion. The result, plotted in Figure 5-13, clearly highlights the efficiency of the method: the seven source positions are recovered along the borehole axis (red line).

Note that the deepest source position (brown in Fig. 5-13) corresponds to a small number of data and not to a better focus efficiency of the data locations. We can estimate the location accuracy from these measurements to be around

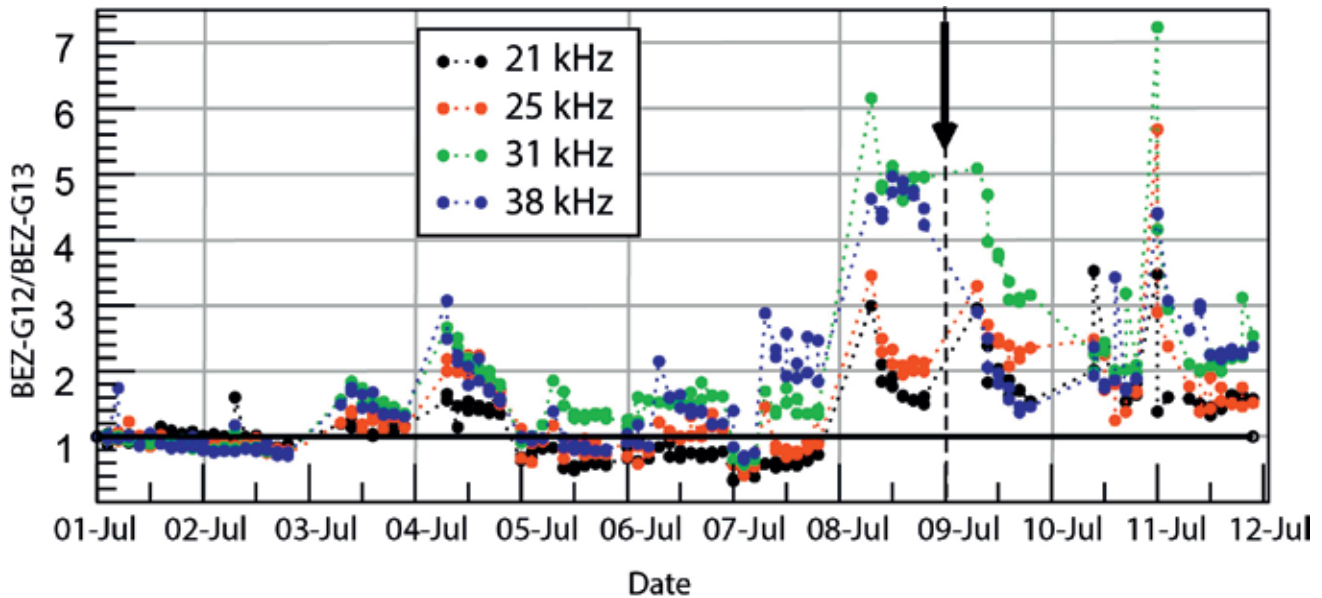


Fig.5-9: Ratio of the temporal energy variations (from LE GONIDEC et al., 2012). The black arrow indicates when the excavation front reached BEZ-G5.

20 cm, a location approach promising for the following study of micro-seismic events for which source locations are *a priori* unknown (LE GONIDEC et al. 2014).

5.4 Micro-seismic events: space-time identification and location

We now focus on the identification of the so-called MSEs, i.e. the micro-seismic events induced by the excavation procedure in the surrounding of the excavated Ga08 front. An MSE is a sudden release of elastic energy induced by micro-cracking in response to local stress variations, i.e. to stress redistribution in the surroundings of the excavated gallery.

5.4.1 Description of the experiments

The acquisition mode of these passive acoustic measurements, i.e. when the acoustic source was turned off, involved mainly the acoustic array A2 comprising 16 acoustic receivers used to detect and record MSEs. We set a threshold on the amplitudes to record the waveforms associated with each detected acoustic event. This allowed us to avoid weak events, for instance, those corresponding to strong ambient noise. The threshold was adapted during the experiment to the ambient noise level, such as when the ventilation was active or turned off. The following criteria were used to record (or not record) the events: if a given number of channels (typically 4) reached a given threshold value (typically 50 mV), within a given time-window (typically 1 ms), the system triggered and recorded the 16 signal waveforms the first 25% of which consisted in pre-triggered points.

At the end of the experiment, more than 56,000 events had been detected and recorded by the multichannel acous-

tic monitoring system. Not all of these corresponded to MSEs from in or around the EZ-G08 segment during or after the excavation procedure. For instance, two different acoustic events are illustrated in Figure 5-14: the first event is associated with the excavation procedure recorded by the A1 acoustic network within a time windows of 50 ms, i.e. long enough to identify the nature of the event, which is not accessible in the 4 ms time window of the A2 acquisition setup. The repetition rate of 80 impacts per second is associated with a sledgehammer that had an acoustic frequency of roughly 3 kHz per impact.

Note that in the A1 configuration, the 16 acoustic receivers of one holding pole are aligned inside one borehole, and the source of the event is located at the end-face of the Ga08 Gallery, i.e. the source of the event is nearly aligned with the receivers. With this alignment we can estimate the S-wave velocity as depicted in Figure 5-15.

A quick overview of the recorded events shows that most of the events comprising the raw data set are electronic noise. Moreover, 98% of the events were detected between July 11 and 12, that is, during the excavation procedure. As an initial rough approach, we identified manually several thousands of events not considered as noise based on their good signal-to-noise ratio and shape of the waveforms. We processed the location of the selected events, according to the procedure developed for the acoustic surveys and plotted the locations in Figure 5-16.

The location shown in Figure 5-16 is clearly not random and the events cluster close to the end-face of the Ga08 Gallery. Most of these events had been detected during the excavation procedure and not all of them belong to the class of micro-seismic events. To further refine our analysis of the very large dataset of recorded events, we developed a specific detection method to identify induced MSEs.

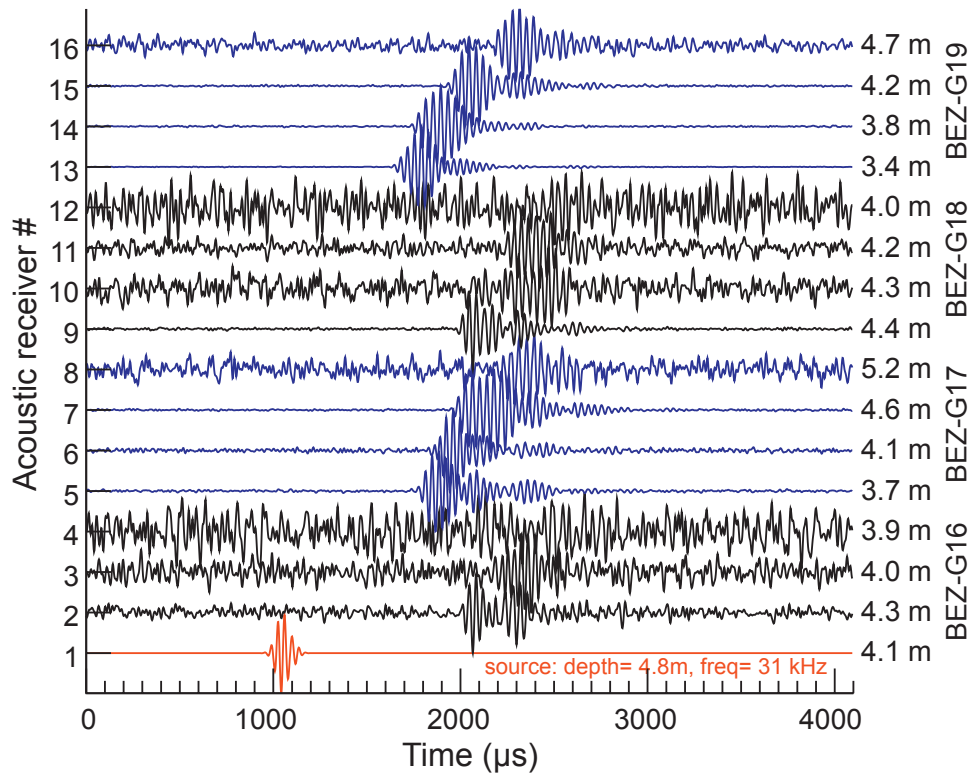


Fig. 5-10: Illustration of the waveforms recorded during a seismic survey with an acoustic source located at 4.8 m deep inside BEZ-G5. The red curve is the source wavelet signal.

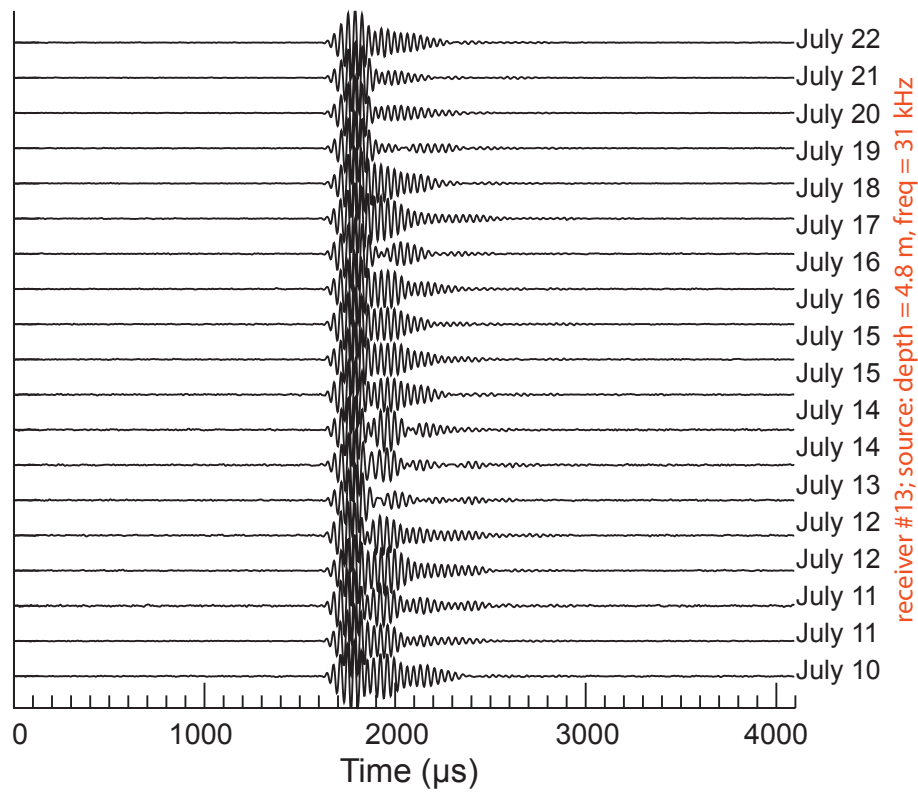


Fig. 5-11: Acoustic waveforms recorded at one receiver as a function of the date.

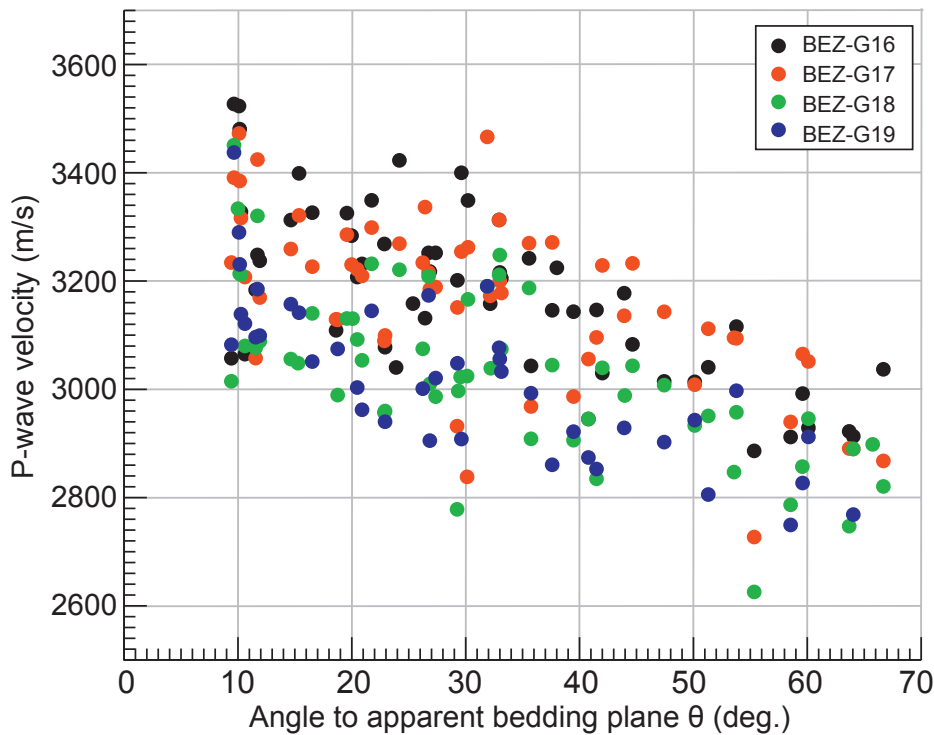


Fig. 5-12: Compilation of the P-wave velocities determined from the seismic surveys along different ray paths relative to the bedding plane.

5.4.2 Identification of micro-seismic events in the raw data set

We associated each acoustic event to 15 waveforms, each being recorded on the acoustic receivers of the A2 acoustic. In addition to electronic noise and artefacts recorded during the EZ-G08 experiments, many other acoustic activities were induced by the excavation operation (cracking and crushing of rock directly in contact with the excavating tools), noisy anthropomorphic activities, and actual MSEs induced by stress redistribution around the gallery. In order to identify MSEs events in the raw data set of acoustic events, we performed a three-step selection described in the following.

First, we applied a frequency selection to all waveforms. Because of the limited time window of the waveforms (4,096 μ s), we considered a low frequency limit at 250Hz under which the waveform was not processed. A quick overview of the frequency spectra of the waveforms indicated a dominant frequency around 8kHz. No energy was observed for frequencies higher than 20kHz. Finally, we applied a zero-phase band-pass filter in the range 200Hz–20kHz to the data. This frequency range corresponds to audible frequencies.

In a second step, we rejected all filtered waveforms with low signal-to-noise ratio, and if more than 5 waveforms were flagged, the associated event was not considered as a potential MSE. According to these two first steps, more than 80% of events of the raw data set were rejected, which means that most of the data were noisy signals. We refer to all events remaining after this second step as selected events.

In the third and last step of MSE identification, we further refined the selected events based on the time history.

The time schedule of the operations was available and we used this to identify particular periods of activity/inactivity at the excavated front of the Gallery 08. After July 6 at 6 PM, the excavation activity completely ceased.

The results of the successive steps of the selection method are plotted in Figure 5-17.

Figure 5-17a and Figure 5-17b show respectively the time history of the events detected before and after the excavation stopped. The numerous events of the raw data set, in brown colour, do not highlight any particular period of time. After the second step of the selection method, only 20% of the events can still be considered as candidates for MSEs. These are plotted in blue colour. Obviously, the time distribution of the remaining events is not random and most of them appear during the excavation procedure, i.e. before July 12. Interestingly, when the time schedule of the excavation operations is superimposed on the event history (grey in Fig. 5-17a), both time histories are in good agreement. This highlights the strong relation between the excavation operations and the detection of acoustic events (Fig. 5-17a) and points out the efficiency of the identification method. Nevertheless, we manually checked the remaining events and identified a particular burst of hundreds of MSEs on July 11.

Following the last step of the method, only few events could be considered as potential MSEs after July 12. Some of these, detected on July 14 and 22, were induced during borehole drilling operations. As a result, only 87 MSEs were detected: 71 on July 12, and 16 on July 13. To assess the origin of remaining MSEs we confirmed the temporal identification by processing for their spatial location.

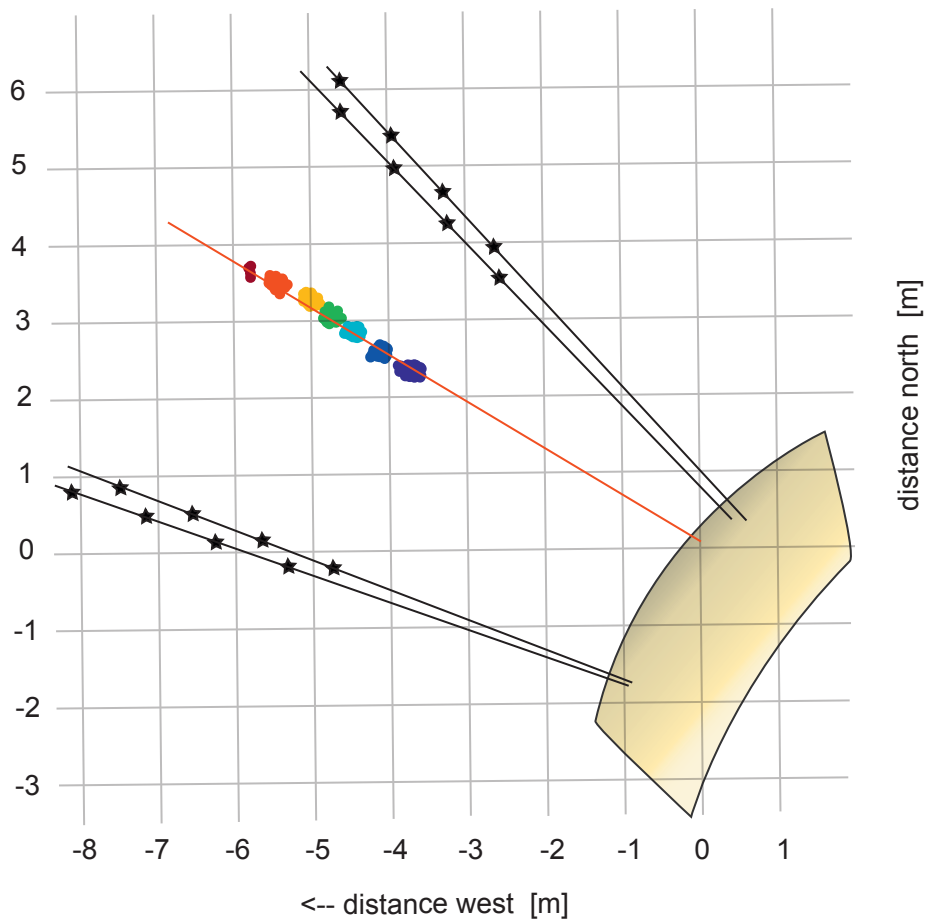


Fig. 5-13: Spatial location of the active acoustic sources introduced at different positions inside the borehole BEZ-G5 (red). The blue lines and crosses indicate the positions of the acoustic receivers inside the four boreholes (modified from LE GONIDEC et al. 2014).

5.4.3 Spatial location of the micro-seismic events

Following the location procedure previously applied to the active acoustic survey measurements (to validate the efficiency of the location algorithm), we located three groups of MSEs, i.e. the burst of hundreds of MSEs identified on July 11, the 71 MSEs on July 12, and the 16 MSEs on July 13.

Among the events detected on July 11, that is, during the excavation procedure, we tagged a series of successive events based on their similar waveforms. According to their spatial location we identified these to a burst of events. Because we could not pick enough first arrival times for part of these, we processed only the spatial location of 191 MSEs. The MSEs located on July 11 are plotted in blue in Figure 5-18 where the events cluster on the right-hand side of Ga08. It is of prime importance to highlight that this location corresponds to the shaly facies sidewall and that no microseismic activity was observed in the sandy facies of the opposite sidewall. On July 12, the events located on the excavated front are plotted as green points in Figure 5-18. In that figure the yellow surface represents the end-face of the Gallery 08. Interestingly, the MSEs detected one day later, on July 13, cluster in the same area. This suggests that both series of events correspond to similar failure mechanism as described in the following.

5.4.4 Analysis of damage initiation and propagation in the Opalinus Clay formation

Once the MSEs were identified with confidence among the numerous recorded events of the raw data set and these were located in the surrounding rock mass, we could assess their failure mechanism. This represents an initial approach to such an original excavation procedure.

In order to identify the failure mechanism, we used the inversion algorithm based on the time-domain Moment Tensor (MT), implemented in the Insite software (PETTITT 1998, YOUNG et al. 2000). In that method, both the first motion and associated amplitude of the P-waves are considered for the algorithm. In our case, we could not accurately identify these two attributes for the MSEs of the burst detected on July 11. Thus we could not process these. Accordingly the associated source mechanisms could not be determined due to the low signal-to-noise ratio of the recorded waveforms. Our focus was limited to the 61 MSEs detected on July 12 and 13. The result of the MT inversion is plotted in the Hudson T-k plot (Fig. 5-19), with the error ellipses related to the inversion accuracy (LE GONIDEC et al. 2014). In such diagram, $(T,k)=(0,1)$ corresponds to pure dilatation mechanism (ISO), $(T,k)=(-1,0)$ to compensated linear vector dipole mechanism (CLVD) and $(T,k)=(0,0)$ to pure double-couple (DC).

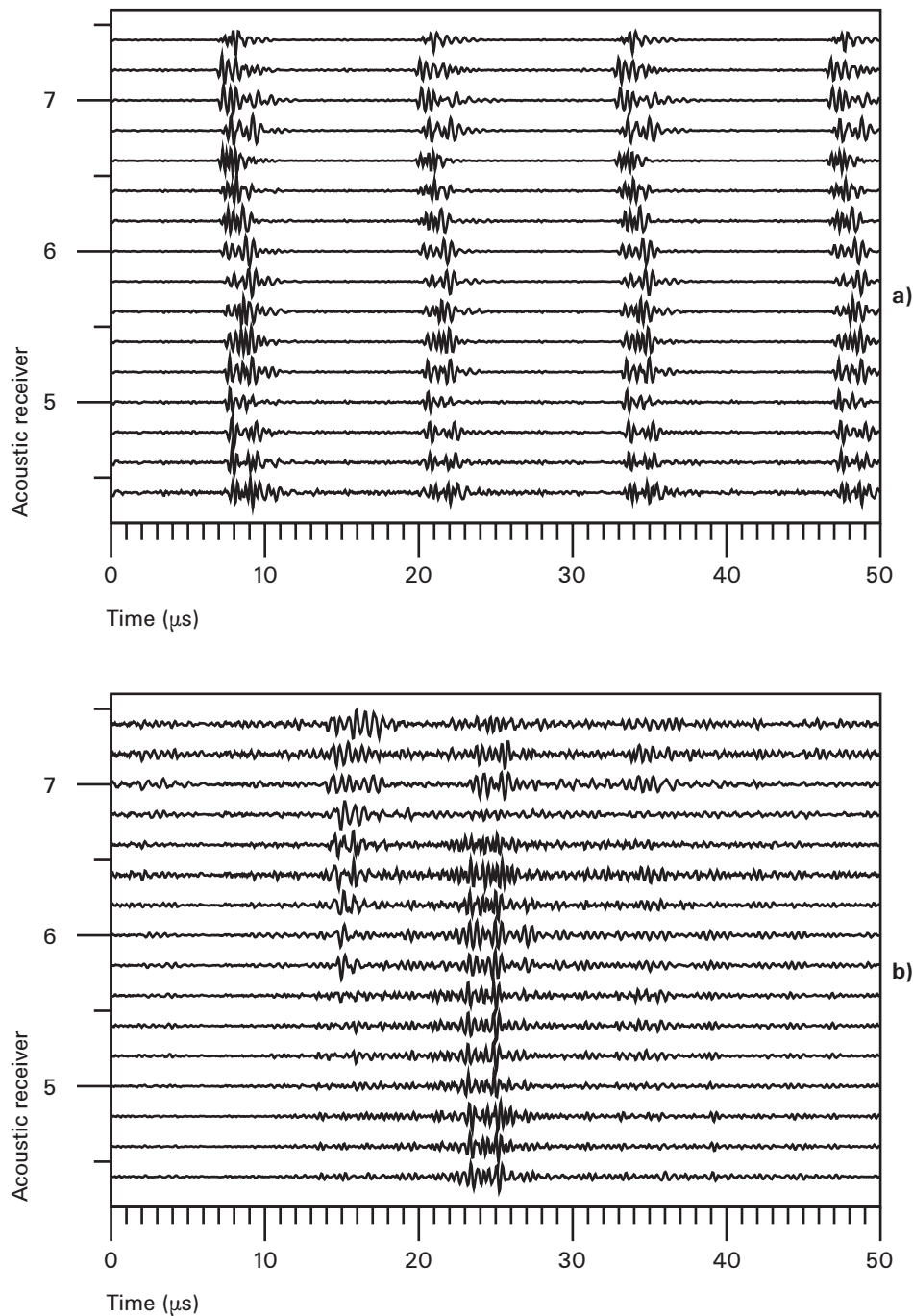


Fig. 5-14: Acoustic events identified with the 16 receivers introduced in BEZ-G12: (a) acoustic event associated to rock-breaking (sledgehammer) equipment and (b) acoustic event associated to a micro-seismic event.

From these results we see that the distribution of failure mechanisms is not random but clusters in the DC and positive CLVD domain.

In the Hudson T-k plot, information on the spatial location of the events is lost. A solution consisted in associating a RGB colour scale to the failure mechanism, a colour used to plot the event in the surrounding of the rock mass: red, green and blue designate respectively a dominant ISO, DC and CLVD mechanism (Fig. 5-20).

The CLVD-dominated mechanisms locate mainly at the right-hand side when facing the excavated Ga08 front. The

DC-dominated mechanisms are located mostly at the Ga08 excavation front itself. This clearly highlights a correlation between three main attributes of the MSEs in relation with the stress redistribution processes: namely their spatial, temporal, and failure mechanism attributes (LE GONIDEC et al. 2014). When facing the Ga08 end-face, we observe a dominant CLVD component for the MSEs located in the shaly facies sidewall. This suggests a dominant extensive cracking, in agreement with the bedding and sub-parallel faults which are not free to slip (no free boundary). Such faults are free to slip ahead of the excavation front, inducing a reactiva-

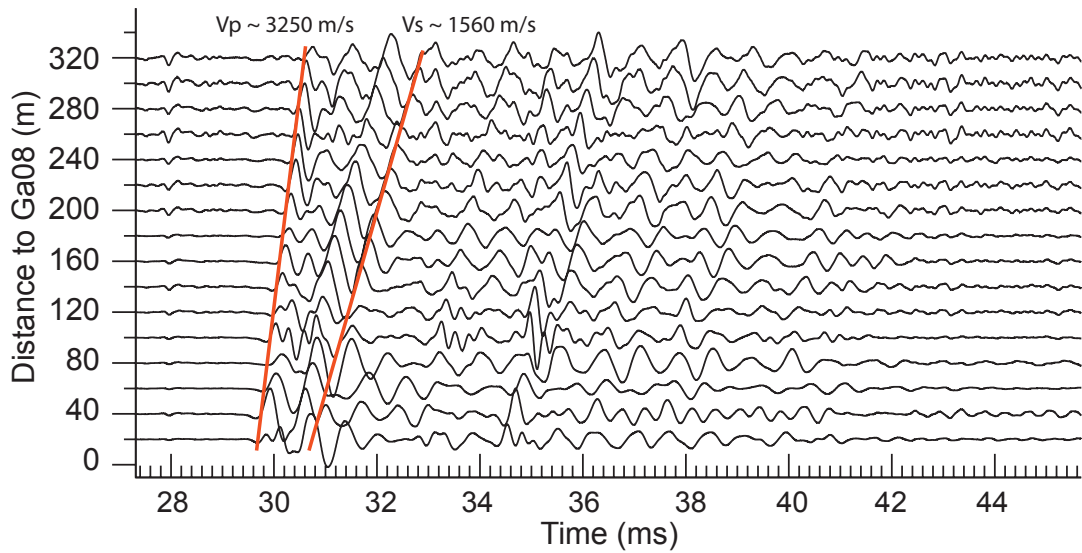


Fig. 5-15: Identification of the P- and S-waves and their velocities (red lines) from a recorded event induced at the Ga08 front during the excavation procedure (modified from LE GONIDEC et al. 2012).

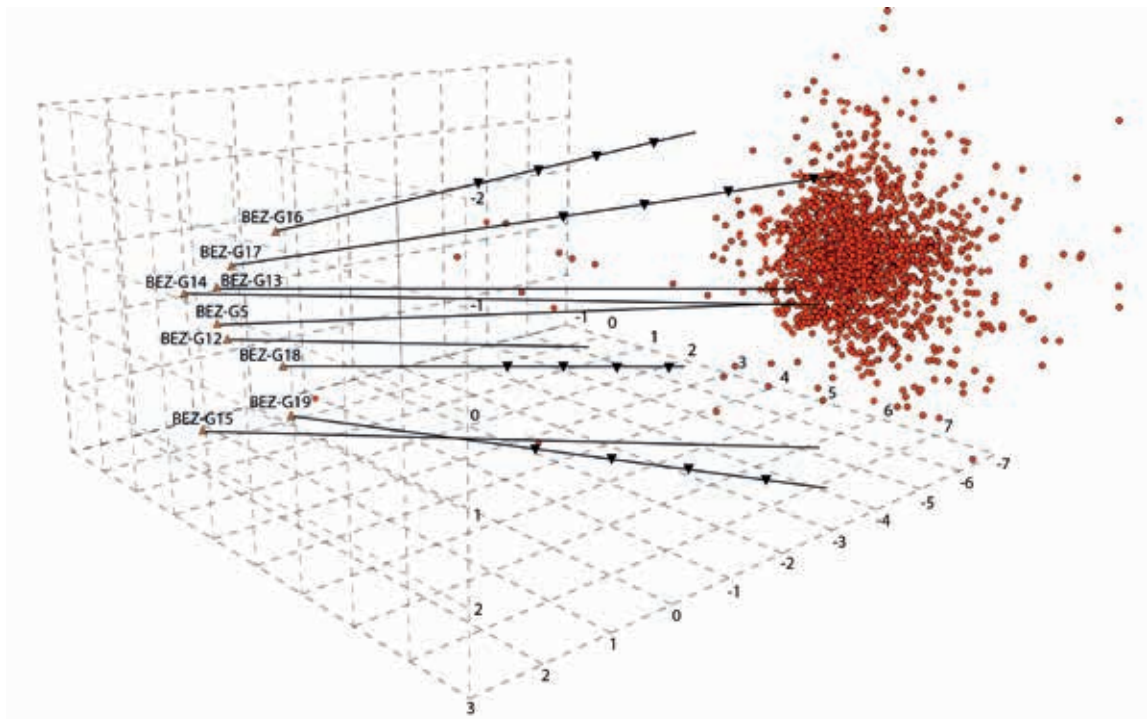


Fig. 5-16: Spatial location of manually selected acoustic events. The 16 acoustic receivers located in the four boreholes of the A2 acoustic network are indicated by the black symbols.

tion of the pre-existing features. This suggests another damage mechanism. We consider this to highlight a dominant DC component highlighted for these MSEs relating to a bedding plane reworking where wing cracks are expected to develop.

5.5 Conclusion

During the EZ-G08 experiments to monitor the EDZ induced by an excavation procedure in the Opalinus Clay formation of the Mont Terri URL, we acquired a very large set of acoustic data, including both active and passive measurements. The active measurements indicated a strong elastic anisotropy of the P-wave velocity wavefield: a low velocity of 2750 m/s in the direction of wave propagation perpendicular to the bedding structure, and a high velocity of 3300 m/s parallel to the bedding. This velocity model was used to locate

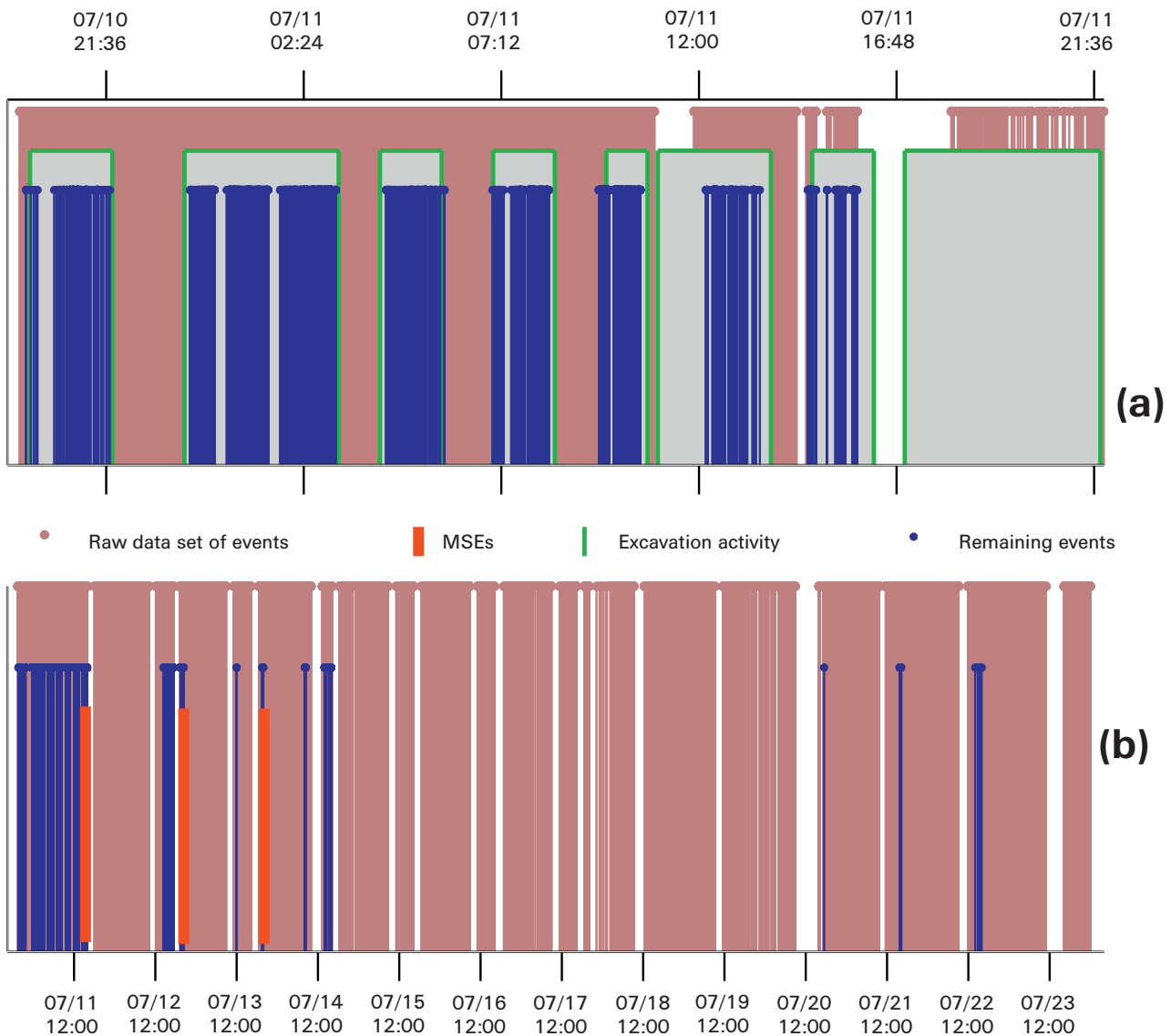


Fig. 5-17: Time history of the events detected (a) during the excavation and (b) after the excavation stopped (modified from LE GONIDEC et al. 2014).

the active acoustic surveys, evidencing the efficiency of the location algorithm. After pre-processing steps to organize and control the passive acoustic measurements, i.e. the acoustic emission detected during the experiment, only a few hundred events could be identified as micro-seismic events (MSEs).

A burst of MSEs was highlighted in the shaly facies sidewall of the gallery but, unfortunately, we could not determine the associated source mechanisms due to the low signal-to-noise ratio of the recorded waveforms. A second cluster of 61 MSEs occurred on July 12 and 13, i.e. up to two days after the excavation stopped. Both their spatial and temporal locations and their damage mechanisms are consistent and allowed to interpret the damages induced in the rock mass surrounding by the excavation operation (Fig. 5-21). In the vicinity of the excavation front, we identify a dominant DC component due to shear movement along pre-existing fea-

tures such as bedding-parallel faults and bedding planes oriented sub-parallel to the major axis of the ambient stress field. In the mid part of the shaly facies sidewall of the front-face, the dominant CLVD component suggests an axial splitting, and indicates a possible zone of spalling damage initiation (BLÜMLING et al. 2007, YONG et al. 2010).

In conclusion, the EDZ initiation during a mine-by of the Opalinus Clay developed in a particularly complex zone in relation to the lithology (MSEs detected in the shaly facies, none in the sandy facies: both facies are anisotropic, with contrasting mechanical properties), and a complex perturbation of the stress field (increase, decrease, and rotation of the stress around the opening (MARTIN 1997). These *in-situ* results, published in LE GONIDEC et al. (2012, 2014), are consistent with previously published observations in crystalline rocks and clearly contribute to filling our knowledge gap for clayey formations.

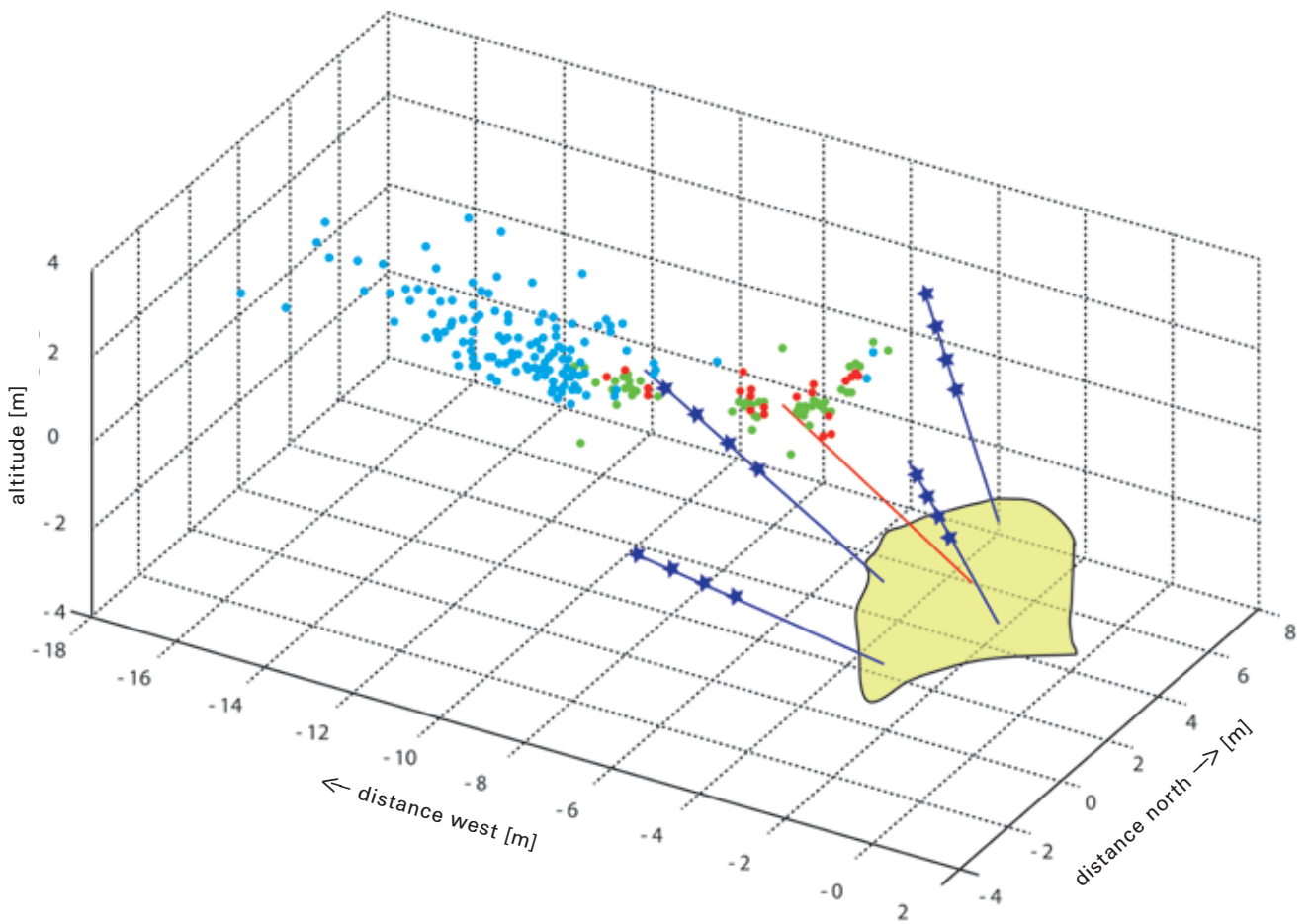


Fig. 5-18: Spatial location of the events identified as micro-seismic events (MSEs), detected on July 11 (blue), 12 (green) and 13 (red). The four dark blue lines represent the boreholes with the 16 acoustic receivers (blue stars). The red line is the BEZ-G5 borehole. The yellow surface indicates the face of Ga04 Gallery (modified from LE GONIDEC et al. 2014).

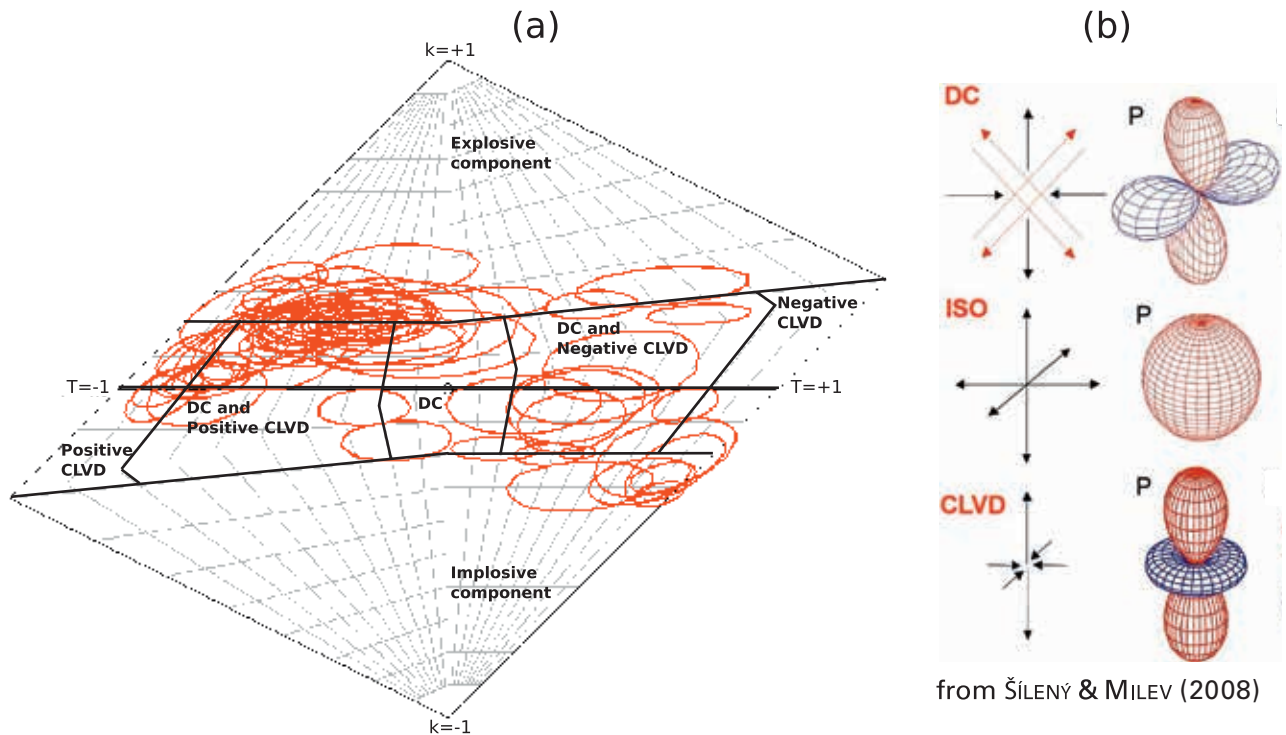


Fig. 5-19: (a) Hudson T-k plot showing the damage mechanisms of microseismic events recorded on July 12 and 13 after the excavation stopped (from LE GONIDEC et al. 2014). (b) Illustrations of the DC, ISO and CLVD mechanisms.

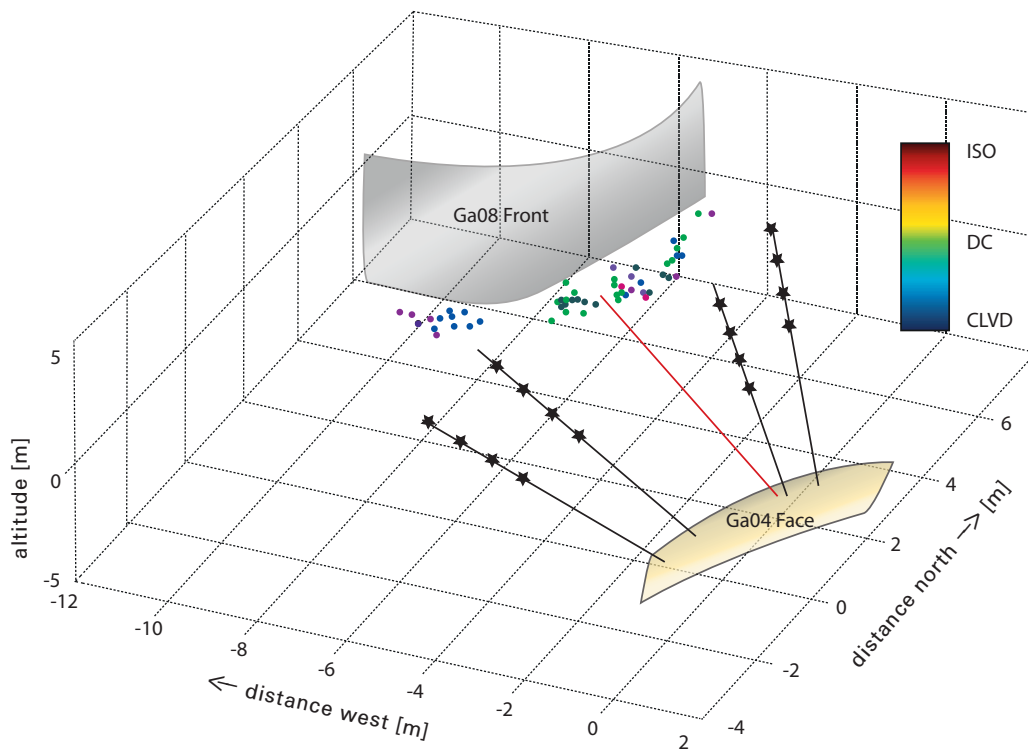


Fig. 5-20: Spatial location of the MSEs, where the colour scale indicates the failure mechanism (dominant CLVD, DC and ISO in blue, green and red, respectively). The red and blue lines represent the BEZ-G5 borehole and the four boreholes with the 16 acoustic receivers (blue stars). The black polygon and dots stand for the Ga08 front and Ga04 faces, respectively (modified from LE GONIDEC et al. 2014).

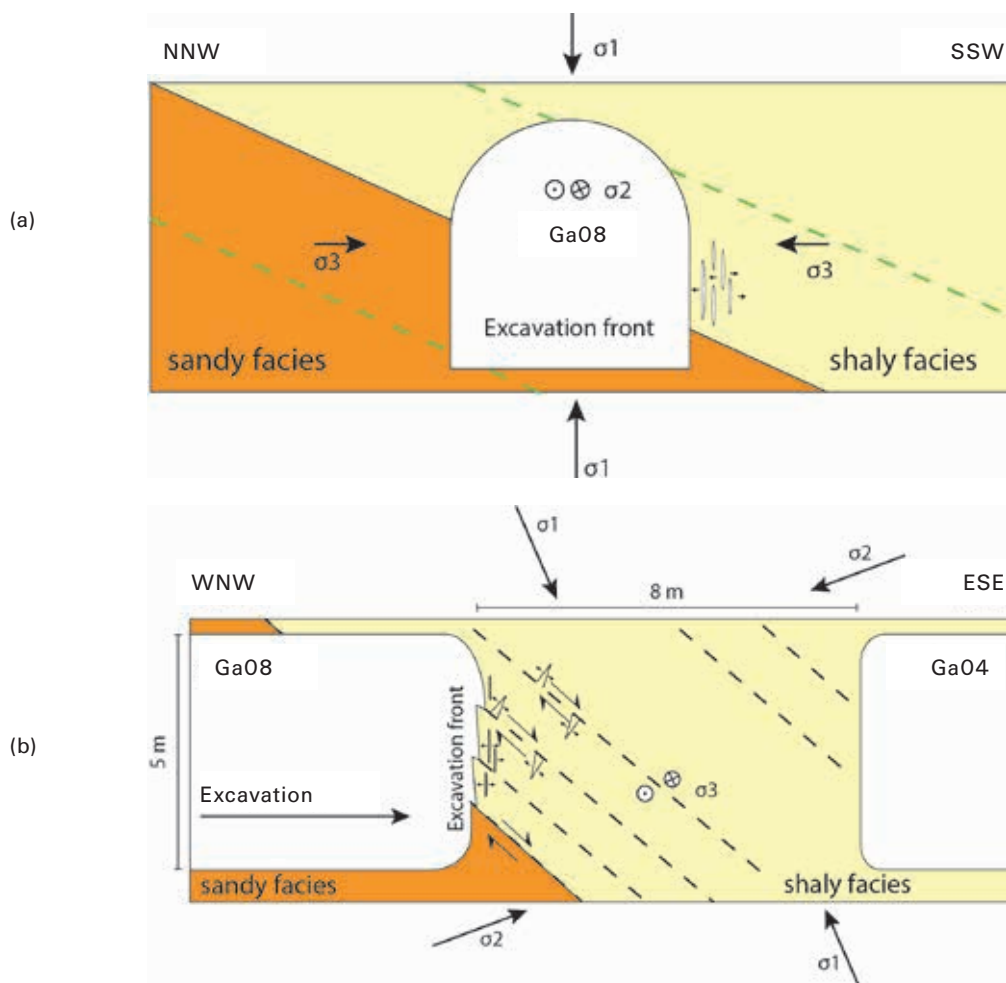


Fig. 5-21: Conceptual representation of the stress pattern around the excavated Gallery 08 (modified from LE GONIDEC et al. 2014): (a) View from Ga08 in the direction of the excavation front and (b) Side view from shaly facies sidewall (modified from NUSSBAUM et al. 2011).

References

- BLÜMLING, P., BERNIER, F., LEBON, P. & MARTIN, C. D. (2007): The excavation damaged zone in clay formations time-dependent behaviour and influence on performance assessment. – *Phys. Chem. Earth, Parts A/B/C* 32, 588–599.
- LE GONIDEC, Y., SAROUT, J., WASSERMANN, J. & NUSSBAUM, C. (2014): Damage initiation and propagation assessed from stress-induced microseismic events during a mine-by test in the Opalinus Clay. – *Geophys. J. int.* 198, 126–139.
- LE GONIDEC, Y., SCHUBNEL, A., WASSERMANN, J., GIBERT, D., NUSSBAUM, C., KERGOSIEN, B., SAROUT, J., MAINEULT, A. & GUÉGUEN, Y. (2012): Field-scale acoustic investigation of a damaged anisotropic shale during a gallery excavation. – *Int. J. Rock Mech. Min. Sci.* 51, 136–148.
- MARTIN, C. D. (1997): Seventeenth Canadian Geotechnical Colloquium: the effect of cohesion loss and stress path on brittle rock strength. – *Can. Geotech. J.* 34, 698–725.
- NELDER, J. & MEAD, R. (1965): A simplex method for function minimization. – *Comp. J.* 7, 308–312.
- NICOLLIN, F., GIBERT, D., BOSSART, P., NUSSBAUM, C. & GUERVILLY, C. (2008): Seismic tomography of the excavation damaged zone of the Gallery 04 in the Mont Terri Rock Laboratory. – *Geophys. J. int.* 172, 226–239.
- NUSSBAUM, C., BOSSART, P., AMANN, F. & AUBOURG, C. (2011): Analysis of tectonic structures and excavation induced fractures in the Opalinus Clay, Mont Terri underground rock laboratory (Switzerland). – *Swiss J. Geosci.* 104/2, 187–210.
- PETTITT, W. S. (1998): Acoustic emission source studies of microcracking in rock. – Ph.D. Thesis, Keele University, UK.
- PRESS, W. H., FLANNERY, B. P., TEUKOLSKY, S. A. & VETTERLING, W. T. (1994): *Numerical recipes in C: The art of scientific computing*, 2nd ed. – Cambridge Univ. Press.
- RAHMAN, M. K., NASEBY, D. & RAHMAN S. S. (2000): Borehole collapse analysis incorporating time-dependent pore pressure due to mud penetration in shales. – *J. Petroleum Sci. Eng.* 28, 13–31.
- ŠILENÝ, J. & MILEV, A. (2008): Source mechanism of mining induced seismic events: resolution of double couple and non-double couple models. – *Tectonophysics* 456, 3–15.
- THOMSEN, L. (1986): Weak elastic anisotropy. – *Geophysics* 51, 1954–1966.
- YONG, S., KAISER, P. K. & LOEW, S. (2010): Influence of tectonic shears on tunnel-induced fracturing. – *Int. J. Rock Mech. Min. Sci.* 47, 894–907.
- YOUNG, R. P., HAZZARD, J. F. & PETTITT, W. S. (2000): Seismic and micromechanical studies of rock fracture. – *Geophys. Res. Lett.* 27, 1767–1770.

6. Geo-electrical experiments

F. NICOLLIN, D. GIBERT, C. NUSSBAUM & N. LESPARRE

6.1 Introduction

We performed electrical conductivity measurements in the EZ-G08 segment from December 2007 to August 2008 to study the evolution of the EDZ at time scales ranging from hours to months. These measurements were carried out from the end of the Gallery 04, using arrays of electrodes installed on the face and in boreholes perpendicular to the face.

In December 2007, we performed a resistivity survey of the EDZ at the back of the Gallery 04 using Wenner measurements along profiles from the gallery face. In April and May 2008, we measured the anisotropy of the electrical resistivity using combinations of square arrays both on the Ga04 face and in eight small boreholes perpendicular to the face. In May 2008, we equipped four long boreholes perpendicular to the face and in July 2008 we repeated daily resistivity measurements in the EZ-G08 segment.

During this period, the excavation of the Gallery 08 was in progress: in May 2008, the front was a few tens of metres from the EZ-G08 segment; on July 1, 2008, the front was 22 m from the Ga04 face, and the mean excavation rate was then about 1.3 m per day; the north-west edge of the EZ-G08 segment, 8 m away from the Ga04 face (GM159), was reached on July 11, and the excavation stopped until July 28. Between July 29 and August 5, an additional 4 m were excavated, and the last 4 m were excavated during the second half of August 2008 (see Chap. 2).

By inverting the anisotropy data we could recover the resistivity tensor characteristic of the electrical properties associated with 1 m depth in 18 areas of the Ga04 face. The data analysis of the monitoring performed in July 2008 showed spatial and temporal variations of the electrical properties in the EZ-G08 segment when it was reached by the Ga08 excavation front.

6.2 Experimental setup

6.2.1 Layout of electrode arrays

Three sets of electrodes constitute the device shown in Figure 6-1: an array of 715 electrodes on the Ga04 face, an array of 256 electrodes in four long boreholes, and an array of 128 electrodes in eight short boreholes.

Electrodes on the Ga04 face

We introduced 715 electrodes into the rough face aligned to a square mesh with a mean length of 30 cm per side, forming 13 horizontal lines and 16 vertical lines. The electrodes

were stainless steel rods of 8 mm in diameter and 8 cm in length, spaced equally every 15 cm on each line of the mesh. Each of the 10 lowest horizontal lines is 4.65 m long with 32 electrodes per line, and the 3 highest lines are a bit shorter with 30 or 31 electrodes per line. In the vertical direction, the length of the lines varied from 2.79 m (i.e. 19 electrodes) for the shortest line at the NE side to 4.65 m (i.e. 32 electrodes) for the 9 longest lines. A topographic survey identified the precise 3D-location of each electrode in the array

Electrodes in four long boreholes

Four boreholes, BEZ-G12, G13, G14 and G15 were drilled in December 2007 perpendicular to the gallery wall face, each 8 m long and 56 mm in diameter. The boreholes were equipped with lines of 64 electrodes equally spaced every 5 cm, making a total of 256 electrodes. These electrodes comprised strips of lead 7 cm long and 15 mm wide glued onto a PVC half pipe and coupled to the borehole wall with an inflatable balloon. Lines of 64 electrodes, 3.15 m long were placed either in the far end of the boreholes, i.e. at a distance of about 5 to 8 m from the Ga04 face, or in closer to the beginning of the hole, at a distance of about 0 to 3 m from the Ga04 face. Location and orientation of boreholes were measured by topographic survey.

Electrodes in eight short boreholes

We also drilled eight short boreholes, BEZ-G22 to BEZ-G29, in June 2008. Each borehole was oriented perpendicular to the face, up to a depth of 1 m and with diameter 42 mm. Each borehole was equipped with a line of 16 electrodes equally spaced every 5 cm, making a total of total of 128 electrodes in this experiment. Installation of the electrodes was identical to those of the long boreholes, with electrodes placed in the first 80 cm of the boreholes. Here also location and orientation of the boreholes was measured by topographic survey.

6.2.2 Measurement principle

For this electrical tomography experiment we used an ABEM SAS4000 resistivity metre coupled either with one ES464 multi-electrode switcher or with four ES1064 multi-electrode switchers. The ES464 switcher was able to manage up to 64 electrodes, with four ES1064 switchers we able to manage up to 256 electrodes. The switchers could be configured to arbitrarily choose the {A, B, M, N} electrodes to perform a given measurement. The measurement procedure began by injecting, via the A and B electrodes, a low-frequency (~1 Hz) square-shaped alternating current in order to suppress polarisation of the electrodes. At the M and N electrodes, the electrical potential ΔV was measured in phase

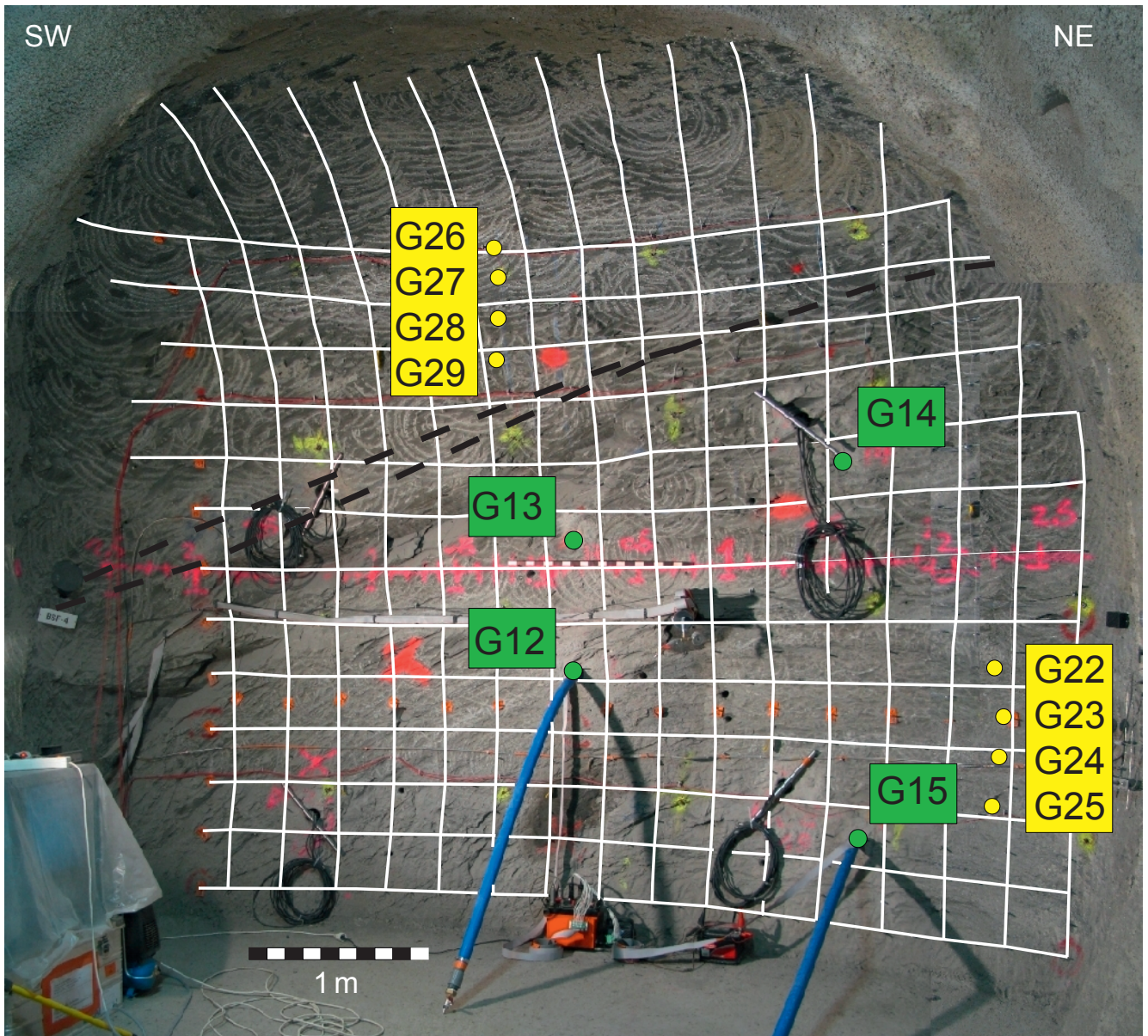


Fig. 6-1: View of the electrical monitoring system installed on the Ga04 face. A tectonic fracture (SW dipping fault N120–20°) is clearly visible on the face and marked by a black dashed line. The white mesh represents the horizontal and vertical lines of the electrode array on the gallery face, the green and yellow dots mark the long and short boreholes respectively. Two long boreholes were equipped with lines of electrodes coupled to the wall with blue inflated balloons.

with the current injection to enhance the signal-to-noise ratio. Reciprocal measurements, obtained by inverting the current injection electrodes with the potential measurement electrodes, were also made in order to check the reliability of the apparatus.

6.3 Field experiment

6.3.1 Electrical resistivity at rear to the Ga04 face

In December 2007, a global resistivity survey of the Ga04 face was performed with Wenner measurements along the horizontal and vertical lines of the face array, using combinations of aligned and equally spaced electrodes placed according to the geometrical sequence {A, M, N, B}. Lines of

32 or 30 electrodes yielded 155 or 145 Wenner measurements respectively, whereas only 40 measurements were possible with lines of 19 electrodes. The electrical structure of the EDZ of the Ga04 face was thus investigated to a depth of about 1 m.

Results of the Wenner measurements performed along the horizontal and vertical lines of the face array are shown in Fig. 6-2 as pseudosections of the apparent resistivity. For the Wenner geometry, pseudosections were obtained simply by placing each measurement j at a point P_j located at the middle of the quadrupole {A, M, N, B} $_j$ and at a depth equal to the distance between electrodes (EDWARDS 1977, BARKER 1989). The value plotted is the apparent resistivity value, ρ_{aj} , computed by applying a geometrical factor K_j to the measured electrical resistance $\Delta V_j/I_j$, where I_j is the electrical current actually injected. The geometrical factor K is such

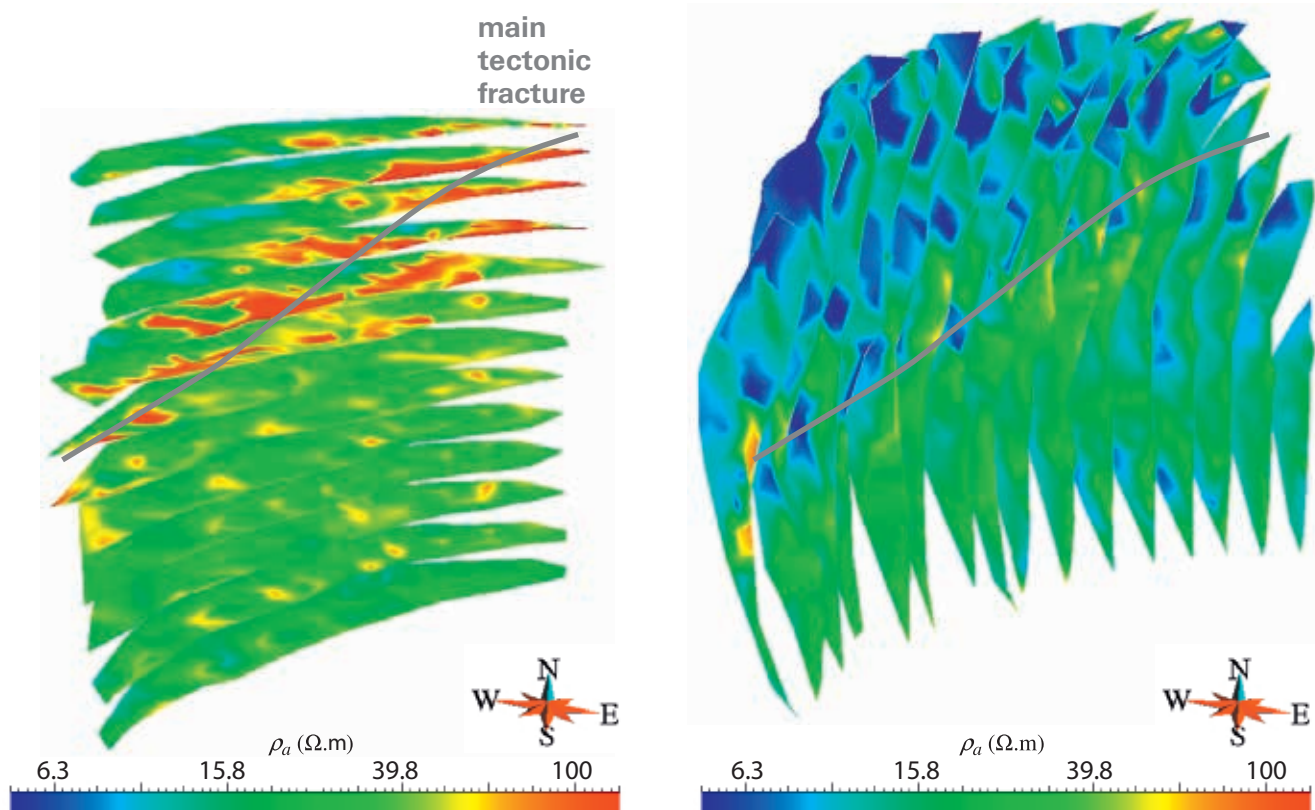


Fig. 6-2: Electrical tomography of the Ga04 face with Wenner profiles performed using the electrode array of the face: pseudosections of apparent resistivity ρ_a measured along the horizontal lines (left) and along the vertical lines (right).

that for a medium with a constant isotropic resistivity ρ , the apparent resistivity ρ_a equals ρ . This implies that the geometrical factor must properly account for the exact 3D-position of each electrode.

Gathers of profiles displayed on Figure 6-2 show the main tectonic fracture as a high-resistive zone that separates two domains with different apparent resistivity. On each of the two assemblages, the measured values are lower in the upper domain than in the lower domain. These assemblages also show that the apparent resistivity depends on the direction in which it is measured, highlighting an anisotropy of electrical resistivity. The apparent resistivity measured along horizontal profiles is higher than the one measured along vertical profiles. According to the paradox of electrical anisotropy (KUNZ & MORAN 1958) when measuring with aligned electrodes, the apparent resistivity appears higher on profiles arranged in a direction of low resistivity than on profiles arranged in a direction of high resistivity. Therefore, to study the electrical anisotropy we adapted our measurements using particular combinations of electrodes on the Ga04 face and in the small boreholes perpendicular to the face.

6.3.2 Electrical anisotropy at rear to the Ga04 face

In order to study the anisotropy of electrical resistivity, measurements were carried out with a square array configuration where electrodes are located at corners of squares with different sizes and orientations (HABBERJAM 1972). With the A and B current electrodes on one side of the square and the M and N potential electrodes on the opposite

side, the apparent resistivity is measured in the direction given by the orientation of the AB side.

On the Ga04 face, 18 areas of ca. 1.2 m height and 0.9 m width were defined, (Fig. 6-3). In each area, 32 electrodes may be combined into 59 square quadrupoles. Thus we could realise, in April and May 2008, 118 measurements of the apparent resistivity in 12 directions in the local plane of each area (Fig. 6-4a,b). In addition, two surfaces close to vertical planes perpendicular to the face were defined by the two series of four short boreholes BEZ-G22 to G25 and BEZ-G26 to G29 (see Fig. 6-1). Each of these two areas was equipped with 64 electrodes that may be combined into 56 square quadrupoles. Thus we could realize 112 measurements of the apparent resistivity according to 8 directions of the plane (Fig. 6-4c,d). With these whole measurements, we could characterize the 3D electrical anisotropy over a depth of ca. 1 m at the rear of the Ga04 face.

In anisotropic media, results from measurements using the square array configuration do not contain ambiguity: the apparent resistivity measured in the direction of the AB segment varies in accordance with the true resistivity tensor (e.g. HABBERJAM 1972, SENOS MATIAS 2002). Figure 6-5 displays such measurements performed on the Ga04 face, with apparent resistivity plotted in polar diagrams. Each diagram gathers either the 118 measurements made in one area of the face or the 112 measurements made in one series of boreholes.

The diagrams of Fig. 6-5 clearly show the anisotropy of electrical conductivity. The highest values of apparent resistivity are measured in a direction close to the vertical, and

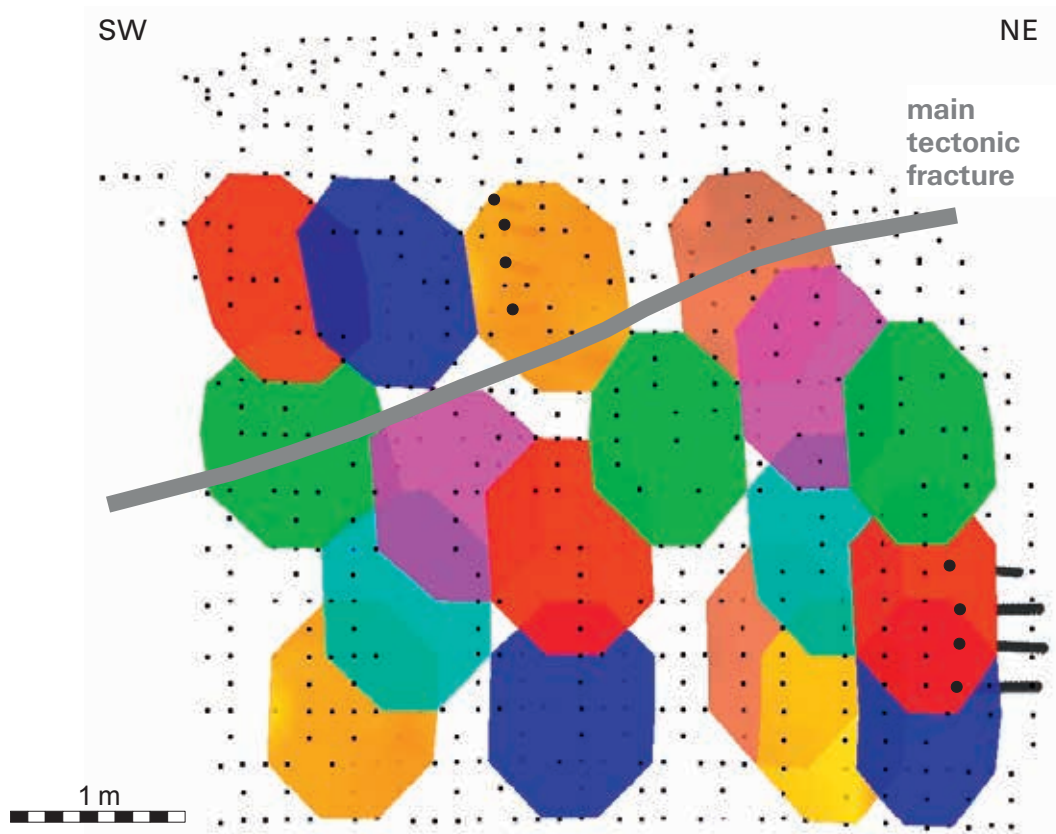


Fig. 6-3: Location of the electrical anisotropy measurements: 18 areas of 32 electrodes on the Ga04 face and two series of four boreholes equipped with lines of 16 electrodes. Five areas of the face and one group of boreholes were located in the domain above the fracture, while the other 13 areas and the other group of boreholes were located in the lower domain.

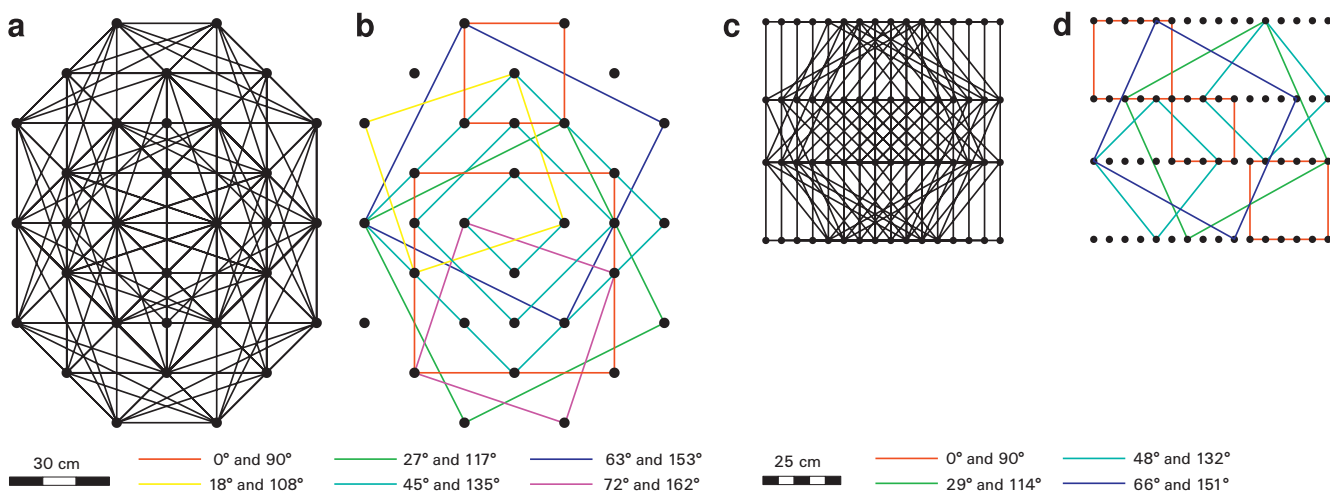


Fig. 6-4: Square array for (a) a set of 32 electrodes on the face (59 squares of various orientations and sizes shown in (b)) and (c) 64 electrodes in the four boreholes of the lower domain (56 squares of various orientations and sizes shown in (d)). The depth of investigation is of the order of size of the side of the square, and the measurement orientation is given by the angle between one side of the square and the horizontal axis.

negative values indicate a strong anisotropy in the upper domain. The paradox of electrical anisotropy contained in the Wenner measurements is confirmed since the apparent resistivity is higher in horizontal profiles than in vertical ones (see Fig. 6-2). The polar diagrams of Fig. 6-5 also show that the direction of highest apparent resistivity turns from the

SW side of the Ga04 face where it makes an angle of about 50° from the vertical, to the NE side where it is close to the vertical. These data, measured according to the square array configuration, were used to recover the tensor of electrical resistivity by an inversion process (see Chapter 6.4).

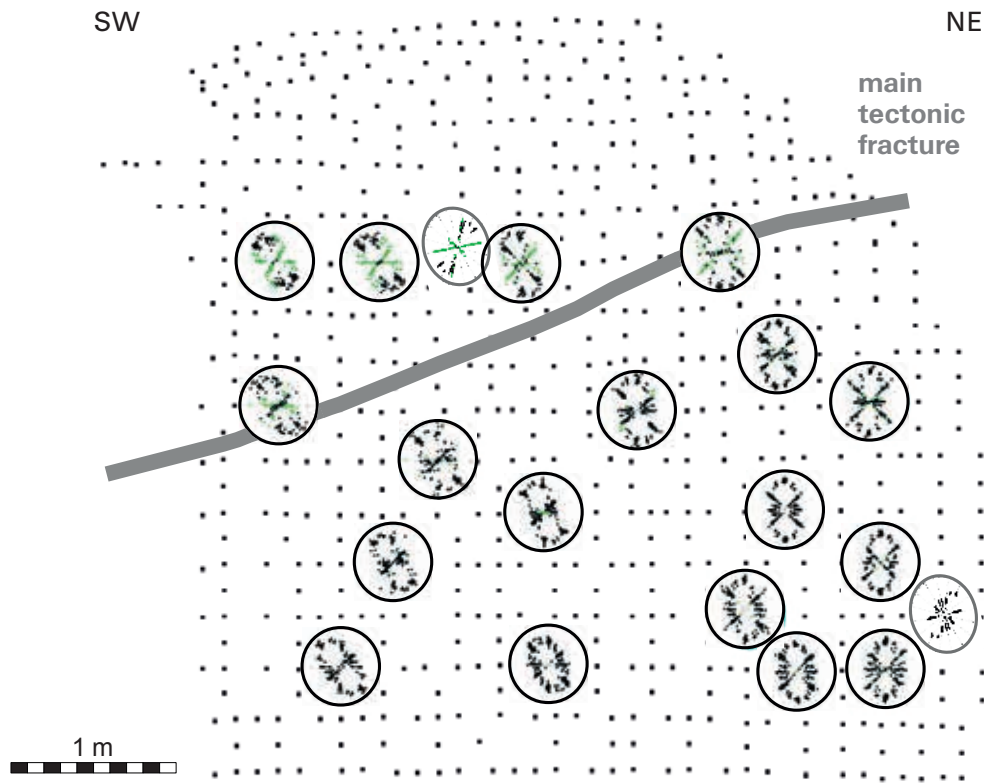


Fig. 6-5: Polar diagrams showing the apparent resistivity measured using the square array configuration, in the 18 areas of the face (diagrams with black border) and in the two areas of four boreholes (diagrams with grey border). The diagram radius represents the resistivity between 0 and 316 $\Omega \cdot m$ using a logarithmic scale. The angle from the horizontal axis of the diagram corresponds to the dip of the AB segment in the local plane. Black dots represent positive values of apparent resistivity, green dots represent negative values of apparent resistivity.

6.3.3 Geo-electrical monitoring in the EZ-G08 segment

In May 2008, we carried out an initial series of measurements in the long boreholes in order to obtain a reference data set when the Ga08 front was far away from the Ga04 face (a few tens of metres). Profiles of 651 Wenner measurements were performed at two depths in each borehole, with lines of 64 electrodes placed either in the nearer part (0–3 m from the Ga04 face) or in the distant part (5–8 m from the Ga04 face). With the lines of electrodes at the same locations, cross-hole measurements were performed using electrodes of two boreholes: the electrical current was injected by two electrodes A and B placed at the same depth each in one borehole, and the electrical potential was measured between 8 pairs of electrodes M and N also located at the same depth in the two boreholes, at ± 5 cm, ± 10 cm, ± 15 cm and ± 20 cm from the current electrodes (Fig. 6-6). With 64 electrodes in each of the two boreholes, 492 measurements were realised, and with four boreholes (BEZ-G12- to G15), we carried out cross-hole measurements in six planes (G12-G13, G12-G14, G12-G15, G13-G14, G13-G15 and G14-G15).

The Wenner profiles performed in May 2008 at the two locations in the four boreholes are shown in Fig. 6-7 as pseudosections of apparent resistivity. Although these representations are surfaces, no directivity is imposed on measurements done in borehole; the apparent resistivity probes the whole volume surrounding the borehole. These measurements are of course characterized by the anisotropy para-

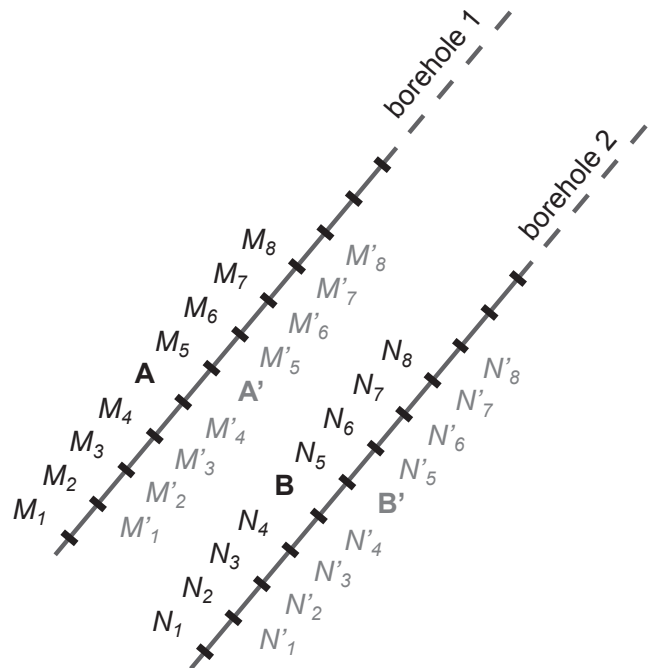


Fig. 6-6: Geometrical setup of electrodes used for cross-hole measurements: 8 pairs of electrodes M and N are used to measure the electrical potential when the current is injected by 2 electrodes A and B, as shown in two examples marked in black and in grey.

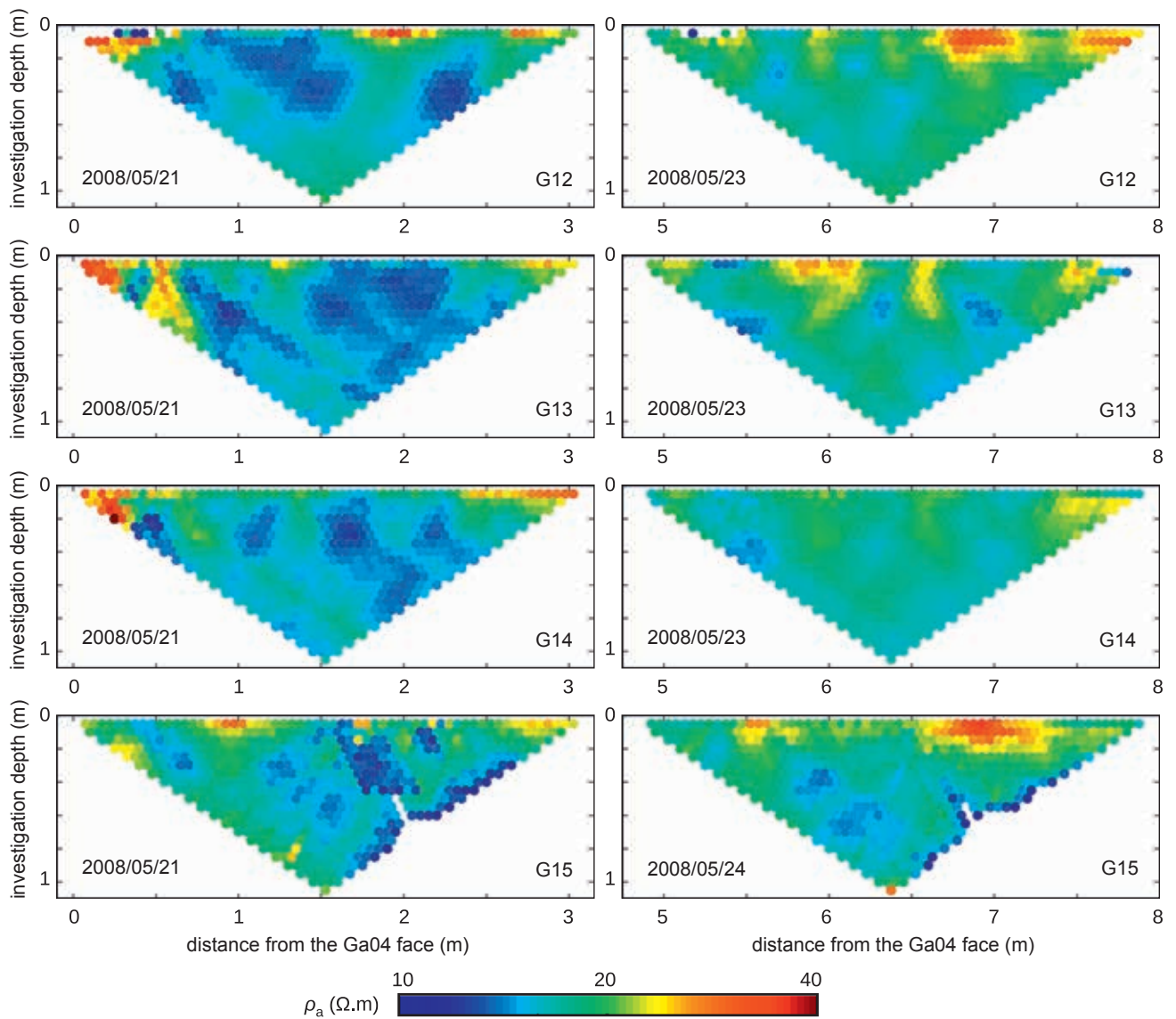


Fig. 6-7: Pseudosections of apparent resistivity measured on Wenner profiles in May 2008, in the near part of the boreholes (left) and in the distant part of the boreholes (right).

dox, but as the boreholes have similar orientations, the profiles must be disturbed in the same way and, therefore, they can be compared. The pseudosections of the apparent resistivity show that the vicinity of the boreholes is locally a zone of higher resistivity, which may indicate the presence of an EDZ around the boreholes (Fig. 6-7). Just behind the Ga04 face, the apparent resistivity is also higher, reflecting the Ga04 EDZ. Farther into the EZ-G08 segment, the resistivity appears lower in the near part (average $\rho_a = 15.4 \pm 1.1 \Omega.m$ between 1 and 3 m from the Ga04 face) than in the distant part (average $\rho_a = 17.6 \pm 1.1 \Omega.m$ between 5 and 8 m from the Ga04 face). This resistivity difference may be related to the lithological facies that passes from the shaly facies (more conductive) to the sandy facies (more resistive) a few metres at the far end of the Ga04 face (see Chap. 3.1).

From July 1 to 24, 2008, we performed Wenner and cross-hole measurements with lines of electrodes placed 5–8 m from the Ga04 face in the four boreholes. From July 24 to August 7, 2008, measurements were performed with lines of

electrodes placed 0–3 m from the Ga04 face. Some electrodes were sometimes poorly connected, causing bad measurements: specifically before July 7 in the G13 borehole, and between July 7 and 9 in the case of the G15 borehole. Every day, we carried out Wenner profile measurements in each borehole and we conducted between 6 and 15 series of cross-hole measurements in the six planes. The whole experiment comprised a total amount of more than one million space-time measurements of electrical resistivity in the EZ-G08 segment.

Comparison of the Wenner profiles measured in May 2008 and in July 2008 shows a global increase in the apparent resistivity, more marked at positions close to the Ga08 front. As an example, Figure 6-8 displays the difference between the apparent resistivity measured in the G14 borehole, in May and that of July 1 in the distant part (5–8 m from the Ga04 face), and in May and in July 24 in the near part (0–3 m from the Ga04 face). Except in the vicinity of the borehole, where the resistivity decreased, and at rear to the Ga04 face,

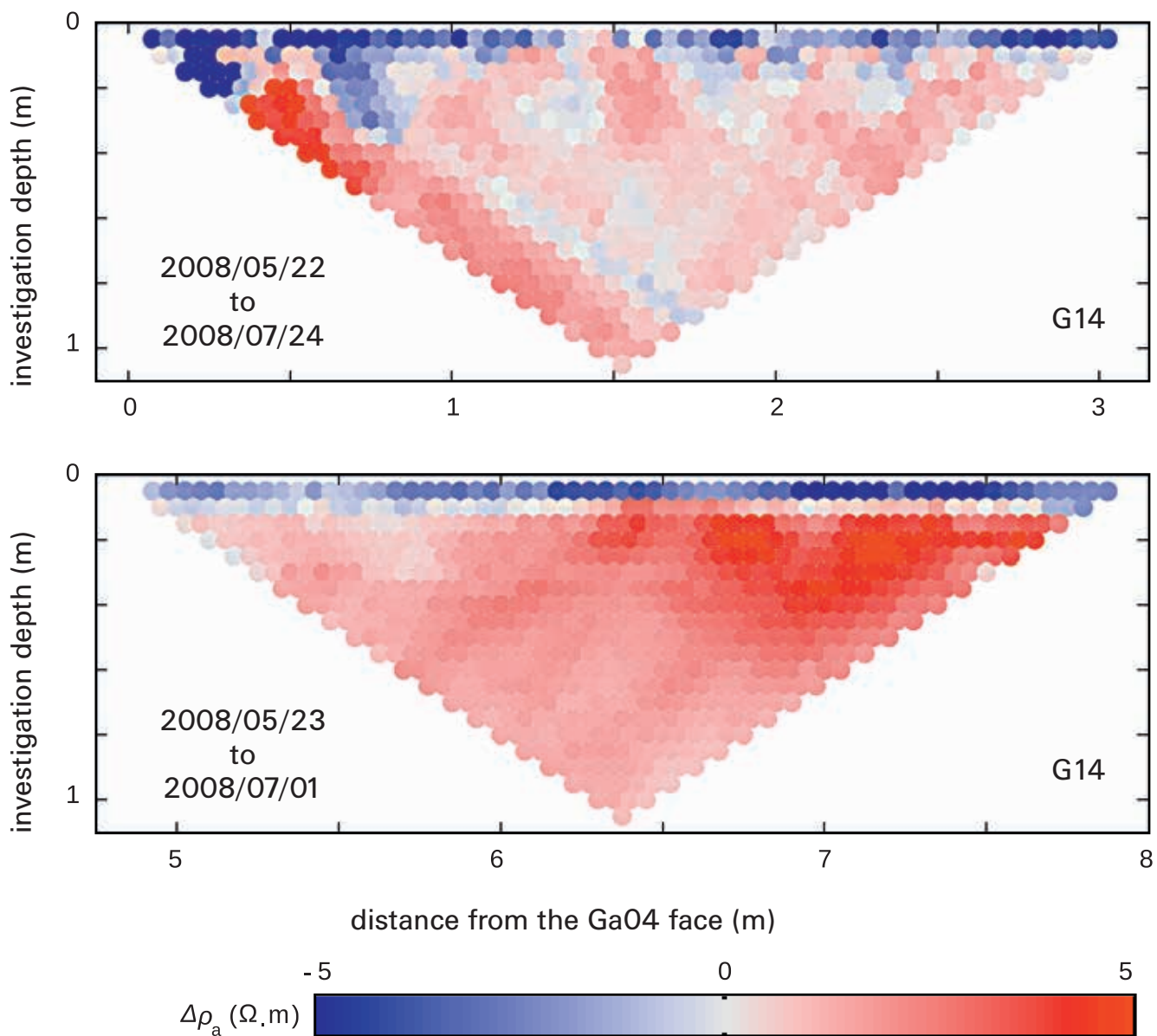


Fig. 6-8: Variations between May and July of the apparent resistivity measured on Wenner profiles in the near part of the G14 borehole (top) and in the distant part (bottom). Red colour denotes an increase in resistivity, blue colour denotes a decrease in resistivity.

where strong variations are positive or negative, the resistivity increased everywhere and even more strongly as the distance to the Ga08 front decreased. This increase in resistivity seems to indicate the development of an EDZ related to the Ga08 excavation.

An example of cross-hole data is presented in Figure 6-9, showing the apparent resistivity measured in the distant position from the July 3 to 24, 2008, between the G12 and G14 boreholes with potential electrodes at 20 cm from the current electrodes. The range of the apparent resistivity values is the same as that of the Wenner profiles, and the presence of higher values close to the Ga08 front is again clear. Concerning the temporal variations, a sharp drop is observed for July 12, when the edge of the EZ-G08 segment was reached. All the spatial and temporal variations will be discussed in Chapter 6.5.

6.4 Inversion of the anisotropy data

This following study was published in the *Geophysical Journal International* in 2010 (NICOLLIN et al. 2010). Here, we present the main steps and the results of the inversion.

We used data measured with the square array configuration on the Ga04 face and in the eight short boreholes to determine a model of anisotropic resistivity by an inversion procedure. This implied forward modelling to calculate synthetic data corresponding to a given resistivity model using the same configuration as the one of the real data. The inverse problem consists in testing numerous models and selecting the one that provides the best fit with the real data. The strategy here adopted is based on a Bayesian approach coupled with a non-linear Monte Carlo method.

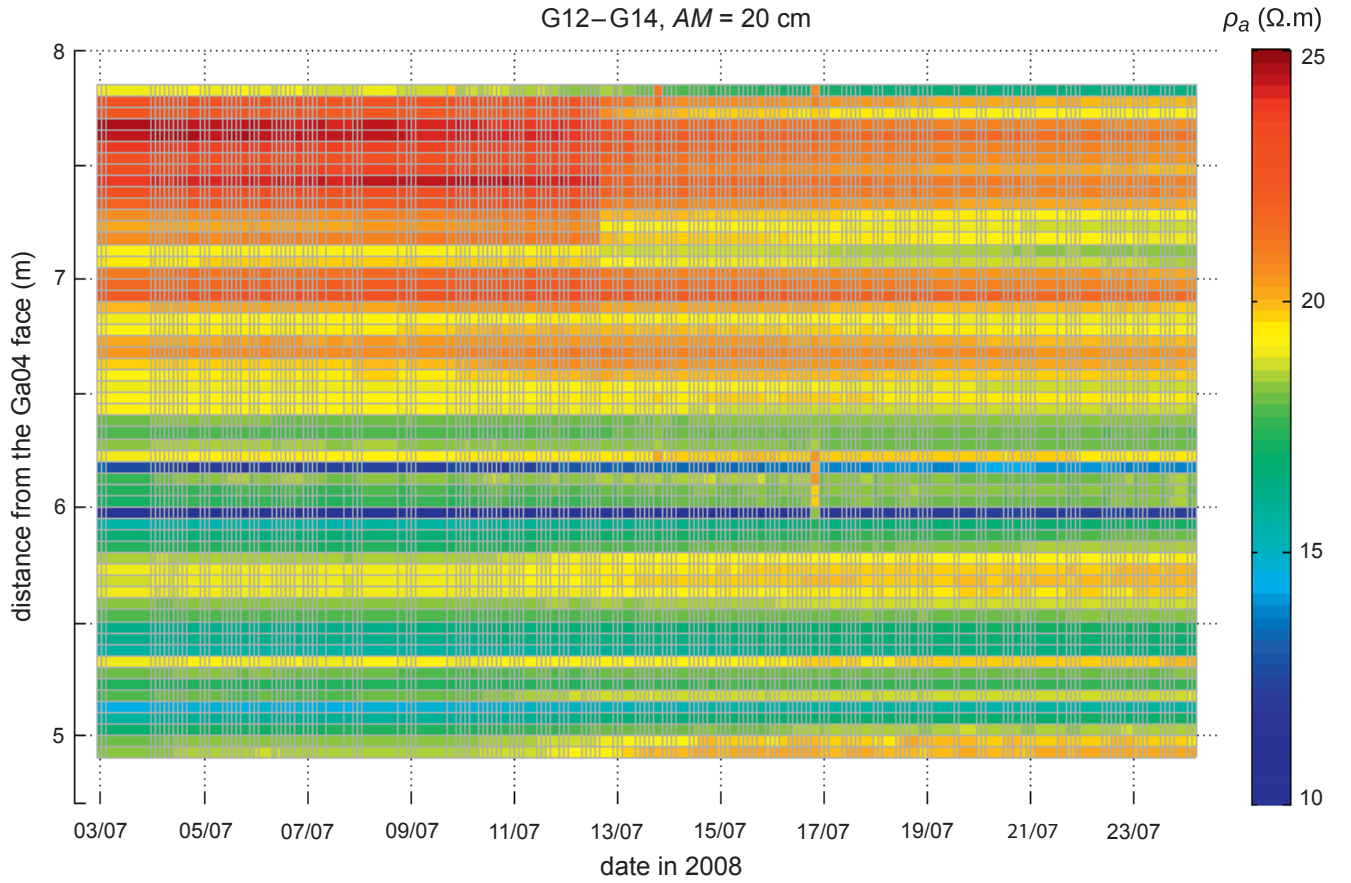


Fig. 6-9: Apparent resistivity obtained from cross-hole measurements in the distant part of the G12 and G14 boreholes between July 3 and 24, 2008.

6.4.1 The forward problem

The forward problem consisted in solving the Ohm's law with suitable boundary conditions. In this study, each area where the anisotropic measurements were done was so small that the Ga04 face could be considered locally as being planar and thus we could adopt a half-space geometry. Furthermore, because of the small amount of data available, we assumed a constant anisotropic resistivity. With these simplifying assumptions, the electrical potential at an electrode \mathbf{r}_e produced by a unit current source point \mathbf{r}_s can be expressed analytically as (DAS & LI 1996):

$$(1) \quad V = \frac{1}{4\pi} \sqrt{\frac{\det \underline{\rho}}{(\mathbf{r}_e - \mathbf{r}_s)' \underline{\rho} (\mathbf{r}_e - \mathbf{r}_s)}}$$

where $\underline{\rho}$ is the electrical resistivity tensor. The boundary condition corresponding to a half-space geometry is imposed by adding the potential produced by an image source (DAS AND LI 1996).

Using its principal values $\{\rho_1, \rho_2, \rho_3\}$, the resistivity tensor reads:

$$(2) \quad \underline{\rho} = R(\theta_x, \mathbf{x}) R(\theta_y, \mathbf{y}) R(\theta_z, \mathbf{z}) \begin{pmatrix} \rho_1 & 0 & 0 \\ 0 & \rho_2 & 0 \\ 0 & 0 & \rho_3 \end{pmatrix}$$

where $R(\theta_a, \mathbf{a})$ is a rotation matrix for angle θ_a and axis \mathbf{a} . Therefore, the angles $\{\theta_x, \theta_y, \theta_z\}$ contain the principal directions $\{Az_1, \varphi_1; Az_2, \varphi_2; Az_3, \varphi_3\}$ of the resistivity tensor, where Az and φ are the azimuth and the dip, respectively.

6.4.2 The inverse problem

The goal of the inverse problem is to recover the resistivity tensor ρ , that is, its six independent components $\{\rho_1, \rho_2, \rho_3, \theta_x, \theta_y, \theta_z\}$ as expressed in Eq. (6.2). This inverse problem is non-linear and, due to the small number of parameters, a fully non-linear method like simulated annealing is both quick and efficient (METROPOLIS et al. 1953, KIRKPATRICK et al. 1983, BHANOT 1988). This modelling method also allows us to avoid local sub-optimal solutions and to perform a Bayesian inversion of the data. The principle of the method, the implementation of simulated annealing for this particular inverse problem, and its performances are illustrated on synthetic examples detailed in NICOLLIN et al. 2010. At the end of the inversion, the parameters $\{\theta_x, \theta_y, \theta_z\}$ of the retained model are converted into principal directions $\{Az_1, \varphi_1; Az_2, \varphi_2; Az_3, \varphi_3\}$ of the resistivity tensor.

6.4.3 Results

The 18 data sets measured with the square array configuration on the Ga04 face were inverted independently. Data measured in the group of boreholes located below the main fracture (BEZ-G22 to G25) were used to constrain the inversion of the 13 data sets measured in the lower domain; data measured in the group of boreholes located above the main fracture (BEZ-G26 to G29) were used to constrain the inversion of the five data sets measured in the upper domain.

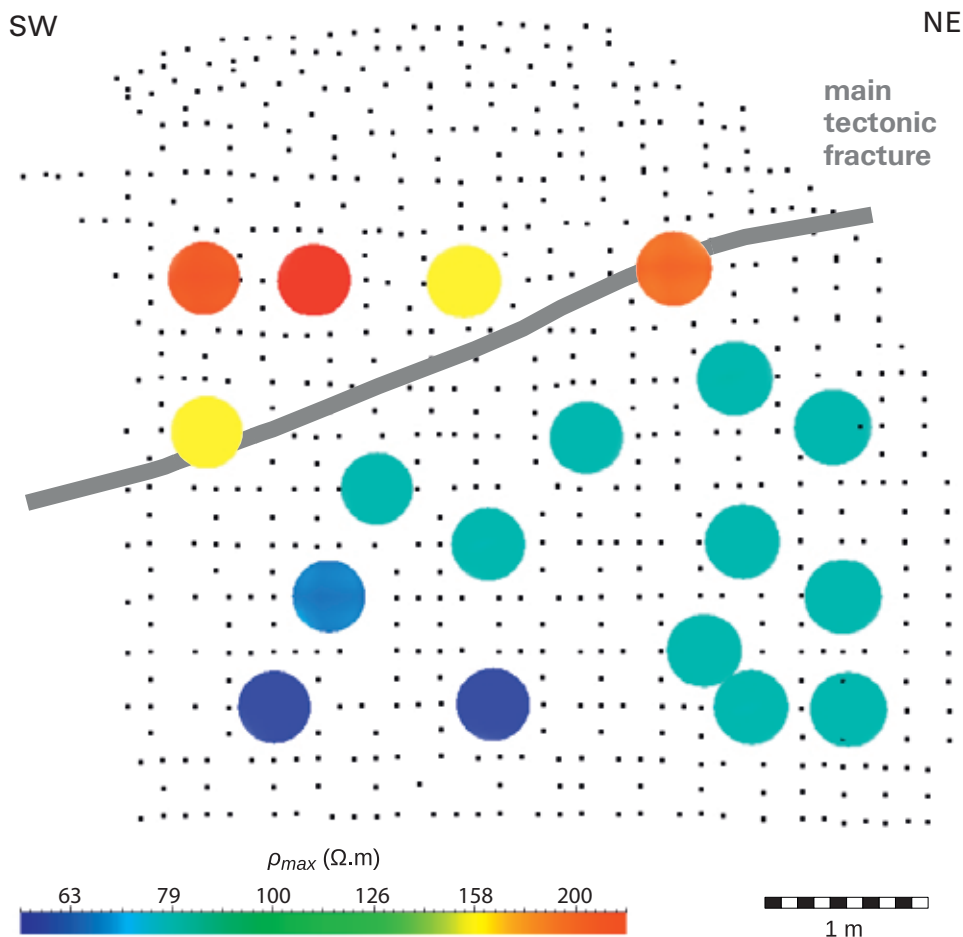


Fig. 6-10: Maximum value of the resistivity tensor found by inversion in the 18 areas of the Ga04 face.

The values found by inversion are summarized in Table 6-1, mean and standard deviation were computed for results corresponding to three zones: the upper domain located above the main fracture (five data sets), the SW half of the lower domain (six data sets), and the NE half of the lower domain (seven data sets).

The inversion results confirmed a strong anisotropy of electrical resistivity behind the Ga04 face. The maximum value ρ_1 of the resistivity tensor is 2 to 7 times greater than the intermediate value ρ_2 , which is 2 to 4 times greater than the minimum value ρ_3 . Also, we note that although the intermediate and minimum values are rather constant in the whole area ($\rho_2 = 26.5 \pm 7.3 \Omega.m$ and $\rho_3 = 8.5 \pm 2 \Omega.m$), the maximum value differs significantly between the upper domain ($\rho_1 = 200.1 \pm 37.1 \Omega.m$ for the subset A) and the lower domain ($\rho_1 = 73.6 \pm 14.5 \Omega.m$ for the whole subsets B and C). The maximum values of resistivity are displayed in Fig. 6-10, located on the Ga04 face, at the place of the 18 areas of measurement. The main fracture clearly separates two domains: an upper domain characterised by high resistivity values and a lower domain characterised by low resistivity values.

Tab. 6-1: Results of inversion of the 18 data sets measured on the Ga04 face, divided into three subsets: subset A above the tectonic fracture (five data sets), subset B in the SW half below the tectonic fracture (six data sets), subset C in the NE half be-

low the tectonic fracture (seven data sets). A direction indicated with a negative dip at a given azimuth is equivalent to the direction of opposite dip at the azimuth $\pm 180^\circ$.

	A		B		C	
	mean	SD	mean	SD	mean	SD
ρ_1 ($\Omega.m$)	200.1	37.2	66.0	17.2	80.1	8.2
ρ_2 ($\Omega.m$)	28.6	12.0	28.0	5.0	23.6	4.4
ρ_3 ($\Omega.m$)	6.7	2.8	8.3	1.0	9.9	0.5
Az_1 ($^\circ N$)	321.7	5.3	316.4	5.7	324.0	4.0
Az_2 ($^\circ N$)	142.8	11.1	88.1	16.9	139.0	19.2
Az_3 ($^\circ N$)	234.9	6.4	207.0	12.8	232.9	7.0
φ_1 ($^\circ$)	37.2	7.4	32.9	4.3	30.9	3.9
φ_2 ($^\circ$)	53.4	7.5	44.8	7.7	58.0	3.2
φ_3 ($^\circ$)	-0.1	5.8	26.5	7.8	2.2	8.1

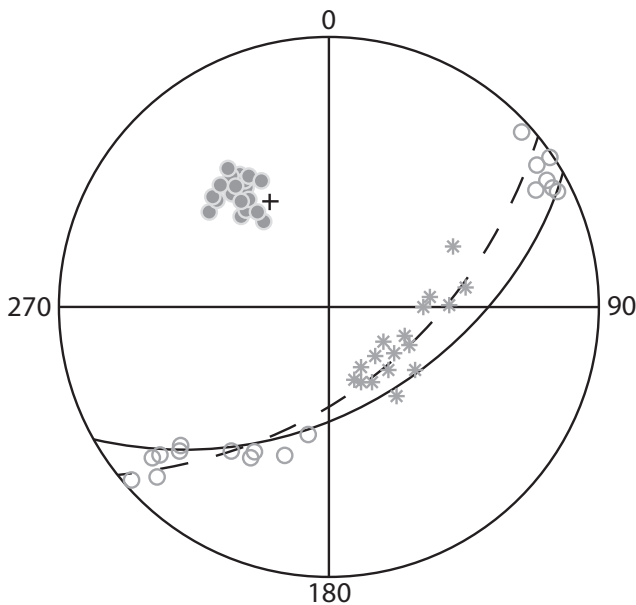


Fig. 6-11: Wulff stereographic projection (lower hemisphere) showing the results of the inversion of the 18 data sets of the Ga04 face. The maximum value of resistivity is plotted with a filled circle, the minimum value of resistivity is plotted with an empty circle, and the intermediate value of resistivity is plotted as a star. The plane N51-57°SE, normal to the direction of the mean value of maximum resistivity, is represented as a dashed line. The bedding plane (N60-48°SE) is represented as a black line and its normal with a black cross.

The principal directions of the resistivity tensor found by inversion of the 18 data sets are plotted in a stereographic diagram, using the Wulff projection of the lower hemisphere where the angle are preserved, the azimuth being read on the perimeter and the dip on the radius from the edge (Fig. 6-11). This diagram and Table 6-1 show that the direction of the maximum resistivity is very concentrated around its mean value over the whole area ($Az1 = 320.8^\circ N \pm 5.8^\circ$, $\phi1 = 33.3 \pm 5.5^\circ$), close to the normal to the bedding plane N60-48°SE. Consequently, the directions of the intermediate and minimum values of resistivity are contained in a plane close to the bedding plane. They spread according to the curved shape of the Ga04 face, the direction of the minimum value making an almost right angle ($87 \pm 16^\circ$) with the normal to the local plane defined by the 32 electrodes of each area. Thus, the direction of minimum resistivity is contained in the plane of the face and the intermediate resistivity component is perpendicular to the face.

6.4.4 Discussion

The geometrical characteristics of the resistivity tensor appear to be controlled by both the stratigraphy and the geometry of the gallery which, in turn, determines the spatial organisation of the stress perturbations in the rock mass. Owing to both the mineralogical structure and the stratigraphic characteristics of Opalinus Clay, the resistivity tensor should be approximately transversely isotropic with respect to the normal to the bedding plane. The deviation from transverse isotropy ($\rho2 \neq \rho3$) may be explained by the superimposition of a secondary anisotropy produced by the

presence of EDZ unloading microfractures oriented parallel to the gallery end-face. The existence of these microfractures may be due to both stress redistribution and desaturation.

That the maximum resistivity is higher in the upper domain may be explained by a greater desaturation. This desaturation could occur mainly along the bedding planes, reducing electrical contact between adjacent planes and increasing resistivity in the perpendicular direction. In contrast, we observed wet spots and water outflows from three boreholes drilled in the lower domain. This humidity has certainly contributed to eliminating any desaturation in this rock mass and hence maintaining the electrical contact between the beds.

6.5 Monitoring in the EZ-G08 segment

In July 2008 we performed electrical monitoring of the EZ-G08 segment when the excavation of Gallery 08 was approaching using boreholes measurements described in Chapter 6.3.3.

6.5.1 Orientation of the boreholes

The four boreholes G12 to G15 had a similar orientation, all were horizontal with an azimuth around $138^\circ N$ ($139^\circ N$ for G12, $141^\circ N$ for G13, $137^\circ N$ for G14 and $135^\circ N$ for G15). The mean azimuth was $318^\circ N$, that is close to the mean azimuth of the direction of maximum resistivity $\rho1$ found in section 6.4.3 ($Az1 \approx 321^\circ N$). Considering the average dip of this direction ($\phi1 \approx 33^\circ$), the orientation of the horizontal boreholes was between the direction of $\rho1$ and the orthogonal plane that contains the directions of $\rho2$ and $\rho3$. The spatial organisation of this information is shown in a stereographic diagram, also with the six planes of cross-hole measurements containing the direction of current injection (Fig. 6-12). This current injection direction was often within or very close to the plane normal to the $\rho1$ direction, the difference in orientation ranging from a minimum divergence of a few degrees (G13-G14 measurements contained in the bedding plane) to a maximum divergence of about 30° (G14-G15 measurements).

6.5.2 Wenner profiles

As the four boreholes all had the same orientation, the Wenner measurements were affected by anisotropy in the same way. Beyond the first m from the Ga04 face, the resistivity tensor in Opalinus Clay is probably transverse isotropic with $\rho2 = \rho3$ in the whole plane perpendicular to $\rho1$. Hence, Wenner measurements in the boreholes were performed along a direction intermediate between the directions of maximum and minimum resistivity (Fig. 6-12).

To visualize both spatial and temporal variations of apparent resistivity, we computed the difference between data acquired during consecutive days. The results are presented in Figure 6-13 as pseudosections of differences for measurements in the distant part of the G12 borehole between July 1

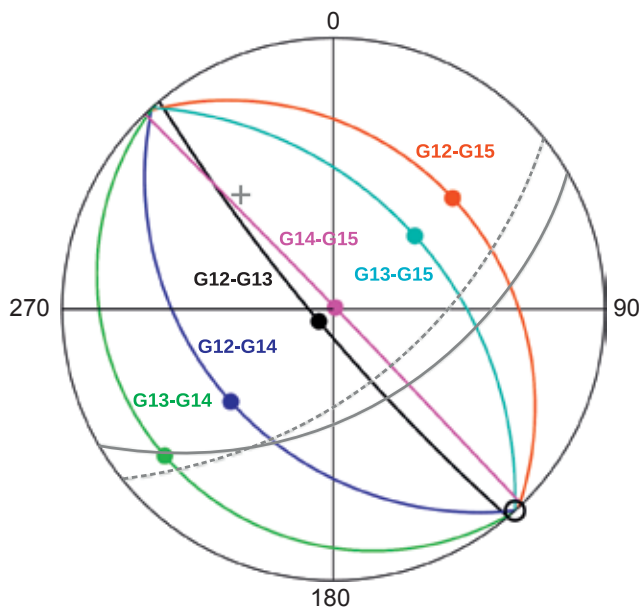


Fig. 6-12: Wulff stereographic projection (lower hemisphere) showing the spatial organisation of the borehole measurements. The direction N138-0° of the four boreholes is represented with a black empty circle; the cross-hole planes are represented with coloured lines each containing the current injection direction represented with a filled circle; the bedding plane is represented with a grey line; the mean direction of maximum resistivity is represented with a grey cross and its normal plane is represented with a grey dashed line.

and 21, and in Figure 6-14 for measurements in the near part of the G12 borehole between July 25 August 6. Except for noise present in the vicinity of the borehole and in the first m from the Ga04 face, the highest differences are not localized in any particular zone. They are \pm a few tenths of an $\Omega.m$ compared to a mean apparent resistivity of 15 to 20 $\Omega.m$, and they occur mainly in measurements obtained before July 4, between July 9 and 12, and between August 3 and 6. The two last periods correspond to the dates when excavation of Ga08 was reaching the portion equipped with the lines of electrodes, first in the distant part, then later in the near part of the boreholes. These alternate positive and negative variations may reflect pore water displacements caused by de-compression in the boreholes connected to the new gallery. On the other hand, we did not observe any significant variation in resistivity during the pause in excavation between July 12 and 29 beyond the first behind the Ga04 face.

In order to evaluate its temporal evolution, we averaged the apparent resistivity over each daily Wenner profile, except in the vicinity of 10 cm around the boreholes, and in the first m behind the Ga04 face, where data were often noisy. The curves of these mean values computed for the measurements in the four boreholes have similar trends (Fig. 6-15). As in May (Chap. 6.3.3 and Fig. 6-7), the apparent resistivity was always lower in the near part compared to the distant part, reflecting changes in lithological facies. The global discrepancy between the four curves may be related to slightly different electrode coupling from one borehole to the other. After a global increase of 1 to 2 $\Omega.m$ between May and July (Fig. 6-8), the mean apparent resistivity slowly increased until July 12 and then stabilized (G14) or decreased slowly (G12, G13 and G15) during the first period (Fig. 6-15, top). We observed a sudden drop with high intensity on July 11 on the

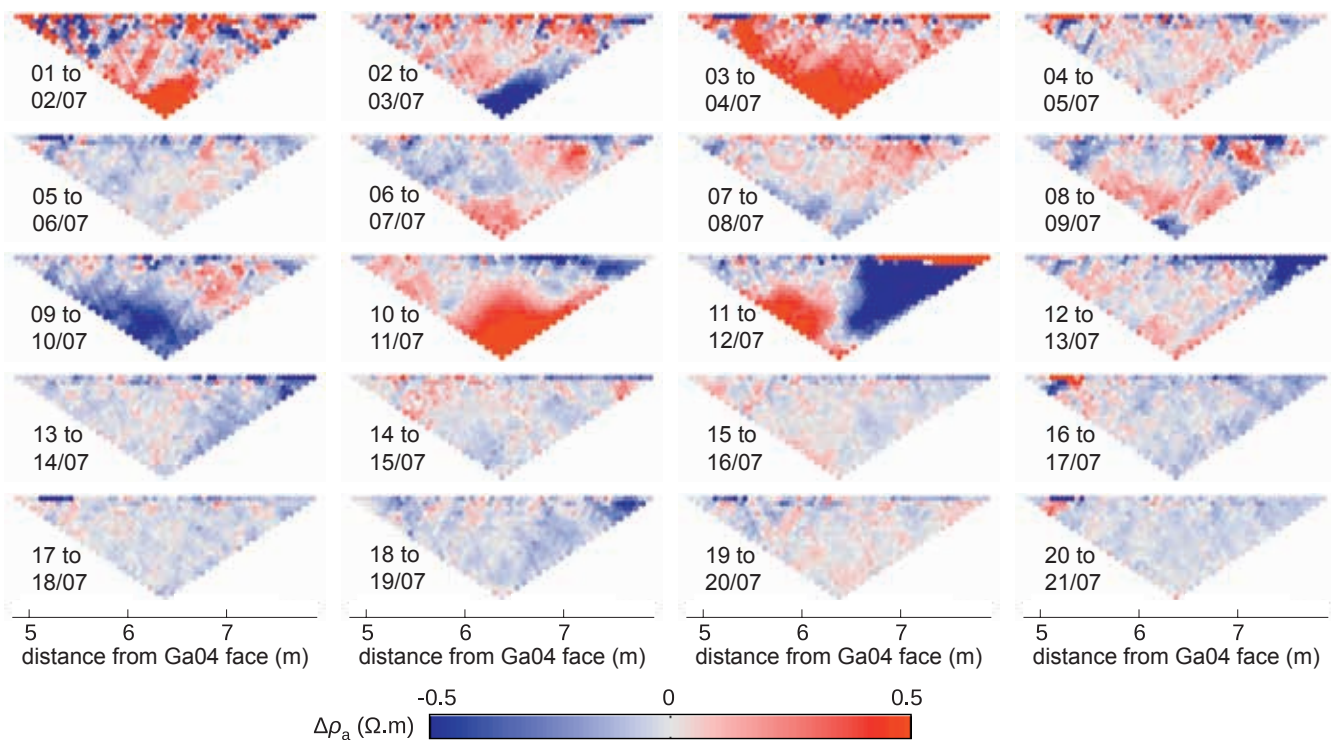


Fig. 6-13: Variations of apparent resistivity between consecutive days during the first period, measured on a Wenner profile in the distant part of the G12 borehole. Red color denotes an increase in resistivity, blue color denotes a decrease in resistivity.

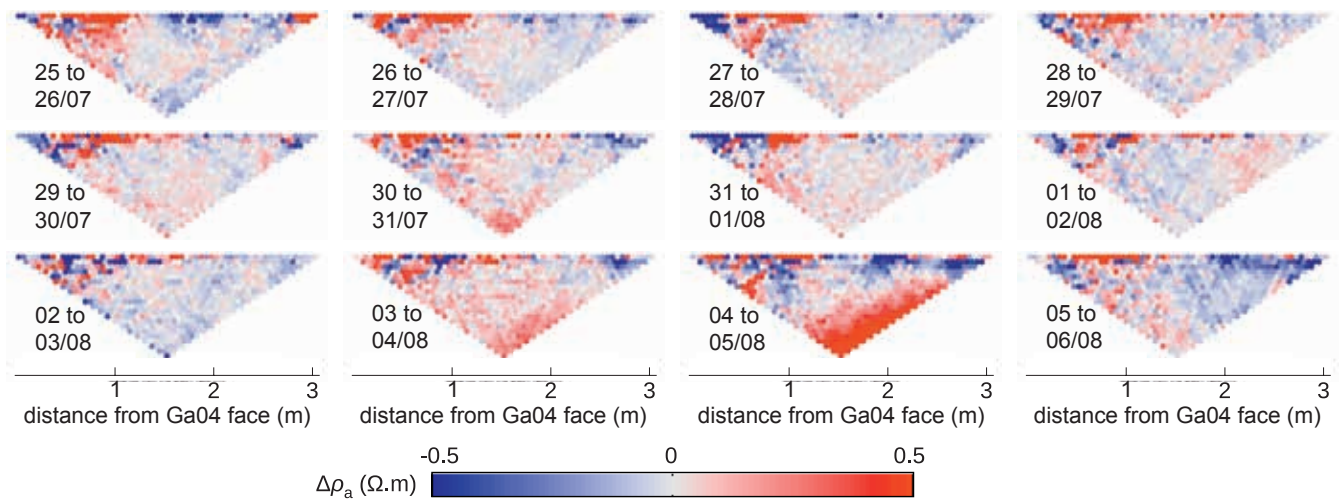


Fig. 6-14: Variations of apparent resistivity between consecutive days during the second period, measured on a Wenner profile in the near part of the G12 borehole. Red color denotes an increase in resistivity, blue color denotes a decrease in resistivity.

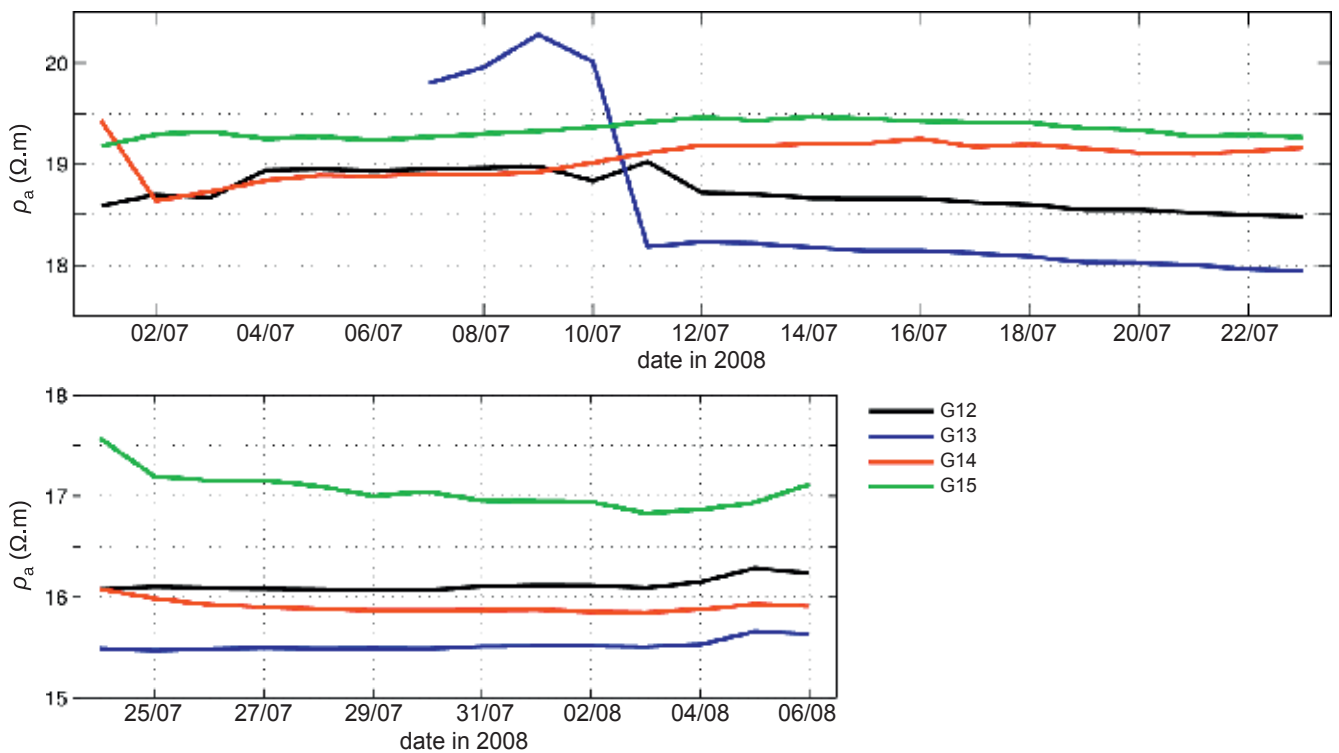


Fig. 6-15: Mean apparent resistivity measured on Wenner profiles, in the distant part of the boreholes (5–8 m from the Ga04 face) during the first period (top), and in the near part of the boreholes (1–3 m from the Ga04 face) during the second period (bottom).

blue curve (G13), and then with less intensity on July 12 on the black curve (G12). This occurred when the end of the corresponding borehole was reached by the Ga08 excavation front (see Chap. 6.5.5). During the second period, the mean apparent resistivity did not vary (G12, G13 and G14) or decreased slowly (G15), before a slight increase from August 3 onwards (Fig. 6-15 bottom). The increase in mean apparent resistivity, observed during the periods preceding the arrival of the excavation front at the extremity of the portion equipped with the lines of electrodes, seems to reveal damages in the EZ-G08 segment caused by the last steps of the Ga08 excavation.

6.5.3 Cross-hole measurements

In contrast to the Wenner measurements, the cross-hole measurements are free of the anisotropy paradox because they use a nearly square array configuration of electrodes. As described in Chapter 6.3.3, the measurements were made using four spacings from 5 to 20 cm, between the current (A or B) and potential (M or N) electrodes. Those made with the shortest spacing exhibited more noise and often disagree with values from the three other series that show similar trends (Fig. 6-16). The curves plotted on this graph represent the apparent resistivity averaged over 3 m in the distant part

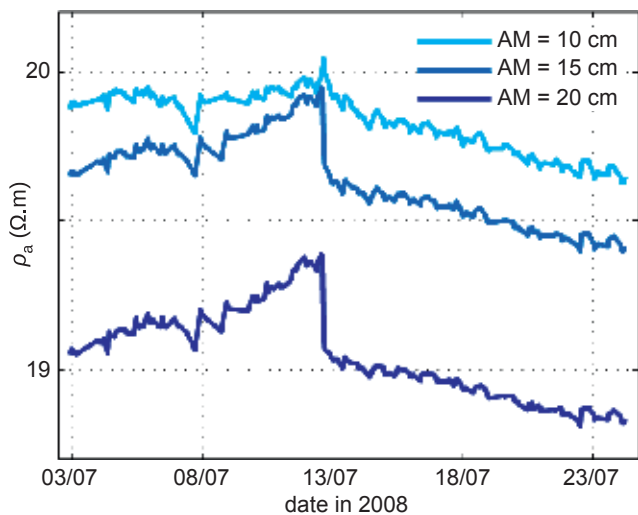


Fig. 6-16: Cross-hole measurements made with three spacings between the current and potential electrodes: the apparent resistivity is averaged over the length of the lines placed in the distant part (5–8 m from the Ga04 face) of the G12 and G14 boreholes.

of the G12 and G14 boreholes. Thus, the dark blue curve (AM=20 cm) corresponds to the spatial mean of the data shown in Figure 6-9.

The remarkable similarity between the three curves of Fig. 6-16 proves the data quality, and the shift of a few tenths of $\Omega.m$ can be explained by how to calculate the apparent resistivity. The computation is performed as if the electrodes were embedded in a rock volume without boreholes. However, the electrodes were coupled to the walls of boreholes 5.6 cm in diameter, increasing the apparent resistivity even more strongly that the AM spacing is short. But the spatial and temporal variations are independent of the electrode spacing, and results obtained with the largest spacing are shown in next sections.

6.5.4 Spatial variations

In order to visualize the spatial variations of apparent resistivity, temporal means are computed over the whole period of measurement for each of the two positions of electrode lines: between July 3 and 24 for the distant part (mean of 196 to 266 series depending on the pair of boreholes), and between July 24 and August 7 for the near part (mean of 185 series for the six pairs of boreholes). The resulting curves of 55 values represent the spatial variations between 0.25 and 2.95 m from the Ga04 face and between 5.05 and 7.75 m from the Ga04 face (Fig. 6-17).

The six curves shown in Figure 6-17 vary in the same apparent resistivity range, confirming the similar orientation of the cross-hole measurements with respect to the direction of maximum resistivity (Fig. 6-12). Moreover, the lowest values are often observed in the G13–G14 plane and the highest values often in the G14–G15 plane. This agrees with the variation of the angle between the directions of current injection and maximum resistivity, from about 90° for G13–G14 to about 60° for G14–G15 (see Chap. 6.5.1).

The general shape of the six curves is similar and may be divided into five parts:

- a global decrease of nearly $5 \Omega.m$ in the first 1.6 m at rear to the Ga04 face but with rather large and inconsistent positive or negative variations,
- an increase of about $4 \Omega.m$ between 1.6 and 3 m,
- values of the same order of magnitude at 3 and 5 m,
- an increase of nearly $4 \Omega.m$ between 5 and 8 m from the Ga04 face,
- a portion with larger and more inconsistent variations between 5.8 and 6.8 m.

We note that all these observations are in good agreement with the images provided by the Wenner profiles (Fig. 6-7, 6-8). The five parts described above may be explained by:

- presence of a Ga04 EDZ in the shaly facies, with even more dense microfractures where the distance to the Ga04 face is less,
- transition of the shaly facies more conductive to the sandy facies more resistive a few m at rear to the Ga04 face,
- identical sandy facies with little damage at the end of the near part and at the beginning of the distant part, (there is no data available in the intermediate zone to confirm this hypothesis),
- presence of a Ga08 EDZ in the sandy facies with even more dense microfractures where the distance to the Ga08 front is less,
- presence of tectonic faults N60-48°SE and an occurrence of more sandy beds observed in this zone (Chap. 3.1).

6.5.5 Temporal variations

In order to study temporal variations of apparent resistivity, spatial means were computed over 1 m in three zones of the EZ-G08 segment: between 7 and 8 m and between 5 and 6 m from the Ga04 face during the period July 3 to 24, and between 2 and 3 m from the Ga04 face during the period July 4 to August 7 (Fig. 6-18). In each of these three zones, the six curves display similar variations with the lowest values often in the G13–G14 plane and the highest values often in the G14–G15 plane, as noted in the previous chapter.

At the extremity of the Ga08 segment between 7 and 8 m from the Ga04 face, the six curves of apparent resistivity evidence two periods: a first period with a slow increase of a few tenths of $\Omega.m$ until July 11, followed by a period with a slow decrease of nearly $1 \Omega.m$ until July 24 (Fig. 6-18 top). At the border between the two periods, we see sudden drops; one of more than $2 \Omega.m$ in the middle of July 11 for the measurements involving the G13 borehole (G12–G13, G13–G14 and G13–G15), and another of about $1 \Omega.m$ in the middle of July 12 for the measurements involving the G12 borehole (G12–G13, G12–G14 and G12–G15). Only the G14–G15 curve does not present such a discontinuity.

Inside the EZ-G08 segment between 5 and 6 m from the Ga04 face, the six curves display an increase in apparent resistivity during the whole period July 3 to 24 (Fig. 6-18 middle). This increase is slow until July 10 (about $0.1 \Omega.m$), then it accelerates between July 10 and 16 (nearly $1 \Omega.m$), and it

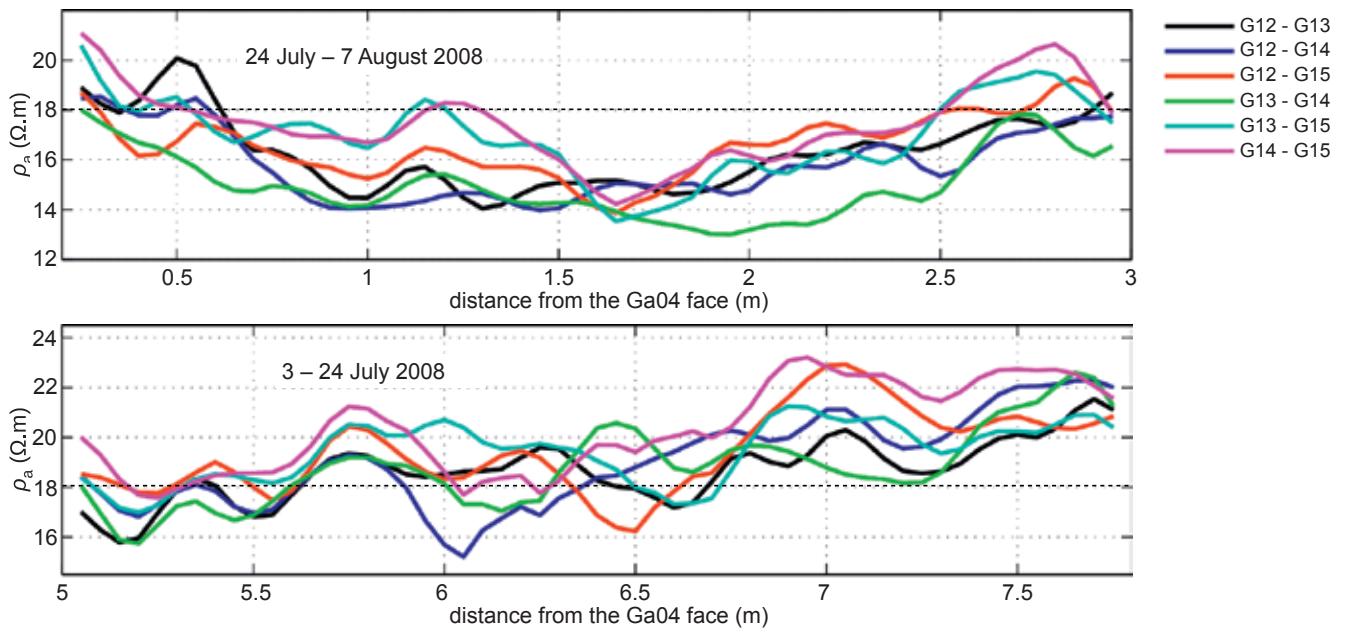


Fig. 6-17: Mean apparent resistivity averaged over the two periods of cross-hole measurement for the six pairs of boreholes: between July 3 and 24 in the distant part (bottom) and between July 24 and August 7 in the near part (top).

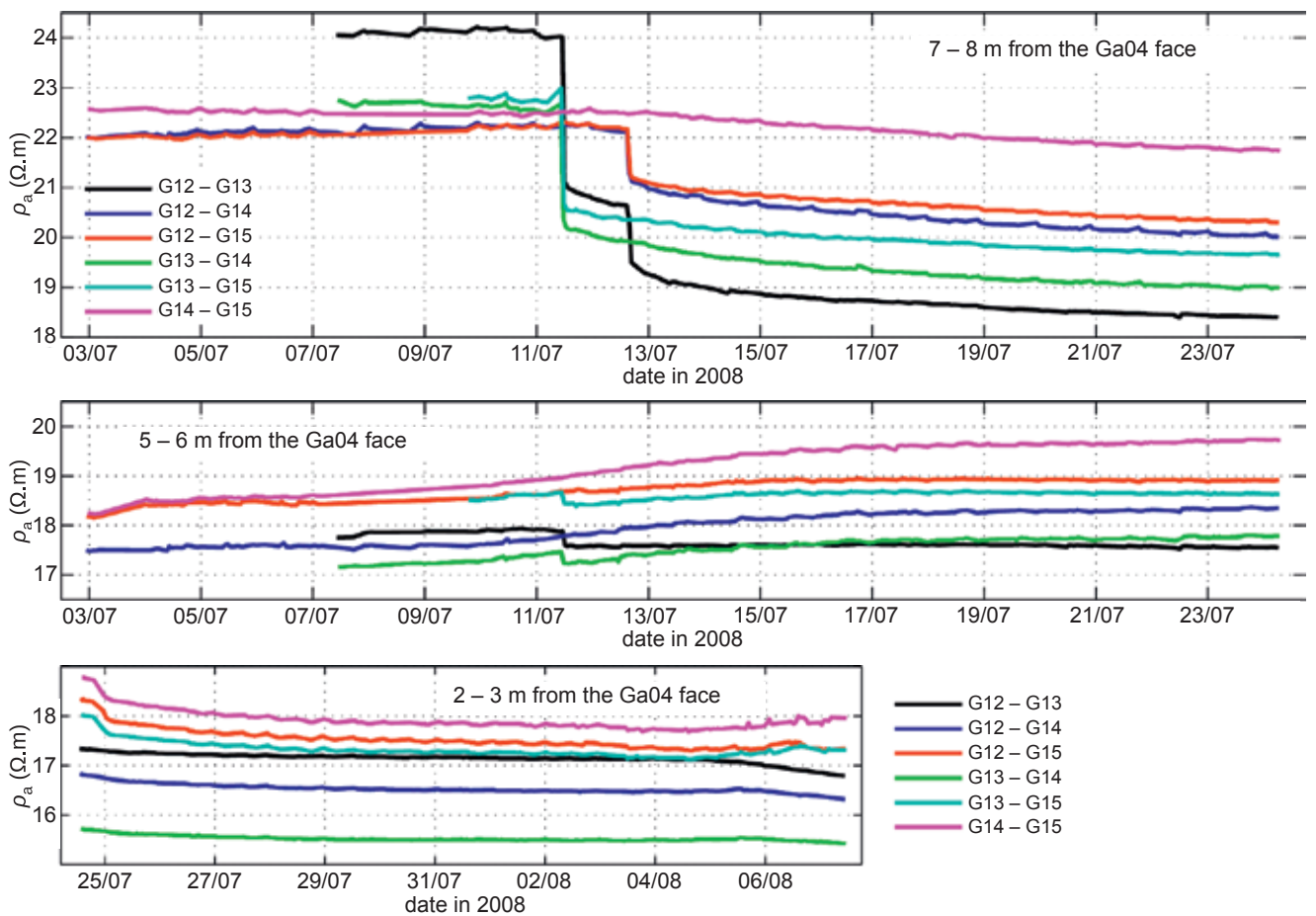


Fig. 6-18: Mean apparent resistivity averaged over 1 m in three zones of cross-hole measurement for the six pairs of boreholes: between 7 and 8 m from the Ga04 face during the period July 3 to 24 (top), between 5 and 6 m from the Ga04 face during the period July 3 to 24 (middle) and between 2 and 3 m from the Ga04 face during the period July 24 to August 7 (bottom).



Fig. 6-19: Views of the Ga08 front at GM 159: the end of BEZ-G13 was opened July 11 when the upper part of the gallery was excavated (left photo, 11/07/2008 evening), the end of BEZ-G12 was opened July 12 when the lower part of the gallery was excavated (right photo, 14/07/2008 evening).

slows until July 24 (0.1 to $0.2 \Omega.m$). In the middle of July 11, the three curves of the measurements involving the G13 borehole show a sudden drop of about $0.3 \Omega.m$ that interrupts the regular increase.

Inside the EZ-G08 segment between 2 and 3 m from the Ga04 face, the six curves do not show significant variations of apparent resistivity between July 24 and August 7, except in the beginning of the period with a decrease for the measurements involving the G15 borehole (G12–G15, G13–G15 and G14–G15), and at the end of the period with a slight increase for the same measurements and a slight decrease for the three other series (Fig. 6-18 bottom).

To explain the temporal variations of apparent resistivity we must look at the schedule of the Ga08 excavation in detail. Indeed, point GM 159, located 8 m from the Ga04 face, was reached in two days: on July 11 for the upper part where the end of the G13 borehole was opened (Fig. 6-19 left), and on July 12 for the lower part where the end of the G12 borehole was opened (Fig. 6-19 right). Significant amounts of water came out of the boreholes when opened, as evidenced by the humidity traces visible on the photos of the Ga08 front. Thus, G12 and G13 boreholes were purged when the excavation stopped at GM 159, but not G14 and G15, which were opened only on July 29 when the excavation restarted.

The sharp discontinuity that we observed on some curves occurred when one borehole of a pair was opened: on July 11 for BEZ-G13 (curves G12–G13, G13–G14 and G13–G15 on Fig. 6-18 top and middle) and on July 12 for BEZ-G12 (curves G12–G13, G12–G14 and G12–G15 on Fig. 6-18 top). Thus, the drop in apparent resistivity may be explained by the sudden presence of water along the electrode lines due to opening of boreholes that mobilized pore water by suction effects due to decompression.

The slow increase in apparent resistivity observed on the temporal curves may be attributed to the opening of microfractures due to the Ga08 excavation. The increase observed during the whole period of measurement inside the EZ-G08 segment at 5–6 m from the Ga04 face suggests that damage would have continued after cessation of excavation, but less intensely after a few days (Fig. 6-18 middle). At the extremity of the EZ-G08 segment, damage could also have continued after cessation of excavation, but there it would have been masked by an increase in water content that could explain the decrease in apparent resistivity (Fig. 6-18 top). In this EDZ close to the Ga08 front, suction processes would be favoured by a high hydraulic gradient caused by the excavation.

6.6 Conclusion

The geoelectrical experiments performed in the EZ-G08 segment show that resistivity is a useful parameter to characterize and monitor the EDZ. The inversion of data devoted to the study of anisotropy yielded a resistivity tensor whose geometry in Opalinus Clay appears controlled by both the stratigraphy and the presence of an EDZ at rear of a gallery. All the data acquired from boreholes for monitoring the EZ-G08 segment during the last steps of the Ga08 excavation are very consistent and reflect:

- a transition of shaly facies to sandy facies a few metres at rear to the Ga04 face,
- an old Ga04 EDZ,
- a new EDZ caused by the Ga08 excavation, with changes observed even after cessation of excavation up to several m behind the Ga08 front,
- displacements of pore water by suction effects due to de-compression.

References

- BARKER, R. D. (1989): Depth of investigation of collinear symmetrical four-electrodes arrays. – *Geophys.* *54*, 1031–1037.
- BHANOT, G. (1988): The metropolis algorithm. – *Rep. Prog. Phys.* *51*, 429–457.
- DAS, U. C. & LI, P. (1996): Analytical solution for direct current electrical potentials in an arbitrarily anisotropic half-space. – *J. appl. Geophys.* *35*, 63–67.
- EDWARDS, L. S. (1977): A modified pseudosection for resistivity and induced polarization. – *Geophys.* *42*, 1020–1036.
- HABBERJAM, G. M. (1972): The effects of anisotropy on square array resistivity measurements. – *Geophys. Prospect.* *20*, 249–266.
- KIRKPATRICK, S., GELATT, C. D. & VECCHI, M. P. (1983): Optimization by simulated annealing. – *Science* *220*, 671–680.
- KUNZ, K. S. & MORAN, J. H. (1958): Some effects of formation anisotropy on resistivity measurements in boreholes. – *Geophys.* *23*, 770–794.
- METROPOLIS, N., ROSENBLUTH, A., ROSENBLUTH, N., TELLER, A. & TELLER, E. (1953): Equation of the state calculations by fast computing machines. – *J. Chem. Phys.* *21*, 1087–1092.
- NICOLLIN, F., GIBERT, D., LESPARRE, N. & NUSSBAUM, C. (2010): Anisotropy of electrical conductivity of the excavation damaged zone in the Mont Terri Underground Rock Laboratory. – *Geophys. J. int.* *181*, 303–320. DOI 10.1111/j.1365-246X.2010.04517.x.
- SENOS MATIAS, M. J. (2002): Square array anisotropy measurements and resistivity sounding interpretation. – *J. appl. Geophys.* *49*, 185–194.

7. A noble gas study in the Excavation Damaged Zone

B. THOMAS, B. LAVIELLE, A. MAINEULT, C. NUSSBAUM & E. GILABERT

7.1 Introduction

Noble gases are particularly suitable for studying gas transport processes in rocks and the existence of connected fracture networks since they do not react with constituents of the host media (e.g., STUTE et al. 1995, ZUBER et al. 1997, OSENBRÜCK et al. 1998, RÜBEL et al. 2002). In claystones, radiogenic ^4He atoms are produced by alpha decay of thorium and uranium. They are released from the host mineral by recoil during production and then diffuse through damages created in the minerals by energetic alpha particles (TORGERSEN & CLARKE 1980; ANDREWS 1985; SOLOMON et al. 1996). They accumulate in pore water as a function of the transfer rate between rock and water, and of the diffusive process occurring since the formation time of the rock (OSENBRÜCK et al. 1998). Depletion in He can be observed in the EDZ. Other noble gases (Neon, Argon, Krypton and Xenon) trapped in the claystones (PODOSECK et al. 1981) have essentially an atmospheric origin except ^{40}Ar , which is produced *in situ* by decay of radioactive potassium ^{40}K . Their content can consequently increase as desaturation processes occur (OSENBRÜCK et al. 1998, RÜBEL et al. 2002).

We carried out the measurements reported here to characterize the evolution of profiles of noble gas concentrations in the EDZ and interpret them in terms of gaseous exchanges between the rock-mass and the atmosphere of the gallery. In other words, we would like to determine how the *in-situ* gases diffuse to the gallery. And, reciprocally, how deep can the gallery air invade the rock mass? To access to the long-term dynamics of the noble gas evolution, we studied the core of the 12-m long borehole BEZ-G5 (see Chap. 1). This borehole was drilled in the end-face of Gallery 04 on September 12, 2007, 4 years after tunnelling. For short-term dynamics, we considered the cores of the 3-m long boreholes BEZ-G36, BEZ-G39 and BEZ-G44 drilled close to each other in the front of Ga08 on July 14, 21 and 28, 2008, respectively, i.e., during the pause in the excavation of Gallery 08 from July 11, 2008 (see Chap. 2).

7.2 Method

During the air drilling of borehole BEZ-G5, we prepared 11 samples for noble gas analysis from distances of 0.4 m to 10.4 m to the end-face of Gallery 04. For the three other boreholes, we extracted 8 samples from each core.

Gas extraction from pore water was done following the procedure described by OSENBRÜCK et al. (1998). The core was sampled within 2–3 h after drilling to avoid any significant gas loss due to the very low solubility of noble gases in

water. Prior to storage, about 1 to 2 cm of the rock was removed by chiselling in each direction to eliminate outer parts potentially affected by He loss and by atmospheric contamination. Core samples between 200 g and 400 g were weighed with precision and loaded into a vacuum-tight cell of about 650 cm³ (Fig. 7-1). Each cell was pumped for 30 s until a vacuum of a few millibars was obtained, then filled with pure N₂ to atmospheric pressure, and finally pumped again for about 30 s. This protocol removed most of the air that might have been trapped in the cell or at the surface of the sample. Noble gases diffused out of the pore water over a period of at least 4 to 5 weeks due to the low solubility of noble gases in water (WEISS 1971) and the porosity of Opalinus Clay (i.e., 12–18%, MAIS 1998; RÜBEL et al. 1999; THURY 2002; PEARSON et al. 2003).

After storage, gases were extracted from the cell by a flux of water vapour through a capillary tube using a cold trap (Fig. 7-2). The procedure we used was similar to that described by BEYERLE et al. (2000). We repeated this extraction procedure twice. Yields better than 99% were found for He and Ne, and better than 98% for Ar, Kr and Xe. Purification was done using a molecular sieve trap for water vapour and hot Ti and Cu powders for active species. He and Ne were separated from Ar, Kr and Xe cryogenically, on activated charcoal, before being introduced into a VG Micromass 1200 mass spectrometer (12 cm radius, 60° deflection angle) for isotopic analysis. Ar, Kr and Xe were also separated cryogenically and successively introduced into the spectrometer. Absolute concentrations were determined using an isotopic dilution method with a typical precision of 1 to 2% for all noble gases.

Rock water contents were measured by weighing the samples in which the noble gas concentrations were determined before being loading into the cell, and after the gas analysis, by dehydration at 105 °C.

7.3 Results

7.3.1 BEZ-G5 borehole

Table 7-1 lists the noble gas contents in core BEZ-G5, expressed in cubic centimeter of gas at standard pressure and temperature per gram of pore water (cc STP g⁻¹) with analytical errors (twice the standard deviation). The He profile exhibits depletion relative to the deepest samples in the first two metres of the core (Fig. 7-3). In the shaly facies from 0 to 2 m, He values ranged from 145 to 4×10^{-7} cc STP g⁻¹, a value significantly lower than the average value of 850×10^{-7} cc STP g⁻¹ measured in the shaly facies by RÜBEL et al. (2002). This



Fig. 7-1: Vacuum-tight cells for the samples.



Fig. 7-2: Extraction equipment for gas analysis.

discrepancy underlines the influence of EDZ and fractures crossed in this zone on He contents. The mean He content at greater depth was $513 \times 10^{-7} \text{ cc STP g}^{-1}$, a value slightly higher than the average value reported by RÜBEL et al. (2002) for the sandy facies ($444 \times 10^{-7} \text{ cc STP g}^{-1}$). The position of the studied area relative to adjacent formations can explain this discrepancy. Indeed, RÜBEL et al. (2002) showed that the He content in the sandy facies increases with distance to limestone rocks.

A less marked but significant depletion in He, linked to enrichment with other gases, Ne excepted, occurs at 5 m, where a main SE-dipping fault (called F_5 in Chap.8, see Fig. 8-12) crosses borehole BEZ-G5 (see Chap.3.1). At 7 m, enrichment is observed only in Ne for which we have no explanation. We did not observe any evolution of the water content (mean value of $4.46 \pm 1.25\%$) with depth, whereas the water content in the shaly facies is usually 1–2% higher than in the sandy facies (RÜBEL et al. 2002).

Tab.7-1: Content in water (in weight-%) and concentrations in noble gases (in 10^{-7} cc STP g^{-1}) with analytical errors (twice the standard deviation) of the core of borehole BEZ-G5.

Depth (m)	Water	Helium	Neon	Argon	Krypton	Xenon
0.4	6.4	—	—	—	—	—
1.0	5.1	145 ± 5.0	1.10 ± 0.04	4435 ± 149	1.41 ± 0.04	0.348 ± 0.01
1.6	4.2	61 ± 2.1	1.62 ± 0.06	1683 ± 73	0.54 ± 0.02	0.154 ± 0.004
2.0	4.4	4 ± 0.1	3.54 ± 0.16	6760 ± 221	2.05 ± 0.06	0.853 ± 0.021
2.5	3.5	706 ± 25	2.55 ± 0.10	4558 ± 134	1.15 ± 0.03	0.259 ± 0.007
2.9	5.3	558 ± 24	1.71 ± 0.07	4015 ± 117	0.98 ± 0.03	0.229 ± 0.006
4.1	4.3	636 ± 33	2.15 ± 0.09	4827 ± 152	1.29 ± 0.04	0.297 ± 0.007
5.1	3.5	417 ± 18	1.99 ± 0.07	6138 ± 189	1.70 ± 0.05	0.386 ± 0.01
7.1	4.6	483 ± 23	4.86 ± 0.28	4307 ± 131	0.93 ± 0.02	0.197 ± 0.005
8.8	5.1	467 ± 23	1.75 ± 0.07	3264 ± 97	0.95 ± 0.03	0.204 ± 0.005
10.5	4.7	328 ± 11	1.94 ± 0.08	2255 ± 61	0.53 ± 0.01	0.099 ± 0.002

Tab.7-2: Content in water (in weight-%) and concentrations in noble gases (in 10^{-7} cc STP g^{-1}) with analytical errors (twice the standard deviation) of the core of boreholes BEZ-G36, G39 and G44.

Borehole	Depth (m)	Water	Helium	Neon	Argon	Krypton	Xenon
BEZ-G36	0.14	4.8	418 ± 14	1.85 ± 0.07	2064 ± 58	0.53 ± 0.01	0.107 ± 0.003
	0.36	4.4	840 ± 29	1.83 ± 0.06	2473 ± 70	0.65 ± 0.02	0.128 ± 0.003
	0.64	3.5	875 ± 30	2.60 ± 0.10	2279 ± 62	0.56 ± 0.02	0.103 ± 0.003
	0.96	4.4	664 ± 23	2.07 ± 0.46	2189 ± 59	0.59 ± 0.02	0.129 ± 0.003
	1.34	5.4	673 ± 23	3.17 ± 0.13	2766 ± 79	0.69 ± 0.02	0.133 ± 0.003
	1.74	5.2	675 ± 23	2.18 ± 0.08	2609 ± 72	0.70 ± 0.02	0.147 ± 0.004
	2.36	4.7	838 ± 29	2.53 ± 0.09	2398 ± 66	0.64 ± 0.02	0.130 ± 0.003
	3.02	5.1	714 ± 25	1.98 ± 0.07	2548 ± 72	0.70 ± 0.02	0.145 ± 0.004
BEZ-G39	0.07	5.3	378 ± 13	2.00 ± 0.07	2149 ± 61	0.59 ± 0.02	0.122 ± 0.003
	0.39	2.9	901 ± 31	2.58 ± 0.09	2200 ± 60	0.52 ± 0.01	0.089 ± 0.002
	0.80	4.7	495 ± 17	1.68 ± 0.07	2041 ± 56	0.61 ± 0.02	0.133 ± 0.005
	0.94	3.7	919 ± 32	2.67 ± 0.09	2428 ± 67	0.55 ± 0.01	0.088 ± 0.003
	1.16	4.2	638 ± 22	2.02 ± 0.07	2167 ± 58	0.56 ± 0.02	0.112 ± 0.003
	1.84	5.2	765 ± 26	2.27 ± 0.08	2315 ± 66	0.62 ± 0.02	0.122 ± 0.003
	2.34	5.0	579 ± 20	3.10 ± 0.11	2681 ± 75	0.68 ± 0.02	0.140 ± 0.004
	3.04	5.0	502 ± 17	2.25 ± 0.08	2433 ± 66	0.64 ± 0.02	0.134 ± 0.004
BEZ-G44	0.07	5.4	191 ± 7	3.25 ± 0.14	2651 ± 76	0.65 ± 0.02	0.038 ± 0.001
	0.29	5.2	518 ± 18	2.18 ± 0.08	2269 ± 62	0.62 ± 0.02	0.126 ± 0.003
	0.64	4.0	878 ± 30	1.62 ± 0.06	1883 ± 50	0.45 ± 0.01	0.064 ± 0.002
	0.99	4.6	733 ± 25	3.21 ± 0.12	1856 ± 50	0.48 ± 0.01	0.087 ± 0.003
	1.34	5.7	606 ± 21	2.44 ± 0.09	2489 ± 73	0.62 ± 0.02	0.103 ± 0.003
	1.84	4.5	629 ± 22	2.59 ± 0.21	1866 ± 51	0.48 ± 0.01	0.093 ± 0.003
	2.59	4.2	644 ± 22	2.45 ± 0.11	1925 ± 52	0.50 ± 0.01	0.092 ± 0.002
	3.04	3.2	573 ± 20	1.19 ± 0.04	1708 ± 45	0.45 ± 0.01	0.085 ± 0.003

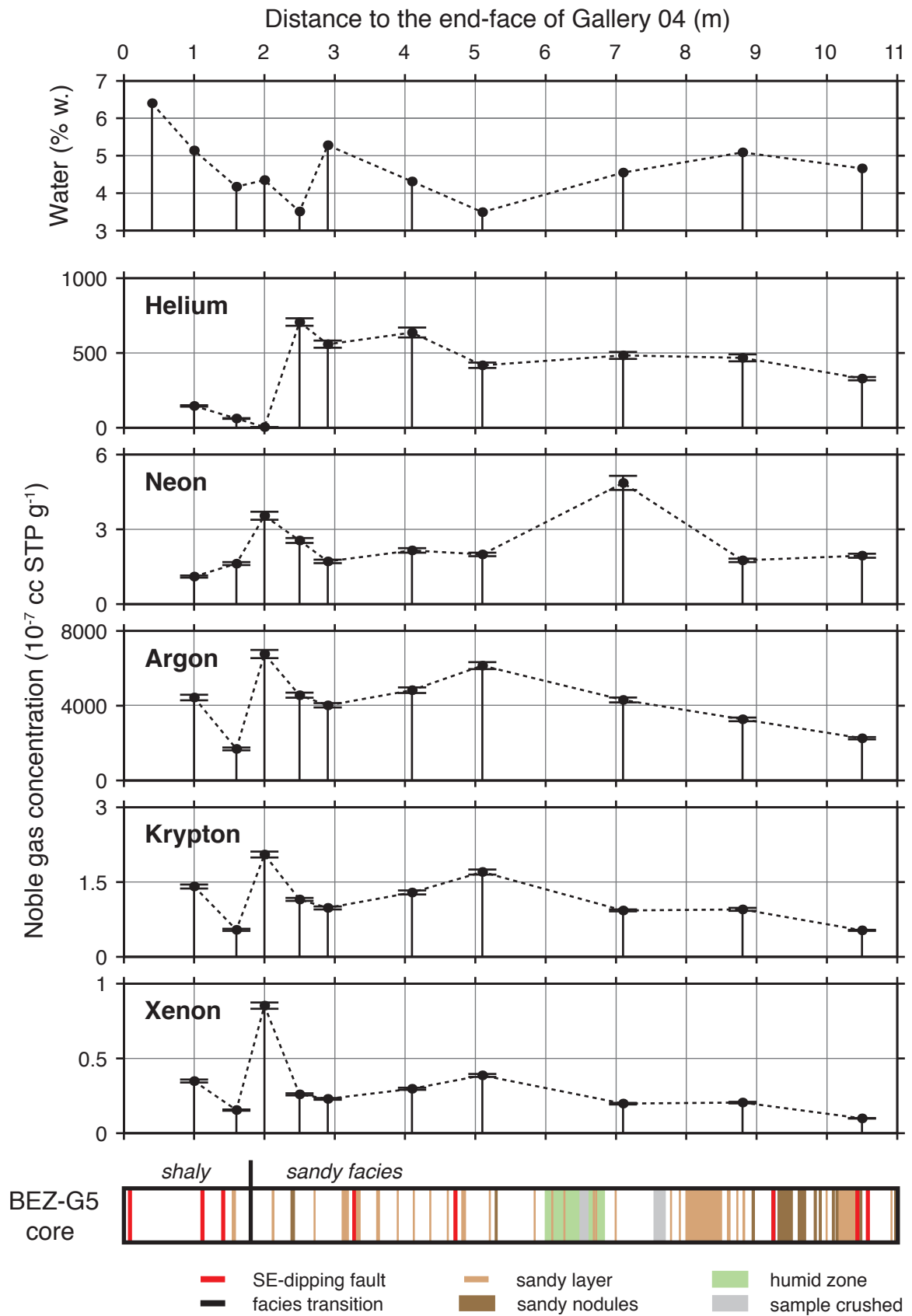


Fig. 7-3: Water content, concentration of noble gases, and geological facies in the core of borehole BEZ-G5.

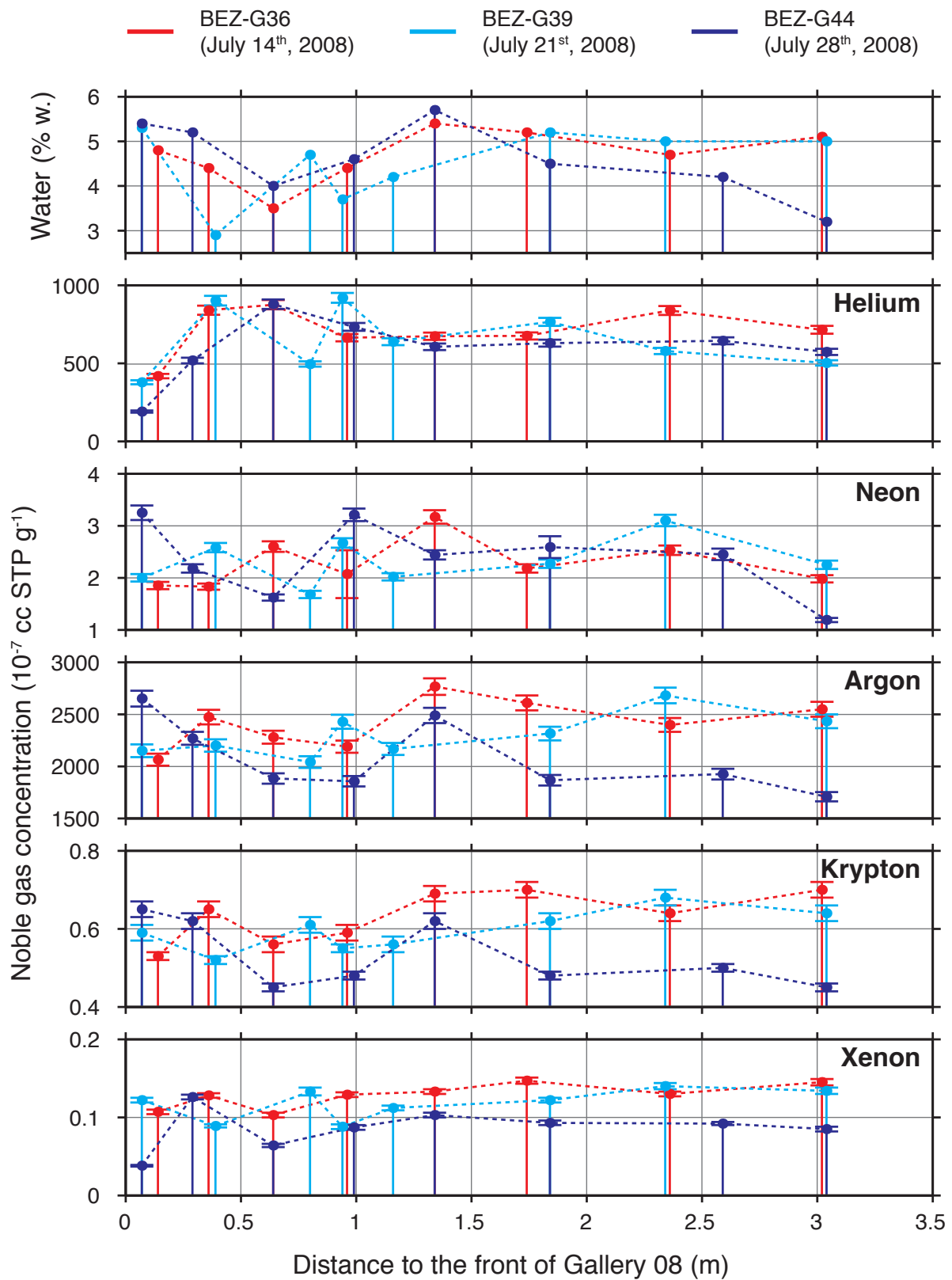


Fig. 7-4: Water content and concentration in noble gases of the cores of boreholes BEZ-G36, BEZ-G39 and BEZ-G44.

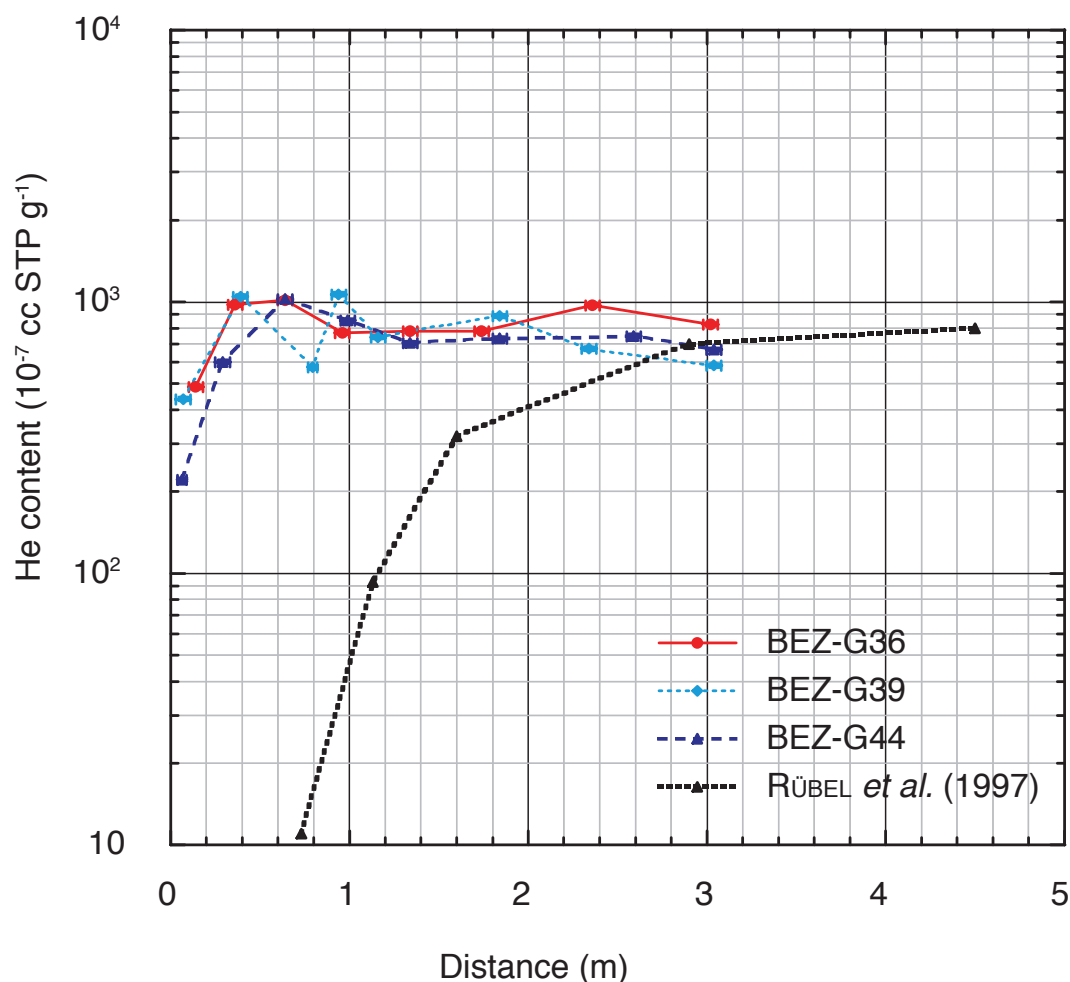


Fig. 7-5: Helium content in boreholes BEZ-G36, G39 and G44, and in borehole WS-A5 (RÜBEL et al., 1997).

Values for Ar content are mainly ranged from 3000 to 5000 10^{-7} cc STP g^{-1} , with some specific values at 1600 and 6000 10^{-7} cc STP g^{-1} . This is coherent with data reported by RÜBEL et al. (1997) in boreholes WS-A1, WS-A2 and GP1, ranging between 3000 and 4000 $\times 10^{-7}$ cc STP g^{-1} .

Finally, we note that the first sample (at 0.4 m) has been seriously contaminated by air. Since the air volume corresponding to noble gas enrichment observed in that sample is of the order of the sample volume (165 cm^3), a desaturation of the medium cannot explain this contamination, rather it must be due to a problem with a defective valve or a leak in the flange device during storage. Air was mixed to the gas sample to such an extent that a reliable correction was not possible. Nevertheless, Ne content indicates that no air contamination occurred during sampling and storage for the other samples.

7.3.2 BEZ-G36, BEZ-G39 and BEZ-G44 boreholes

Results displayed in Table 7-2 and Figure 7-4 do not show any significant variation in water content, at least over the two weeks considered. The values are near those measured in BEZ-G5. Contents in Ne, Ar, Kr and Xe also do not vary with distance. Note however that the mean values are significantly lower than those reported by RÜBEL et al. (1997). For

instance, in boreholes WS-A1, WS-A2 and GP1 Ar content ranged between 3000 and 4000 $\times 10^{-7}$ cc STP g^{-1} , and Kr content between 0.9 and 1.1 $\times 10^{-7}$ cc STP g^{-1} . The difference in facies and the presence of fractures in the Ga08 segment (see Chap. 3.1) may explain these differences.

The He profile exhibits a relatively constant plateau at depths greater than 1 m, corresponding to the He concentration in the undisturbed rock, i.e., 820×10^{-7} cc STP g^{-1} . This value is close to the value of 930×10^{-7} cc STP g^{-1} measured by RÜBEL et al. (2002) in the undisturbed zone of borehole WS-A5 (Fig. 7-5), but it is higher than the mean value we measured at depth in borehole BEZ-G5 (i.e., 513×10^{-7} cc STP g^{-1}). Close to the front of excavation (i.e., at depths lower than 1 m), a loss in He already occurred three days after the end of excavation (July 2011), as evidenced by the BEZ-G36 profile (July 2014). Two weeks later, the He at 7 cm from the front had a value of 191×10^{-7} cc STP g^{-1} in BEZ-G44, representing a 72% loss compared to the average undisturbed value of 820×10^{-7} cc STP g^{-1} . At that time, the disturbed zone appeared to extend to more than 50 cm in depth. We note that the shape of the three He profiles is in agreement with the profile measured in borehole WS-A5 (Fig. 7-5), drilled 10 years after tunnelling and showing an excavation disturbed zone up to a depth of 3 m.

7.4 Discussion

We explain the He loss in the first two metres of BEZ-G5 by the existence of the EDZ. The fact that the lowest He value is located at 2 m depth and not near the end-face of Gallery 04, as one can expect from degassing through the EDZ (for which the density of fractures decreases with distance to the tunnel), might be due to the tectonic fracture seen at the bottom of the end-face of Gallery 04 (Chap. 3.1). This is confirmed by the enrichment in other noble gases at 2 m. The unusual He concentration profile through the EDZ is related to presence of tectonic fractures within the EDZ perturbing the regular degassing of helium that one would expect from a typical EDZ fracture network characterized by a decrease of fracture density with depth. The change in stress triggered by excavation of Gallery 04 was accommodated by reactivation of a dense fault system in the first two metres. This system comprises pre-existing, SE and SW-dipping fractures rather than newly created fractures. Indeed new EDZ fractures, oriented parallel to the end-face, were actually rare, being restricted to the first 50 cm behind the end-face, and observed only at microscale (NICOLLIN et al. 2010; see also Chap. 6). Moreover, during the final stage of excavating Gallery 08 (after the pause in the digging, when the front Ga08 was 8 m from the end-face of Gallery 04), the majority of acoustic events occurred near the main fault crossing BEZ-G5 at 5 m, indicating that the main part of the stress was accommodated by pre-existing structures and thus implying that an EDZ with new fractures was very limited (LE GONIDEC et al. 2012; see also Chap. 5). The low He content values between 0 and 2 m probably result from gas transfer between the claystone and the reactivated, shallow fault system.

Injections of epoxy resin (Chap. 3.2) also evidenced that these fractures were opened in the first two metres. The air circulation that occurred since 2004 led to desaturation of the matrix and a transfer of fluids into the reactivated fracture network. In turn, this caused He depletion and noble gas enrichment (see also OSENBRÜCK et al. 1998, RÜBEL et al. 2002). This hypothesis is supported by the water content being lower than expected in the first two metres (Tab. 7-1). NICOLLIN et al. (2010) also explained the higher resistivity measured along horizontal lines in the upper compartment of the end-face Ga04 in April 2008 by the desaturation of the rock along bedding planes and tectonic fracture planes in the first metre of the rock mass (Chap. 3.1). The noble gas anomaly at 5 m could result from similar, but much less important, exchanges occurring in the significant fault crossing BEZ-G5.

Finally, the rapid decrease in He content observed in boreholes BEZ-G36, G39 and G44 is unlikely to be related to pure diffusion only, but also results from an advective transfer, through fractures created (or reactivated) by the excavation.

7.5 Conclusion

Noble gas concentrations in the core of borehole BEZ-G5 evidenced that the first two metres of rock mass behind the end-face of Gallery 04 exhibit behaviour different from the deeper ones. The noble gas content attests to the development of an EDZ after the excavation of the Gallery 04, yielding desaturation and exchange processes by reactivating pre-existing tectonic fractures that accommodated the stress change in the near field, rather than the development of new fractures induced by tunnelling. Noble gas concentrations in BEZ-G36, G39 and G44 show that the loss in He is very rapid (on the order of days), at least in the first 50 cm, implying that dynamic gas transfer occurred in fractures created or reactivated by the excavation process, here again attesting to the formation of an EDZ.

References

- ANDREWS, J.N. (1985): The isotopic composition of radiogenic Helium and its use to study groundwater movement in confined aquifers. – *Chem. Geol.* *49*, 339–351.
- BEYERLE, U., AESCHBACH-HERTIG, W., IMBODEN, D., BAUR, H., GRAF, T. & KIPFER, A. (2000): A mass spectrometric system for the analysis of noble gases and tritium from water samples. – *Environ. Sci. Technol.* *34*, 2042–2050.
- LE GONIDEC, Y., SCHUBNEL, A., WASSERMANN, J., GIBERT, D., NUSSBAUM, C., KERGOSIEN, B., SAROUT, J., MAINEULT, A. & GUÉGUEN, Y. (2012): Field-scale acoustic investigation of a damaged anisotropic shale during a gallery excavation. – *Int. J. Rock Mech.* *51*, 136–148.
- MAIS, A. (1998): DI Experiment: mercury porosimetry and H₂O determination. – *Mont Terri tech. Note TN 98-64*.
- NICOLLIN, F., GIBERT, D., LESPARRE, N. & NUSSBAUM, C. (2010): Anisotropy of electrical conductivity of the excavation damaged zone in the Mont Terri Underground Rock Laboratory. – *Geophys. J. int.* *181*, 303–320.
- OSENBRÜCK, K., LIPPMANN, J. & SONNTAG, C. (1998): Dating very old porewaters in impermeable rocks by noble gas isotopes. – *Geochim. Cosmochim. Acta* *62*, 3041–3045.
- PODOSEK, F.A., BERNATOWICZ, T.J. & KRAMER, F.E. (1981): Adsorption of xenon and krypton on shales. – *Geochim. Cosmochim. Acta* *45*, 2401–2415.
- PEARSON, F.J., ARCOS, D., BATH, A., BOISSON, J.Y., FERNANDEZ, A.M., GÄBLER, H.E., GAUCHER, E., GAUTSCHI, A., GRIFFAULT, L., HERNAN, P. & WABER, H.N. (2003): Mont Terri project – Geochemistry of water in the Opalinus Clay formation at the Mont Terri Rock Laboratory. – *Rep. fed. Office Water Geol. (FOWG) 5*.
- RÜBEL, A., LIPPMANN, J., OSENBRÜCK, K., SONNTAG, C., LEHMANN, B. & TOLSTIKHIN, I.N., (1997): Stable isotopes and noble gases in pore water and rock samples of the Opalinus Clay at Mont Terri (WS-B experiment). – *Mont Terri tech. Note TN 96-17*.
- RÜBEL, A., LIPPMANN, J. & SONNTAG, C. (1999): WS-A Experiment: profiles of stable isotopes and noble gases in pore water across the Opalinus Clay formation at Mont Terri. – *Mont Terri tech. Note TN 99-18*.
- RÜBEL, A., SONNTAG, C., LIPPMANN, J., PEARSON, F.J. & GAUTSCHI, A. (2002): Solute transport in formations of very low permeability: Profiles of stable isotope and dissolved noble gas contents of pore water in the Opalinus Clay, Mont Terri, Switzerland. – *Geochim. Cosmochim. Acta* *66*, 1311–1321.

- SOLOMON, D.K., HUNT A. & PODERA, R.J. (1996): Source of radiogenic ^4He in shallow aquifers; implications for young groundwater. – *Water Resources Res.* 32, 1805–1813.
- STUTE, M., SCHLOSSER, P., CLARK, J.F. & BROECKER, W.S. (1992): Paleotemperatures in the Southwestern United States derived from noble gases in ground water. – *Science* 256, 1000–1003.
- TORGENSEN, T. & CLARKE, W.B. (1985): Helium accumulation in groundwater, I: An evaluation of sources and the continental flux of crustal ^4He in the Great Artesian Basin, Australia. – *Geochim. Cosmochim. Acta* 49, 1211–1218.
- THURY, M. (2002): The characteristics of the Opalinus Clay investigated in the Mont Terri underground rock laboratory in Switzerland. – *C. R. Phys.* 3, 923–933.
- WEISS, R.F. (1971): Solubility of helium and neon in water and seawater. – *J. Chem. Eng. Data* 16, 235–241.
- ZUBER, A., WEISE, S.M., OSENBRÜCK, K. & MATENKO, T. (1997): Origin and age of saline waters in Busko Spa (southern Poland) determined by isotope, noble gases and hydrochemical methods: evidence of interglacial and pre-Quaternary warm climate recharges. – *Appl. Geochem.* 12, 643–660.

8. Self-potential monitoring in BEZ-G5 borehole

A. MAINEULT, C. NUSSBAUM, K. WIECZOREK, D. GIBERT, B. KERGOSIEN, F. NICOLLIN, K. MAHIOUZ & N. LESPARRE

8.1 Introduction

A few weeks after drilling borehole BEZ-G5 in September 2007, inflows of water occurred that continued until the junction of Galleries Ga08 and Ga04 in August 2008. The water produced by the borehole muddied the surface of end-face Ga04, as illustrated in Figure 8-1.

Even though the hydraulic conductivity of Opalinus Clay is extremely low, in the range 10^{-14} to 10^{-12} m s⁻¹ (NAGRA 2002, THURY 2002, FERNÁNDEZ-GARCIA et al. 2007 and references therein, MAYOR et al. 2007), volumes of water amounting to a few litres were commonly released in other boreholes and are called “wet spots”. Analysis of water routinely sampled from these areas yielded a chemical fingerprint of ancient seawater trapped during the deposition of the sediments some 175 Ma ago (DEGUELDRE et al. 2003). The Opalinus Clay Formation acts as an aquiclude (THURY 2002). Indeed, in the fine pores of Opalinus Clay about 150 litres of water is trapped in each cubic metres of rock mass in free and bound form. A small proportion of this water can be squeezed out of the rock when pressure change is applied, for instance, as a result of stress modifications induced by tunnel construction.

To obtain information about the water flow-paths and their dynamics, we monitored natural electrical potentials, or self-potentials (SP), on the end-face of Gallery 04 and in borehole BEZ-G5, from February 21 to April 25, 2008. SP signals result from movement of fluids and/or diffusion of ionic concentration or temperature fronts. Interestingly, they are sensitive to any change occurring in these fluid movements (e.g., JOUNIAUX et al. 2009 and references therein). The so-called electrokinetic potential difference between two given points, denoted ΔV , originates through movement of a circulating electrolyte through a porous medium. This potential is directly proportional to the hydraulic pressure difference, denoted ΔP , applied between these two points, provided that the mineral surface is electrically charged and that fluid can circulate. The electrokinetic coupling coefficient C , equal to the ratio $\Delta V/\Delta P$, depends on the surface properties of the rock and on the chemical properties of the fluid, such as its salinity, pH, or temperature. Due to the small size of pores and to the high electrically charged surface of minerals, the behaviour of C can be rather complex in clayey materials. Water saturation also has a major influence. In the context of the URL, we argue that the only possible source for SP signals is the electrokinetic phenomenon, since pore water does not present significant variations in salinity or temperature. Because the existence of a hydraulic pressure difference results in a hydraulic flow, provided that the medium is adequately permeable, any local variation of the potential could be reasonably associated

with a flow-path. Moreover, any change in DP, which could be related to a modification of the local permeability or of the hydraulic pressure field linked to a damage or stress field, will result in a proportional change in ΔV .

SP monitoring could therefore provide clues on the temporal dynamics of water flow. To date, only few studies report on the use of the SP method to characterize the fluid circulation in fractured media (e.g., MURAKAMI et al. 2001, MARQUIS et al. 2002, FAGERLUND & HEINSON 2003, DARNET et al. 2004, MAINEULT et al. 2006, 2008, NISHI & ISHIDO 2012). We note that in all these works, fluid movement was artificially forced by pumping, contrary to the case reported here, in which the fluid movement, i.e. the natural inflow of pore water into the borehole, occurred naturally.

8.2 Instrumentation

In mid-February 2008, we equipped borehole BEZ-G5 and end-face Ga04 for SP monitoring. As the normal amplitude of the SP signal was commonly less than 100 mV, we had to take special care with the electrodes to minimize any noise triggered by the polarization effect. This effect can occur when a highly conductive metallic core contacts a medium with much less conductivity. Unpolarisable electrode (see for example PETIAU & DUPIS 1980) were preferred to simple metallic rods classically used for active electrical measurements (as described, for instance, in Chap. 6). Such electrodes are usually made of a metallic wire in chemical equilibrium with a surrounding solution saturated with a salt of the same metal. A porous material ensures good electrical contact between the solution and the medium.

To instrument borehole BEZ-G5, we devised and constructed a device that we called the “caterpillar”. It consisted of a 10-m long half PVC drainpipe (Fig. 8-2a), on which we glued two series of 65 PVC annuli (1 cm in height and 2.8 cm in internal diameter, Fig. 8-2b), the first one for unpolarisable electrodes and the second one for classical metallic electrodes. After assembling the half pipes in Gallery 04 (Fig. 8-2c), flat lead strips with a surface of 4 cm² were inserted into the annuli and then welded to the internal IDE wires (Fig. 8-2d, e). Then a circular piece of highly absorbing sponge, which served as solution container and also as a contact surface with the medium, was adjusted in one of two consecutive annuli, above the lead strip. After being carefully fixed, the sponges were soaked with distilled water that was over-saturated with PbCl₂ and NaCl salts (Fig. 8-2f). The spacing between two electrodes of the same kind was equal to 15 cm (Fig. 8-2g). The normal electrodes were also used for classical DC measurements not reported here.

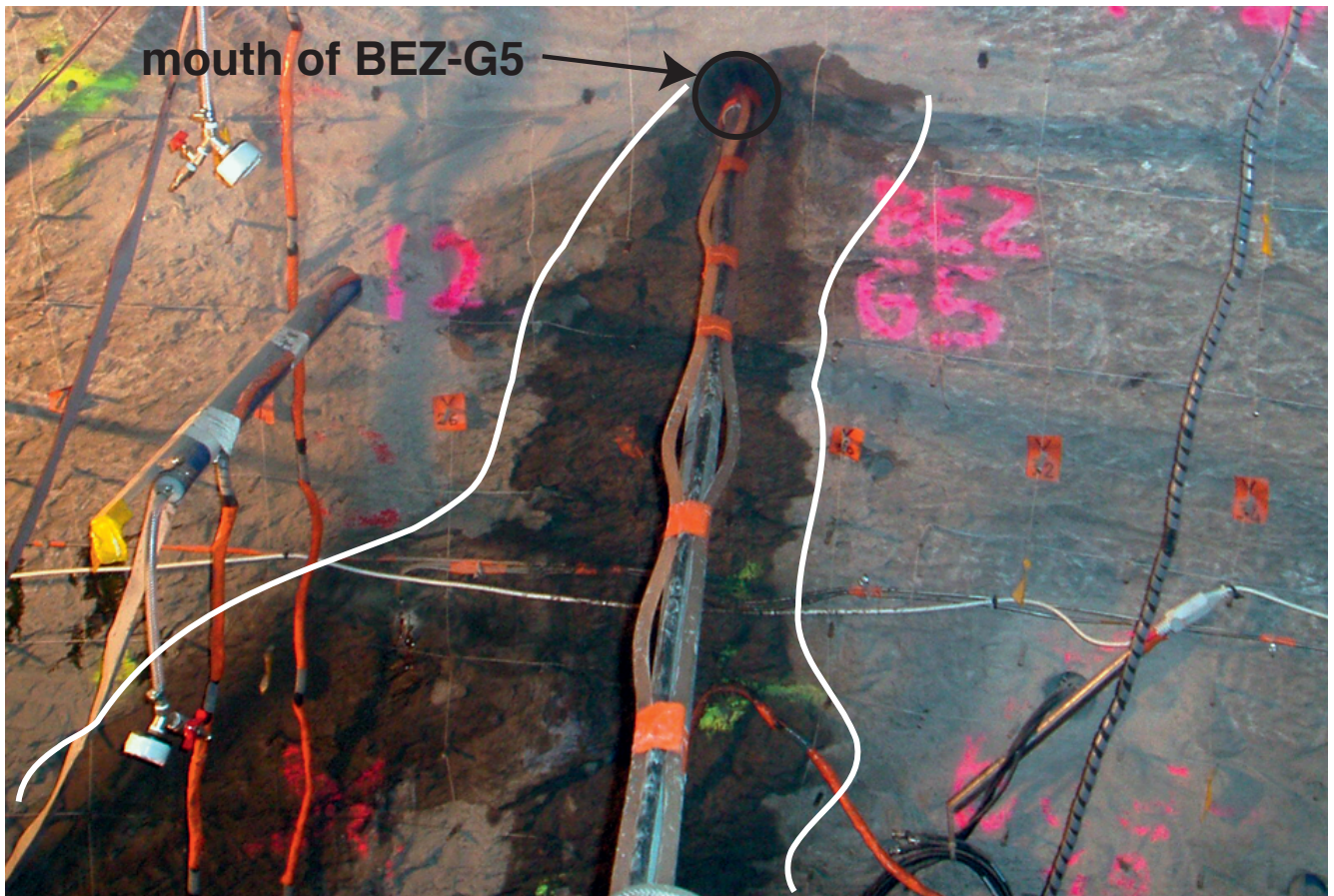


Fig. 8-1: Close-up view of the end-face of borehole Ga04, showing traces of water that outflowed from borehole BEZ-G5 during the acoustic measurements carried out in July 2008 (see Chapter 5 and LE GONIDEC et al. 2012).

The caterpillar was then fixed onto an inflatable pipe and introduced into borehole BEZ-G5, with the electrodes turned upward. We succeeded in pushing only 9.7 m of the pipe into the borehole. The unpolarisable electrode closest to the end-face, numbered CH64, was located inside BEZ-G5 at 5 cm from its opening (Fig. 8-3a), and the farthest, numbered CH01, at 9.5 m. Finally, the internal pipe was inflated to ensure a good electrical contact between the electrodes and the borehole wall (Fig. 8-3b).

The electrodes for the end-face of Ga04 were made of a lead strip (5 cm in length and 1 cm in width) wrapped in a sponge sheath (Fig. 8-4a). These 6-cm long electrodes were inserted into small holes drilled in the end-face (Fig. 8-4b) and afterwards saturated with the PbCl_2 -NaCl solution. A series of 17 electrodes formed a roughly regular network with a 1-m mesh-size on the end-face (Fig. 8-5).

All the electrodes were connected to a Keithley-2701 multiplexer with two acquisition cards DMM-7708, each with 40 channels measuring potential differences. The electrical potential differences between each electrode and reference electrode BIG5 were recorded with a sampling rate of 1 point per minute, starting on February 2, 2008 at 13:44 local time, and ended on April 25 at 18:17 local time. The acquisition was unfortunately interrupted between March 21 at 18:54 and March 28 at 10:39 for unknown reasons.

8.3 Raw self-potentials

All raw SP signals recorded in borehole BEZ-G5 (Fig. 8-6) display remarkably similar features and are relatively noise-free, at least before day 40. For sake of clarity, the two characteristic behaviours that we observed will be discussed hereafter by focusing on signals at depth of 6.35 m (CH22) and 6.65 m (CH20), since they are representative (Fig. 8-7a).

The signals were roughly stable from the beginning, forming a plateau around 20 mV, implying that the equilibration time between the electrodes and the medium was very short. After day 4 (elapsed time since February 2, 00:00 local time), a decrease of about 70–80 mV occurred. This decrease, which affected all the electrodes in a similar manner, is probably due to a modification of reference electrode BIG5, resulting from partial desiccation by evaporation and/or by suction of the solution saturating the sponge by the rock. Once the definitive equilibration of the reference electrode was reached, that is after day 10, the signals remained constant.

The signals showed coherent perturbations between days 18 and 23 (Fig. 8-7b), the we link to drilling operations in end-face of Ga04. Indeed, the four horizontal 4-m long boreholes BEZ-G12, G13, G14 and G15 (Fig. 8-5 and Chap. 1,

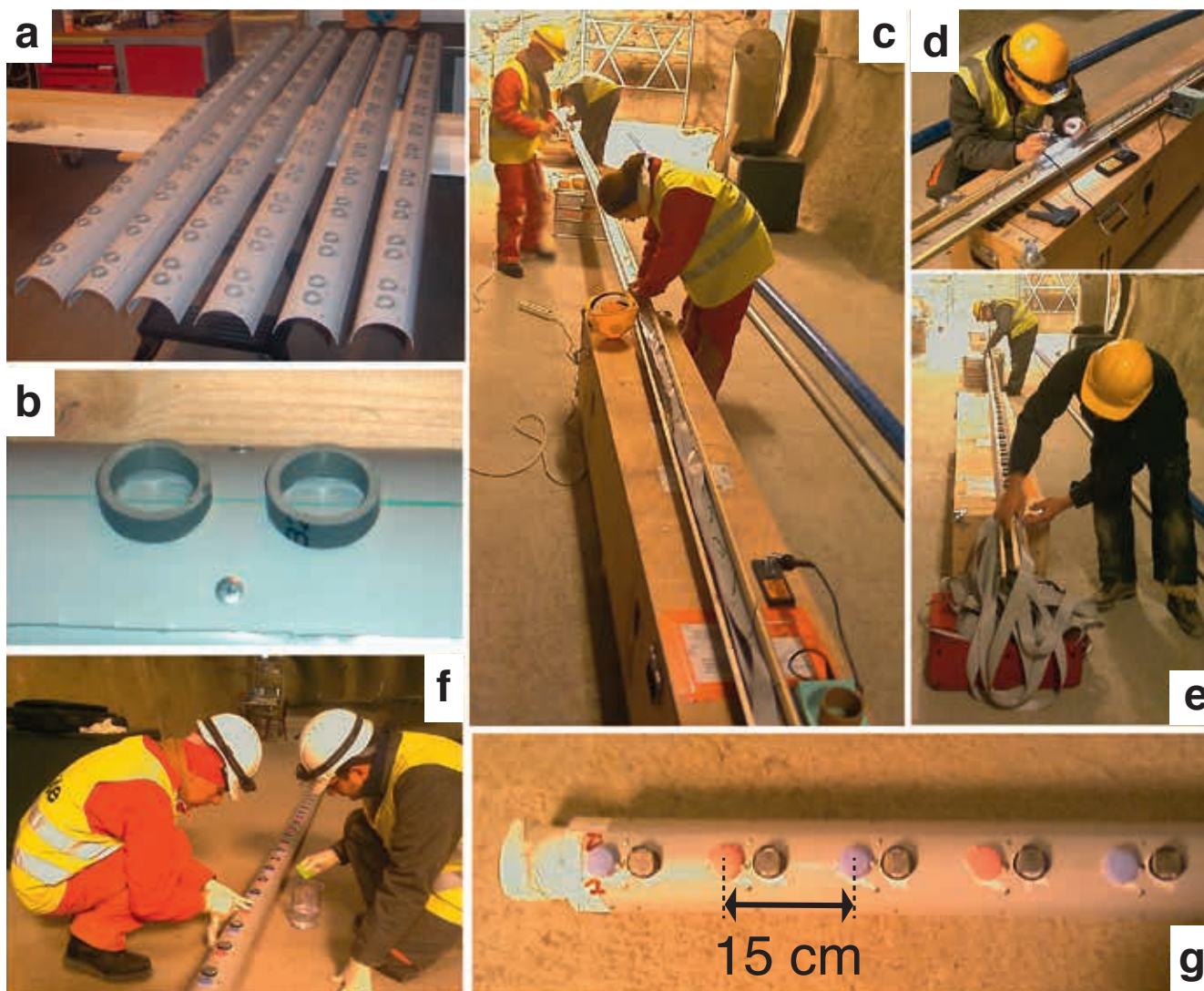


Fig. 8-2: **a)** PVC-pipes before assembly. **b)** close-up view of the PVC annuli for the electrodes. **c)** fixing the IDE wire inside the assembled “caterpillar”. **d)** welding lead strips inserted in each annulus to the internal IDE wire. **e)** IDE wires at the tail of the caterpillar. **f)** saturating the sponges placed over one of two lead strips. **g)** top-view of the head of the caterpillar. The coloured sponges correspond to the unpolarisable electrodes and the grey (exposed) lead strips to the normal ones.

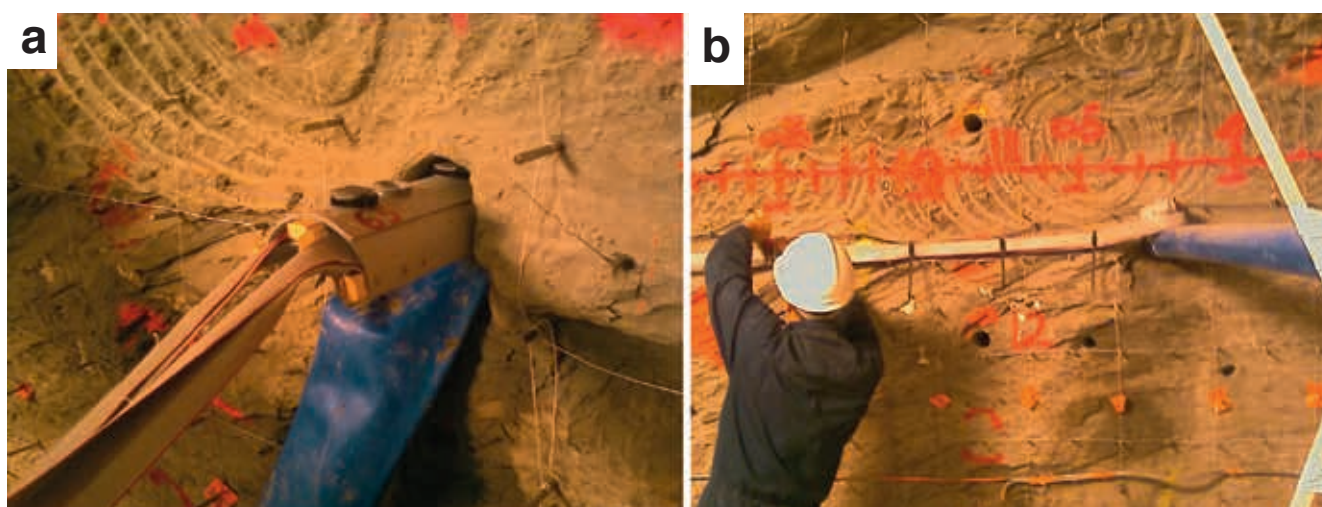


Fig. 8-3: Tail of the caterpillar after insertion into the borehole, before **(a)** and after **(b)** inflating the internal pipe.

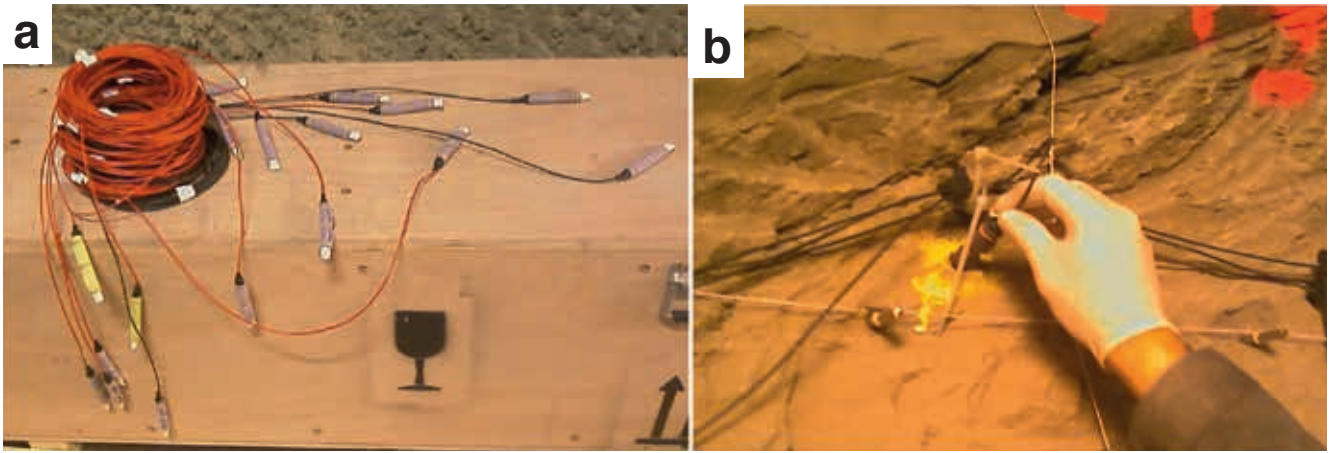


Fig. 8-4: a) unpolarisable electrodes for end-face Ga04. b) inserting an electrode into a cm hole drilled in the end-face.

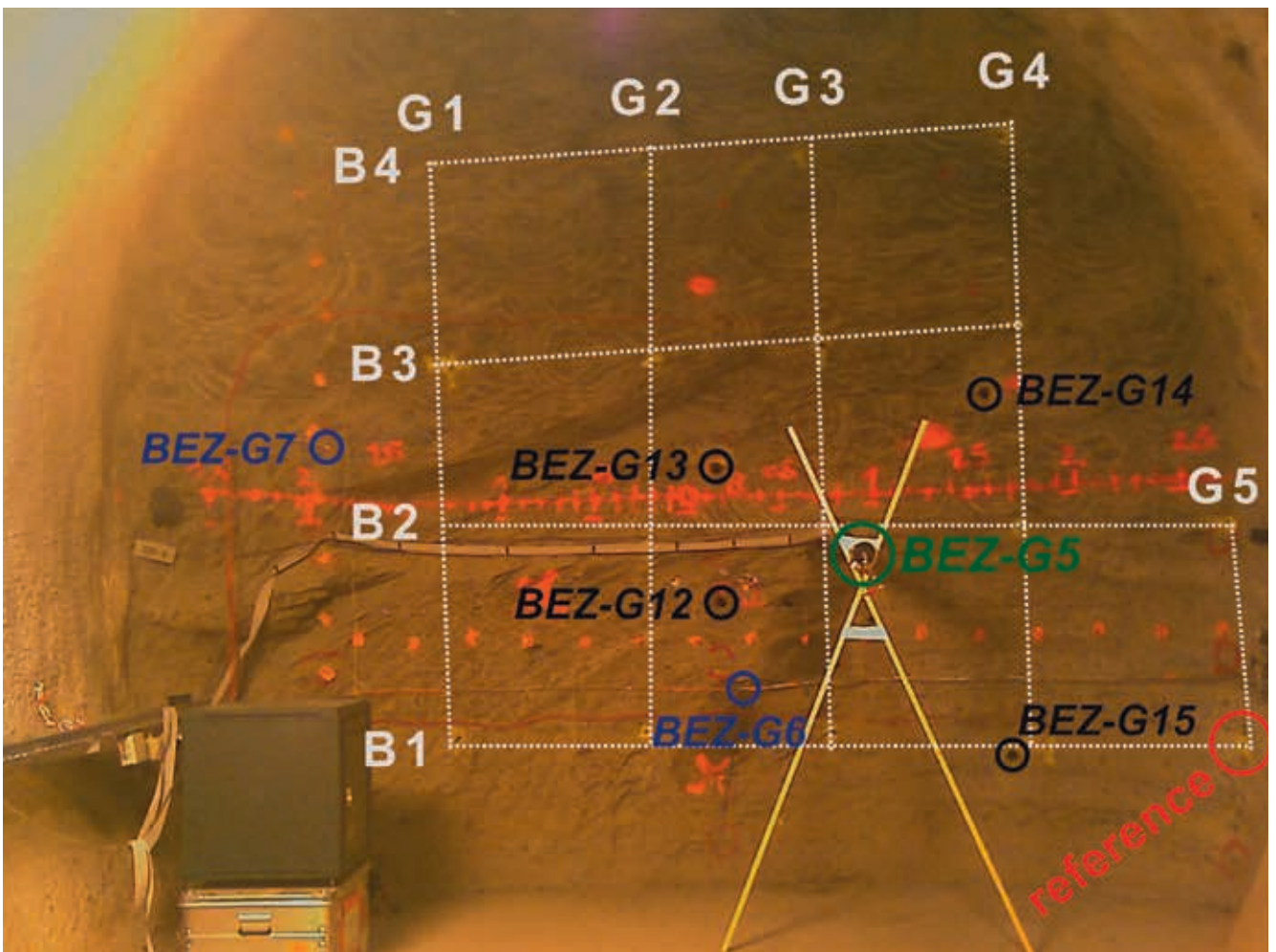


Fig. 8-5: Network of unpolarisable electrodes on end-face Ga04 (February 21, 2008). Note that electrode B2G3 corresponds to electrode CH64 of the caterpillar. Electrode B1G5 served as reference electrode for all the measured potential differences.

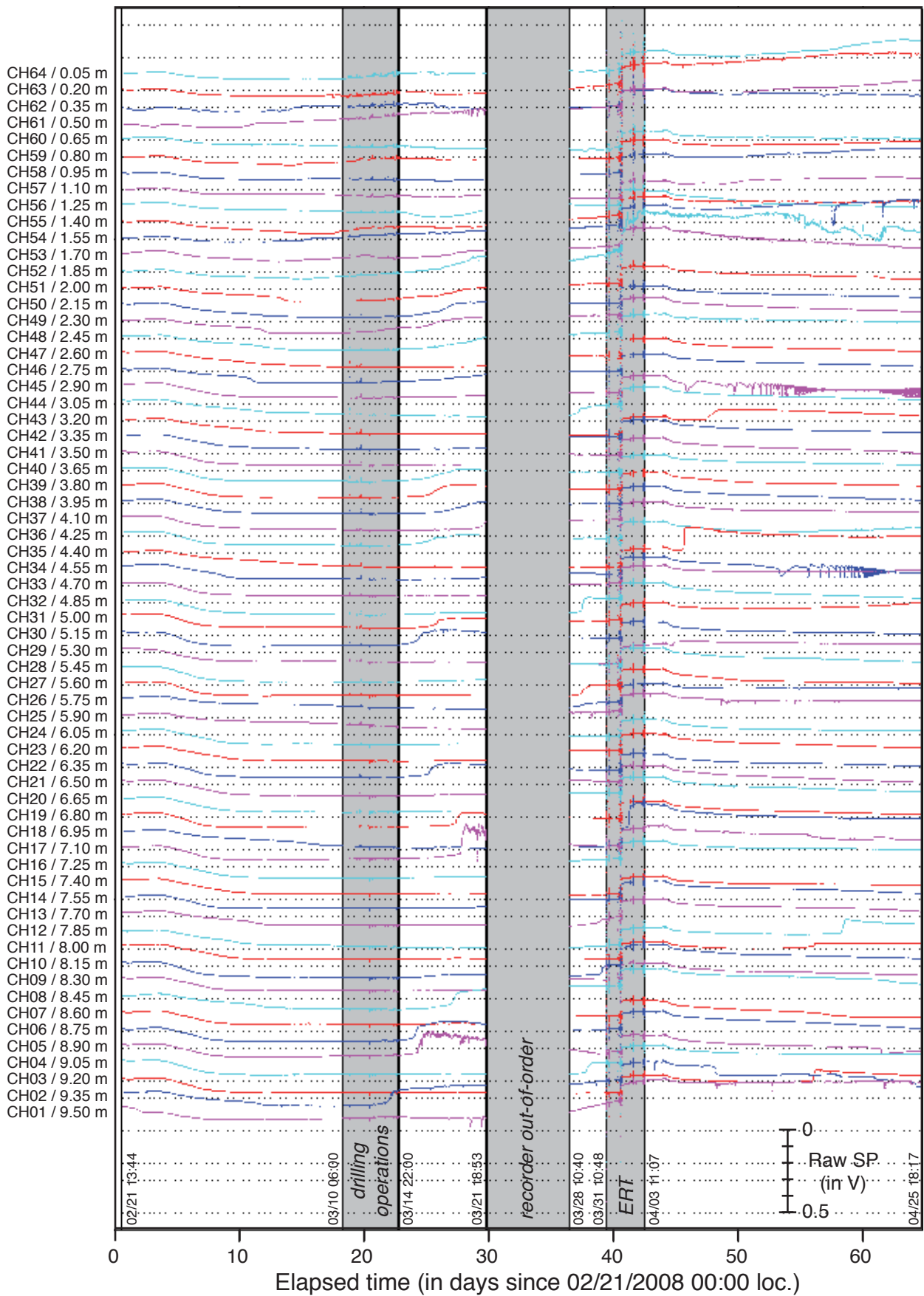


Fig. 8-6: Raw self-potential differences between the electrodes in borehole BEZ-G5 and reference B1G5. Drilling operations in BEZ-G12 to G19 took place between March 10 and March 14, 2008. The recorder went out of order between March 21 and March 28. Finally, electrical resistivity tomography measurements were carried out on end-face Ga04 between March 31 and April 3.

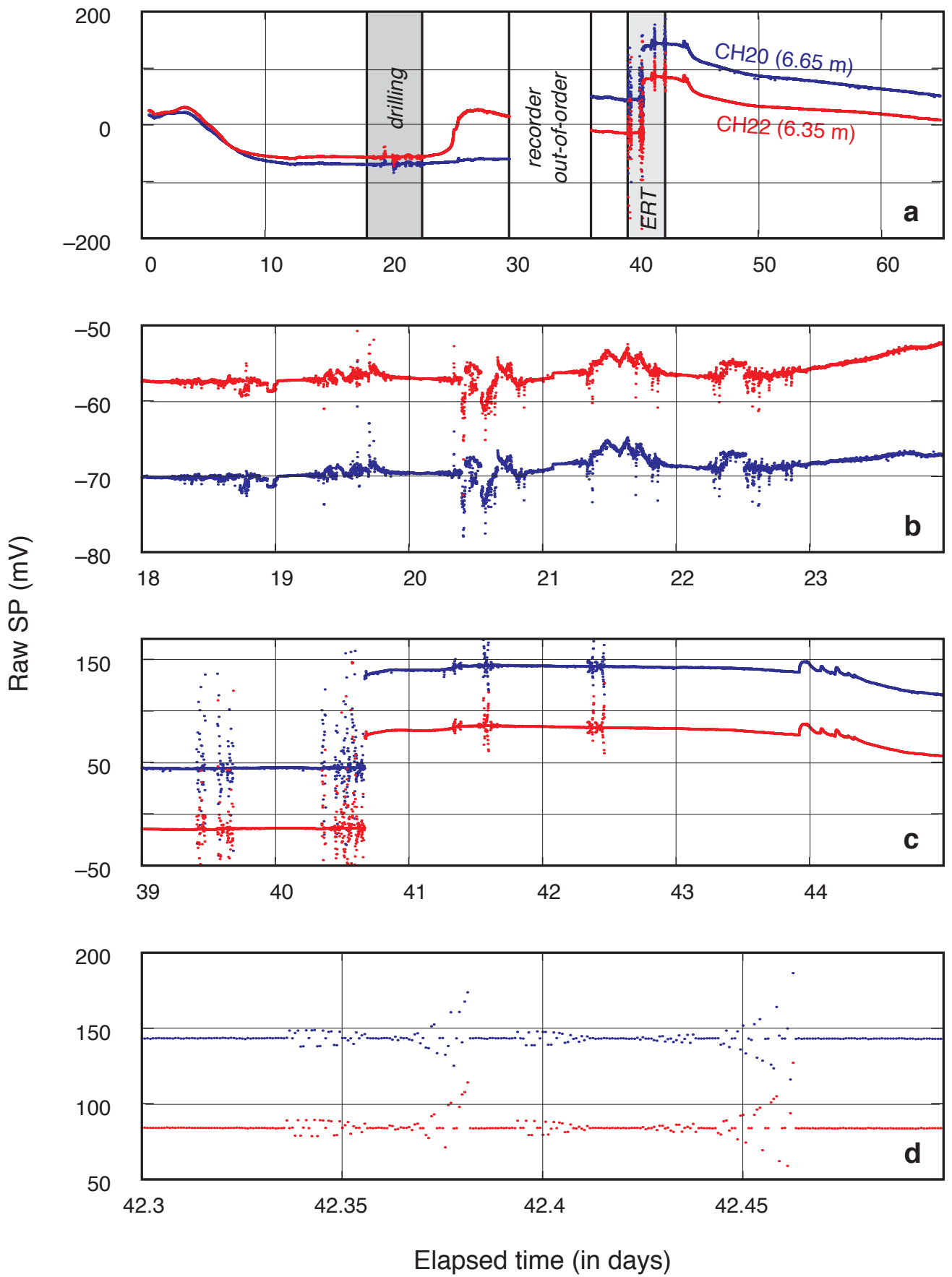


Fig. 8-7: **a)** example of raw self-potential signals recorded in borehole BEZ-G5 at 6.35 m (CH22, red) and 6.65 m (CH20, blue). **b)** close-up of the period during which drilling operations were carried out in end-face Ga04. **c)** and **d)** perturbations resulting from ERT acquisitions carried out on the end-face and also from the resaturation of the reference electrode (around day 40.5).

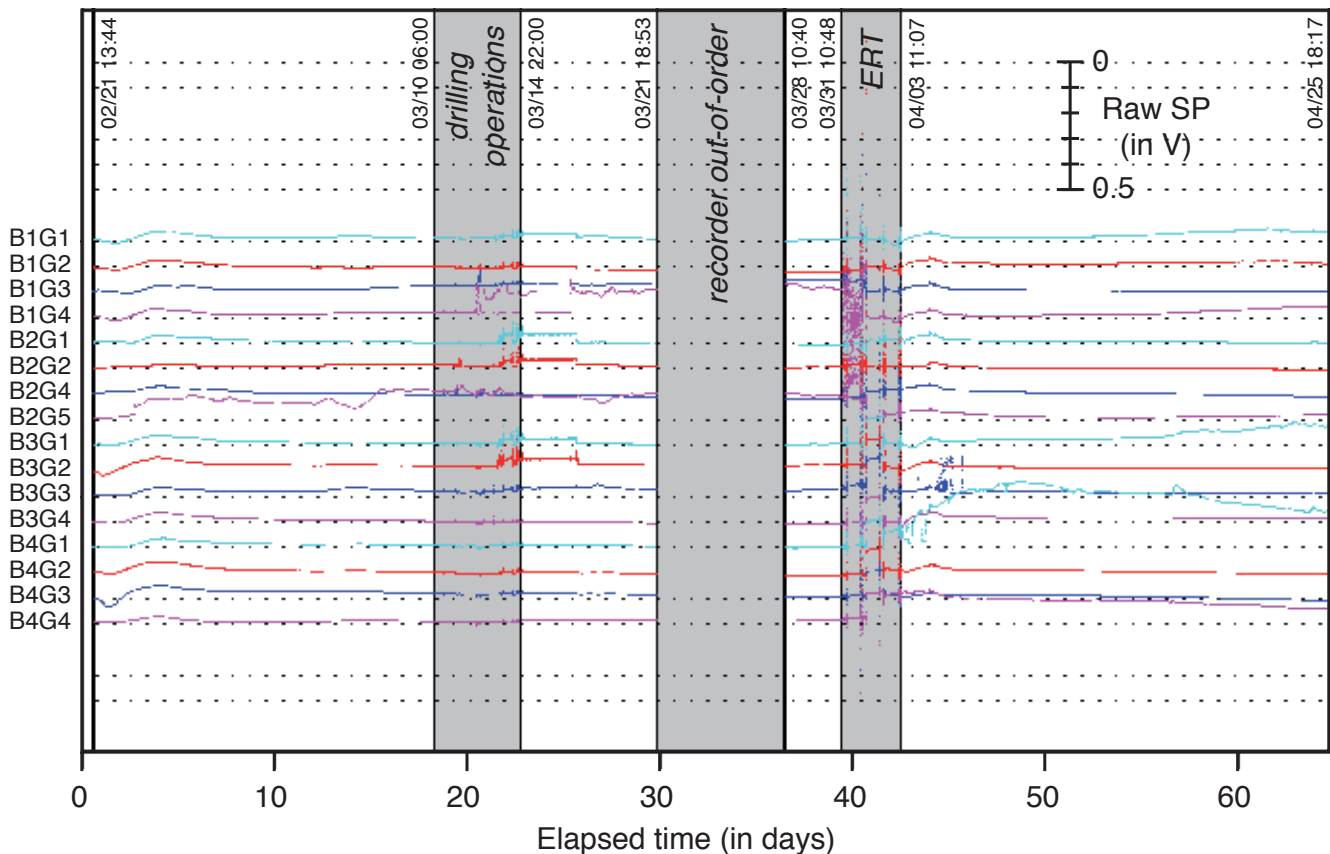


Fig. 8-8: Raw self-potential differences between the electrodes placed on end-face Ga04 and reference electrode BIG5.

Fig. 1-3), which were drilled in December 2007 for electrical and acoustic measurements, were extended by drilling up to 8 m and the boreholes BEZ-G16, G17, G18 and G19 were drilled between March 10 and 14, 2008.

After the end of the drilling operations, the noise level returned to its prior value. From day 23, we observed in some signals (for example at 6.35 m) an early, strong, but rather smooth increase of a few tens of millivolts, followed by a very slow decrease. At day 39, the major part of the electrodes had encountered a similar positive change, as seen at 6.65 m (see also Fig. 8-6).

Between March 31 and April 3, acquisition of electrical resistivity tomography (ERT) was performed on the end-face (see Chap.6), which coherently disturbed the SP signals (Fig. 8-6, 8-7 c and d) as a response to the current injections on the end-face. Moreover, the unpolarisable electrodes at the end-face were resaturated around day 40.5. This changed the chemical state of reference electrode BIG5; as a consequence the potential differences measured between the electrodes in the borehole and BIG5 jumped to 100 mV.

From day 43, it seems that the signals were unfortunately disturbed in the long term (non-coherent jumps, oscillations and drifts that can be observed in Fig. 8-6). As a result, we do not consider the signals from the beginning of the ERT measurements onwards as being usable.

Finally, the signals recorded on end-face Ga04 remained globally flat (Fig. 8-8). All the electrodes of the end-face underwent desiccation at the beginning, but remained stable after day 5. Even when the noise level increased during the

drilling operations, we observed no subsequent, smooth increases afterwards, contrary to what happened in BEZ-G5 borehole. We note also that resaturation of the end-face electrodes at day 40.5 did not disturb the potential differences significantly in the long term, because the chemical state of the measurement electrodes and reference BIG5 was modified in a similar way. In conclusion, no significant variations in the SP signals recorded on end-face Ga04 occurred.

8.4 Self-potential anomalies

From the raw signals (SP values versus time for each electrode), we extracted an SP profile in borehole BEZ-G5 and studied its evolution with time, in order to link the spatial SP field to the geology. For the analysis developed in the following, we do not consider the time required for the initial equilibration of the electrodes, i.e. days 0 to 10, nor the signals after day 40 that were perturbed due to the ERT measurements.

8.4.1 Static anomaly

Considering that the reference electrode achieved stability after day 10, we consider the SP values between days 10 and 18, which are almost unchanged in time, as reflecting a “static” distribution of the self-potential inside borehole BEZ-G5 (Fig. 8-9). The mean value between 0 and 2 m is sig-

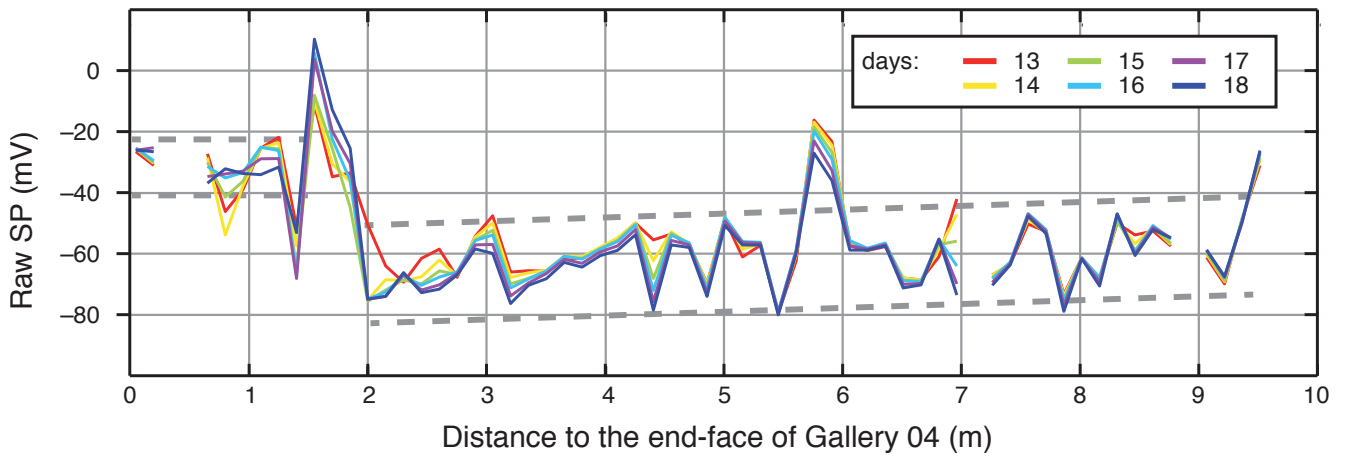


Fig. 8-9: Initial (static) self-potential anomaly in borehole BEZ-G5 after the stabilisation of the reference electrode and before the drilling operations. A change in the baseline can be observed between 1.5 and 2 m. An anomaly also seems to appear around 6 m.

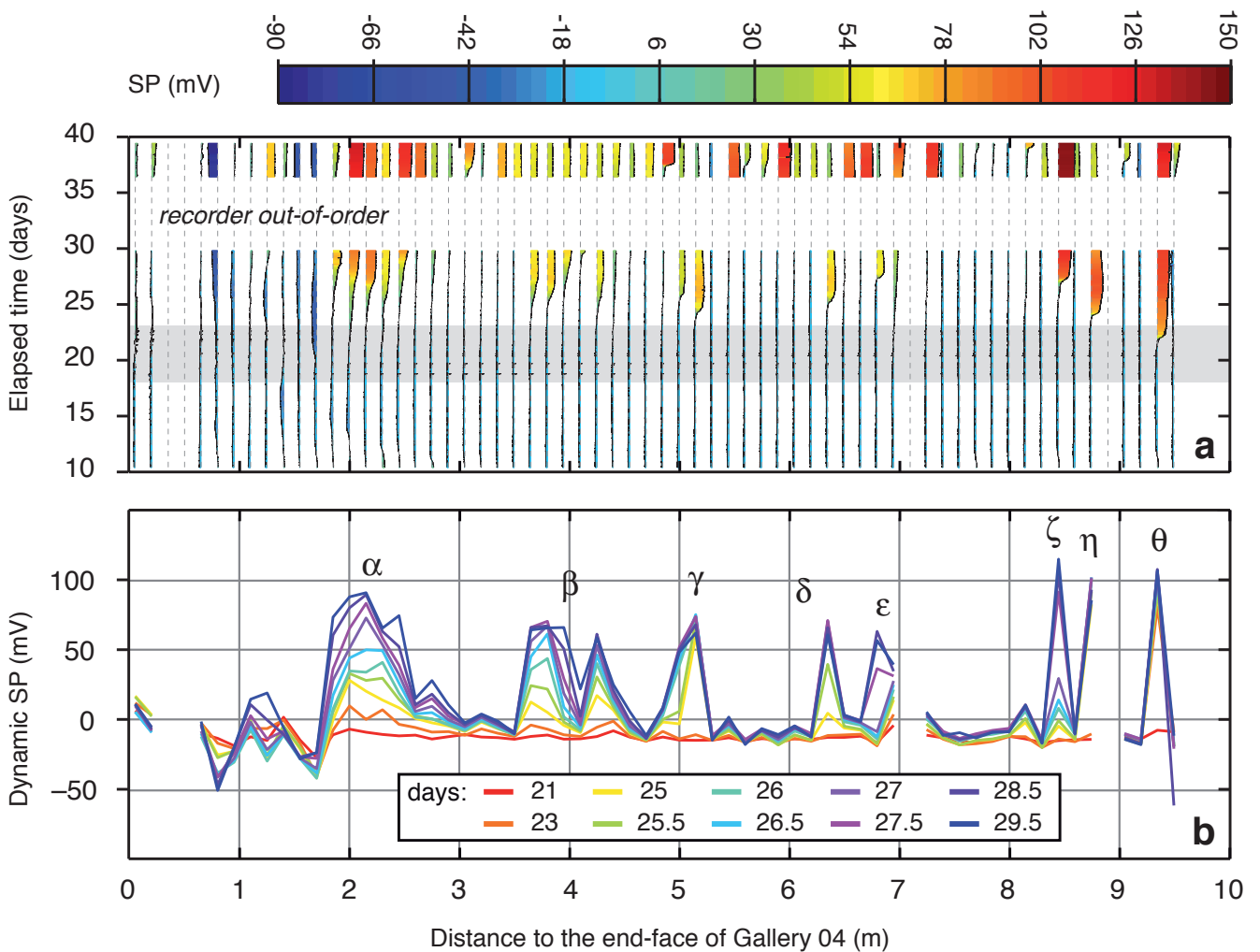


Fig. 8-10: Evolution of the self-potential variations with respect to the initial, static anomaly in borehole BEZ-G5, in wiggle view (a) and time shots (b). In a, the grey zone denotes the period of drilling operations. In b, Greek letters stand for the noticeable anomalies of the self-potential variation.

nificantly higher (about 30 mV) than the mean value between 2 and 9.5 m. It also seems that a positive anomaly occurred between 5.5 and 6 m, but we are not sure of its significance since it affects only two points.

8.4.2 Dynamic anomaly

To examine the localised, sudden changes occurring after the drilling operations, we consider the dynamic variations of SP with respect to the static anomaly described above. To do so, all the raw SP signals were de-trended, using offset and gain coefficients computed over the plateau measured between days 12.5 and 20. The space-time variations of the SP field (Fig. 8-10) reveal 8 localised anomalies occurring just after the drilling operations, all occurring in the sandy facies of borehole BEZ-G5 (i.e., after 2 m; see Chap. 3.1 for the geological description of the core of BEZ-G5). Two of these anomalies (α and β) are more extended in space, and seem to extend laterally with time from a central point. The other anomalies are point anomalies. It also seems that 7 supplemental point anomalies appear after day 30 (as for the electrode at 6.65 m, Fig. 8-7a), but unfortunately during the recorder breakdown.

Since the sponges of the electrodes were still saturated and covered by clayey mud when we dismantled the caterpillar, we do not think that these variations resulted from a degradation of the electrodes, such as polarization after desiccation, or degradation of the electrical contact with the rock.

Finally, one can object that the stability of reference electrode BIG5 could constitute a major impediment by adding an unquantifiable component to the signals. Nevertheless, when restraining the interval of study to days 10 to 40, the use of another reference such as the shallowest electrode CH64 (at 5 cm) or the deepest one CH01 (at 9.5 m), which could be done numerically by subtraction, does not change the shape nor amplitude of the SP variations, but only the baseline. As a consequence, we are confident in the physical meaning of the observed anomalies.

8.5 Interpretation

We hypothesize that the dynamic SP anomalies reflect a response to localised inflows of pore water into borehole BEZ-G5, and that these inflows result from modification of the hydraulic pressure field in the rock-mass after drilling boreholes BEZ-G12 to G19 (MAINEULT et al. 2013, 2014). The drilling operations could have reactivated pre-existing fractures and, consequently, induced pore-water flows in the rock-mass towards borehole BEZ-G5. Indeed, in Opalinus Clay, the mechanisms of expulsion of water from pores may be related to two types of damage induced by excavation or drilling: extensional fracturing by the unloading of joints and brittle reactivation of pre-existing fractures, like fault planes and bedding planes (MARTIN et al. 2002). These water inflows are limited in time, and are supposed to come from the immediate vicinity of the borehole (i.e., they do not involve the rock mass at a large scale). This suggestion is rein-

forced by the fact that no water exudation and no SP perturbations were observed for the electrodes placed on end-face Ga04, and that no dynamic anomalies occurred in the first two m of borehole BEZ-G5, which have a very low water content due to desaturation of the EDZ since 2004 (see Chap. 6, 7).

The major argument is that the pore pressure, which was continuously recorded in the packed-off boreholes BEZ-G6, BEZ-G7 and BEZ-G8 (see Chap. 1, Tab. 1-1 for their description and Fig. 1-3 for location) with mini-packer piezometers developed by GRS, was disturbed by the drilling operations and then subjected to a long-term re-equilibration (Fig. 8-11). Pore pressure and SP disturbances are clearly similar. Since pore pressure in borehole BEZ-G8 increased relative to pressure in boreholes BEZ-G7 and BEZ-G6 after day 23, a downward flow could have occurred in the upper-part of the rock-mass; in particular, towards borehole BEZ-G5. We also note that an increase in water production was observed in boreholes BEZ-G12 to G15 in July 2008 when the front of Gallery 08 reached their vicinity, implying that similar processes of joint unloading induced by the excavation should have occurred at that time. The free water expelled from the rock in the vicinity of the new boreholes circulated through the complex fracture network that served as flow-paths, provided it was intercepted.

By comparison with the geological log of the core of BEZ-G5 and with the structural mapping of the segment Ga08 (drawn after its excavation, see Chap. 3.1 for more details), it seems that the dynamic SP anomalies α , γ , δ , ζ and θ are clearly associated with macroscale faults (Fig. 8-12). Among them, faults f_2 , f_3 and f_4 (α), f_5 (δ) and f_7 (ζ) were not observed in the drillcore mapping (i.e., they were sealed at the initial state). Therefore, they should have been reactivated by the drilling operations. On the other hand, fault F_4 and f_6 did not produce any SP anomaly, the first one probably because it was not directly intercepted (due to its short length), and the second one because either non-connection or that it had been re-activated not by the drilling operations but later by the excavation of segment Ga08.

The anomalies β , ϵ and η , were located in sandy layers and cannot be associated with faults, at least faults visible to the naked eye. However, free water is unlikely to circulate through the sandy lenses because their matrix has a higher degree of cementation and a lower porosity, as suggested by nanostructural studies, and a permeability either similar to the embedding claystone or even lower. However, sandy lenses often contain very thin fractures commonly observed at microscale. Note also that the slow decrease of the SP signal after the initial jump (Fig. 8-10) may be explained by a decrease in fluid velocity with time.

Interestingly, no flow seems to have taken place in the first two m, i.e., in the EDZ that developed during and after the tunnelling of Gallery 04 in 2004. Indeed, the EDZ was probably much too desaturated to contain releasable free water (see Chap. 7). The higher mean value in the static SP anomaly occurring in the first two m (Fig. 8-9) could also be linked to the EDZ, rather than to the transition between the shaly and sandy facies. Indeed, the mineralogy of both facies is similar: only the mineral contents are different (from 15% quartz in the shaly facies up to 50% locally in the sandy faci-

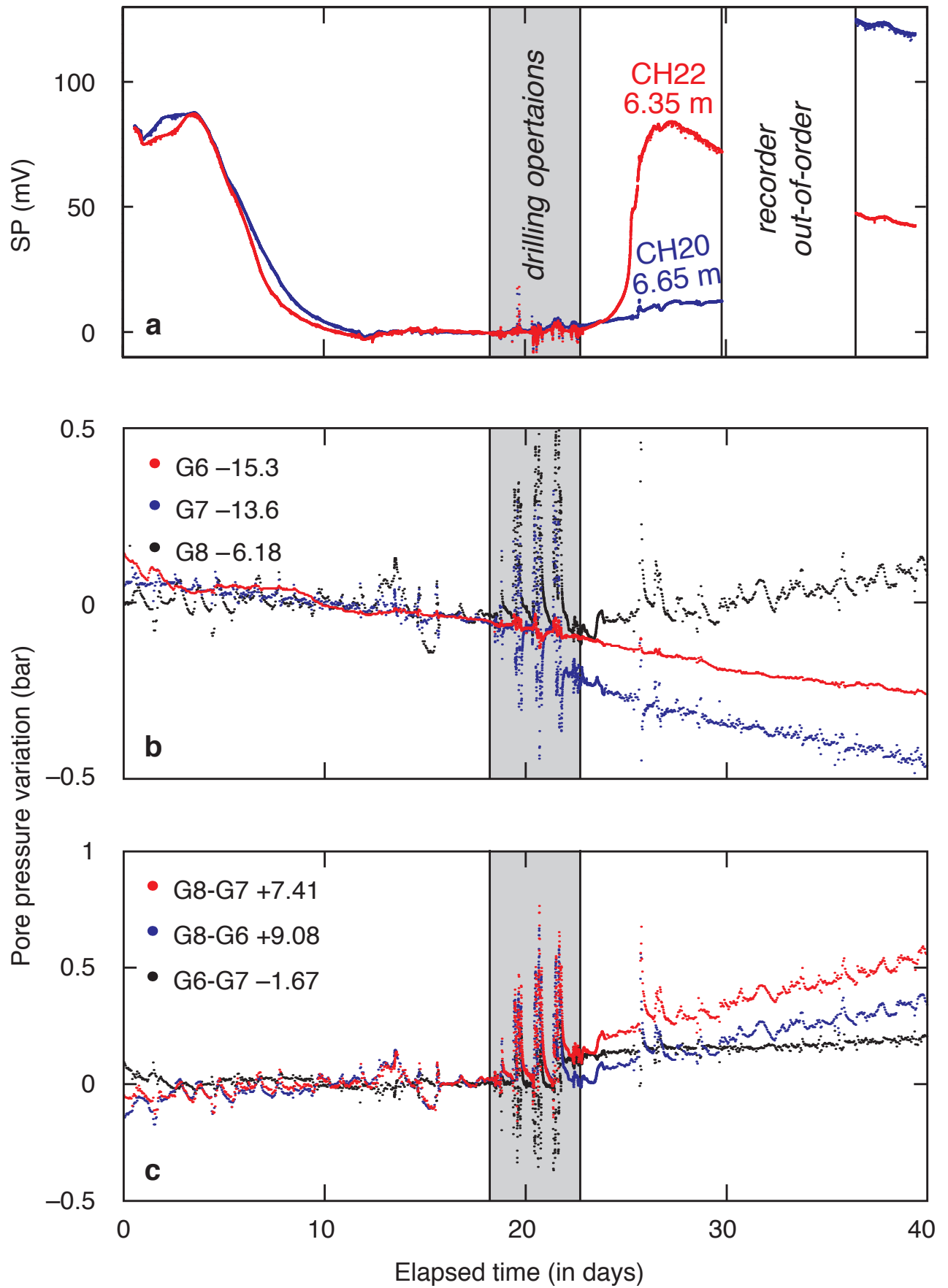


Fig. 8-11: **a)** evolution of the self-potential variations with respect to the initial anomaly at 6.35 m (CH22, red) and 6.65 m (CH20, blue) in BEZ-G5. **b)** and **c)** absolute and relative evolution of the pore pressure measured in packed-off boreholes BEZ-G6, BEZ-G7 and BEZ-G8.

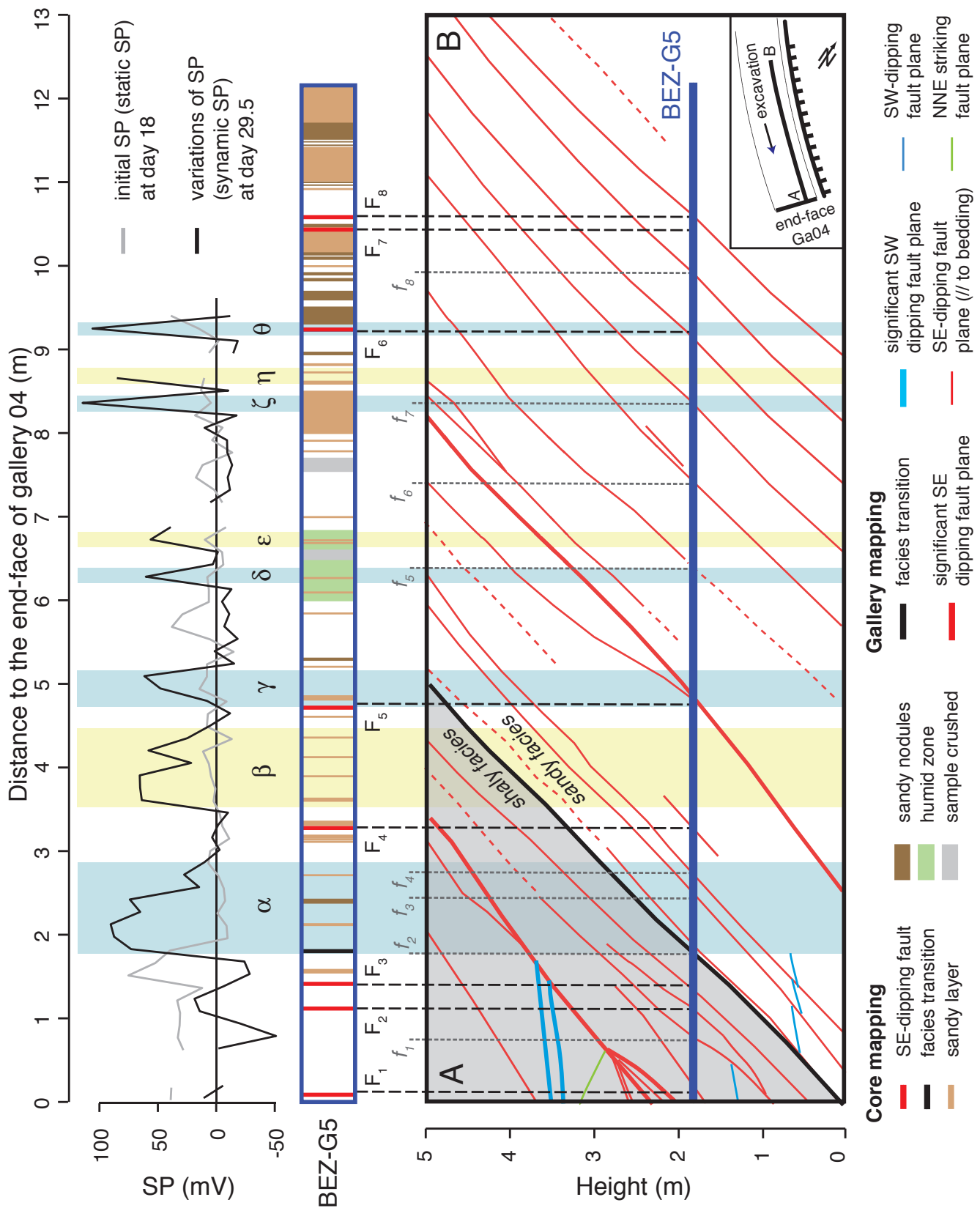


Fig. 8-12: Comparison between the self-potential anomalies in borehole BEZ-G5 and the geology, i.e. the interpreted core of borehole BEZ-G5 (initial state) and the last 13 metres of the structural cartography of the wall of segment Ga08 drawn after its excavation (final state). Fractures labelled F_1 to F_8 were observed in the core, whereas fractures labelled f_1 to f_8 were not, since they were sealed with calcite and clay minerals. Fractures f_1 to f_8 are unlikely to result from drilling operations and/or excavation of Gallery 08, but could have been reactivated by them. Greek letters denote the noticeable self-potential anomalies (blue: linked to macroscale faults; yellow: possibly linked to microscale fractures).

es). Moreover, the transition is so progressive that the difference in clay content could not explain the sharp SP variation. A difference in the velocity of circulating fluids (if any) also cannot explain the variation, since hydraulic conductivities in both facies are of the same order of magnitude (e.g., CROISÉ et al. 2004).

8.6 Conclusion

The SP anomalies evidenced that the first two m of rock mass behind the end-face of Gallery 04 exhibit behaviour different from the deeper ones. This is consistent with the conclusions drawn from the geo-electrical measurements (Chap. 6) and from the noble gases concentrations (Chap. 7).

We relate the dynamic SP anomalies occurring after the drilling of boreholes BEZ-G12 to G19 in the end-face of Gallery 04 to modifications in the near stress field, which led to free water being released from the claystone. This subsequently resulted in a variation of pore pressure and thus to fluid circulation. Comparison of the location of the SP anomalies with the position of fractures mapped after excavation of segment Ga08 suggest that drilling operations (primarily the earlier excavation of Gallery 04) had reactivated pre-existing, sealed, macroscale faults, which then acted as flow-paths. We also observed some anomalies located in sandy lenses, which could result from fluid circulation in microscale fractures. Inflow of water in boreholes (observed from the tunnel construction in 1998, or in BEZ-G12 to 15 in July 2008 at the end of the tunnelling of Gallery 08) probably resulted from similar processes induced by excavation operations.

A tentative explanation for the origin and amount of inflowing fluids may be the existence of suitable petrophysical and mechanical properties of Opalinus Clay. Mechanical strain (“squeezing”) of grain skeleton and pore space due to stress redistribution can be considered to cause release of free pore water, even if modifications in pore pressure triggered by drilling and excavation are very small. Water is also unlikely to be released from sandy lenses, since they are less porous and less permeable, as well as being highly cemented.

Even though the mechanism of water production is not understood, we argue that self-potential measurements could be useful as a passive tool for monitoring of “wet spots” in argillaceous formations.

References

- CROISÉ, J., SCHLICKENRIEDER, L., MARSCHALL, P., BOISSON, J.Y., VOGEL, P. & YAMAMOTO, S. (2004): Hydrogeological investigations in a low permeability claystone formation: the Mont Terri Rock Laboratory. – *Phys. Chem. Earth* 29, 3–15.
- DARNET, M., MAINEULT, A. & MARQUIS, G. (2004): On the origins of self-potential (SP) anomalies induced by water injections into geothermal reservoirs. – *Geophys. Res. Lett.* 31, L19609.
- DEGUELDRE, C., SCHOLTIS, A., LAUBE, A., TURRERO, M.-J. & THOMAS, B. (2003): Study of the pore water chemistry through an argillaceous formation: a paleohydrochemical approach. – *Appl. Geochem.* 18, 55–73.
- FAGERLUND, F. & HEINSON, G. (2003): Detecting subsurface groundwater flow in fractured rock using self-potential (SP) methods. – *Environ. Geol.* 43, 782–794.
- FERNÁNDEZ-GARCIA, D., GÓMEZ-HERNÁNDEZ, J.J. & MAYOR, J.-C. (2007): Estimating hydraulic conductivity of the Opalinus Clay at the regional scale: Combined effect of desaturation and EDZ. – *Phys. Chem. Earth*. 32, 639–645.
- JOUNIAUX, J., MAINEULT, A., NAUDET, V., PESSEL, M. & SAILHAC, P. (2009): Review of self-potential methods in hydrogeophysics. – *C.R. Geosci.* 341, 928–936.
- LE GONIDEC, Y., SCHUBNEL, A., WASSERMANN, J., GIBERT, D., NUSSBAUM, C., KERGOSIEN, B., SAROUT, J., MAINEULT, A. & GUÉGUEN, Y. (2012): Field-scale acoustic investigation of a damaged anisotropic shale during a gallery excavation. – *Int. J. Rock Mech.* 51, 136–148.
- MAINEULT, A., DARNET, M. & MARQUIS, G. (2006): Correction to “On the origins of self-potential (SP) anomalies induced by water injections into geothermal reservoirs”. – *Geophys. Res. Lett.* 33, L20319.
- MAINEULT, A., NUSSBAUM, C., NICOLLIN, F. (2014): Corrigendum to “Anomalies of noble gases and self-potential associated with fractures and fluid dynamics in a horizontal borehole, Mont Terri Underground Rock Laboratory”, *Eng. Geol.* 156, 47–57. – *Eng. Geol.* 176, 93–94.
- MAINEULT, A., STROBACH, E., RENNER, J. (2008): Self-potential signals induced by periodic pumping tests. – *J. geophys. Res. Solid Earth*, 113, B01203.
- MAINEULT, A., THOMAS, B., NUSSBAUM, C., WIECZOREK, K., GIBERT, G., LAVIELLE, B., KERGOSIEN, B., NICOLLIN, F., MAHIOUZ, K. & LEPARRE, N. (2013): Anomalies of noble gases and self-potential associated with fractures and fluid dynamics in a horizontal borehole, Mont Terri Underground Rock Laboratory. – *Eng. Geol.* 156, 46–57.
- MARQUIS, G., DARNET, M., SAILHAC, P., SINGH, A. & GÉRARD, A. (2002): Surface electric variations induced by deep hydraulic stimulation: an example from the Soultz HDR site. – *Geophys. Res. Lett.* 29, 1662.
- MARTIN, C.D., LANYON, G.W., BLÜMLING, P., & MAYOR, J.C. (2002): The excavation disturbed zone around a test tunnel in the Opalinus Clay. In: HAMMAH, R., BADEN, W., CURRAN, J. & TELESNICKI, M. (Ed.): Proceedings of the 5th North America rock mechanics symposium and 17th tunnelling association of Canada conference (p. 1581–1588). – University of Toronto Press.
- MAYOR, J.C., VELASCO, M. & GARCIA-SINERIZ, J.L. (2007): Ventilation experiment in the Mont Terri underground laboratory. – *Phys. Chem. Earth* 32, 616–628.
- MURAKAMI, H., HASHIMOTO, T., OSHIMAN, N., YAMAGUCHI, S., HONKURA, Y. & SUMIMOTO, N. (2001): Electrokinetic phenomena associated with a water injection experiment at the Nojima fault on Awaji Island, Japan. – *The Island Arc* 10, 244–251.
- NAGRA (2002): Projekt Opalinuston – Synthese der geowissenschaftlichen Untersuchungsergebnisse. Entsorgungsnachweis für abgebrannte Brennelemente, verglaste hochaktive sowie langlebige mittelaktive Abfälle. – Nagra tech. Rep. NTB 02-03
- NISHI, Y. & ISHIDO, T. (2012): Characterization of fractured reservoirs using a combination of downhole pressure and self-potential transient data. – *Int. J. Geophys.*, Art. ID 148919.
- PETIAU, G. & DUPIS, A. (1980): Noise, temperature coefficient, and long time stability of electrodes for telluric observations. – *Geophys. Prospect.* 28, 792–804.
- THURY, M. (2002): The characteristics of the Opalinus Clay investigated in the Mont Terri underground rock laboratory in Switzerland. – *C.R. Phys.* 3, 923–933.

9 Recommendations for further works and perspectives

J. WASSERMANN, Y. LE GONIDEC, D. GIBERT, F. NICOLLIN, A. MAINEULT & B. THOMAS

As introduced in the Chapter 1, we paid particular attention to the coordination and flexibility of the multidisciplinary teams of the EZG-08 experiment that permitted the monitoring of a large rock volume during a long period of excavation from 2007 to Summer 2008. In particular, the very complete geophysical monitoring sets (acoustical, active and passive, and electrical) in boreholes and gallery walls and faces have produced a very large amount of data. Further analyses of this data are still in progress.

Data processing provided several results both in terms of metric scale petro-physical characterizations of the damaging rock mass (see NICOLLIN et al.2010, LE GONIDEC et al.2012) and in terms of damage processes (MAINEULT et al.2013, LE GONIDEC et al.2014).

Nevertheless, we encountered difficulties both during the experiments, due to several inflows of free water coming from boreholes and “wet spots”, and/or due to deformation of the boreholes, and for the post-processing, especially for the acoustical data.

Hence, we would like to propose recommendations for further work focus on micro-seismic monitoring; because a lot of post-processing troubles have been encountered. In making these recommendations we keep in mind that the perfect in situ experiments only take place in a perfect world, and we focus on the compromises required in the real world. Our perspectives evoke the need for additional but “ahead” tools useful to better understand the EDZ development through a mine-by experiment such as hydro-mechanical modelling, with a particular focus on encountered induced phenomena such as water inflows, saturation/desaturation processes.

9.1 Recommendation 1: experiment scaling, geometry and orientation

In such a dispersive rock like Opalinus Clay rock, scaling and geometry of the acoustic sensor array are of particular importance. The geometry and dimensions of the sensor array have to be discussed with a critical look at the tunnelling characteristics such as scale and geometry of the sections to be excavated.

Beyond the difficulties of drilling several boreholes around an excavation, when placing sensor arrays the researcher should be able to receive and transmit elastic energy in a cross-hole way with a particularly good raypath coverage both in azimuth and deviation. The spacing between boreholes should neither be too large nor too divergent. The orientation and deviation of the boreholes, the position of

each sensors and acoustic sources, should be carefully controlled. In this way, the wave-velocity models can be well defined and, as a consequence, very useful in the localization algorithms for the sources of Acoustic Emissions (AE) or Microseismic events (MSe). Source localization is a necessary step to determine the damage mechanisms (from moment tensor inversion and focal mechanism determination).

The experiments performed in the EZ-G08 segment showed that electrical resistivity is a useful parameter to characterize and monitor the EDZ. The design and the geometry of the electrode network were concluding. It consisted of a square grid of electrodes installed on an accessible side of the rock mass (end-face of an existing gallery in this study) and electrode lines installed in horizontal boreholes drilled perpendicularly to the side. With such a network, the electrical properties in the rock volume can be described entirely in 3D and can be monitored during excavation.

On the face, electrodes were formed with thin steel rods introduced in the rock. In boreholes, the coupling between electrodes (lead strips about 10 square centimeters) and walls was insured by inflated balloons (2 bar pressure). We recommend that horizontal boreholes be slightly inclined towards their mouth in order to drain any pore water arrivals. We recommend also placing the electrodes against the top wall of the boreholes to prevent their immersion in case of water flow. Also it could be interesting to collect the water outflows and estimate the total quantity of mobilized pore water.

Finally, the experiment could be complemented by measuring electrical properties in drill cores and by monitoring temperature, pressure and humidity in the gallery during the geo-electrical monitoring.

9.2 Recommendation 2: instrument characteristics and their emplacement in the monitored rock mass

Instrument (acoustic/microseismic sensors) characteristics, in particular their frequency response, are strongly affected by attenuation in clay rocks. There should be a compromise between volume to be monitored and expected resolution. Frequency response of the sensor should be as flat as possible over a wide range of frequencies and also sensitive (in amplitude). Those used by LE GONIDEC et al. (2012) have piezoelectric ceramic component characterized by a quasi-flat response between 2 and 60 kHz. One may argue that to be sure of available localization, 3 direction (x, y and z) accelerators should be employed. This permits source localization even if two sensors receive the events. Indeed, in

LE GONIDEC et al. (2012 and 2014), data preprocessing pointed out many isolated events, i.e. events detected only by two or three sensors, and thus unusable for localization.

Acoustic active (man-made) sources (for wave-velocity measurements) need to be impulsive and very low frequency to be received by numerous sensors and have a good coverage of the rock mass characteristics. Piezoelectric elements used as receivers and transmitters in LE GONIDEC et al. (2012) did not allow cross-hole transmission experiments. The emission signals were too attenuated from one borehole to another, being spaced at 3 to 6 m.

Attenuation of elastic signals can be also due to interface effects between borehole face and sensors (receivers and transmitters). Hence, particular attention should be paid to borehole drilling; surfaces should be as smooth as possible. Emplacement of sensor antenna should be in place soon after borehole drilling to avoid any deformation due to the more-or-less well-known, plastic behavior of clay rocks. Sensors should have concave coupling faces. Moreover their borehole positioning should be as accurate as possible. In regard to tools for mechanical coupling, pressurized inflatable membranes seem to be a practical method to ensure long-term mechanical coupling of sensors to borehole faces (LE GONIDEC et al. 2012).

Results of experiments detailed in this report showed that changes in the electrical resistivity are noticeable at distances of several tens of m behind the front of a gallery excavation. However, the main changes occur in the first metres behind the front, at the rate of excavation i.e. during the few days preceding the arrival of the front. And if the excavation is stopped, small changes in the electrical resistivity are still noticeable during a few days after cessation of excavation.

Consequently, the experimental setup has to be installed in the zone to be studied several weeks before excavation, in order to get reference data of the undisturbed medium. Then, in order to record damage induced by the excavation, “continuous” measurements of electrical resistivity should start when the excavation front is located at some ten metres from the instrumented zone, and should continue during a few days after the stop of excavation if any. The rate of the repeated measurements has to be fast enough to track changes that can occur over short periods (a few hours sometimes).

As for seismic experiments, a highly detailed time schedule of the excavation procedure is necessary for the data interpretation, especially the precise date when the boreholes are opened by the excavation.

9.3 Perspectives

The rock mass involved during this mine-by test was located at the transition between the sandy and shaly facies and was intersected by three fault systems identified in the Mont Terri rock laboratory. This quite complex petrological and tectonic context impacts clearly the rock mass response to the stress redistribution processes. Indeed, an asymmetric EDZ appears to develop around the Ga08 with microfractures opening (spalling) in the vicinity of the shaly facies wall, and without any damage phenomenon detected in the

sandy facies wall. It is obvious that, this asymmetry should be confirmed by additional numerical mechanical modelling of the induced stress field due to the excavation. Stress field modelling should also reinforce interpretation of fault reactivation and/or bedding reworking processes that took place into the EZ-G08 segment. In a strictly experiment design point of view, this additional numerical modelling should have been performed several months in advance to determine the best mine-by test geometry. The mechanical interpretation should also be enriched by mechanical tests on rock samples. A laboratory scale approach of the two facies should provide information on heterogeneities and anisotropy impact on mechanical behaviour related to principal stress orientation.

The EZ-G04 face was exposed to tunnel ambient air for four years and was not covered by any shotcrete layer; hence significant desaturation occurred along the large tectonic fractures, in particular along the major SW-dipping fault that intersects the ceiling and sidewalls of the Gallery 04. Short term desaturation processes should also impact EZ-G08 front and walls. As confirmed by the electrical tomography results, desaturation occurs mainly along bedding planes and fractures; the major SW-dipping fault dividing two compartments, upper domain with higher resistivity and a lower rock domain less resistive. Observed wet spots and water outflows from three boreholes drilled in the lower domain have certainly contributed to eliminating any desaturation in this rock mass and hence maintaining the electrical contact between the beds. Observed drop in apparent resistivity may be explained by the sudden presence of this water along the electrode lines.

Indeed, significant amounts of water came out of the boreholes when opened. Beyond the experimental adaptation needed to avoid water infiltration inside our sensors; the water production mechanism remains a key question as it greatly could affect the electrical properties and the noble gas diffusion process. Opening of boreholes should have mobilized pore water by suction effects due to decompression; suction processes would be favoured by a high hydraulic gradient caused by the excavation. We argue that self-potential measurements could be useful as a passive tool for monitoring of “wet-spots” in argillaceous formations. Laboratory scale experiments to determine suction mechanisms should also bring additional information.

Moreover, as the ability of the damaged zone to carry fluid over some distance along the walls of the gallery depends on the connectivity of the EDZ fractures and on the percolation status of the network that they constitute. Additional information about the EDZ fractures depth and density, from several boreholes analysis, should help the prediction of hydromechanical properties.

References

- LE GONIDEC, Y., SAROUT, J., WASSERMANN, J. & NUSSBAUM, C. (2014): Damage initiation and propagation assessed from stress-induced microseismic events during a mine-by test in the Opalinus Clay. – *Geophys. J. int.* *198*, 126–139.
- LE GONIDEC, Y., SCHUBNEL, A., WASSERMANN, J., GIBERT, D., NUSSBAUM, C., KERGOSIEN, B., SAROUT, J., MAINEULT, A. & GUÉGUEN, Y. (2012): Field-scale acoustic investigation of a damaged anisotropic shale during a gallery excavation. – *Int. J. Rock Mech.* *51*, 136–148.
- MAINEULT, A., THOMAS, B., NUSSBAUM, C., WIECZOREK, K., GIBERT, G., LAVIELLE, B., KERGOSIEN, B., NICOLLIN, F., MAHIOUZ, K. & LESPARRE, N. (2013): Anomalies of noble gases and self-potential associated with fractures and fluid dynamics in a horizontal borehole, Mont Terri Underground Rock Laboratory. – *Engineering Geology* *156*, 46–57.
- NICOLLIN, F., GIBERT, D., LESPARRE, N. & NUSSBAUM, C. (2010): Anisotropy of electrical conductivity of the excavation damaged zone in the Mont Terri Underground Rock Laboratory. – *Geophys. J. int.* *181*, 303–320.

ISSN 1661-9285
ISBN 978-3-302-40090-7



9 783302 400907